Performance analysis of bioanode materials and the study of the metabolic activity of *Rhodopseudomonas palustris* in photo-bioelectrochemical systems

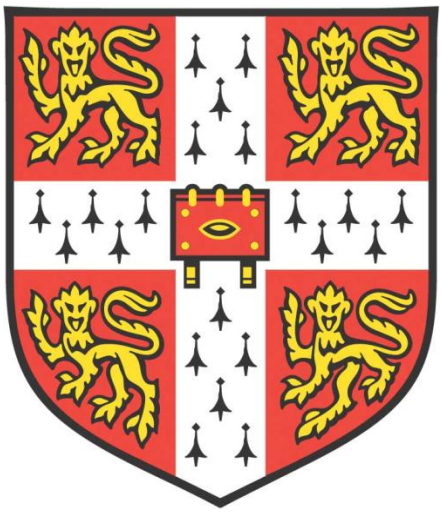

Aazraa Oumayyah Pankan

Department of Chemical Engineering and Biotechnology

University of Cambridge

This dissertation is submitted for the degree of Doctor of Philosophy

Selwyn College September 2018

Performance analysis of bioanode materials and the study of the metabolic activity of *Rhodopseudomonas palustris* in photo-bioelectrochemical systems

Aazraa Oumayyah Pankan

Abstract

A sustainable and low-cost system, namely a photo-bioelectrochemical system (photo-BES), based on the natural blueprint of photosynthetic microorganisms was studied. The aim of this research work is to improve the efficiency of electron transfer of the microorganisms for bioelectricity generation. The first strategy adopted was the evaluation of the exoelectrogenic activity of oxygenic photosynthetic cyanobaterium, *Synechococcus elongatus* PCC 7942, in biophotovoltaic (BPV) platforms through a comparative performance analysis of bioanode materials. The second approach involved improving the performance of anoxygenic photosynthetic bacterium, *Rhodopseudomonas palustris* ATCC® 17001™, by varying the ratio of nitrogen to carbon sources (N:C) to maximise both biohydrogen production and exoelectrogenesis for conversion into bioelectricity in photosynthetic microbial fuel cells (photoMFCs). A linear correlation was obtained between average surface roughness/surface area and maximum power density of ITO-coated and graphene/ITO-coated substrates. Graphene/ITO-coated PET bioanodes produced the highest maximum power output of 29±4 μW m^{-2} in a single chamber BPV device due to improved biofilm formation and improved electrochemical activity. XG Leaf®, also known as graphene paper, helped to bridge the shortcomings of carbon fibres in terms of wettability. The most hydrophilic, 240 μm thick graphene paper, produced the highest maximum power output of 393±20 μW m^{-2} in a membrane electrode assembly (MEA)-type BPV device, mainly due

to reduced electrochemical polarisation. A proof of concept study compared the performance of screen-printed graphene onto a membrane separator against 3D-printed bioanodes coated with carbon nanotubes. One mm thick 3D-printed bioanode was better performing as its structures promoted a much denser biofilm with extensive fibrous extracellular matrix. Using a ratio of N:C=0.20 resulted in higher biohydrogen production and higher exoelectrogenic activity, generating a maximum power output of 361±157 mW m^{-2} and 2.39±0.13 mW m^{-2}, respectively. This study provided additional insight in improving the electron transfer efficiency, which could be used to further optimise photo-BESs as part of future research and development for sustainable technologies.

To Mom, Dad, Loubna and Nani…

Declaration

This dissertation is the result of my own work and includes nothing, which is the outcome of work done in collaboration except as specified in the text.

It is not substantially the same as any that I have submitted, or, is being concurrently submitted for a degree or diploma or other qualification at the University of Cambridge or any other University or similar institution except as specified in the text. I further state that no substantial part of my dissertation has already been submitted, or, is being concurrently submitted for any such degree, diploma or other qualification at the University of Cambridge or any other University or similar institution except as specified in the text.

This dissertation contains fewer than 65,000 words including appendices, references, tables and equations and has fewer than 150 figures.

Aazraa Oumayyah Pankan

September 2018

Acknowledgements

I am thankful to a multitude of people. First and foremost, I would like to express my appreciation of the support provided by my supervisor, Dr Adrian Fisher. My most sincere gratitude goes out to my advisor, Dr Kamran Yunus for his generous guidance throughout my PhD and for his technical advice on design engineering. I would, also, like to thank him for all the 3D drawings that are included in this thesis. I received a Cambridge International Scholarship from Cambridge Trust without which the journey would not have been possible.

I would like to extend my thanks to my collaborators at the Cambridge Graphene Centre, especially Dr Stephen Hodge and Professor Andrea Ferrari for the development of all the graphene-based bioanodes. My special thanks go to my other collaborators, Ela Sachyani at The Hebrew University and Dr Kamal Elouarzaki at Cambridge CARES, Nanyang Technological University for the development of multi-walled carbon nanotubes coated 3D-printed bioanodes. I would, also, like to acknowledge Professor John Dennis and Martin Chan from the Combustion Group for the use of the gas chromatograph.

The PhD would not have been as enjoyable without the group members at CREST, especially Arely with whom I have thoroughly enjoyed working in the lab. She has been a confidant and no less than a mentor throughout. Antonio, Fabio, Hassan and Dongda have been supportive friends. The 'Lunch Crew' has been an important part of the last year of my PhD; thank you to Parminder, Sukanya, Hirak and Xiangming for the support and most importantly for the stress-buster moments. Ammara, Raihana and Rezvan have been like family away from home.

The research would not have been as smooth without the help of the lab technicians, especially Peter, Chris and Sue, the staff in Electronics, Mechanical workshop and in the Domestic section. Ian and Stuart from Stores have been patient with my constant requests. Many thanks to Dr Hassan Rahmoune who helped with proofreading.

I am indebted to my parents, sister and extended family for their love, support and encouragement. Adilah, Aslam, Parwez and Roubeena were always around for home comfort.

Table of Contents

List of Figures

List of Tables

Nomenclature

Symbol/Acronym	Description	Units
ΔG	Gibbs free energy	J
ΔG_r	Gibbs free energy of experiment	J
ΔG_r^o	Gibbs free energy of experiment under standard conditions	J
Y_P	Activity coefficient of products	
Y_R	Activity coefficient of reactants	
σ^d	Charge density in diffuse layer	$\mu C\ cm^{-2}$
σ^i	Charge density in inner layer	$\mu C\ cm^{-2}$
ϕ^1	Potential at distance x_1	$J\ C^-$
ϕ^2	Potential at distance x_2	$J\ C^-$
ϕ^M	Potential at the metal electrode	$J\ C^{-1}$
A	Electrode area	cm^2
A_o	Chlorophyll *a* monomer	
A_1	Molecule of phylloquinone	
ADP	Adenosine diphosphate	
AEM	Anion exchange membrane	
AEMs	Artificial electron mediators	
AFM	Atomic Force Microscope	
Ag/AgCl	Silver/silver chloride	
ATCC	American Type Culture Collection	
ATP	Adenosine triphosphate	
BChl *a*	Bacteriochlorophyll *a*	
BESs	Bioelectrochemical Systems	
BG11	Blue-green medium	
BPh	Bacteriopheophytin	
BPV	Biophotovoltaic	
C	Capacitance	F

C_i	Concentration of species i	mol cm^{-3}
C_p	In-plane electrical conductivity	S m^{-1}
CAIC	Cambridge Advanced Imaging Centre	
CBB	Calvin-Benson-Bassham	
CbcL	Putative quinol oxidases	
CCAP	Culture Collection of Algae and Protozoa	
CEM	Cation exchange membrane	
CGA009	Strain number of *Rhodopseudomonas palustris*	
Chl *a*	Chlorophyll *a*	
CL	Catalyst layer	
Cl^-	Chloride ions	
CM	Cytoplasmic membrane	
CMC	Carboxymethylcellulose	
CNT	Carbon nanotube	
COP	Conference of Parties	
CSP	Concentrated Solar Power	
CV	Cyclic voltammetry	
CW	Cell wall	
Cyma	Multihaem *c*-cytochrome	
cyt	Cytoplasm	
cyt bc_1	Cytochrome bc_1	
cyt b_6f	Cytochrome b_6f complex	
cyt c_2	Cytochrome c_2	
cyt c_6	Cytochrome c_6	
D_i	Diffusion coefficient of species i	cm^2 s^{-1}
DEET	Direct extracellular electron transfer	
DMSO	Dimethylsulfoxide	
DNA	Deoxyribonucleic acid	
DX-1	Strain number of *Rhodopseudomonas palustris*	
E	Potential across capacitor	V

E^f	Midpoint potential	V
e^-	Electron	
E_1	First applied potential	V
E_2	Second applied potential	V
E_{ano}	Potential of anode	V
E_{cat}	Potential of cathode	V
E_{cell}	Cell voltage	V
E_{emf}	Cell electromotive force	V
E_{pA}	Anodic peak potential	V
E_{pC}	Cathodic peak potential	V
EAB	Electroactive biofilm	
EEMs	Endogenous electron mediators	
EET	Extracellular electron transfer	
EFCs	Enzymatic Fuel Cells	
F	Faraday's constant	C mol^{-1}
FccA	Multihaem *c*-cytochrome	
Fd	Ferredoxin	
Flvs	Flavodiiron proteins	
FNR	Ferredoxin-$NADP^+$ reductase	
FT	Fully treated	
FTO	Fluorine tin oxide	
g	Relative centrifugal force	
GG	Glycogen granules	
GDE	Gas Diffusion Electrode	
GDL	Gas Diffusion Layer	
GHG	Greenhouse gas	
GNP	Graphene nanoplatelets	
H^+	Proton	
HEE	Hydrogen evolution electrode	
HER	Hydrogen evolution reaction	
HT	Hydrogen peroxide treated	
I	Current	A
i	Current transient	A

I_{pA}	Anodic peak current	A
I_{pC}	Cathodic peak current	A
ICM	Intracytoplasmic membrane	
IEA	International Energy Agency	
IEET	Indirect extracellular electron transport	
IHP	Inner Helmholtz plane	
ImcH	Putative quinol oxidases	
ITO	Indium tin oxide	
IUPAC	International Union of Pure and Applied Chemistry	
$J_i(x)$	Flux of species i	mol s^{-1} cm^{-2}
LHI	Light harvesting I	
LHII	Light harvesting II	
LPE	Liquid phase exfoliated	
LSV	Linear sweep voltammetry	
MDCs	Microbial desalination cells	
MEA	Membrane electrode assembly	
MECs	Microbial electrolysis cells	
MERS	Microbial electrochemical remediation system	
MESs	Microbial electrosynthesis systems	
MFCs	Microbial fuel cells	
MSCs	Microbial solar cells	
MtrA	Multihaem *c*-cytochrome	
MtrB	Porin	
MtrC	Multihaem *c*-cytochrome	
MWCNT	Multi-walled carbon nanotube	
n	Number of electrons per reaction mole	
NAD^+	Nicotinamide adenine dinucleotide	
$NADP^+$	Nicotinamide adenine dinucleotide phosphate	

NADPH	Nicotinamide adenine dinucleotide phosphate hydrogen	
N:C	Nitrogen to carbon	
NT	Non-treated	
O	Oxidised species	
OCP	Open circuit potential	V
OD	Optical Density	
OHP	Outer Helmholtz plane	
OmaB	*c*-cytochrome	
OmaC	*c*-cytochrome	
OmbB	Porin	
OmcA	Outer membrane cytochrome A	
OmcB	Outer membrane cytochrome B	
OmcC	Outer membrane cytochrome C	
OmcS	Outer membrane cytochrome S	
ORR	Oxygen reduction reaction	
OTS	Octadecyltrimethoxysilane	
P	Power	W
P_{680}	Main chlorophyll donor of PSII	
P700	Chlorophyll *a* dimer	
PBS	Phosphate buffer solution	
Pc	Plastocyanin	
PCA	Strain number of *Geobacter sulfurreducens*	
PCC	Pasteur Culture Collecion	
PDMS	Polydimethylsiloxane	
PET	Polyethyleneterephthalate	
PHB	Poly(hydroxybutyrate)	
photo-BESs	Photo-bioelectrochemical Systems	
photoMFCs	Photosynthetic Microbial Fuel Cells	
Pi	Inorganic phosphate	
pilA	Pilin protein	
PM(NF)	Nitrogen fixing photosynthetic medium	

PNSB	Photosynthetic Non-sulphur Bacteria	
PANI	Polyaniline	
PANI-NN	Polyaniline nanowire network	
poly P	Polyphosphate	
PpcA	*c*-cytochrome	
PpcD	*c*-cytochrome	
pps	Periplasmic space	
PQ	Plastoquinone	
PQH_2	Plastoquinol	
PSI	Photosystem I	
PSII	Photosystem II	
PT	Plasma treated	
PTFE	Polytetrafluoroethylene	
PV	Photovoltaic	
Q	Charge	C
q	Charge stored	C
Q_A, Q_B	PQ molecule	
q^M	Charge on electrode	C
q^S	Charge in solution	C
Q_BH_2	Hydroquinone	
R	Universal gas constant	J mol^{-1} K^{-1}
R	Reduced species	
R^2	Coefficient of determination	
R_a	Surface roughness	nm
R_{ext}	Resistance of external resistor	Ω
R_{int}	Internal resistance, sum of internal losses	Ω
R_{rms}	Mean roughness	nm
R_s	Surface electrical resistivity	Ω/square
R_z	Maximum roughness	nm
RC	Reaction Centre	
RGO	Reduced graphene oxide	
Ri	Ribosomes	

RP2	Strain number of *Rhodopseudomonas palustris*	
rpm	Revolutions per minute	
Rubisco	Ribulose-1,5-biphosphate carboxylase/oxygenase	
SEM	Scanning Electron Microscope	
SHE	Standard hydrogen electrode	
TM	Thylakoid membrane	
T	Absolute temperature	K
t	Time	s
t_m	Thickness of material	m
TCA	Tricarboxylic acid	
TCD	Thermal conductivity detector	
TEOS	Tetraethyl orthosilicate	
TMAO	Trimethylammonium oxide	
UMACC	University of Malaya Algae Culture Collection	
UNFCC	United Nations Framework on Climate Change	
V_{anode}	Voltage of anode	V
$V_{cathode}$	Voltage of cathode	V
v	Velocity	cm s^{-1}
VRFB	Vanadium redox flow batteries	
W	Work	J
WH	Strain number	
WtE	Waste-to-Energy	
x	Distance from surface of electrode	cm
Z	Tyrosine	
z_i	Charge of species i	C

1 Introduction

1.1 Global Energy Scenario

As Nobel Laureate Richard Smalley pointed out, "Energy is the single most critical challenge facing humanity."[1] Adequate and secure energy is one of the principal facilitators for the welfare and economic development of society. As a result, we have long been dependent on fossil fuels, with oil being the leading fuel at 33% of the global energy mix as illustrated in Figure 1-1.

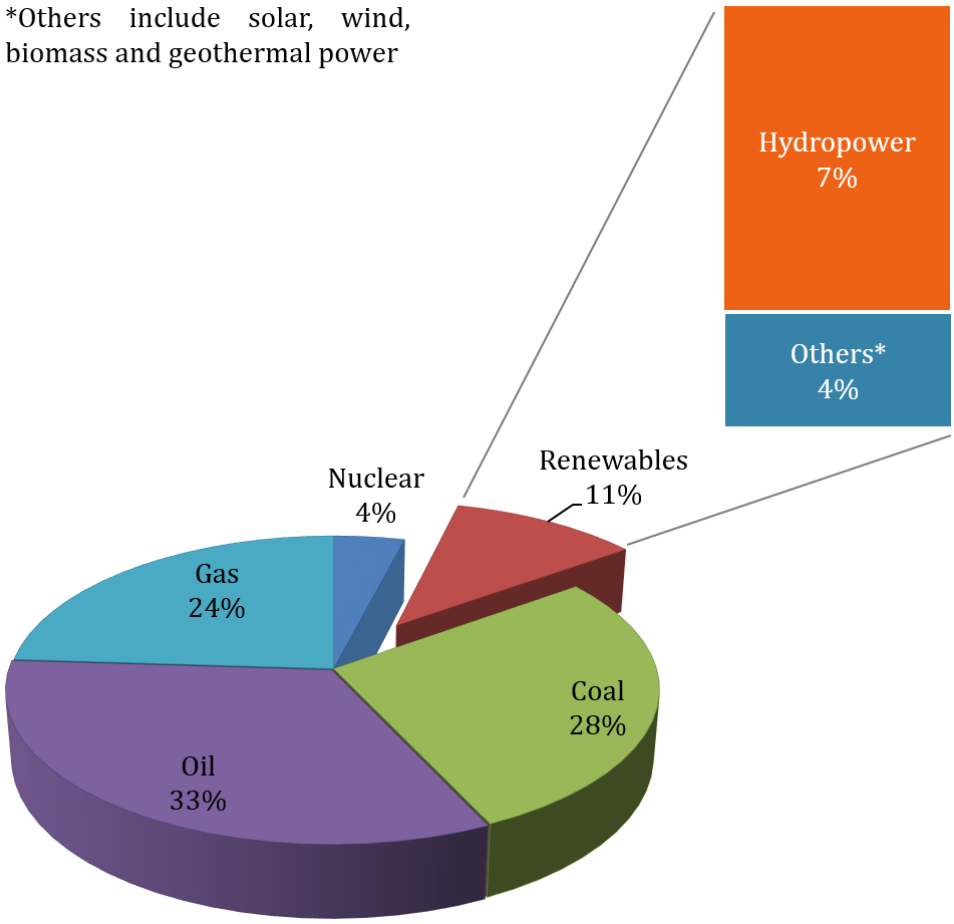

Figure 1-1: The global energy consumption in 2016 as stated in the BP Energy Outlook 2018.[2]

However, energy transitions are occurring worldwide and the major driver is known as the Energy Trilemma, which encompasses safeguarding the energy supply, developing low-cost energy technologies to increase competitiveness and

environmental considerations. This is not to say that that demand for fossil fuel is decreasing as the installed capacity for fossil fuel through 2030 is on a rise.[3]
Nevertheless, concerns for the environment are growing and, hence, as part of the United Nations Framework on Climate Change (UNFCC), the COP21 Paris meeting reached a legally binding and universal agreement on international climate policy on keeping the increase in temperature below 2°C, to keep warming at 1.5°C above pre-industrial levels and to facilitate implementation measures.[3–5] Additionally, the EU's Renewable Energy Directive has set a binding target of 20% final energy consumption from renewable sources by 2020 and has recently set a new renewable energy target of 32% for 2030.[6] Subsequently, the shift in the global energy landscape towards renewable energy technologies is gaining momentum to mitigate greenhouse gas (GHG) emissions. Renewable power grew by 14% in 2016, the largest increase recorded.[3–5] Additionally, projected values of 2040 show that other renewables will have a significant 3.5-fold increase as compared to 2016 while the use of coal will drop significantly as the shift to energy sources with less emission takes place.[2,7]

To pursue the 2°C pathway, alternative sustainable sources of energy with zero-CO_2 emissions must be developed. The International Energy Agency (IEA) spent about 20% of its research, development and demonstration budget on renewable energy sources in 2015, illustrating that research and development in cleaner energy technologies is becoming more essential.[8] Amongst the renewable resources, solar energy is the most attractive option as it is the most abundant sustainable source of energy available. The amount of light energy striking Earth is at an annual rate of 178 000 TW[9], which enormously exceeds the present annual energy consumption rate of approximately 18 TW as well as any probable future energy needs.[8,10] Therefore, solar energy presents a vast source of energy that can be tapped. However, solar energy is diffused, intermittent and varies according to the geographical location. One of the greatest challenges of our time is to design mechanism to efficiently harvest and store this energy for societal use.

1.2 Capture of Solar Energy

Solar energy can be harnessed by using three different methods, namely (1) the solar fuel route, (2) the solar thermal route and (3) the solar electricity route.

Solar fuel is generated when solar energy is captured and stored directly in the chemical bonds of a material. The concept is based on photosynthesis, where sunlight is used to convert water and carbon dioxide into oxygen and sugars and other chemical energy carriers, which can be termed as fuels. Two important types of solar fuels production have achieved significant progress by employing artificial photosynthesis.[4,11] The first type of fuel is hydrogen produced by splitting water with sunlight at a current average solar-to-fuel efficiencies of about 7%. Laboratory prototype systems in Germany and the United States have achieved efficiencies of about 14%.[4] A newer type of solar fuel is carbon-based fuels such as methane, carbon monoxide, synthesis gas and methanol generated by using sunlight, carbon dioxide and for instance water.[11] Current efficiencies of this method are approximately 18% and hythane, which is a blend of hydrogen and methane, can be produced at an efficiency of 20%.[4] Solar fuels overcome the challenge of infrequency of solar irradiation and storage as the energy from the sun are stored in the chemical bonds of the fuels. They can be burnt to generate heat, be converted into electrical or mechanical work and be used to generate electricity directly in fuel cells and batteries.[12,13] Figure 1-2 illustrates the process of artificial photosynthesis currently used to generate solar fuels.

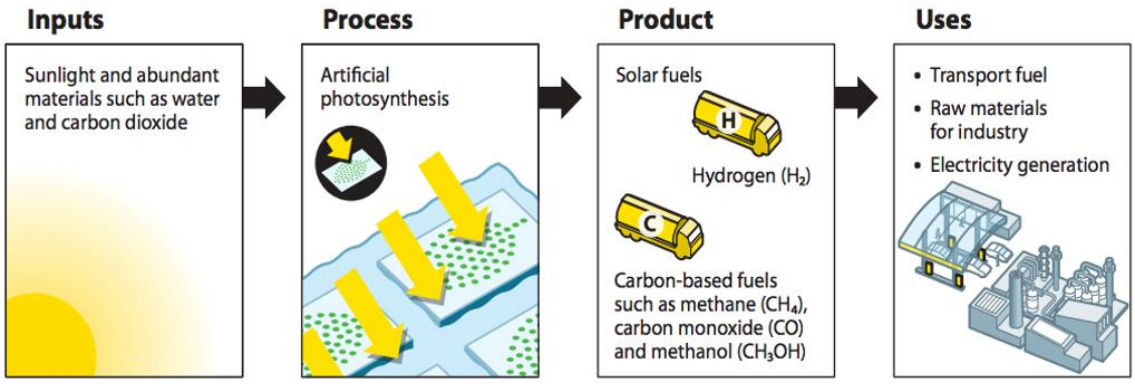

Figure 1-2: The pathway of artificial photosynthesis from sunlight to solar fuels. Reproduced from Royal Society of Chemistry.[11]

Solar thermal energy is characterised by concentrated solar power (CSP) by using solar thermal collectors. The technology involves focusing solar energy by using mirrors and lenses to generate heat energy. The mirrors follow the sun to heat a working fluid, such as oils, molten salts, air and carbon dioxide to very high temperatures. The heat generated can be used for heating and cooling applications, to drive a heat engine or a generator to produce electricity. The variation in CSP technologies is due to

parameters such as optical design, shape of receivers, nature of the transfer fluid and capability to store heat. Thus, solar thermal collectors can be categorised into parabolic trough collectors, linear Fresnel reflectors, central receivers or solar towers and parabolic dishes as depicted in Figure 1-3. Even though the efficiency of these systems ranges between 70 to 80%, the technology has limited capacity with currently 4 GW and a projected 256 GW in 2040. [4,11]

However, solar thermal plants have significant land and water footprints. Utility-scale generation requires a considerable amount of land with approximately 7.3 acres per MW of power. Moreover, they have a higher water demand than both coal and nuclear generation plants with the same cooling system. Therefore, the impact on both land and water usages should be taken into consideration.[4]

Figure 1-3: Different types of concentrated solar power technologies (a) parabolic trough collectors (b) linear Fresnel reflectors (c) solar tower and (d) parabolic dishes. Reproduced from World Energy Council.[4]

Solar electricity is mainly defined by photovoltaics (PV) or solar cells, where a semi-conductor is used to convert sunlight directly into electricity. The current photovoltaic technology is largely based on crystalline silicon, typically of two types[4,11], as shown in

Figure 1-4. Although, polycrystalline solar PV has a lower cost of production, the highest efficiency rates of 17-21% are achieved by monocrystalline solar cells. The technology is continuously evolving at research level as solar PV cells are near an efficiency of 50% by using new techniques, such as multi-junction cell configurations and concentrated photovoltaic. Furthermore, the costs of solar PV are falling due to new markets opening up in developing countries, oversupply of installation components and progress in the technology. PV was the main solar power technology with an installed capacity of 227 GW at the end of 2015.[4]

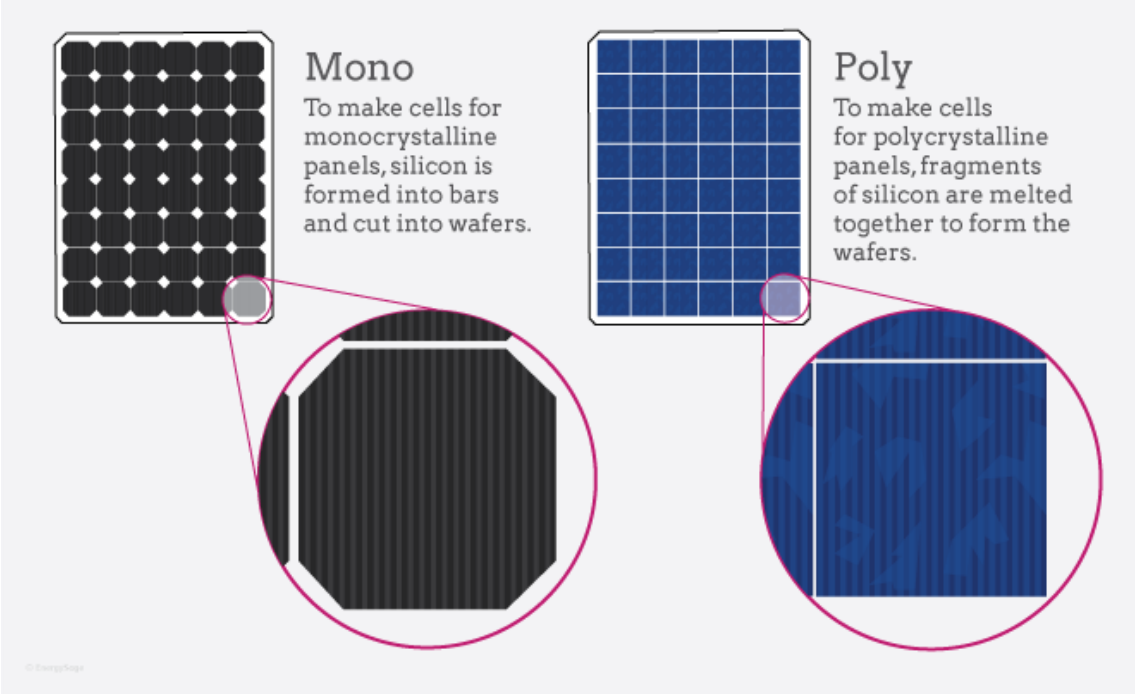

Figure 1-4: Manufacturing and structural differences between monocrystalline and polycrystalline silicon.

As the PV industry is heavily dependent on silicon, alternative materials are being investigated. Research about different organic solar cells, such as dye-sensitised solar cells, antenna cells, molecular organic solar cells and polymeric devices is being carried out. However, only the dye-sensitised solar cell is closest to market introduction. Other compound such as perovskite is being developed as the next generation of solar PV cells. The efficiency of perovskite cells on laboratory scale has increased from 3.8% in 2011 to 20% in 2014. Graphene is being described as the material for future low cost solar cells, with the prospect of devising high efficiency solar cells on flexible plastic substrates.

While the main advantage of solar energy is the low level emission of GHG, other environmental concerns might arise with implementing the technology. They have high land footprint and thus compete with other land applications. However, the main concerns occur at the manufacturing, transportation and installation phases as hazardous materials are involved. Moreover, there is yet no specific protocol for the disposal of solar panels as recycling them is not economically feasible.[4]

1.3 Photo-bioelectrochemical Systems

An alternative technology, which is not commercially available yet but falls under the umbrella term of solar electricity is photo-bioelectrochemical systems (photo-BESs).[11] BESs are typically electrochemical cells that employ biological materials, termed as biocatalysts, to generate electricity as well as value-added products.[14] These systems rely on the ability of certain microbes to export electrons outside of their cells, a mechanism referred to as exoelectrogenesis.[15] The electrons can, then, be harvested for reductive power and chemical products. In these electrochemical systems, a low redox potential of an oxidation reaction at the anode and a high redox potential of a reduction reaction at the cathode create a potential difference. Electroneutrality is guaranteed by the movement of ions, usually hydrogen ions, through an ion-permeable medium or membrane.

Similarly to photovoltaic cells, electrode materials development is a key research area for photo-BESs. However, the biological species is an additional component to the system. Therefore, the exoelectrogenic activity of the microorganisms needs to be understood to further elucidate the material-biological interface.

Based on the type of biocatalyst used and the mode of operation, BESs can broadly be classified as Microbial Fuel Cells (MFCs), Biophotovoltaics (BPVs) and Enzymatic Fuel Cells (EFCs). MFCs can be further sub-divided into photosynthetic Microbial Fuel Cells (photoMFCs), Microbial Electrolysis Cells (MECs), Microbial Electrosynthesis Systems (MESs), Microbial Desalination Cells (MDCs) and Microbial Solar Cells (MSCs). Figure 1-5 summarises the different types of BESs.[16,17]

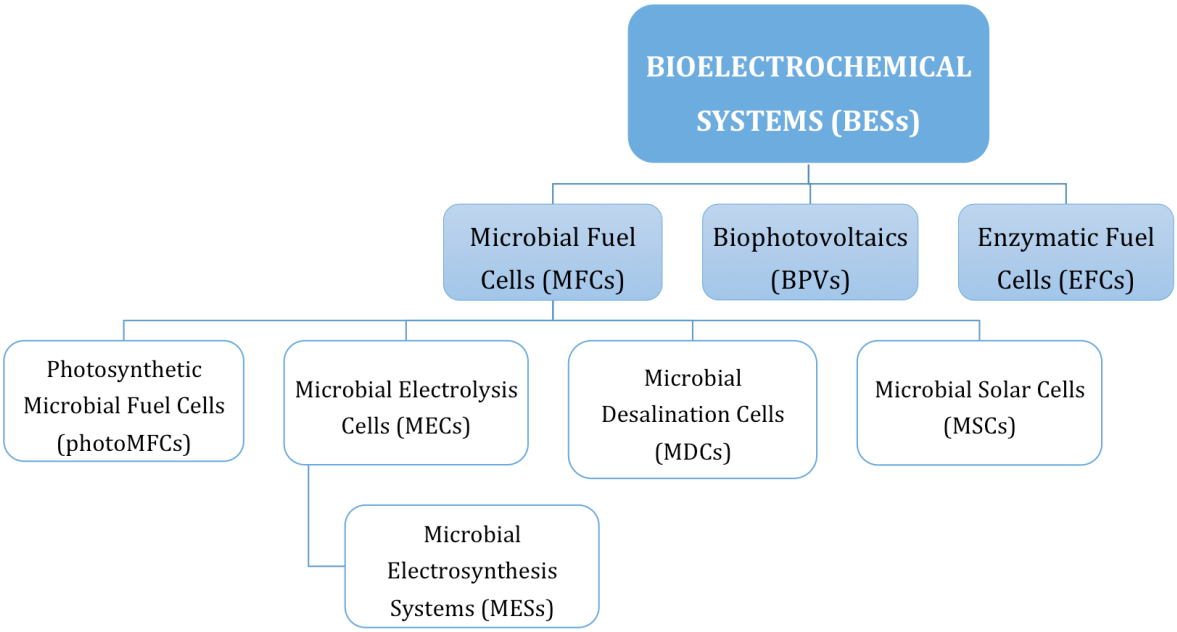

Figure 1-5: Schematic overview of various types of bioelectrochemical systems (BESs).

1.3.1 Microbial Fuel Cells

Microbial fuel cell or MFC is the very first prototype of BESs and most commonly studied. Its main function is bioelectricity generation by electrogenesis. The concept of producing electricity by microbial oxidation of organic molecules was first introduced in 1911 by British Botanist M.C Potter. The yeast *Saccharomyces cerevisiae* and certain species of bacteria catalytically broke down glucose to produce a maximum voltage of 300-500 mV with platinum serving as electrodes.[18] Later in 1931, Cohen ascertained these results by producing a voltage of 35 V at a current of 0.2 mA by stacking bacterial fuel cells.[14] After these two initial studies, interest in the technology was renewed in early 1960s as part of the NASA space programme because of its possible potential of converting human waste into electricity during space flights. The first patent to detail the MFC technology was issued to John Davis in 1967. The bacterium *Nocardia salmonicolor* isolated from sludge oxidised hydrocarbons to alcohols, aldehydes and carboxylic acids.[17]

In MFCs, heterotrophic microorganisms oxidise organic substrates to convert their chemical energy to electrical energy. A wide range of bacterial species can be used for bioelectricity production and amongst them; *Shewanella* and *Geobacter* species were initially widely used. They have been identified as excellent exoelectrogens and are usually referenced as model microorganisms for use in MFCs. Exoelectrogens are

microorganisms that can export electrons outside of their cells to the external environment. Early laboratory studies particularly used acetate, glucose and other simple substrates as a source of energy. The catalytic breakdown of organic matter takes place in the anodic compartment to generate electrons and protons. The electrons travel through an external circuit to a terminal electron acceptor, namely the cathode while the protons move through a membrane or the electrolyte to the cathodic chamber. [17,19,20]

Since the electron transfer rate at the electrode-biofilm interface is one of the important factors determining the performance of MFCs, several studies have focused on improving the morphology and chemistry of the electrode. Thus, biofilm formation and attachment can be promoted for subsequent enhanced electron transfer.[21–23]

1.3.2 Photosynthetic Microbial Fuel Cells

Photosynthetic microbial fuel cell or photoMFC is described as a system where sunlight is converted into electricity within the metabolic schema of a MFC.[24] It intrinsically uses anoxygenic photosynthetic microorganisms, typically purple non-sulphur bacteria (PNSB).[15] Since the microorganisms possess only one type of photosystem, an exogenous supply of reducing equivalents is required for the functioning and growth of the microorganisms. A photoMFC was initially evaluated in 1964 with PNSB *Rhodospirillum rubrum* and malate as the carbon source. A voltage of about 0.6 V was recorded when malate was metabolised into hydrogen, which was subsequently electrocatically oxidised to an electric current.[25] In the 1980s, the catalyst was replaced by artificial redox mediators in the anodic chamber for the generation of electric power. This type of photoMFC was eventually phased out due to the unsustainable use of mediators.[24]

PhotoMFCs are not strictly confined to PNSB. When *Shewanella oneidensis* MR-1 was used in an illuminated MFC, there was a substantial increase in current outputs and was even higher than respiratory-driven current outputs. It was revealed that the increase in current was proportional to the intensity of light used. Another non-PNSB system consisted of green algae *Chlamydomonas reinhardtii* fed with acetate. Depriving the algae of oxygen activated hydrogenase for the light-dependent evolution of hydrogen.[15]

1.3.3 Microbial Electrolysis Cells

The concept of microbial electrolysis cell or MEC emerged in 2005 for the generation of hydrogen from organic substrates by electrohydrogenesis. In a MEC, which is a modified MFC, electrons are obtained from the microbial oxidation of substrates in the anode. Unlike the MFC, the cathode operates anaerobically and, thus, no spontaneous current generation is feasible in the absence of oxygen. Therefore, an external voltage is needed in addition to the electrical potential produced by the bacteria to allow hydrogen gas evolution at the cathode through the reduction of protons. Usually the external voltage required for hydrogen evolution ranges from 0.2 to 1.0 V, which is lower than the 1.8 to 2.0 V needed for conventional water electrolysis. The extra power needed to operate a MEC can eventually be obtained from a MFC.[17,19,20]

1.3.4 Microbial Electrosynthesis Systems

Microbial electrosynthesis systems or MES is a new branch of BES, which produces value-added chemicals at the cathode by the microbial reduction of carbon dioxide and other chemicals. In MES, electrons are exclusively supplied by an external power source, which drives the oxidation of water at an abiotic anode. The resulting electrons and protons are transferred to the cathode so that they can be consumed by electroactive microbes for reduction reactions.[26,27] Acetate has been the main product of CO_2 reduction but recent research has synthesised a mixture of acetate, ethanol and butyrate. The concept of microbial electrosynthesis was introduced in 2009-2010. Methane generation was detected in a reactor with an abiotic anode and a biocathode acclimatised with methanogen *Methanobacterium palustre*. Another study observed that biofilms of *Sporomusa ovata* could accept electrons from the cathode to reduce carbon dioxide into acetate and minimal amount of 2-oxobutyrate. MESs is a promising technology for carbon sequestration and for organic chemicals production. It may also address the harvesting, storage and distributions issues associated with energy crops, solar and wind farms.[19,20,28]

1.3.5 Microbial Desalination Cells

A microbial desalination cell or MDC is a newly developed technology that incorporates a MFC process, electrodialysis for water desalination along with bioelectricity generation. It consists of three compartments with an anion exchange membrane

(AEM) next to the anode and a cation exchange membrane (CEM) by the cathode and a middle chamber between the membranes containing the water to be desalinated. Bacteria oxidise organic matter at the anode producing electrons and protons. The electrons flow to the cathode through an external circuit while the protons are blocked any movement by the AEM. Therefore, anions such as Cl^- and SO_4^{2-} migrate from the middle chamber across the AEM into the anodic compartment. In the cathodic compartment, protons are consumed for the reduction reaction and, thus, cations such as Na^+ and Ca^{2+} move from the middle chamber to the cathodic compartment. The movement of the ions maintain electroneutrality. The process can remove up to 99% of salt as well as produce more energy than the external energy required to operate the system.[29,30] Water desalination using MDC was first investigated in 2009 as a proof-of-concept study. Carbon felt was used as electrodes with sodium acetate as the organic substrate in the anodic chamber and ferricyanide as the catholyte in the cathodic chamber. The desalination chamber contained sodium chloride and 90% salt removal was achieved in one single batch desalination cycle.[31]

1.3.6 Microbial Solar Cells

Microbial solar cells or MSCs integrate photosynthetic reaction with microbial electricity or chemical production by using the synergy between photosynthetic microorganisms and heterotrophic bacteria. The photosynthetic microorganisms that convert solar energy to organic matter include higher plants, photoautotrophic bacteria and algae. The heterotrophic bacteria are electroactive species used in the other types of MFCs. The basic principle of MSCs can be broken down into four steps: (i) photosynthesis of organic matter (ii) transport of the organic matter to the anode chamber (iii) anodic oxidation of organic matter by heterotrophic bacteria and (iv) cathodic reduction of oxygen or other electron acceptors.[19,20]

Plant MSCs are the most popular, where organic rhizodeposits produced are fed to electroactive bacteria for electricity production. Reed mannagrass and rice plants were the first to be used for syntrophic power production of 67 mW m^{-2} and 26 mW m^{-2}, respectively.[20]

1.3.7 Biophotovoltaics

Biophotovoltaics or BPVs utilise oxygenic photosynthetic microorganisms, such as microalgae and cyanobacteria, to harness light energy for the generation of electric current through the photolysis of water.[15] When the microorganisms undergo photosynthesis, water is split into electrons, protons and oxygen in the anodic chamber. The electrons obtained from photosynthesis flow through an external circuit to recombine with protons and oxygen to form water at the cathode.[32,33] The key feature of BPVs is that they do not require an exogenous supply of reducing equivalents. Moreover, these systems can generate power in the dark by the respiratory breakdown of carbon reserves accumulated during the light period. BPVs have the added benefit of being carbon neutral as the photosynthetic microorganisms can fix carbon dioxide into their biomass.[15,34]

Initial studies of light-dependent current generation were observed with both filamentous and unicellular cyanobacteria in the anodic chamber, using mostly artificial electron mediators to extract electrons from within the cells.[15] Zou et al.[35] was one of the first researchers to demonstrate a positive light response in a mediatorless BPV device with a biofilm of *Synechocystis* sp. PCC 6803 growing on a carbon-based anode. This study led to the finding that light-dependent exoelectrogenic activities are common across a wide spectrum of oxygenic photosynthetic microorganisms.

However, BPVs produce lower power densities as compared to MFC systems[34], described above. One of the strategies adopted to overcome this shortcoming is to enhance the electrochemical interaction between the anode and the biofilm. Several research work focus on improving the anode material through comparative studies.[36,37]

1.3.8 Enzymatic Fuel Cells

Enzymatic fuel cells or EFCs employ enzymes as biocatalysts and based on their specific redox functions, they can be used for both anodic and cathodic reactions.[17,19] Davis and Yarbrough[38] detected an electric current when the enzyme glucose oxidase was added in a solution of glucose in a biofuel cell. EFCs usually generate power densities of higher orders of magnitude than MFCs, which is regarded to be due to the mass transfer resistances across the cell membranes. Moreover, enzymes are highly

specific, which eliminate the need for a membrane separator. However, enzymes can only partially oxidise the fuel and generally have a limited shelf life of about 7 to 10 days. The operating lifetime of enzymes has been extended by developing novel polymers for immobilisation and stabilisation. Redox enzymes are commonly used for the fabrication of amperometric enzyme electrodes. The biocathode is usually made of multi-copper oxidases having the capacity of a four-electron reduction of oxygen to water and additionally have a high specificity for this reaction.

Current EFCs have low efficiencies as single enzymes are typically employed and the fuel is only partially oxidised. Two methods can be used to overcome these deficiencies. Multi-enzyme based EFCs can help to improve substrate conversion and subsequently the performance of the system. Moreover, immobilisation of enzymes on the surface of electrodes significantly enhanced the performance of the systems by increasing selectivity, mass transfer and long-term stability. Immobilisation techniques include physical adsorption and entrapment in conducting polymers.[17,19]

Figure 1-6 summarises the different types of BESs described above with respective general reactions being depicted.

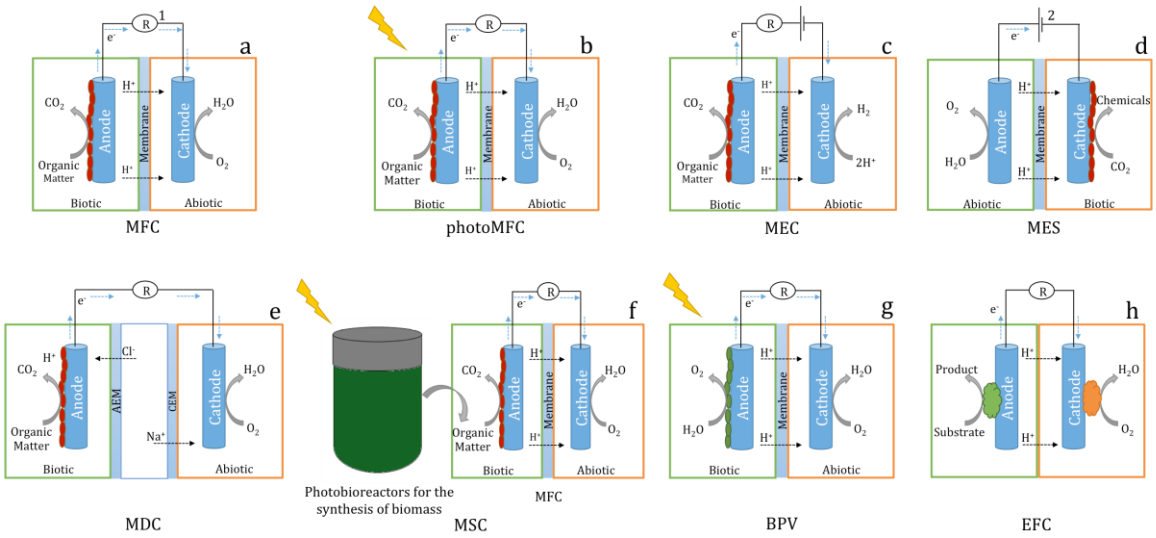

Figure 1-6: The various forms of bioelectrochemical systems (BESs) (a) microbial fuel cell (b) photosynthetic microbial fuel cell (c) microbial electrolysis cell (d) microbial electrosynthesis system (e) microbial desalination cell (f) microbial solar cell (g) biophotovoltaic and (h) enzymatic fuel cell without a membrane. 1 represents electron harvested from the system and 2 illustrates electrons supplied by external power source.

1.4 Current Research Focus

The two types of BESs that strictly utilise solar energy to drive their reactions are BPVs and photoMFCs, as observed in Figure 1-6. Light-harvesting BESs are emerging as promising sustainable technologies due to the inexhaustible supply of energy from solar radiation.[15] Therefore, BPVs and photoMFCs will be evaluated as two potential platforms for the study of the electrode-biofilm interface for the end output of solar electricity generation as shown in Figure 1-7. For the sake of analysis and clarity, the two platforms will be differentiated into case studies. **Case Study 1** will involve the use of oxygenic photosynthetic cyanobacterium *Synechococcus elongatus* PCC 7942 (*S. elongatus* hereafter) in BPVs while **Case Study 2** will include anoxygenic photosynthetic purple non-sulphur bacterium *Rhodopseudomonas palustris* ATCC® 17001™ (*R. palustris* hereafter) in photoMFCs.

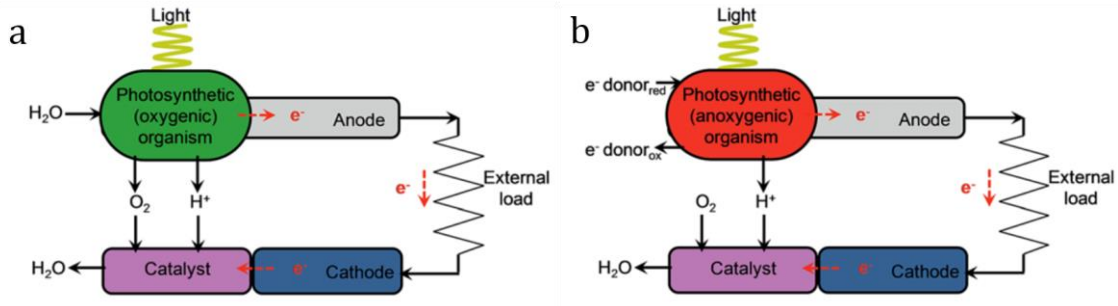

Figure 1-7: Schematic depiction of the two platforms of interest (a) BPV and (b) photoMFC. Reproduced from McCormick et al.[15]

There is general consensus that not one type of technology will solve future energy needs but rather a mix of sustainable technologies will be required.[39] The framework, thus, being proposed for solar energy capture and conversion is based on the natural blueprint of photosynthetic microorganisms in bioelectrochemical systems (BESs).

The research focus, moreover, aligns with the European Commission's Bioeconomy Strategy for a resource efficient and sustainable economy. The bioeconomy consists of the use of renewable biological resources from both land and ocean, such as crops, forests, animals and microorganisms, for the production of food, materials and energy.[40]

The following section highlights the similarities and differences between BPVs and photoMFCs.

1.4.1 Photo-pigments

The photosensitive components of both BPVs and photoMFCs are assembled and maintained by living organisms, namely *S. elongatus* and *R. palustris*, respectively. These photosynthetic microorganisms have the ability of self-repair and reproduction. They are resilient, self-sustainable, inexpensive and are easily available. Moreover, they have the ability to store energy for power generation in the dark.[29,35,36]

S. elongatus is identified by the photosynthetic pigment chlorophyll *a* (Chl *a*) whereas *R. palustris* synthesises a related but a more reduced derivative, known as bacteriochlorophyll *a* (BChl *a*). These pigments both contain Mg-tetrapyrrole and the analysis of its intermediates has led to the current understanding of their biosynthetic pathways. As shown in Figure 1-8, both pathways use the common intermediates from 5-aminolevulinate via Mg-protoporphyrin IX to form chlorophyllide *a*. At this stage, the reaction is split into two. The formation of Chl *a* is catalysed by the enzyme chlorophyll synthase in an esterification process while an additional step is required for the synthesis of BChl *a* by converting the chlorophyllide *a* ring to a more reduced structure of bacteriochlorophyllide *a*. The latter undergoes an esterification process, catalysed by the enzyme bacteriochlorophyll synthase to form BChl *a*.[43]

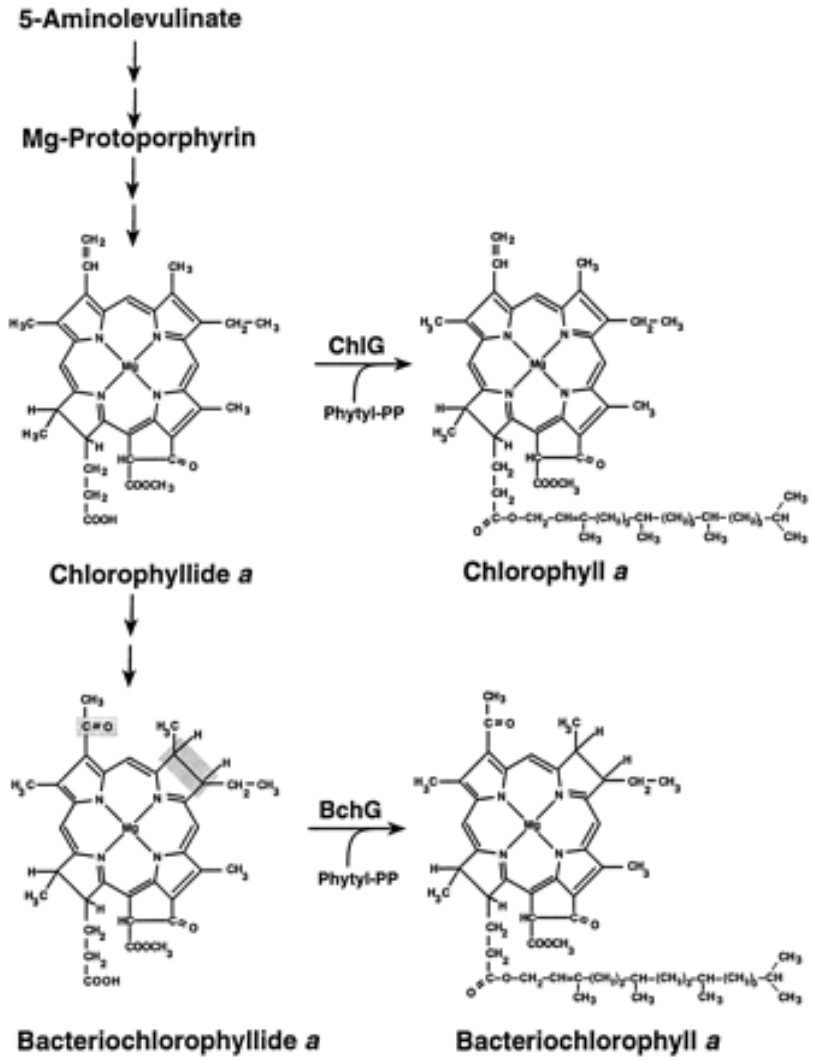

Figure 1-8: Common intermediates involved in chlorophyll and bacteriochlorophyll biosynthetic pathways. Reproduced from Oster et al.[43]

Both Chl *a* and BChl *a* are membrane-bound and serve dual roles; they act like antenna to harvest light and participate as a redox compound in electronic excitation trapping and electron transporting events in the reaction centres of Photosystem II and I, as it applies.[44,45]

Chl *a* in *S. elongatus* absorbs blue light (430 nm) strongly and red light (662 nm) weakly.[44,45] BChl *a* in *R. palustris* absorbs light at 390 nm (near ultraviolet), 590 nm, 804 nm and 861 nm (near infrared).[44,46,47] For laboratory scale studies, cool white fluorescent light tubes are more appropriate to illuminate cultures of *S. elongatus* while incandescent/halogen light bulbs are more suitable for cultures of *R. palustris*. Moreover, these two types of light spectrum match that of the daylight, as illustrated in Figure 1-9. It indicates that an efficient harvest of sunlight by the photo-pigments of

both *S. elongatus* and *R. palustris* will be highly probable. More information on light absorption by the microorganisms is provided in Appendix A.

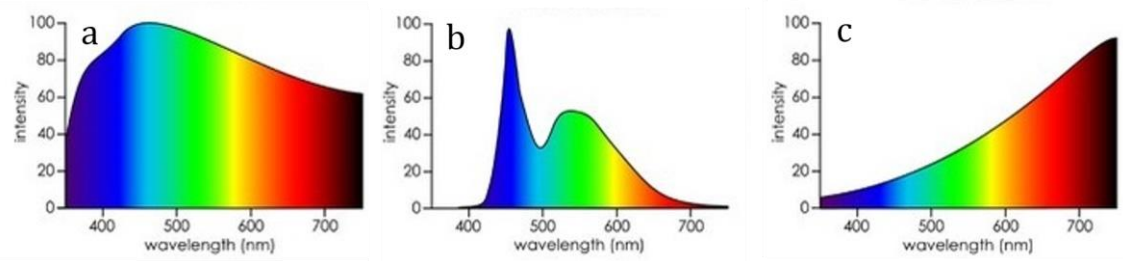

Figure 1-9: Light spectrum of (a) daylight (b) cool white fluorescent light tube and (c) incandescent/halogen light bulb.

1.4.2 Electron Donor

BPVs and photoMFCs differ in the type of biocatalysts employed and in the use of electron donors. *S. elongatus* undergoes oxygenic photosynthesis, which results in the production of oxygen, an important part of the global oxygen flux. However, *R. palustris* carries out anoxygenic photosynthesis that does not generate oxygen.[48] Unless water is the ultimate source of electrons as with oxygenic photosynthetic microorganisms, a sacrificial electron donor is required. However, anoxygenic photosynthetic bacteria do not have the ability to oxidise water and, thus, rely on the addition of an exogenous supply of reducing equivalents, such as sulphide, hydrogen or organic substrates. Consequently, *R. palustris* does not produce oxygen as a by-product of photosynthesis. Therefore, one important distinction between BPVs and photoMFCs is the requirement of a continual supply of an external fuel source for photoMFCs.[34,48]

However, this liability can be overcome by coupling photoMFCs with wastewater treatment. The EU Future Brief on Science for Environment Policy assessed the potential of BESs to concomitantly treat wastewater, generate electricity and value-added products. Substantial amount of wastewater is produced from industrial and agricultural activities. Wastewater generated could, thus, be a potential renewable resource for some photoMFCs as it is rich in organic pollutants. It has been reported that these pollutants contain more internal energy than the amount of energy required to treat wastewater.[49] In this context, photoMFCs can contribute to biological Waste-to-Energy (WtE) technologies, which is expected to grow at an average of 9.7% per annum as new technologies become commercially viable.[4]

1.5 Exoelectrogenic Activity: Intra and Extracellular Electron Transport

Bioelectricity generation by both BPVs and photoMFCs directly depend on the exoelectrogenic capacity of *S. elongatus* and *R. palustris*, respectively. Therefore, to make the microorganisms useful for electricity production and to better understand the material-biological interface, it is imperative to understand the intracellular electron transport mechanism that would eventually lead to extracellular electron transport.

1.5.1 Intracellular Electron Transport

1.5.1.1 Case Study 1: *S. elongatus* in BPVs

1.5.1.1.1 Background

S. elongatus is a unicellular freshwater cyanobacterium. It is a rod-shaped prokaryote and typically less than 10 μm in length or diameter.[50] It is an obligate photoautotroph, that is it uses the reducing equivalents produced by light reactions of photosynthesis to fix carbon and grow. The usual source of carbon is carbon dioxide.[51] It is used as the model organism in this study as cyanobacteria are commonly used in BPVs as compared to eukaryotic organisms, such as green algae as they have simpler physiology and lower basal energy requirements.[15] Moreover, cyanobacterial metabolism is well-characterised which leads towards potential use of genetic manipulations if any specific trait needs to be enhanced.[33,52]

1.5.1.1.2 Mode of Operation: Oxygenic Photosynthesis

The Gram-negative cell envelope of *S. elongatus* consists of three separate layers with a plasma membrane (often known as cytoplasmic membrane), a peptidoglycan layer and an outer membrane, as depicted in Figure 1-10. The inner cellular structures are formed by the thylakoid membranes which are associated with the plasma membrane by the thylakoid associated semi-circular structures and the thylakoid centres. However, the distribution of photosynthetic and respiratory elements between thylakoid and plasma membranes is not clear at present.[53]

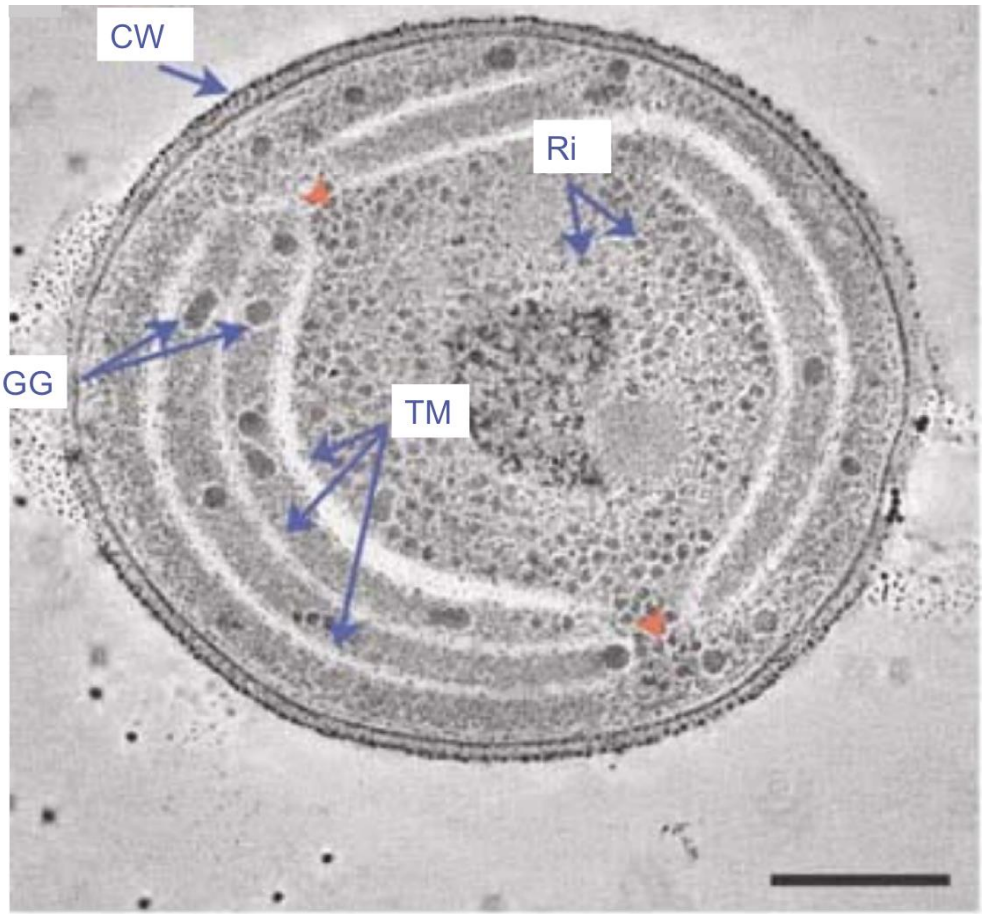

Figure 1-10: Electron micrograph of a cross-section of *Synechococcus elongatus* PCC 7942. TM represents thylakoid membranes that are perforated at multiple sites (shown by orange arrow heads), CW is cell wall, both the inner and outer cell membranes are apparent, Ri is ribosomes and GG is glycogen granules. The scale bar represents 200 nm. Reproduced from Nevo et al.[53]

Oxygenic photosynthesis evolved in the thylakoid membrane of ancient cyanobacteria. The thylakoid membrane contains integral membrane proteins, which play an important role in light harvesting and light-dependent reactions of photosynthesis, as shown in Figure 1-11.

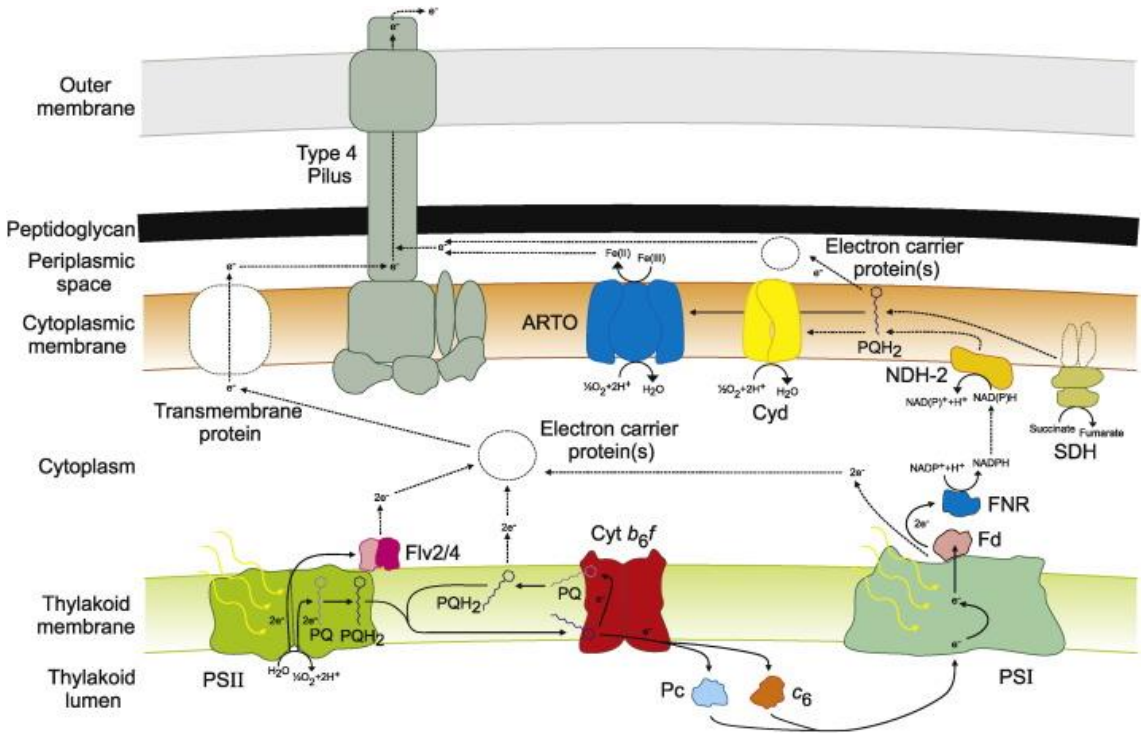

Figure 1-11: Schematic diagram of the possible electron transport routes between the membranes of *Synechocystis* PCC 6803 and the external environment. Broken lines indicate possible electron transport pathways or proteins not yet verified. An example of extracellular electron transport is being shown via a Type IV pilus. Reproduced from Lea-Smith et al.[54]

The four major protein complexes are photosystem I (PSI), photosystem II (PSII), cytochrome b_6f complex (cyt b_6f) and ATP synthase. The linear electron flow in photosynthetic light reactions is carried out by PSI, PSII and cyt b_6f, accompanied by specific soluble proteins, such as plastocyanin and ferredoxin-$NADP^+$ reductase (FNR). The latter catalyses the generation of NADPH. Along with the linear electron flow, a pH gradient is formed across the thylakoid membrane that activates the ATP synthase. The energy amassed in the form of NADPH and ATP is further used for the fixation of carbon dioxide by ribulose-1,5-biphosphate carboxylase/oxygenase (Rubisco) and for other metabolic processes. Besides linear electron flow, alternative electron transfer modes exist in the thylakoid membrane and the surrounding, which include (i) cyclic electron transfer in PSI via NAD(P)H:Quinone oxidoreductases which assist in the production of ATP and NADPH (ii) flavodiiron proteins (Flvs) essential for photoreduction of oxygen and for the photoprotection of PSI and PSII and (iii) terminal oxidases and other respiratory enzymes that provide energy for cell life in the dark.[55]

PSII is the reaction centre that carries out the light catalysed oxidation of water and reduction of plastoquinone (PQ). The main chlorophyll donor of PSII is P_{680}. After light is absorbed, an electron is transferred from an excited state of P_{680} to a phenophytin, which in turn reduces a bound PQ molecule, called Q_A. The latter reduces a second PQ, Q_B, which unlike Q_A can function as a two electrons acceptor. Q_B is then reduced to plastoquinol (PQH_2) while accepting two protons from the cytoplasmic side of the thylakoid membrane. On the donor side of PSII, the chlorophyll cation radical P_{680}^+ oxidises a tyrosine residue, which in turn oxidises a cluster of four manganese atoms. This metal centre is the catalytic site of water oxidation and it is able to gather the four oxidising equivalents which are needed to release oxygen from two molecules of water.[54,56]

After being released from PSII, PQH_2 diffuses through the membrane to cyt b_6f, where it loses two protons to be oxidised on the luminal side of the membrane. One electron is transferred by cyt b_6f to either plastocyanin (Pc) or to cytochrome c_6 (cyt c_6). The other electron is relocated via heme units to the cytoplasmic side where it reduces PQ to PQH•. The reaction is repeated so as to reduce PQH• to PQH_2. Overall, 2 PQH_2 are oxidised on the luminal side of the membrane, releasing to 2 PQs, 2 electrons to Pc or cyt c_6 and 4 protons into the lumen. A reduced PQH_2 is re-formed on the cytoplasmic side.[54]

Pc is the dominant redox carrier while cyt c_6 expression is minimal when copper is plentiful. Both Pc and cyt c_6 reduce PSI with similar kinetics. PSI reaction centre is a membrane-bound, multiprotein complex which usually functions as a light-driven cytochrome c_6:ferredoxin oxidoreductase. It contains all the biochemical machinery needed to generate efficient charge separation across the thylakoid membrane for the conversion of a red photon into free chemical energy. The machinery consists of about 110 antenna chlorophyll *a* molecules to provide a large optical cross-section for incoming photons and a series of inorganic and organic cofactors for charge separation and stabilisation. A matrix of 11 polypeptides provide ligands to the photoactive components. In reaction centre PSI, the initial events follow the sequences in Equation 1-1.

$$P700\ A_o\ A_1 \overset{h\nu}{\rightarrow} P700^+\ A_o^-\ A_1 \rightarrow P700\ A_o\ A_1^-$$

Equation 1-1

P700 is a chlorophyll *a* dimer and the primary electron donor, A_o is a chlorophyll *a* monomer and an electron acceptor and A_1 is a bound molecule of phylloquinone and a secondary electron acceptor. According to Equation 1-1, the absorption of a photon by one of the 110 chlorophyll antenna molecules results in the transient charge separation between P700 and A_o. The electron on A_o^- is quickly shifted to A_1, the bound phylloquinone to stabilise the separated charges against the quick and inevitable charge recombination that would happen between the primary electron donor and acceptor pair.

The excited electron generated in the core complex replaces the resulting electron obtained from Pc or cyt c_6 and it is transferred via iron-sulphur clusters to ferredoxin (Fd). It is, then, moved to ferredoxin-$NADP^+$ reductase for the conversion of $NADP^+$ to NADPH.

For each NADPH generated, two electrons are required. In short, to generate 1 molecule of NADPH molecule, one molecule of water is split and an electrochemical gradient across the thylakoid membrane is created which is equivalent to 6 protons. The proton gradient is used to drive ATP production via ATP synthase. Moreover, the cyclic electron transport in PSI helps in increasing ATP production.[54,56]

Inhibitor and mutant studies have generally indicated that electrons generated by PSII for exoelectrogenic activity leaves the photosynthetic electron transport chain at PSI.[33] The different possible ways of exporting electrons to a solid electron acceptor will be discussed in Section 1.5.2.

Figure 1-12 highlights the main reactions that are involved in oxygenic photosynthesis, in what is called the Z-scheme. The photo-excitation of the two redox-coupled photosystems, PSI and PSII, mediate the transfer of electrons from water to NADPH, yielding molecular oxygen and a build-up of protons in the thylakoid membrane.

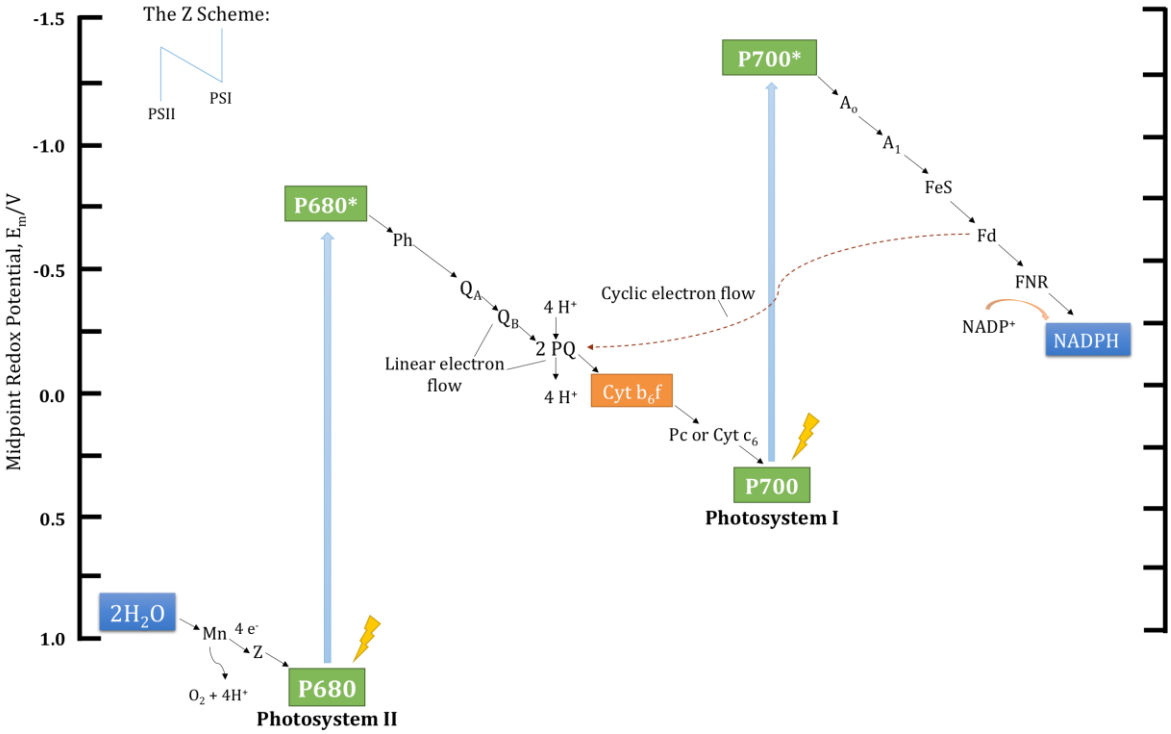

Figure 1-12: Z-scheme illustration of oxygenic photosynthesis. Mn represents manganese complex and Z is tyrosine. Adapted from Mielke et al., Govindjee and Senge et al.[57–59]

1.5.1.2 Case Study 2: *R. palustris* in photoMFCs

1.5.1.2.1 Background

R. palustris is a facultative photosynthetic purple non-sulphur bacterium (PNSB) and it belongs to the taxonomic group *Alphaproteobacteria*.[60] It is usually rod-shaped and measure about 0.6-0.8 µm in diameter and 1.2-2 µm in length and possesses a Gram-negative cell envelope.[61] It is the most metabolically versatile bacterium known as it can function on any one of the four modes of metabolism that supports life: chemoheterotrophy, chemoautotrophy, photoautotrophy and photoheterotrophy as shown in Figure 1-13. It displays exceptional flexibility with each mode of metabolism. It can grow in an aerobic or an anaerobic environment and can use light, inorganic compounds or organic compounds as sources of energy.[60]

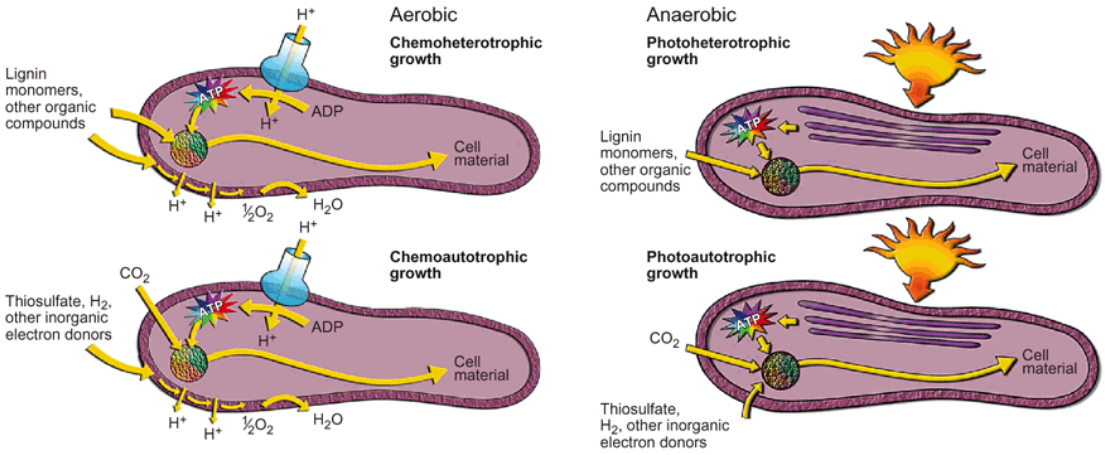

Figure 1-13: The four modes of metabolism that *R. palustris* can express. The multi-coloured circle in each cell represents the enzymatic reactions of the central metabolism. Reproduced from Larimer et al.[60]

1.5.1.2.1.1 Chemotrophs

In this mode, *R. palustris* does not express its photosystem and uses oxygen as a terminal electron acceptor. *R. palustris* produces ATP through the oxygenic respiration of organic compounds chemoheterotrophically. It oxidises inorganic compounds such as thiosulfate and hydrogen gas as energy sources for respiratory growth and as sources of reducing power for carbon dioxide and nitrogen fixation chemoautotrophically.[60,62] Chemoautotrophy can also occur anoxically, where electron acceptors, include compounds of denitrification, dimethylsulfoxide (DMSO) and trimethylammonium oxide (TMAO).[63]

1.5.1.2.1.2 Phototrophs

In this mode, photosynthesis genes enable the use of light as an energy source by cyclic photophosphorylation under anaerobic conditions.[60]

Photoautotroph *R. palustris* utilises inorganic compounds, such as thiosulphate, iron (II) compounds and hydrogen as electron donors for carbon dioxide fixation via the Calvin-Benson-Bassham pathway.[64]

The preferred mode of growth is photoheterotrophically. *R. palustris* can use a wide range of organic compounds, such as lignin monomers, fatty acids, organic acids and alcohols both as a carbon and electron source. Under nitrogen limitation, the nitrogen fixation pathway is expressed. Nitrogenase, the main enzymatic component, reduces

atmospheric nitrogen to synthesise ammonia with hydrogen as an obligatory product.[63,64]

1.5.1.2.2 Mode of Operation

R. palustris has been the most used anoxygenic photosynthetic bacterium in photoMFCs. It is a model microorganism for anoxygenic photosynthesis as it possesses a photosynthetic apparatus that efficiently harnesses energy from sunlight.[60,65,66] It is an appropriate biocatalyst for the nitrogenase-dependent process of biohydrogen production and it is known to metabolise a wide range of carbon compounds.[66–69] Additionally, it allows the monitoring of metabolic reactions when parameters such as changes in light, carbon, nitrogen and electron sources are manipulated experimentally.[60]

In this study, the photoheterotrophic mode of metabolism is chosen as it is the preferred mode of growth and, moreover, it has the added benefit of producing a value-added product in the form of hydrogen. The two main mechanisms involved, namely anoxygenic photosynthesis and photofermentation, are analysed in the sections below.

1.5.1.2.2.1 Anoxygenic Photosynthesis

In a photosynthetic mode of growth, *R. palustris* manifests infolding of the cytoplasmic membrane (CM), which extends into the cell to form stacks of flattened thylakoid membrane sacks, as illustrated in Figure 1-14. The latter are termed as intracytoplasmic membranes (ICMs), which contain the pigment proteins and other constituent related to the photosynthetic activity of the cells. Low oxygen levels favour the synthesis of the ICMs and the components of the photosynthetic apparatus.[70]

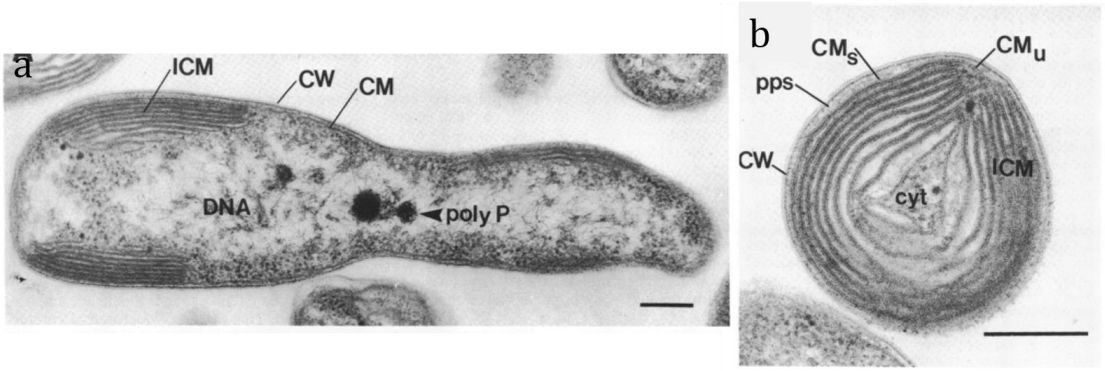

Figure 1-14: Electron micrograph of photosynthetic *R. palustris* (a) Longitudinal cross section showing the intracytoplasmic membrane (ICM), cytoplasmic membrane (CM) and the cell wall

(CW) distinctively. Polyphosphate (poly P) granules and DNA are visible in the central area of the cell (b) Cross-section of cell with additional features, such as a small amount of cytoplasm (cyt) and a relatively wider periplasmic space (pps). CM_u indicates the point where the two ends of the ICM stack converge. The scale bar represents 200 nm. Reproduced from Varga and Staehelin.[70]

Anoxygenic photosynthesis requires only one type of reaction centre and like any other purple bacteria, *R. palustris* possesses photosystem II (PS II) only.[48] The main aim of anoxygenic photosynthesis for heterotroph *R. palustris* is to generate a proton gradient for ATP synthesis.[63,71]

As shown in Figure 1-15, the light reactions are usually initiated with a photon absorption by light-harvesting II (LHII), formed of bacteriochlorophyll *a*, carotenoids and associated proteins. LHII has two absorption bands in the near-infrared at about 800 and 850 nm. The photon is then quickly and efficiently transferred to light harvesting I (LHI), which is housed in the reaction centre (RC) of PSII. LHI typically has a single and strong absorption band at 870 nm. The latter, also, acts as a light-harvester and starts the cyclic electron transport between RC, cytochrome bc_1 (cyt bc_1) and cytochrome c_2 (cyt c_2). Bacteriopheophytin (BPh) is reduced by the excited state of P_{870}* and it, in turn, reduces a quinone molecule, Q_A. An electron from Q_A is then transferred to Q_B, which is loosely bound to the membrane.[72] Once the quinone is doubly reduced, it takes up protons from the cytoplasmic space to form hydroquinone Q_BH_2. The latter diffuses through the membrane to cyt bc_1. At this point, electrons are transferred to cyt c_2 while protons are released into the periplasmic space. Cyt c_2, then, transfers electrons back to the RC, closing the cyclic electron transport chain. The protons accumulated in the periplasm form an electrochemical gradient, which is used to drive ATP production via ATP synthase.[63]

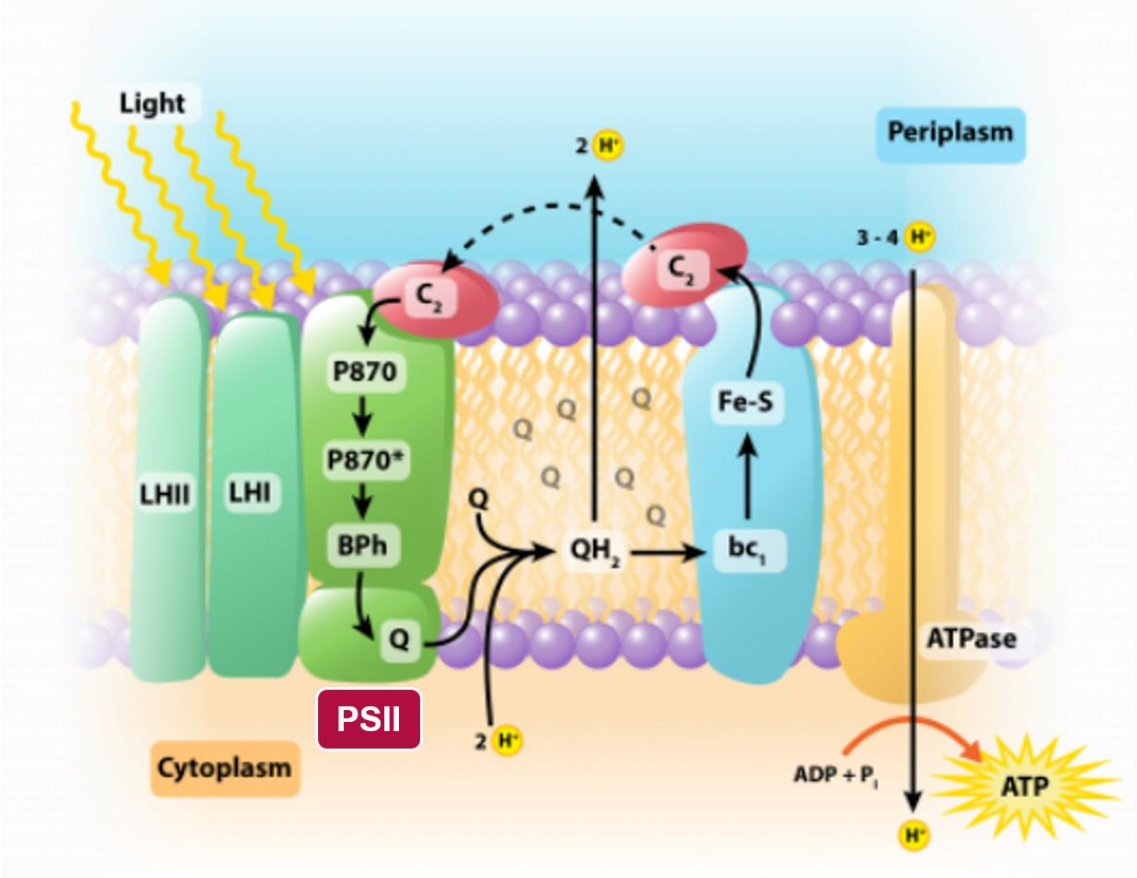

Figure 1-15: A schematic representing major membrane proteins involved in the photosynthetic electron flow. Adapted from Bruslind and Roszak et al.[71,72]

Figure 1-16 summarises the main reactions that are involved in anoxygenic photosynthesis carried out by heterotrophic *R. palustris* in a cyclic electron flow. Electrons are repeatedly energised by the photosystem using light and they are channelled through an H^+-pumping electron transfer chain. The cycling allows for the continuous maintenance of the proton motive force and ATP pools in a process, called cyclic photophosphorylation. The latter is particularly beneficial under starvation conditions as cycling a few electrons can produce useful energy for cell maintenance and repair.[63]

The photosystem is termed as 'cyclic' not because it is a closed loop but because there is no terminal electron acceptor, the electrons are cycled back to the RC. As a result, *R. palustris* has to use other means to dispose of extra electrons that are generated during the oxidation of the carbon source in order to maintain a pool of oxidised electron carrier molecules, such as NAD^+, as needed by important metabolic reactions. The mechanism involves channelling the excess electrons to both the Calvin cycle for

biosynthesis and to nitrogenase for the production of hydrogen. Thus, these two components can potentially compete for reductant because of their common roles.[63,73]

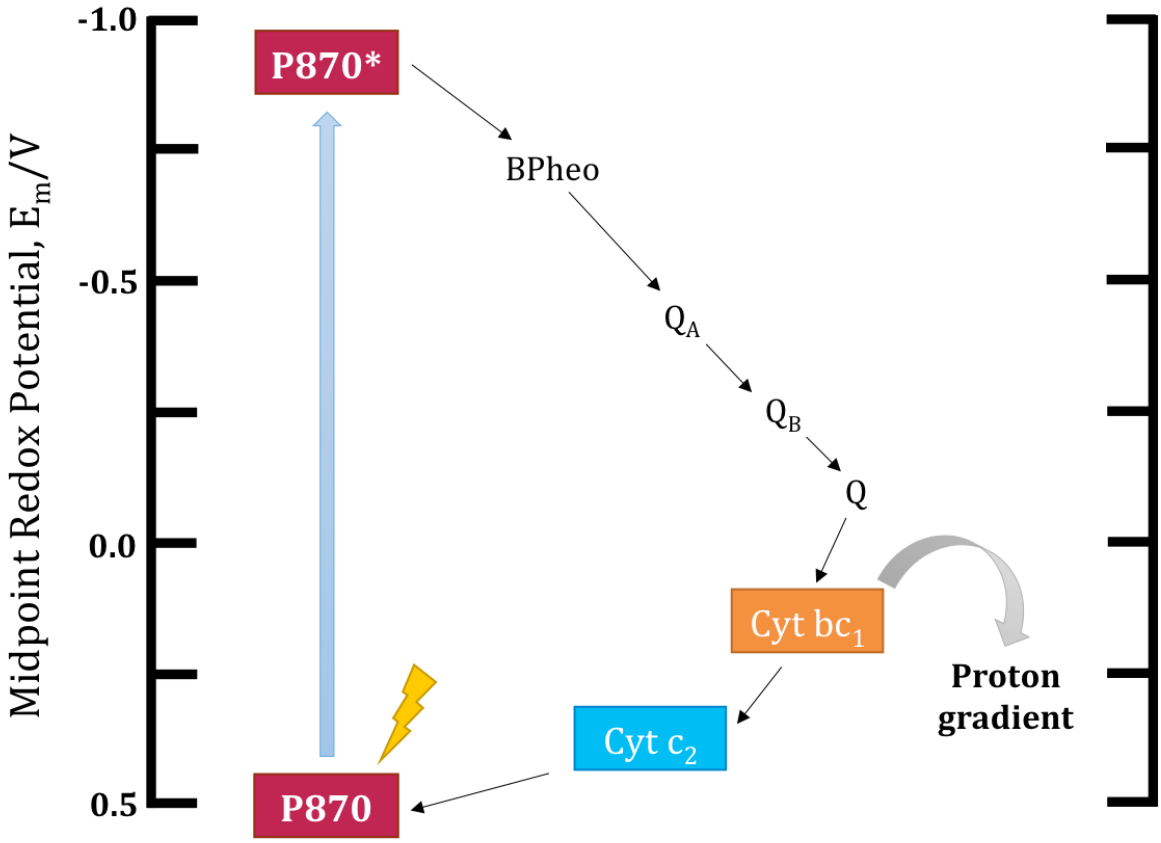

Figure 1-16: Illustration of reactions involved in anoxygenic photosynthesis in heterotroph *R. palustris*. ATP is subsequently generated via a process of cyclic photophosphorylation. Modified from Arnon et al. and Bruslind.[71,74]

1.5.1.2.2.2 Hydrogen Production by Photofermentation

Hydrogen production by *R. palustris* is generated by photofermentation under a photoheterotrophic mode of metabolism. Several individual components are involved in the metabolic production of hydrogen, namely two enzyme systems of nitrogenase and hydrogenase, the TCA cycle for carbon flow and the photosystem. These components are interlinked within the hydrogen production system through the transfer of electrons, protons and ATP.[62,75]

As illustrated in Figure 1-17, when a carbon source is supplied to *R. palustris*, it is simultaneously used as a carbon source for biosynthesis and as an electron source for biohydrogen production. The carbon substrate is oxidised in the TCA cycle to generate carbon dioxide, protons and electrons. The transfer of electrons and protons from the

TCA cycle to nitrogenase occurs by the successive oxidation/reduction of the electron carriers, which include nicotinamide adenine dinucleotide (NAD) and ferredoxin (Fd). In parallel, the photosynthetic apparatus, PSII, converts light energy into ATP, which is channelled to nitrogenase. As a result, the nitrogenase reduces protons to hydrogen gas by consuming ATP. The hydrogenase operates in antithesis to nitrogenase by consuming hydrogen for the production of protons and electrons for ATP synthase. Therefore, the total hydrogen produced is the balance between hydrogen synthesised by nitrogenase and hydrogen consumed by hydrogenase.[75,76]

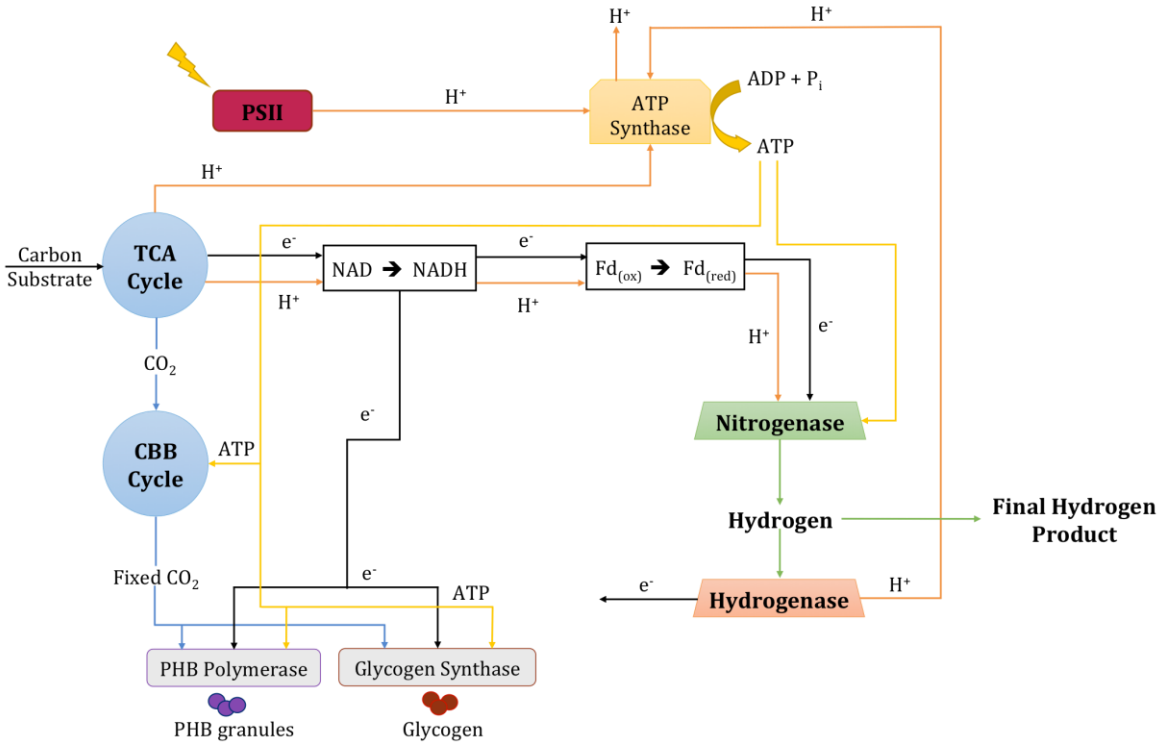

Figure 1-17: Schematic diagram of the main processes involved in hydrogen metabolism by *R. palustris* under photoheterotrophic conditions. CBB is the Calvin-Benson-Bassham cycle (Calvin cycle) and PHB is polyhydroxybutyrate. Modified from Koku et al., Kim and Kim and Pott.[62,75,76]

1.5.1.2.2.2.1 Nitrogenase

As mentioned above, nitrogenase is the main enzyme responsible for hydrogen production. As most nitrogen fixing prokaryotes, *R. palustris* encodes a molybdenum-dependent nitrogenase, which contains an Fe-Mo cluster in the active site. However, *R. palustris* CGA009 is the only photosynthetic microbe known to encode two alternative nitrogenases, namely vanadium-dependent and iron-dependent nitrogenases.[63]

Nitrogenase is more commonly associated with the generation of ammonia by reducing atmospheric nitrogen, its physiological substrate. Hydrogen is obtained as an obligate product as a result of nitrogen fixing. It is a very complex enzyme as it needs over 20 accessory genes for its proper assembly and the individual components of the active enzyme must associate and dissociate 8 times in one catalytic cycle to convert N_2 into 2 NH_3, while consuming 16 ATP as shown in Equation 1-2.

$$Mo-nitrogenase:\ \ N_2 + 8\,H^+ + 8e^- + 16\,ATP \rightarrow 2NH_3 + H_2 + 16\,(ADP + Pi)$$

Equation 1-2

The ATP requirement allows nitrogenase to generate high levels of hydrogen without slowing down the reaction, with the risk of it running in reverse. The need for high ATP is not a hindrance for PNSB as ample ATP is produced by recycling electrons via cyclic photophosphorylation.[63,64,66]

However, the generation of ammonia has repressive effects on both nitrogenase and on hydrogen production. Accumulation of ammonia acts as an inhibitor of posttranslational nitrogenase and, hence, affects hydrogen production. Moreover, the synthesis of ammonia by nitrogenase is highly energy intensive. The strategy devised to eliminate ammonia is to suppress the supply of nitrogen so that the cells use nitrogenase for the sole production of hydrogen with a lower ATP requirement as shown in Equation 1-3.

$$Mo-nitrogenase\ in\ absence\ of\ N_{2:}\ \ 2H^+ + 2e^- + 4\,ATP \rightarrow H_2 + 4\,(ADP + Pi)$$

Equation 1-3

Since ammonium ions are completely excluded, glutamate cannot be synthesised by glutamine synthetase for nitrogenase activity. Therefore, glutamate is provided as a nitrogen source to the bacteria to induce nitrogenase expression. Since oxygen also represses nitrogenase activity, argon is sparged to keep all activities anaerobic.[63,66,77]

1.5.1.2.2.2.2 Hydrogenase

Hydrogenase is an important enzyme in the metabolism of hydrogen production. The hydrogenase present in *R. palustris* belongs to the class of [NiFe]-hydrogenase as per the metal atoms present at the active sites. It is mainly inhibited by carbon monoxide and oxygen, though the resistance to the latter is significantly higher than nitrogenase.

Hydrogenase is involved in energy metabolism by either catalysing hydrogen oxidation (hydrogen consumption) or H^+ reduction (hydrogen evolution) as illustrated below in Equation 1-4.

$$2H^+ + 2e^- \leftrightarrow H_2$$

Equation 1-4

However, since hydrogen production is associated mainly with nitrogenase in *R. palustris*, evolution of hydrogen by hydrogenase is negligible. Studies have shown that hydrogen production by hydrogenase is less than 10% of its hydrogen consumption. Additionally, the maximum activity of hydrogenase only occurs at conditions favourable for hydrogen uptake. Therefore, hydrogenase is said to be the 'metabolic antagonist' of nitrogenase as it operates in the direction of hydrogen uptake.[75,76,78]

The point where electrons leave the intracellular environment to a solid electron acceptor is indistinct in PNSB. Therefore, this remains a challenge for the bioelectrochemical processes in a photoMFC.[65]

1.5.2 Extracellular Electron Transport

Following the intracellular electron transport, it is crucial to establish the ways electrons are transferred from the cells to an electrode, which forms the basis of BESs. Figure 1-8 illustrates the proposed point of electrons export in *S. elongatus* and *R. palustris*. Studies on cyanobacteria have revealed that electrons leave the photosynthetic electron transport chain at PSI. However, no pathway has yet been identified for PNSB. As illustrated in Figure 1-8 (b), it is hypothesised that electrons may leave the intracellular compartment at the electron carrier of NAD, as represented by X.

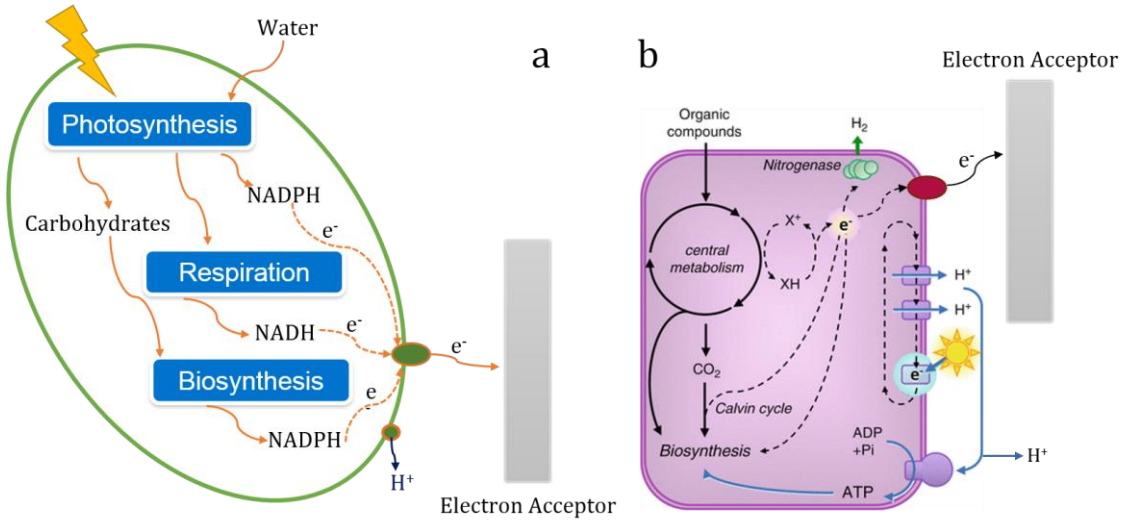

Figure 1-18: Summarised reactions of intracellular and extracellular electron transport mechanisms for (a) Case Study 1: *S. elongatus* and (b) Case Study 2: *R. palustris*, where the schematic was modified from McKinlay.[63]

The mechanism of electron transport from the microbe to a solid electron acceptor, namely an anode, is still a matter of debate. It is due to the fact that it is a complex mechanism and there may be no single answer. It is hypothesised that electrons can reach an anode by two routes, namely by indirect extracellular electron transport (IEET) and by direct extracellular electron transport (DEET) as depicted in Figure 1-19.[15,33,79]

IEET can occur through endogenous electron mediators (EEMs) or exogenously added artificial electron mediators (AEMs). EEMs are redox active compounds that can include naturally occurring molecules, such as humic acids, soluble metal ions and dimethyl sulfoxide. EEMs can also be excreted by the microorganisms. It has been reported that flavins are secreted by *Shewanella* spp., phenazines by *Pseudomonas* spp. and quinone derivatives by *E. coli*. Common AEMs used in BESs include potassium ferricyanide, phenazines, phenothiazines, phenoxazines and quinones.[15,80–82]

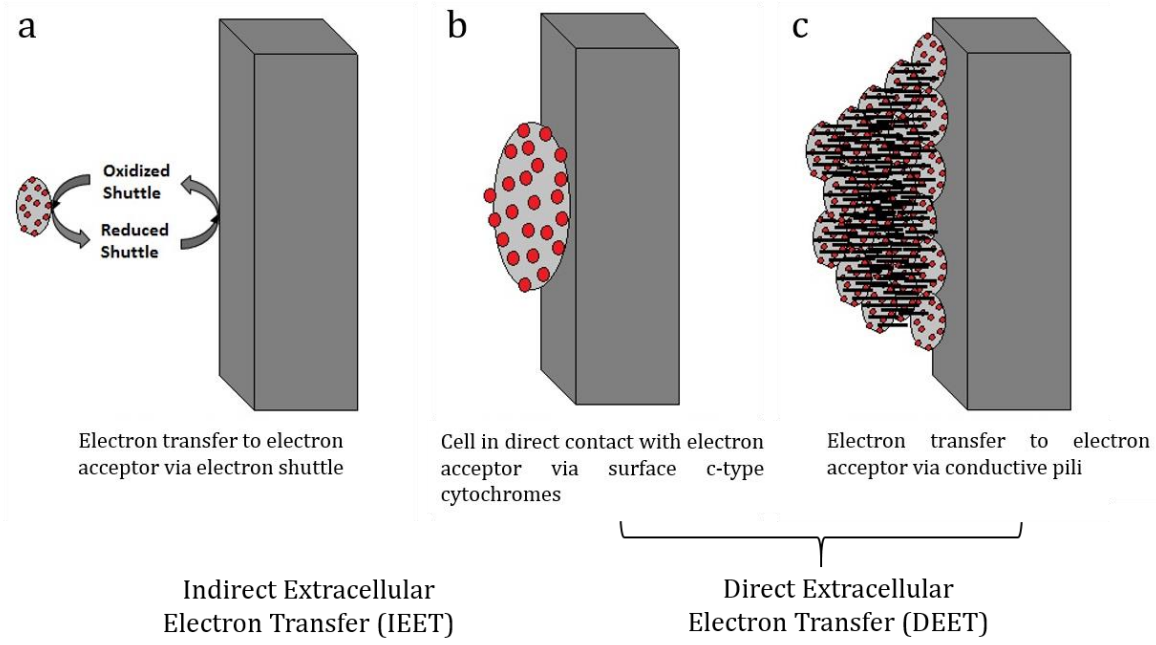

Figure 1-19: Schematic diagram illustrating extracellular electron transport (EET) to a solid electron acceptor (a) electron transfer through endogenous or exogenous electron shuttle (b) electron transfer via surface *c*-type cytochromes and (c) electron transfer through conductive pili or nanowires. Modified from Kadier et al.[79]

DEET builds on the basis of the microbes forming a physical contact with the electrode with no diffusional redox species being involved in the electron transfer from the cell to the electrode. Therefore, electron transfer relies on cells directly attached to the electrode surface rather than planktons.[14,15,83] DEET usually occurs by membrane bound electron transport protein that relay electrons from inside the cell to an electrode. They usually include *c*-type cytochromes and multi-heme proteins. Another suggested mechanism is through extracellular appendages extended into the extracellular matrix, termed as conductive pili or nanowires. These nanowires are used for cell-electrode connections and/or for cell-cell connections.[14,15,81]

It has been reported that the cell envelope/membrane represents a physical as well as an electrically nonconductive barrier due to the presence of external structural compounds, such as the peptidoglycan layer, the outer membrane and the S-layer. However, it has been found that microorganisms have developed specialised mechanisms for the exchange of electrons. The two model microbes that have been studied for extracellular electron transfer were *Shewanella oneidensis* MR-1 and *Geoabacter sulfurreducens*.[80,81]

Genetic studies of *S. oneidensis* showed that 6 multihaem *c*-cytochromes were involved in the extracellular reduction of minerals containing Fe(III), such as CymA, Fcc_3 or FccA, MtrA, MtrC, OmcA and small tetrahaem cytochrome. Porin-like outer membrane protein MtrB was also involved. These outer membrane extensions are proposed to mediate the transfer of electron extracellularly by a multistep hopping mechanism.[80] It was, also, disclosed that *S. oneidensis* produces nanowires that demonstrate nonlinear electrical transport properties along their length.[81]

Multihaem *c*-cytochromes play an important role in electron transfer across the cell envelope in *G. sulfurreducens*. The identified *c*-cytochromes include putative quinol oxidases ImcH and CbcL in the cytoplasmic membrane, PpcA and PpcD in the periplasm and OmaB, OmaC, OmcB and OmcC in the outer membrane. The latter form porin-cytochrome trans-outer membrane protein complexes with porin-like outer membrane proteins OmbB and OmcC. The *c*-cytochromes and porin-like proteins work in tandem for the extracellular transfer of electrons. Conductive nanowires in *G. sulfurreducens* are pili that are formed by protein filaments anchored in the cell envelope, namely by pilin protein pilA. It is proposed that the nanowires transfer electrons by a metallic-like electron transfer mechanism.[80]

Initial studies of BESs involved the use of artificially added mediators (AEMs). However, AEMs-based BESs have fallen out of favour because they are deemed to be unsustainable, costly and potentially environmentally toxic. These factors would eventually limit the commercial applications of BESs.[15,33,84] Most studies currently focus on mediatorless systems which rely on the formation of a biofilm. Microbial biofilms are naturally occurring cell aggregations that adhere to the surface of the electrode. The adherent cells are embedded within an extracellular matrix that consists of extracellular polymeric substances.[34] Cell adhesion is a multi-process phenomenon that involves physical, physico-chemical and biological mechanisms. The interactions between the electrode surface and the microorganisms create a contact or process, called cell adhesion or bioadhesion. The adhesion of cells to a surface follows a sequence of events: (1) transport of cells from a planktonic culture (2) molecular or macromolecular adsorption (3) physico-chemical interactions and (4) anchoring process depending on the topography scale and the material surface nature. The adhesion step is followed by the colonisation of the substrate, namely formation of biofilms by the microorganisms.[85,86] Cultivation of biofilms directly onto the electrode

surface is critical as it promotes contact between the cells and the electrode which would enhance DEET.[34] All studies carried out in this thesis involves mechanisms of DEET.

1.6 Other Performance Factors

Besides, the biological aspect of the BES, other factors are important for its architecture, namely the cathode and the membrane separator. Some systems can, also, operate without a membrane and depends on the electrolyte for the transport of ions.

1.6.1 Cathode

Carbonaceous materials, such as carbon paper, carbon cloth and carbon fibre composites are typically used as cathodic materials. The typical reduction reaction at the cathode in BESs is the oxygen reduction reaction (ORR). Since carbon-based materials have poor catalytic activity, an additional catalyst layer is needed to increase the rate of ORR. Traditionally, platinum is used, as it is the most effective catalyst for oxygen reduction to water due to its high surface area and low overpotential for ORR. However, platinum is expensive and has some limitations, which include pH sensitivity and non-sustainable sourcing. The production of platinum is energy intensive and it releases 51.2 tonnes of carbon dixoide per kg of refined platinum. As a result, low cost sustainable devices should not use platinum. However, there is apprehension that the absence of platinum limits the cathodic reaction and governs the current density of the system.[22,87]

1.6.2 Membrane Separator

Nafion™ electrolyte membrane from DuPont Company has found wide application as an ionic membrane because of the attractive features that it provides, namely high ionic conductivity, impermeability to gases, negligible electronic conductivity, chemical stability and good mechanical integrity. It is typically used in a membrane electrode assembly (MEA), which is a common arrangement in fuel cells. A MEA is an assembled system, consisting of an ion conducting membrane with the anode and cathode on either side of the membrane, as illustrated in Figure 1-20.

The anode and cathode are termed as gas diffusion electrodes (GDE). The latter consist of a Gas Diffusion Layer (GDL) and a Catalyst Layer (CL). GDL is a crucial supporting material in a MEA and the two types of GDL most commonly used are carbon paper and carbon cloth. They are porous in nature and provide an electrically conductive pathway. The CL has its own functionalities with regards to chemical reactions. It must have a high electrocatalytic activity, a good ionic transport and a high porosity for efficient transport of reactant and product. The CL is usually a network of catalytic metal nanoparticles on a porous carbon support. Platinum catalyst dispersed in carbon black is usually used, as discussed in Section 1.6.1.[88–92]

Figure 1-20: Structure of a Membrane electrode Assembly (MEA), consisting of a membrane sandwiched between the anode and cathode. In this schematic, the anode is also shown with the catalyst layer (CL). Modified from Koraishy et al.[93]

Low cost membranes are sometimes preferred instead of Nafion™. Filter papers can be used as non-ion exchange separators.[94] A Whatman filter with a pore size of 6 µm was used in a MFC-based sensor to detect biochemical oxygen demand (BOD).[95] Chouler et al.[96] investigated two low cost membrane materials, namely a natural polymer in the form of eggshell and a synthetic polymer of polydimethylsiloxane (PDMS). Devices with PDMS as a separator produced a similar power density as that of devices with the much more expensive Nafion™. However, these form of separators are not impermeable to gases. The selection of a separator needs to be customised as per the needs of the systems.

1.7 Theory

This section provides the necessary theoretical background on the different electrochemical techniques used to understand the functioning and performance of both the BPV and the photoMFC.

1.7.1 Voltage and Power Generation

1.7.1.1 Thermodynamics and Electromotive Force

Electricity is generated in a BPV and a photoMFC if the overall reaction is thermodynamically favourable. Theoretically, in an ideal BES, the entire free energy, ΔG, of the fuel oxidation can be converted into electricity. The maximal work is expressed in Equation 1-5.

$$\Delta G_r = \Delta G_r^{\circ} + RT\ ln(\pi) \quad , \quad \pi = \gamma_P/\gamma_R$$

Equation 1-5

ΔG_r represents Gibbs free energy for the experimental conditions in Joules (J), ΔG_r° is Gibbs free energy under standard conditions in J, R is the universal gas constant at 8.31447 J mol^{-1} K^{-1}, T is the absolute temperature in Kelvin (K), γ_P is the activity coefficient of the products and γ_R is the activity coefficient of the reactants.

However, it is more convenient to gauge the reactions in terms of overall cell electromotive force, E_{emf}. Work (W) in J as produced by the system is illustrated in Equation 1-6.

$$W = E_{emf}Q = -\Delta G_r \quad , \quad Q = nF$$

Equation 1-6

Q is the charge in Coulomb (C) transferred in the reaction, n is the number of electrons per reaction mole and F is Faraday's constant (9.64853 x 10^4 C/mol). Combining these two equations result in Equation 1-7Equation 1-7.

$$E_{emf} = \frac{\Delta G_r}{nF}$$

Equation 1-7

The cell emf is defined as the potential difference between the cathode (E_{cat}) and the anode (E_{ano}) as shown in Equation 1-8.

$$E_{emf} = E_{cat} - E_{ano}$$

Equation 1-8

According to IUPAC convention, all reactions are written in the direction of reduction potential, which explains the minus sign for the anode potential (although an oxidation reaction is occurring).[97–99]

1.7.1.2 Polarisation Curve

The performance of BESs is traditionally characterised by a polarisation plot, in which the cell voltage (E_{cell}) is plotted as a function of current density. With a stepwise decrease in the external resistance (R_{ext}) of the circuit, a voltage drop is recorded and the current density (I) can be calculated by using Ohm's law as shown in Equation 1-9.

$$I = E_{cell}/R_{ext}$$

Equation 1-9

The current is usually normalised to a specific feature of the system in order to facilitate comparisons between different systems. The current reported in this study is normalised to the surface area of the anode, as it is the site for the biological reactions.[97,99,100]

Figure 1-21 depicts a typical polarisation curve and the major segments that are crucial for the performance of the BPV and the photoMFC. The regions stand for performance losses caused by limitations of different electrochemical nature.

1.7.1.2.1 Open Circuit Potential, OCP

The cell emf is a thermodynamic value that does not account for internal losses. As shown in Figure 1-21, the OCP is the cell voltage measured after sometime in the absence of current, that is at infinite resistance. Theoretically, the OCP should approach the cell emf but it is substantially lower. The OCP is limited by the oxidation potential that can be achieved by the bacterial community on the anode and the reduction potential at the cathode. For instance, the typical cathode potential using oxygen at pH 7 is about 0.2 V, considerably lower than the expected value of 0.805 V. This proves that the system suffers from large energy loss, known as overpotential.[97,98]

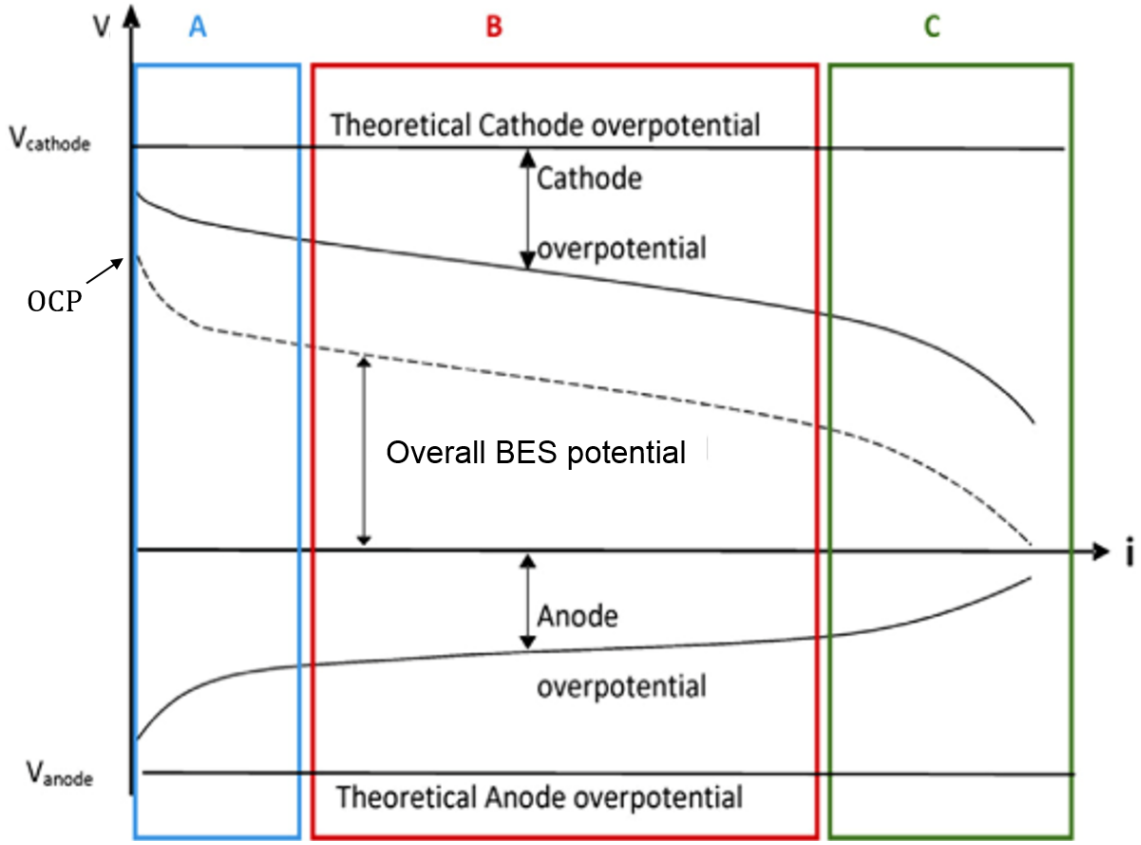

Figure 1-21: Typical polarisation curve showing the different regions of electrochemical losses (A) activation losses (B) ohmic resistance and (C) mass transport. Modified from Kadier et al.[79]

1.7.1.2.2 Activation Losses

On closing the circuit and allowing a small current to run through the system, the system suffers from non-linear voltage drop, known as activation losses. It is demonstrated by the blue region A in Figure 1-21.

Activation losses derive from the slowness and irreversibility of the reactions taking place on the surface of electrodes. The overpotentials are due to the energy lost for initiating the oxidation and reduction reactions at the electrodes. The energy is lost through the transfer of an electron from the cell terminal cytochrome or nanowire to the anode surface as well as during the transfer of electrons to the final electron acceptor at the cathode. Activation losses are prominent at low current densities near to OCP and they become minimal as current densities increase.[79,97,98]

Activation losses depend on the catalysts, electrochemical mediators, the biofilm, the microbial species and their metabolisms as well as operating conditions, such as temperature and pH.[101] To improve the energy efficiency of a BES, some measures can be taken to minimise activation losses:

(1) *Increasing anode surface area*: A reliable approach to decrease activation overpotential is to increase the surface area as when surface area is increased, the current density is reduced. Increasing the electrode surface porosity and roughness increases the surface area.

(2) *Improving anode-microbe interactions*: In order to decrease the activation losses at the anode, it is important to enhance the anode-microbe interactions. This can be achieved through the establishment of an enriched biofilm on the anode. Usually, microorganisms that produce conductive pili have relatively low activation polarisation.

(3) *Effective catalyst*: The activation energy at the electrodes can be decreased by adding catalyst to the electrodes. The activation losses rely on the type of catalyst used; an effective catalyst lowers the activation energy and hence decreases the activation polarisation. For the anode, it would mean to increase the electrochemical reversibility of, for instance, the terminal electron transferring outer membrane cytochrome or the increase of their coverage on the anode surface. Platinum is typically used at the cathode to overcome the activation energy of the oxygen reduction reaction (ORR).[79,99]

1.7.1.2.3 Ohmic Losses

As more current is allowed to flow through the system, ohmic losses become more influential as shown by the red region B in Figure 1-21. The voltage falls more slowly and it is fairly linear with current. Ohmic losses arise both from the resistance to flow of electrons through the electrodes and electrical connections and from the resistance to the flow of ions (protons) through the electrolyte and the exchange membrane (if present). The sum of all internal losses, R_{int}, during current generation can be obtained from the linear part of the polarisation curve as represented by B. The value of R_{int} is the slope of the linear section, which is governed by Ohm's law. As a result of the internal losses, the cell voltage of a BES is obtained as shown in Equation 1-10.

$$E_{cell} = OCP - IR_{int}$$

Equation 1-10

IR_{int} is the voltage, V, obtained as a linear function of current, taking into account the sum of all internal losses.

Overcoming ohmic losses is crucial for an optimum performance of the BES architecture. Ohmic losses can be minimised by increasing the conductivity of the electrodes, improving electrical contacts between the electrode and electrical connections and reducing the total distance travelled by electrons within the electrode. The distance between the anode and cathode must be decreased so that protons have a short distance to travel and if a membrane is used, it must be of low ionic resistivity. Increasing the conductivity of the solution and maintaining a uniform pH value throughout the system, also, curtail ohmic polarisation.[79,97,98,101]

1.7.1.2.4 Mass Transport or Concentration Losses

Increasing the current even more leads to a nonlinear voltage drop, which is attributed to mass transport limitations or concentration losses. The latter occur at high current densities due to the insufficient flux of electrons and protons needed to sustain the generation of current. The accumulation of oxidised products and cations in the biofilm may change the redox conditions and the metabolic activities of the microorganisms. Hindrance in cation transport may further cause a pH gradient between the electrodes leading to a significant reduction in the current production.[79,97,98]

Minimising concentration polarisation is complex. In some cases, improving the cell design, such as better reactor mixing, enhances mass transfer within the system.[99]

1.7.1.3 Power Curve

A power curve can be subsequently obtained from the polarisation curve, as depicted in Figure 1-22. It represents power density as a function of current density. Similarly to current density, the power produced is normalised with respect to the surface area of the anode. Power is obtained as shown in Equation 1-11. Usually, voltage is measured across a fixed external resistor, R_{ext}, while current is obtained from Ohm's law.

$$P = IV = V^2/R_{ext}$$

Equation 1-11

As no current flows during open circuit, no power is generated. As current starts flowing, power density increases to a maximum point, following which the power density drops due to increasing ohmic losses and electrode overpotentials. Normally,

ohmic resistance plays an assertive role in determining the point of maximum attainable power.

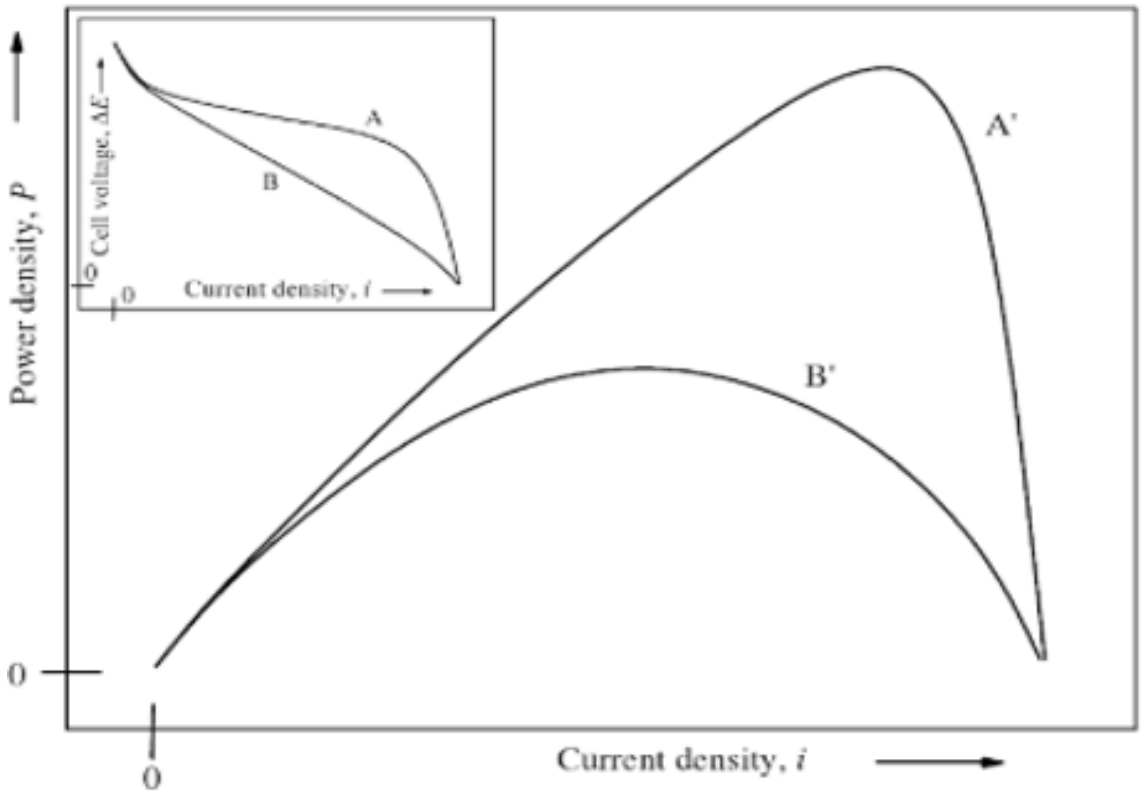

Figure 1-22: Typical power curves as derived from their respective polarisation plots (insets) showing the effects of ohmic resistance. Curves A,A': low ohmic resistance and curves B,B': dominant ohmic resistance. Reproduced from Rabaey et al.[99]

The shape of a suitable power curve would be similar to the shape of curve A', as depicted in Figure 1-22. It has an asymmetric shape, with a long linear up-slope and a sharp decrease after the maximum power point. Ideally, the power density would increase with increasing current density until mass transfer limitations lead to a steep decrease in cell voltage and power concurrently. The higher the internal resistance, the higher the drop in maximum power density. Consequently, the maximum power point tends to shift towards lower current densities and the power curve becomes more symmetrical and bell-shaped. BESs that produce such power performance characteristics are highly inefficient as the operation is limited by ohmic resistance rather than by mass transfer. Moreover, at the point of maximum power output, the internal resistance of the system is equal to the external resistance, that is $R_{int}=R_{ext}$.[97,99]

1.7.1.4 Overshoot Phenomenon

Besides the conventional losses of activation, ohmic and concentration, further losses can be introduced by BES, such as the overshoot phenomenon, where both power and current decrease concomitantly. It is demonstrated by the bending inwards of the curves and signals a system limitation, as shown in Figure 1-23. Although, overshoot is a common occurrence in BESs, it is not fully understood. Aelterman et al.[102] attributed the phenomenon to mass transfer limitations, a theory that could not be verified. Recent studies have suggested that the underperformance is due to ionic and electrical depletion at lower resistance values. At low resistive values, the demand for electrons exceeds the microbial rate at which electrons can be supplied. The anolyte is used up and, thus, current decreases when it is expected to increase. Other factors include an early stage biofilm and insufficient feedstock in terms of organic loading or conductivity.

However, in many cases, the systems appear to recover from the overshoot as supply and demand of electrons is balanced and current starts to increase again. This recovery reveals the robustness of the microorganisms and their ability to adapt under dynamic conditions.[103]

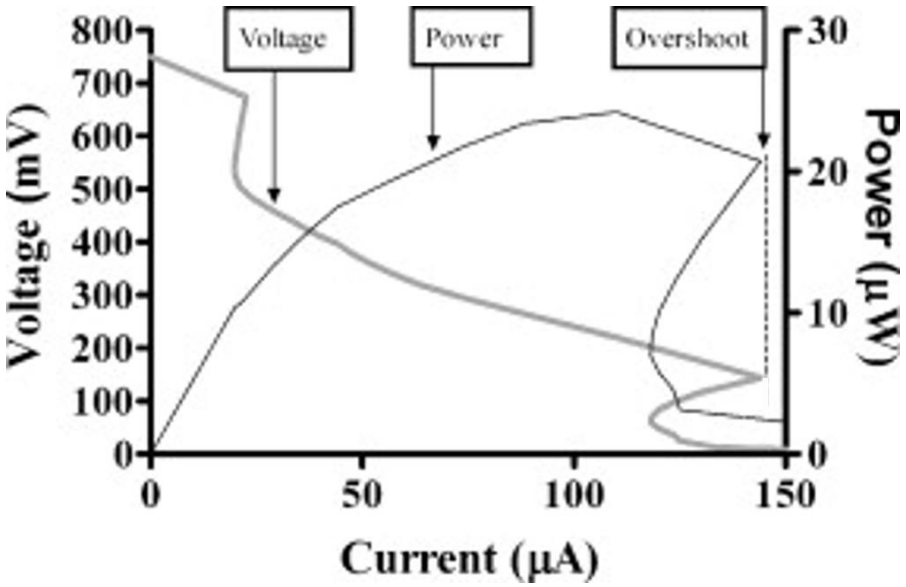

Figure 1-23: Schematic illustration of an overshoot effect on both the polarisation and power curves. Reproduced from Ieropoulos et al.[104]

1.7.2 Electrochemical Methods

This section introduces the fundamental basics of electrochemistry based on electrolyte solutions, which would provide some insights in unravelling the understanding of the reactions at the anode-biofilm interface.

Electrochemical techniques are used in understanding reactions which involve electron transfer for various purposes, such as chemical and biochemical sensors, electroplating and electrochromic displays and energy storage in solar cells and batteries. The electron transfer encompasses loss of electrons in an oxidation reaction or gain of electrons in a reduction reaction, in response to an electrical stimulation. These redox reactions can involve species in the same phase, termed as homogeneous electron transfer reactions or the electron can move through an interface in heterogeneous electron transfer reactions.[105]

Most electrochemical studies are carried out with a three-electrode system as shown in Figure 1-24. The electrochemical reaction of interest occurs at the surface of the working electrode and its potential is monitored with respect to the reference electrode. A counter electrode completes the electrical circuit with the working electrode between which current flows. The purpose of the counter electrode is to prevent any large currents from passing through the reference electrode and causing any variations of its potential.[105,106]

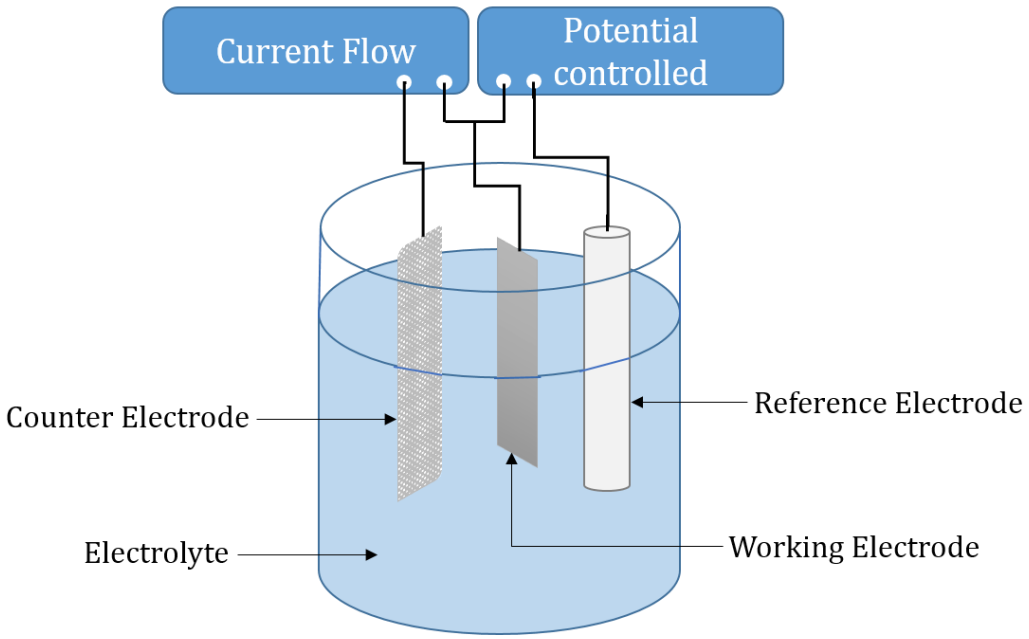

Figure 1-24: Three-electrode arrangement typically used for electrochemical studies.

1.7.2.1 Mass Transfer

The simplest example of an electrochemical reaction is the redox process occurring at an electrode as shown by Equation 1-12.

$$O + n\,e^- \rightleftharpoons R$$

Equation 1-12

The reaction consists of a series of steps that drive the conversion of the dissolved oxidised species, *O*, to a reduced form, *R*, which is also in solution. The current or the rate of electrode reaction is governed by the rate processes of mass transfer, electron transfer at the electrode, chemical reactions following the electron transfer and other surface reactions, such as adsorption, desorption or crystallisation.[106] Figure 1-25 illustrates the pathway associated with general electrode reactions.

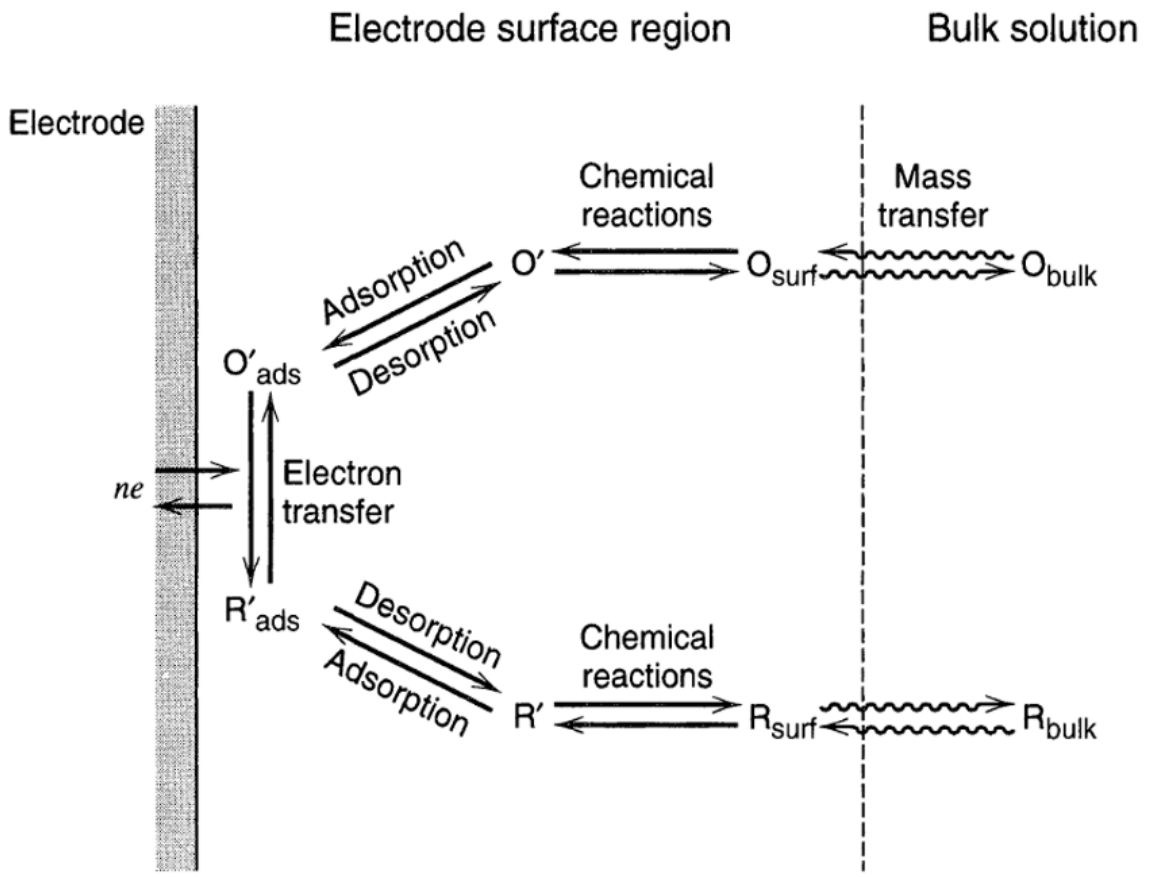

Figure 1-25: Pathway of a general electrode reaction. Reproduced from Bard and Faulkner.[106]

The simplest reactions involve only mass transfer of a reactant to the electrode, heterogeneous electron transfer of non-adsorbed species and mass transfer of the product to bulk solution. Moreover, the rate of all related chemical reactions are very

quick as compared to mass transfer processes. Taking into account these conditions, the chemical reactions can be simplified involving an electrode process with fast heterogeneous charge-transfer kinetics and mobile reversible homogeneous reactions. The latter can be regarded to be at equilibrium and the surface concentrations of species in the faradaic process are related to the electrode potential by an equation of the Nernst form. Such electrode reactions are often known as reversible or nernstian as the main species obey thermodynamic relationships at the electrode surface.

Mass transfer is an important parameter in electrochemical dynamics. It involves the movement of material from one location in solution to another. It arises from differences in electrical or chemical potential at the two locations or from movement of a volume element of solution. The types of mass transfer are classified as:

(1) Migration is the movement of a charged body under the influence of an electric field.

(2) Diffusion involving the movement of a species under the influence of a gradient of chemical potential

(3) Convection occurs during stirring or hydrodynamic transport. The fluid usually flows under natural convection, caused by density gradients and forced convection. It may be identified by stagnant regions, laminar flow and turbulent flow.

Mass transfer to an electrode is governed by the Nernst-Planck equation as shown in Equation 1-13.

$$J_i(x) = -D_i \frac{\partial C_i(x)}{\partial x} - \frac{z_i F}{RT} D_i C_i \frac{\partial \emptyset(x)}{\partial x} + C_i v(x)$$

Equation 1-13

$J_i(x)$ is the flux of species i (mol s^{-1} cm^{-2}) at distance x from the surface, $-D_i$ is the diffusion coefficient (cm^2 s^{-1}), $\frac{\partial C_i(x)}{\partial x}$ is the concentration gradient at distance x, $\frac{\partial \emptyset(x)}{\partial x}$ is the potential gradient, z_i and C_i are the charge and concentration (mol cm^{-3}) of species i respectively and v(x) is the velocity (cm s^{-1}) with which a volume element in solution moves along the axis. The three terms on the right-hand side of the equation describes the part played by diffusion, migration and convection, respectively, to the flux.[106]

1.7.2.2 Faradaic and Non-faradaic Processes

Faradaic and non-faradaic processes are two types of reactions that can take place at the electrodes. Faradaic processes consist of reactions that involve charges being transferred across the metal electrode-solution interface. The redox process is governed by Faraday's law, where the amount of chemical reaction caused by the flow of current is proportional to the amount of electricity generated. Moreover, electrodes at which faradaic processes occur are often called charge-transfer electrodes. Under particular conditions, a given electrode-solution interface will display a range of potentials where no charge transfer reactions take place as they could be thermodynamically or kinetically unfavourable. These processes are known as non-faradaic. Despite charge not crossing the interface, external currents can still flow when the potential, electrode area or solution composition changes.[106] Figure 1-26 illustrates examples of faradaic and non-faradaic processes.

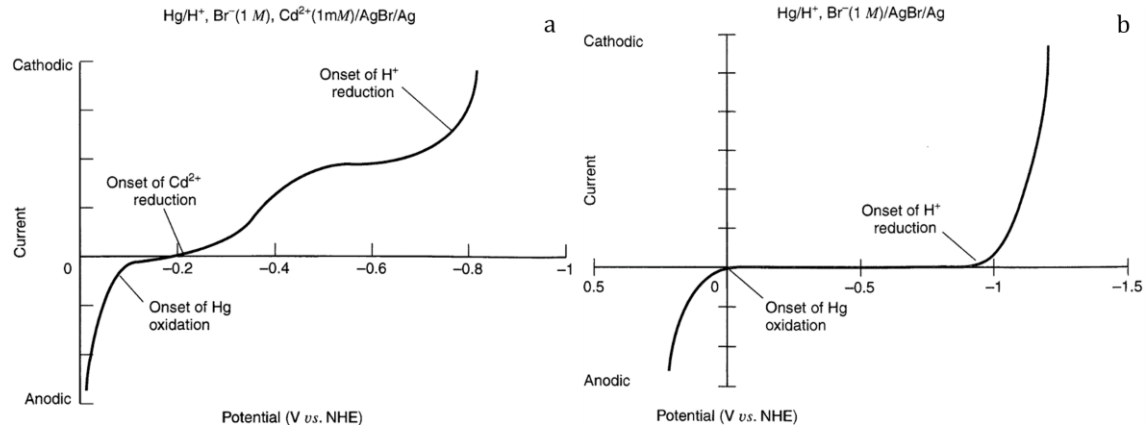

Figure 1-26: Current-potential curve illustrating examples of (a) faradaic process and (b) non-faradic process between 0 and -0.8 V vs. NHE. Reproduced from Bard and Faulkner.[106]

1.7.2.3 Electrical Double Layer

Since charge cannot cross the interface when the potential is varied, the behaviour of the electrode-solution interface is similar to that of a capacitor. A capacitor is an electrical circuit element consisting of two metal sheets, separated by a dielectric material. Its function is governed by Equation 1-14.

$$\frac{q}{E} = C$$

Equation 1-14

q is the charge stored on the capacitor in Coulombs (C), E is the potential across the capacitor in Volts (V) and C is the capacitance in Farads (F).

When a potential is applied across the capacitor, charge accumulates on its metal plates until q satisfies Equation 1-14 and a current flows during the charging process. At a given potential, a charge q^M will exist on the metal electrode and a charge q^S in the solution. The potential across the interface and the composition of the solution determine whether the metal surface is positively or negatively charged with respect to the solution and $q^M = -q^S$ at all times. q^M represents an excess or deficiency of electrons and sits in a thin layer of less than 0.1 Å on the metal surface. q^S consists of an excess of either anions or cations at the vicinity of the electrode surface. The whole array of charged species and oriented dipoles at the metal-solution interface is known as the electrical double layer as shown in Figure 1-27. The layer closest to the electrode contains solvent molecules and some other ions or molecules that are physically adsorbed. This inner layer is known as the compact, Helmholtz or Stern layer. The locus of the electrical centres of the physically adsorbed ions is called the inner Helmholtz plane (IHP), which is at a distance x_1. Solvated ions can only approach the electrode within a distance of x_2 and the locus of centres of the nearest solvated ions is known as the outer Helmholtz plane (OHP). The solvated ions are termed as non-specifically adsorbed since their interactions with the electrode involve only long-range electrostatic forces.[106]

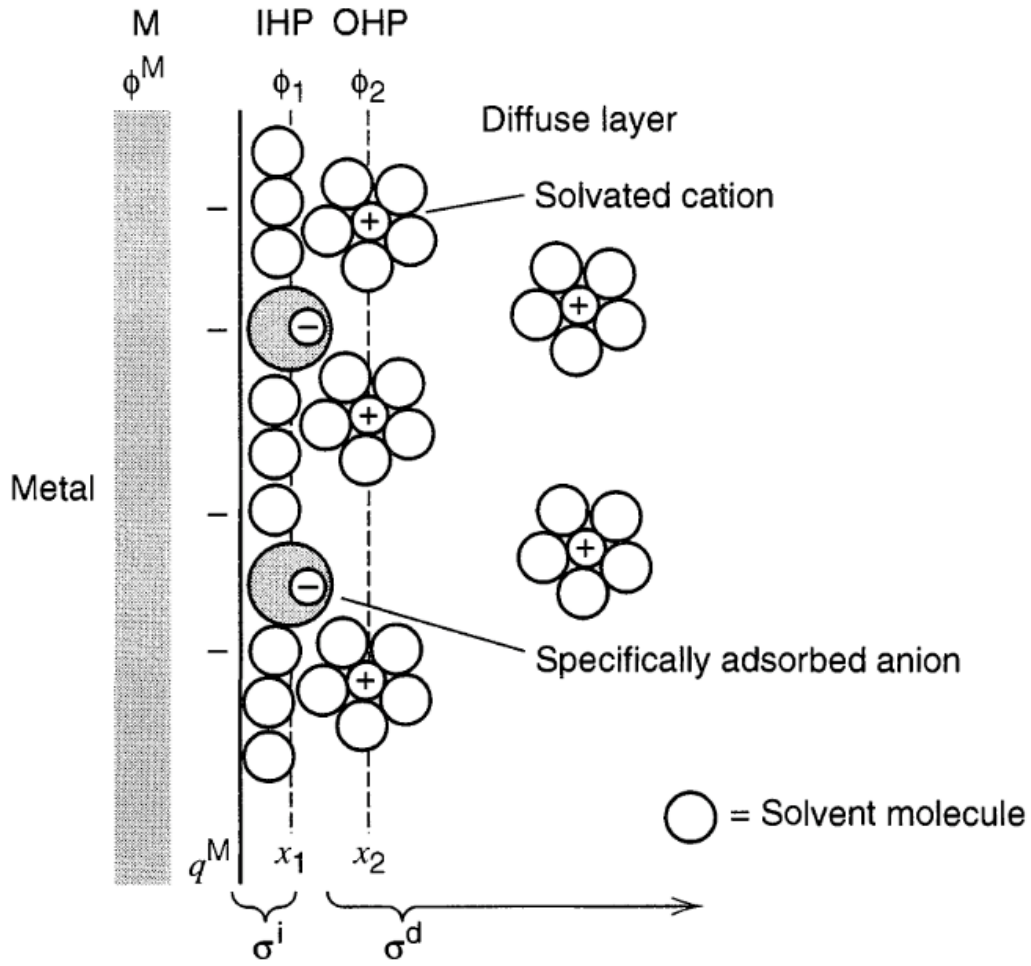

Figure 1-27: Schematic diagram of a proposed model of the electrical double layer where anions are physically adsorbed. σ^i and σ^d represent charge densities in the inner and diffuse layers respectively. ϕ^M is the potential at the metal electrode and ϕ^1 and ϕ^2 are potentials at distances x_1 and x_2 respectively. Reproduced from Bard and Faulkner.[106]

1.7.3 Voltammetric Techniques

Voltammetry is one of the most common techniques employed for electrochemical studies. It refers to the potential of the working electrode being controlled with the measured output being current. Two types of voltammetric techniques are employed, namely cyclic voltammetry and double potential step chronoamperometry to investigate the electroactivity of biofilms grown on the anode materials. Additionally, double potential step chronocoulometry helps to clarify any ambiguities in double potential step chronoamperometry.

Background theory is provided for each technique, followed by their subsequent application in the study of the anode-biofilm interface. It is thus important to illustrate the general reactions occurring at the interface, analogous to Figure 1-25.

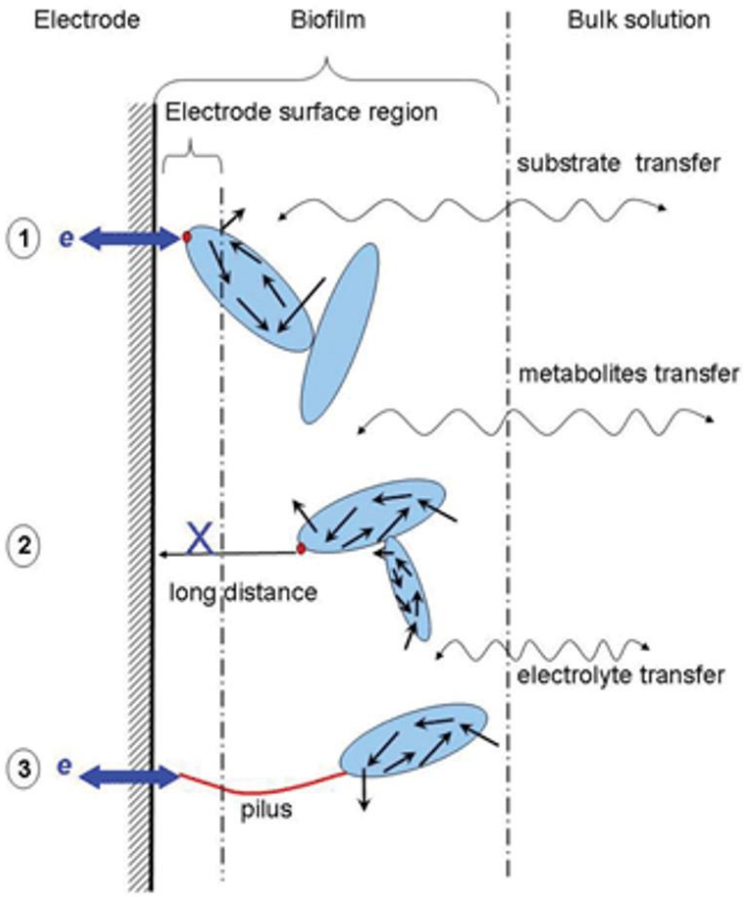

Figure 1-28: Schematic of the pathways involved in solution during direct electron transfer between the biofilm and the electrode. Reproduced from Zhao et al.[107]

A potential pathway for direct extracellular electron transfer (DEET) between a biofilm and an electrode is illustrated in Figure 1-28.

The region of biofilm formation is important for the function of a BES. The following steps can occur during the electrode reaction:

(1) Transport of the substrate from the bulk solution to the biofilm region;

(2) Transport of the substrate in the biofilm region;

(3) Metabolisms inside the different microorganisms that are present;

(4) DEET between the biofilm (*i.e.* the active sites of extracellular enzymes of the microorganisms) and the electrode;

(5) Transport of the metabolites and the reaction products;

(6) Transport of electrolyte including spectator ions and chemical species.

1.7.3.1 Cyclic Voltammetry, CV

CV is an adequate technique that provides information about possible redox reactions occurring within the system but is not appropriate for quantitative analysis.[108] CV can be described as an extension of linear-sweep voltammetry (LSV) as when the potential reaches the value E_2, the direction of sweep is reversed and the electrode potential is scanned back to the initial value of E_1, as shown in Figure 1-29 (a).

The simple redox reaction in Equation 1-15 is considered.

$$R \rightleftharpoons O + n\,e^-$$

Equation 1-15

Initially, no current flows as the potential E_1 is not significant enough to induce electron transfer. But as the voltage is increased from E_1 to E_2, the current begins to increase and the oxidation of *R* at the electrode becomes feasible, as illustrated in Figure 1-29 (b). As even more positive current is reached, the rise becomes less exponential and eventually the maximum is reached, after which the current drops. The exponential part of the voltammogram is said to be Nernst driven and a maximum point occurs due to mass transfer limitation.

On reaching E_2, the potential is swept back; reducing species *O* formed at the electrode during the forward scan of species *R*. A current in the opposite direction is detected due to the reduction of *O* to *R*. This current increases initially as a high concentration of *O* is present in the diffusion layer and the kinetics for the reduction of *O* to *R* become favourable. Slowly, all of species *O* in the diffusion layer is reconverted back to R and the current drops back to 0.[109,110]

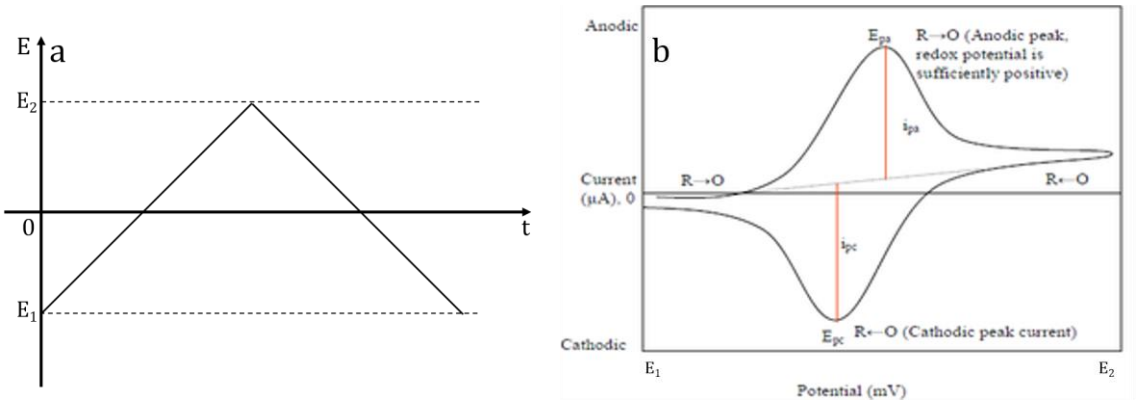

Figure 1-29: Illustration of (a) triangular waveform with variation of applied potential as a function of time and (b) a cyclic voltammogram for a reversible electron transfer reaction.

The maximum current is known as the peak current and denoted as i_{pA} for the anodic oxidation reaction and as i_{pC} for the cathodic process. The respective potential where the maximum current occurs is called peak potential; E_{pA} represents anodic peak potential and E_{pC} reflects the cathodic peak potential.

CV is the main diagnostic technique in protein film voltammetry. It involves examining electron transfer reactions of immobilised enzymes on rotating and stationary electrodes. It is, therefore, employed for the qualitative analysis of extracellular electron transfer of electroactive biofilm, analogous to the case of immobilised enzymes.[111,112]

Harnisch and Freguia[110] attempted to describe the general steps occurring at the electrode-biofilm interface and made a comparison with an inorganic electrocatalytic reaction and an enzymatic bioelectrocatalytic reaction. As shown in Figure 1-30, it can clearly be observed that more steps are involved with a whole microbial cell, making the reaction more complex. Consequently, the pure mass transfer models are mostly invalid.

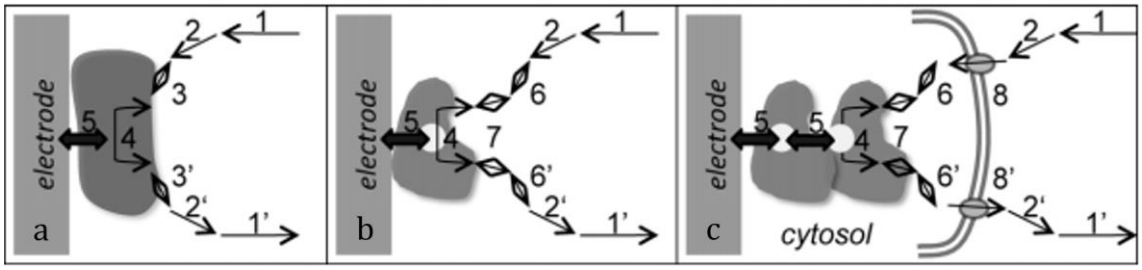

Figure 1-30: Simplified schematic representations of the major, potentially rate-limiting steps during (a) an electrocatalytic reaction, (b) an enzymatic bioelectrocatalytic reaction and (c) a microbial bioelectrocatalytic reaction (considering a two-enzyme cascade in the cell). The steps are: (1/1') mass transport in the bulk solution, (2/2') mass transport in the electrolyte diffusion layer, (3/3') sorption/desorption processes, (4) bioelectrochemical reaction, (5) electron conduction between the active center and the electrode, (6/6') enzymatic uptake/release, (7) enzyme turnover (8/8') and uptake/release of substrate to the cell. Reproduced from Harnisch and Freguia.[110]

For a better understanding of the reactions at the electrode-biofilm interface, the study of two different mass transfer regimes using the redox reaction in Equation 1-15 is compared. The first case is a typical electrochemical reaction for a completely diffusion-controlled process with the species dissolved in solution and the second case

involves a surface-controlled redox regime, imitating cytochromes embedded in the biofilm. The reduced form, *R*, is not regenerated in both cases and this condition is termed as non-turnover. It simulates the depletion of substrate in an anodic microbial biofilm. Figure 1-31 (a) and (b) illustrates the CV curve for the diffusion-controlled oxidation reaction of *R* and its concentration profile near the electrode surface, respectively. When the potential is far too negative as compared to the midpoint potential of the reaction, no faradaic current is generated and the concentration *R* on the electrode surface is similar to that of the bulk solution. As the potential approaches the midpoint potential, the reaction proceeds as per Nernst equation, denoted by regime II. As the potential continues to increase, the current increases as well as the diffusion gradient from the bulk to the electrode surface as represented by regime III. Eventually, the concentration gradient from the electrolyte solution is formed and the current decreases asymptotically due to mass transfer limitation as shown by regime IV.

For the case of the surface-bound system as shown in Figure 1-31 (c) and (d), the concentration of *R* is not infinite. Similarly to the diffusion-controlled process, the current starts to increase in regime II but shows a particular sharper increase until the peak potential is reached. The current drops sharply as well because the amount of *R* to be oxidised by the electrode is limited. The current decreases to zero following the complete stoichiometric oxidation of *R*, denoted by regime III. A significant feature is that the peak potentials of the oxidation and reduction reactions are identical to the midpoint potential.[110]

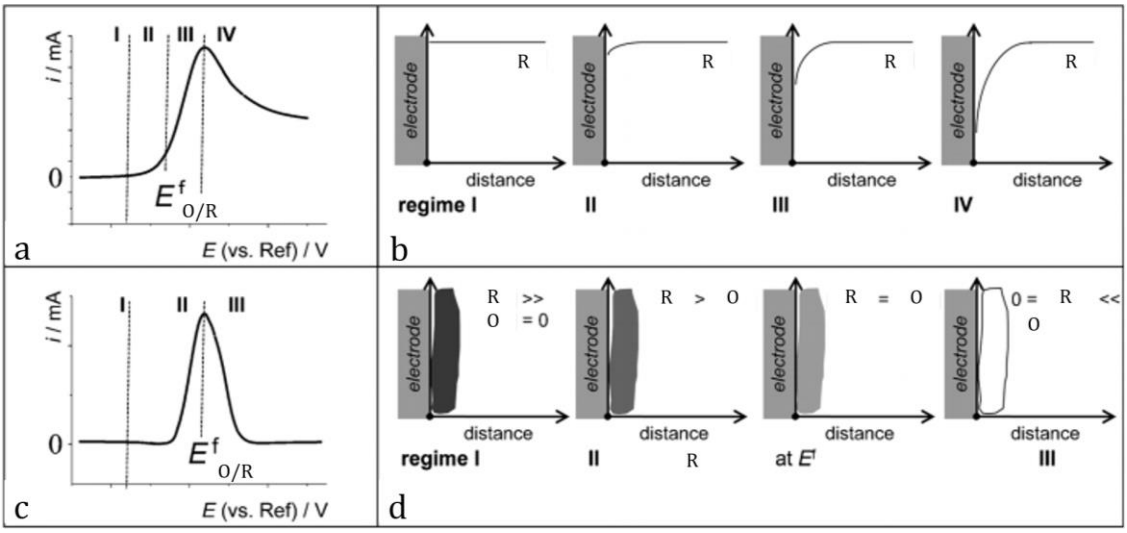

Figure 1-31: CV curves and mass transfer regimes of O/R redox carriers for (a), (b) diffusion-controlled and (c), (d) surface-bound redox regimes. E^f denotes the midpoint potential. Modified from Harnisch and Freguia.[110]

The condition, where an appropriate electron-donating substrate is added, is termed as turnover or bioelectrocatalysis. The electron transfer with the electrode occurs in series with the intracellular biochemical reaction with a constant current being generated at the working electrode, if poised at a sufficiently positive potential. This condition is translated into the continuous reduction of the redox active compound at the bioanode and its subsequent oxidation by the electrode. Thus, the model system, R/O, exchanges electrons with the electrode as well as undergoes a biological reduction reaction, dependent on the metabolism of the microbe, as shown in Equation 1-16.

$$O + n\, e^-_{metabolism} \rightleftharpoons R \rightleftharpoons O + n\, e^-_{electrode}$$

Equation 1-16

Figure 1-32 illustrates the reactions that occur during a turnover condition as represented by Equation 1-16.

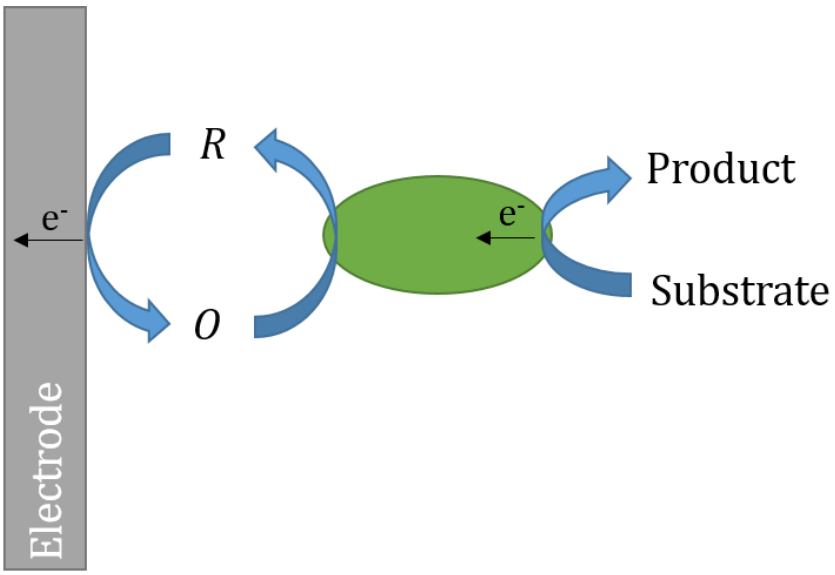

Figure 1-32: A schematic diagram illustrating a turnover condition.

Turnover conditions usually generate current of several orders of magnitude higher as compared to the non-turnover conditions as every redox centre may channel several electrons per unit time to the electrode. Figure 1-33 illustrates both non-turnover and turnover conditions of *Geobacter*-based anodic biofilms. The non-turnover conditions are examined at two scan rates, namely 50 mV s^{-1} in Figure 1-33 (a) and 1 mV s^{-1} in Figure 1-33 (b). Low scan rates produce more distinct redox peaks as compared to a fast scan rate. Four redox peaks are observed at a scan rate of 1 mV s^{-1}, marked with their respective midpoint potentials (Ef_1-Ef_4). For a turnover condition, where a redox couple generates a catalytic effect, an S-shaped CV is obtained as depicted in Figure 1-33 (c). The first derivative, as shown in Figure 1-33 (d) of the turnover curve provides information about the midpoint potentials and are identified to be Ef_2 and Ef_3 out of the four detected midpoint potentials in non-turnover conditions. Hence, it can be concluded that redox centres at Ef_2 and Ef_3 participate in bioelectrocatalysis in the presence of a substrate. The functions of the other two redox sites at Ef_1 and Ef_4 have not yet been identified but it has been suggested that they form part of the cell itself or its extracellular matrix.[110,113]

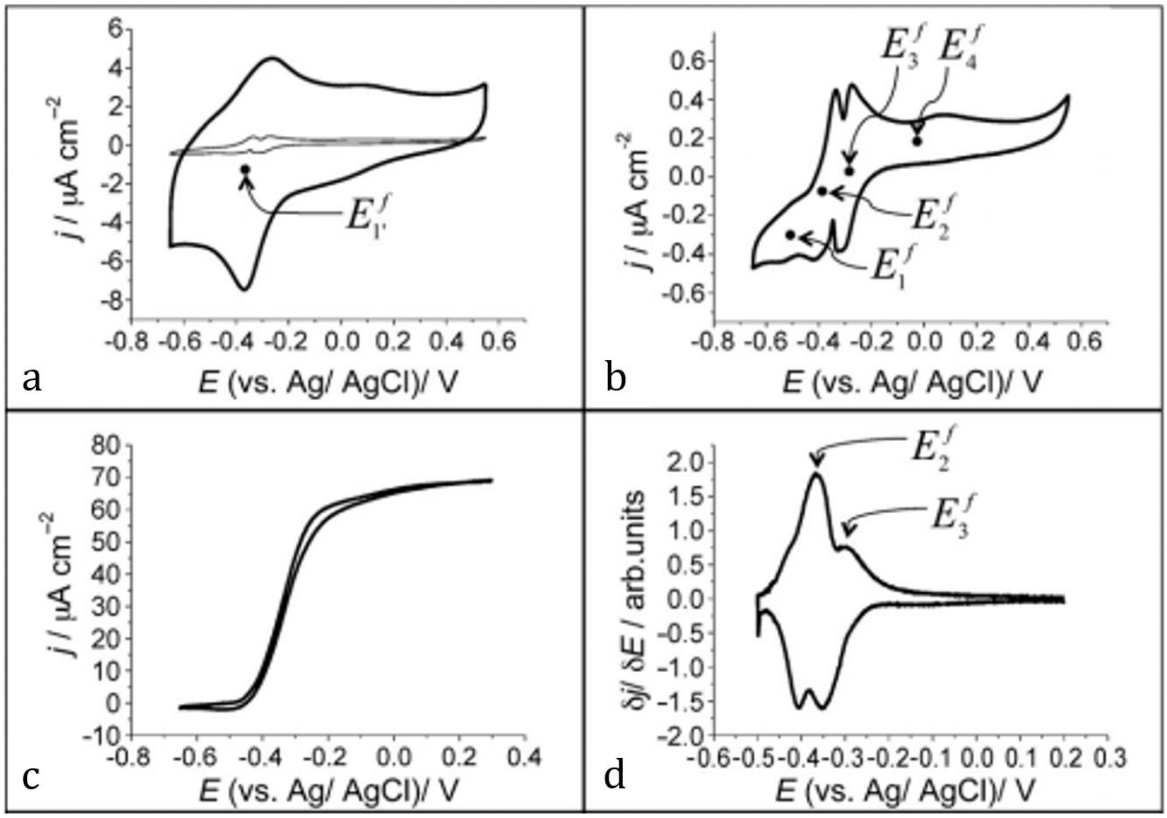

Figure 1-33: Examples of CVs carried out with biofilms of *Geobacter* in (a) non-turnover condition at a scan rate of 50 mV s^{-1} (b) non-turnover condition at a scan rate of 1 mV s^{-1} (c) turnover reaction at 1 mV s^{-1} and (d) first derivative of (c). E^f denotes the midpoint potential of the redox centres. Reproduced from Harnisch and Freguia; Fricke et al.[110,113]

However, CV may not work in all situations. For low biofilm coverage or biofilms with low electrocatalytic activities, capacitive current may mask the faradaic current, even at low scan rates, and thus no CV analysis is possible. As a result, alternative electroanalytical techniques should be used.[110,111]

1.7.3.2 Double Potential Step Chronoamperometry

Usually, the double potential step technique is used to examine the kinetics and mechanisms of chemical reactions following electron transfer. The main advantage of this method is its simplicity since it does not require any complicated potential-time dependences.[114,115] In a double potential step chronoamperometry, the potential of the working electrode is stepped forward for a specific period of time and then stepped backward for a specific period of time. The easiest way to identify the values of the step potentials is to record the cyclic voltammetry of the analyte.

The typical assumption for the analysis of the chronoamperometric curve or current transient is that the diffusion of the active species governs the rate of the whole process. The following is a basic description of the theory behind double potential step chronoamperometry by considering the simple electron transfer reaction of Equation 1-15. At time t=0, a sufficiently positive potential, E_1, is applied which leads to the instantaneous oxidation of *R* at the electrode surface. The surface concentration of *R* nearly goes to 0. For the time period of t_1, current flows in a diffusion controlled manner to maintain the fully oxidised condition at the electrode surface. The initial oxidation process creates a concentration gradient, which induces a continuing flux of *R* to the electrode surface. However, *R* cannot coexist with the electrode at E_1 and must be removed by oxidation. The flux of *R*, hence the current, is proportional to the concentration gradient at the electrode surface. As depletion occurs, the diffusion layer thickness increases and current decreases to eventually zero. Finally, the potential is again switched to a negative enough potential to ensure diffusion-controlled conditions for a reverse reaction, namely a reduction reaction. The duration of the second pulse is denoted by t_2.[106,109,114,116] Current is monitored and plotted as a function of time in a chronoamperogram, as illustrated in Figure 1-34.

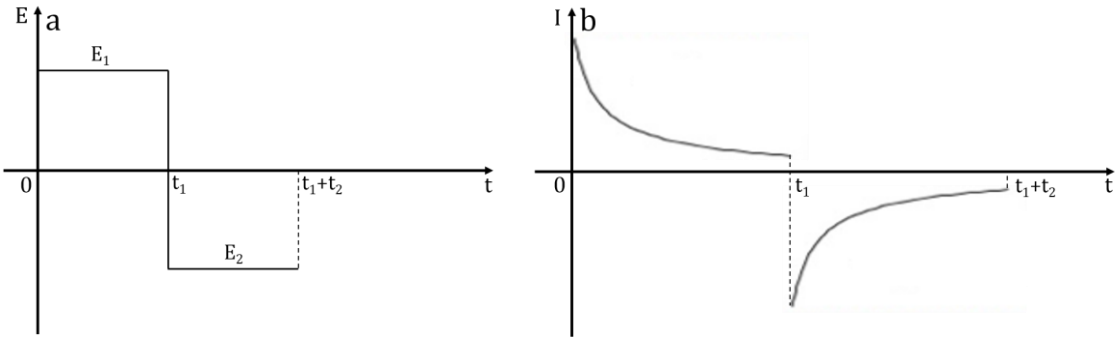

Figure 1-34: Schematic illustration of (a) waveform of potential step and (b) the resulting current variation. Modified from Bard and Faulkner.[106]

The response in Figure 1-34 illustrates a semi-infinite linear diffusion, that is the reaction occurs on a planar electrode in a stagnant solution with a supporting electrolyte to ensure the absence of ion migration.[117] The analysis of the chronoamperogram can, thus, be based on the Cottrell equation, which defines the time-dependent current transient in a diffusion-limited experiment, as represented by Equation 1-17.

$$i = \frac{n\ F\ A\ D^{1/2}\ C_o^*}{(\pi\ t)^{1/2}}$$

Equation 1-17

n is the number of electrons transferred per molecule, F is Faraday's constant (96 485 C/mol), A is the electrode area in cm^2, D is the diffusion coefficient in $cm^2\ s^{-1}$ and C is concentration in mol cm^{-3}.

Under these conditions, there is a linear relationship between the current and $t^{-1/2}$, known as the Cottrell plot. It is important to note that in any potential step experiment, there is a delay in attaining the step potential due to the finite rise time of the potentiostat. This non-ideal behaviour affects the validity of the data points in the Cottrell plot measured during this delay time. The non-linearity of the early data points is most clearly due to the reciprocal time function (i.e. early data points = large x). By minimising the capacitance of the working electrode and the uncompensated resistance between the working electrode and the reference electrode can largely increase the linear range of the Cottrell plot.[118]

The above explanation is based on chemical species and reactions. The use of double potential step chronoamperometry is limited in biological processes.
Zhang et al.[118] evaluated the use of the double potential step chronoamperometry for the measurement of charge-transport parameters of hydrated electroactive biofilms (EABs) dominated by *Geobacter* spp. It is deemed to be an alternative simple, quick and accurate method. The electrochemical responses were described and explained by a model of redox conduction, a phenomenon that also occurs in synthetic redox polymers. It consists of an incoherent multistep electron hopping from reduced to oxidised extracellular redox cofactors. It presents a diffusional behavior driven by a redox gradient across the network of redox cofactors within the EAB. EABs of *G. sulfurreducens* indeed possess abundant redox active multiheme *c*-type cytochromes localised on the bacterium outer membrane, pili and extracellular polymeric substances. The diffusion-like transport of electrons was quantitatively measured as an apparent diffusion coefficient and it was found to be similar to those measured for pure *Geobacter sulfurreducens* EABs as well as some redox polymers with analogous redox centre concentrations. This study confirms the vast evidence existing for the

redox conduction mechanism, which has been investigated for many decades with redox polymers.

The chronoamperometric method was used to study the anaerobic inactivation of an oxygen tolerant enzyme, NiFe hydrogenase. Under oxidising and anaerobic conditions, NiFe hydrogenase generated an inactive site, termed as NiB. It was demonstrated that cyclic voltammetry could not be used to measure the reduction potential of NiB in its inactive state, even in the small scan limit. To use the current transient technique, the enzyme was adsorbed onto an electrode in such a way so as to favour direct electron transfer with the turnover frequency being monitored as current. The research found it useful and simple to study redox-dependent activation/inactivation processes. The relaxation of the current was monitored after the potential was stepped up to inactivate the enzyme or down to force activation. Moreover, since current is proportional to the instant concentration of enzymes, the transient could be used to determine the proportion of active and inactive forms of the enzyme.[115]

However, chronoamperometric studies of the electrode-biofilm interface may sometimes be misleading and ambiguous. Thus, integrating the current may provide additional insight in understanding the reactions. The resulting study is known as chronocoulometry, as illustrated in Figure 1-35. The latter offers the following advantages over chronoamperometry, such as the signal increases over time instead of decreasing and the act of integration minimises noise.[106] Although chronocoulometry is a simple electroanalytical technique, it has not been used in interpreting electrode-biofilm reactions. Thus, this study aims at providing an additional understanding of this technique in a biological setting.

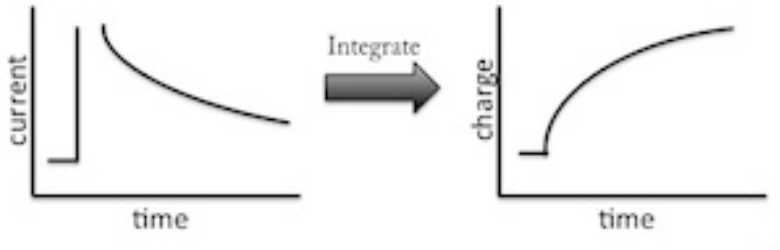

Figure 1-35: The integration of a chronoamperomogram results in a chronocoulomogram.

1.8 Research Motivation

Even though BPVs and photoMFCs are emerging sustainable technologies, they produce low power densities and the devices operate at low efficiencies.[36] The main reason for the poor performance is that microorganisms are not evolutionary conceived to power an electrochemical cell. Most of the relevant redox processes occur within the cells. It is, therefore, a major challenge and an important research issue to find means of diverting electrons from the metabolism to the anode as well as enhancing the electron transfer efficiency. Two different approaches are adopted, namely the performance of bioanodes is improved in Case Study 1 while the performance of the bacteria is improved in Case Study 2.

Case Study 1: *S. elongatus* in BPVs

Electron transfer rate at the biofilm-electrode interface is one of the key factors determining the performance of BESs. The electrode morphology and chemistry should facilitate bacterial attachment and biofilm formation as well as high electrochemical activity to promote fast electron transfer rate. Therefore, novel bioanodes are designed so as to improve their electrochemical interactions with *S. elongatus* as compared to conventional materials.

Case Study 2: *R. palustris* in photoMFCs.

The metabolic reactions of *R. palustris* can be manipulated by changing the ratio of nitrogen to carbon sources. The latter determines what proportion of the electron flux moves towards biosynthesis, biohydrogen generation and extracellular electron export. Therefore, a satisfactory ratio is determined with the overall aim of increasing electrons flux for extracellular export.

1.8.1 Bioanode in Case Study 1

The scope of the present study focuses on developing novel bioanode materials for BPVs. Since the bioanode acts as the carrier of *S. elongatus*, it should possess some optimal surface characteristics that are conducive to a higher bio-catalytic activity and electrochemical efficiency.[101] The following summarise the features that are essential for a performing bioanode.

1.8.1.1 Biocompatibility

Anode materials should actively promote cell adhesion, preferentially by acting as analogues for the natural extracellular matrix. Modulating and optimising cell adhesion is a challenge, which can be met by manipulating the physical and chemical properties of the anodic material surface. Physical features, such as surface roughness and morphology can be enhanced. Material surface chemistry includes tuning the surface energy and wettability.[85,86]

1.8.1.2 Surface area

The surface area of the bioanode largely restricts the power output of BPVs. The ohmic losses are directly proportional to the resistance of the bioanode. One way to decrease the electrode resistance is to increase the effective surface area while keeping the volume constant. Moreover, a high surface area provides more sites for reactions, enhancing the kinetics of the bioanode. One way of improving surface area is to increase surface roughness and porosity.

1.8.1.3 Electrical Conductivity

The electrons released by *S. elongatus* travel along an external circuit after passing through the anode. The high electrical conductivity of the anode reduces the resistance with which electrons have to flow.

1.8.1.4 Stability and Durability

The oxidising environment of the anodic chamber may lead to swelling and decomposition of the materials. As a result, the bioanode materials selected should be durable and stable in a basic environment.

1.8.1.5 Cost and Accessibility

The cost of the bioanode influences the capital cost of the BPV. Therefore, a low cost, sustainable and easily available material must be used. For the practical implementation of a BES technology, the cost of electrode materials must be reduced while the power densities must be maximised. [22,36,119]

1.8.2 Bacteria in Case Study 2

Studies on photoMFCs have been limited. However, many studies have focused on improving the ability of *R. palustris* to generate biohydrogen. One of the factors that has been manipulated experimentally is the nitrogen to carbon ratio. Therefore, this research work will use the same strategy to investigate whether changing the nitrogen to carbon ratio will improve the exoelectrogenic activity of *R. palustris*. Thus, the aim is to maximise both biohydrogen generation and exoelectrogenesis for conversion into bioelectricity.

Hydrogen is often hailed as the Holy Grail for alternative sources of energy to fossil fuels as it is clean, efficient and renewable. It is a promising future energy carrier as it has the highest energy density per unit mass as compared to all other fuels (143 GJ/tonne) and it is carbon-free as it produces only water on combustion.[77,78,120] Hydrogen can be used as a fuel for direct combustion in internal combustion engines or in fuel cells.[120] Traditional methods of producing hydrogen is through the thermochemical process of fossil fuels and the photo-electrochemical action of water, with contributions of 40% from natural gas, 30% from heavy oils and naphta, 18% from coal and 4% from electrolysis. However, these processes are highly energy intensive and not always environmentally benign. Under this perspective, biological hydrogen is a potential candidate for a safe, economical and sustainable hydrogen economy with zero-CO_2 emissions.[120–123] However, the main objective is to enhance the hydrogen yield to make biohydrogen more economically feasible. Biohydrogen production in the context of *R. palustris* in photoMFCs is a value-added product, which contributes to the renewable energy portfolio.

1.9 Thesis Outline

Chapter 2 on Materials and Methods details the experimental methods and analytical techniques used to generate the results chapters 3 to 6.

Chapters 3 to 5 focus on Case Study 1: *S. elongtaus* in BPVs, where the performance of bioanodes is enhanced for better electron transfer rate at the anode-biofilm interface.

Chapter 6 explores Case Study 2: *R. palustris* in photoMFCs where the performance of the bacteria is improved to achieve combined higher biohydrogen production and exoelectrogenesis.

Chapter 3 investigates improving the performance of conventional ITO-coated substrates in single chamber BPV devices by enhancing surface roughness. Graphene was produced by using two different methods and was applied on the ITO-coated substrates for surface modification. The surface chemistry of the bioanodes was analysed using Atomic Force Microscopy (AFM) and exoelectrogenic activity was determined by using Scanning Electron Microscopy (SEM) imaging, double potential step chronoamperometry and polarisation and power curves. A linear correlation between average surface roughness and maximum power density and increase in surface area and maximum power density was obtained.

Chapter 4 consists of improving the performance of carbonaceous materials in a MEA-type BPV device by enhancing the wettability property. An attempt to reduce the degree of hydrophobicity of carbon paper and carbon felt was carried out by introducing oxygen-functional groups. Another type of carbon material, namely graphene paper was analysed as it is inherently hydrophilic. The surface chemistry of the bioanodes was analysed using contact angle and exoelectrogenic activity was determined by SEM imaging, double potential step chronoamperometry and polarisation and power curves. While there was no impact on biofilm formation, wettability was important in minimising both activation and ohmic losses.

Chapter 5 describes some fundamental studies carried out with some newly designed nano-based bioanodes in MEA-type BPV devices. The performance of nitrocellulose membranes coated with an ink of graphene nanoplatelets in carboxymethyl cellulose and 3D-printed bioanodes coated with multi-walled carbon nanotubes were analysed. The surface chemistry of the bioanodes was analysed using AFM and exoelectrogenic activity was determined by using SEM imaging, double potential step chronoamperometry and polarisation and power curves. For the case of screen-printed graphene on nitrocellulose membrane, there was a decrease in maximum power output as average surface roughness and surface area increased. Biofilm formation on the 3D-printed anodes clogged the holes. Thus, the effective electrochemical surface area decreased, undermining their performance. However,

1.00 mm thick bioanode produced the highest maximum power output at the lowest internal resistance.

Chapter 6 focuses on varying the ratio of nitrogen to carbon sources, which affects biohydrogen generation. Moreover, the same strategy was used to improve the exoelectrogenic activity of *R. palustris*, a novel approach in the field. Parameters, such as biomass density, biohydrogen productivity, carbon and nitrogen sources consumed, were evaluated. Two prototypes of photoMFCs were designed for the capture of both biohydrogen and electrons. The exoelectrogenic activity was determined by using SEM imaging, cyclic voltammetry and polarisation and power curves. N:C=0.20 was the optimum ratio for a high yield of hydrogen as well as high exoelectrogenesis.

Chapter 7 ultimately closes the thesis with conclusions and future work.

2. Materials and Methods

This chapter reports the experimental procedures used for *Synechococcus elongatus* PCC 7942 in BPVs (Chapters 3, 4 and 5) and for *Rhodopseudomonas palustris* ATCC® 17007™ in photoMFCs (Chapter 6).

2.1 *Synechococcus elongatus* PCC 7942

2.1.1 Cell Cultivation

2.1.1.1 Bacterial Strain

The freshwater oxygenic photosynthetic cyanobacterium *Synechococcus elongatus* PCC 7942 was obtained from the Pasteur Culture Collection of Cyanobacteria (PCC), Institut Pasteur. The microorganism will be referred to as *S. elongatus* onwards. Axenity of the culture was regularly monitored by plating some culture sample on tryptone soy agar. The agar plate was incubated in the dark at 30°C for at least four days to check for the absence of bacteria.

2.1.1.2 Media Preparation

Cells of *S. elongatus* were cultivated in BG11 medium as recommended by the Culture Collection of Algae and Protozoa (CCAP)[124]. Table 2-1 and Table 2-2 illustrate the composition of the media. All chemicals were obtained from Sigma Aldrich, UK and were of analytical grade.

Table 2-1: Composition of main stock solutions, prepared separately[124]

Stock Solutions	**per litre**
(1) Sodium nitrate, $NaNO_3$	15.0 g
(2) Potassium phosphate dibasic, K_2HPO_4	4.0 g
(3) Magnesium sulphate heptahydrate, $MgSO_4.7H_2O$	7.50 g
(4) Calcium chloride dehydrate, $CaCl_2.2H_2O$	3.60 g
(6) Citric acid, $C_6H_8O_7$	0.60 g
(7) Ammonium ferric citrate green, $(NH_4)_5[Fe(C_6H_4O_7)_2]$	0.60 g
(8) Ethylene diamine tetraacetic acid disodium, $EDTANa_2$	0.10 g
(9) Sodium carbonate, Na_2CO_3	2.0 g

Table 2-2: Composition of trace metal solution[124]

Trace Metal Solution	**per litre**
Boric acid, H_3BO_3	2.86 g
Manganese chloride tetrahydrate, $MnCl_2.4H_2O$	1.81 g
Zinc sulphate heptahydrate, $ZnSO_4.7H_2O$	0.22 g
Sodium molybdate dehydrate, $Na_2MoO_4.2H_2O$	0.39 g
Copper sulphate pentahydrate, $CuSO_4.5H_2O$	0.08 g
Cobalt nitrate pentahydrate, $Co(NO_3)_2.6H_2O$	0.60 g

1 litre of BG11 medium was made of 100 ml of stock solution (1), 10 ml of each stock solution (2) to (8) and 1 ml of trace element solution. The final volume of the medium was made up with deionised water and its pH was adjusted to 7.1 with 1 M NaOH or 1 M HCl. The medium was then autoclaved at 121°C for 15 minutes at 1 bar.

2.1.2 Culture Conditions

Cell cultures of *S. elongatus* were grown in Erlenmeyer flasks with vented caps which have a 0.22 µm membrane to allow sterile gas exchange (Alpha Laboratories, UK). These flasks were incubated at 30±1°C under four cool white fluorescent light tubes with an intensity of 37±1 µmol photons m^{-2} s^{-1} under a 12:12 hours light-dark cycle. The cultures were continuously mixed at a shaking speed of 120 rpm. The experimental set-up is illustrated in Figure 2-1.

Figure 2-1: Growth of *S. elongatus* cultures in 500 ml Erlenmeyer flasks, with a working volume of 150 ml under illumination in a shaking incubator at 120 rpm.

2.1.3 Dry Cell Weight Measurement

The biomass density of *S. elongatus* was determined spectrophotometrically. A correlation between biomass dry weight of cells and absorbance values of the culture suspension measured at an optical density of 730 nm (OD_{730nm}) was developed.

Aliquots of 33 ml of a late exponential culture was spun down at 4696 x g for 10 minutes in a Thermo Scientific™ Heraeus™ Megafuge™ 16 centrifuge, with two washing

steps using an isotonic solution of ammonium bicarbonate (Sigma Aldrich, UK). After the final washing step, the supernatant was discarded and the pellet was re-suspended in 33 ml of ammonium bicarbonate.

30 ml of the bulk suspension was divided equally and placed in 6 pre-weighed aluminium-drying dishes. The latter were then dried in an oven at 105°C until a constant weight was obtained. The dry cell weight was the average of the 6 readings obtained after subtracting the weight of the empty dishes.

The 3 ml of culture left was divided equally into 3 mixing tubes. 6 x two-fold serial dilutions were carried out in triplicates with ammonium bicarbonate. The absorbance of each dilution was measured with a spectrophotometer (Thermo Scientific Evolution 201) at a wavelength of 730 nm against ammonium bicarbonate. The dry cell weight of each diluted solution was obtained by dividing the original average weight by the respective dilution factor. The biomass concentration is correlated to the absorbance as illustrated in Figure 2-2.

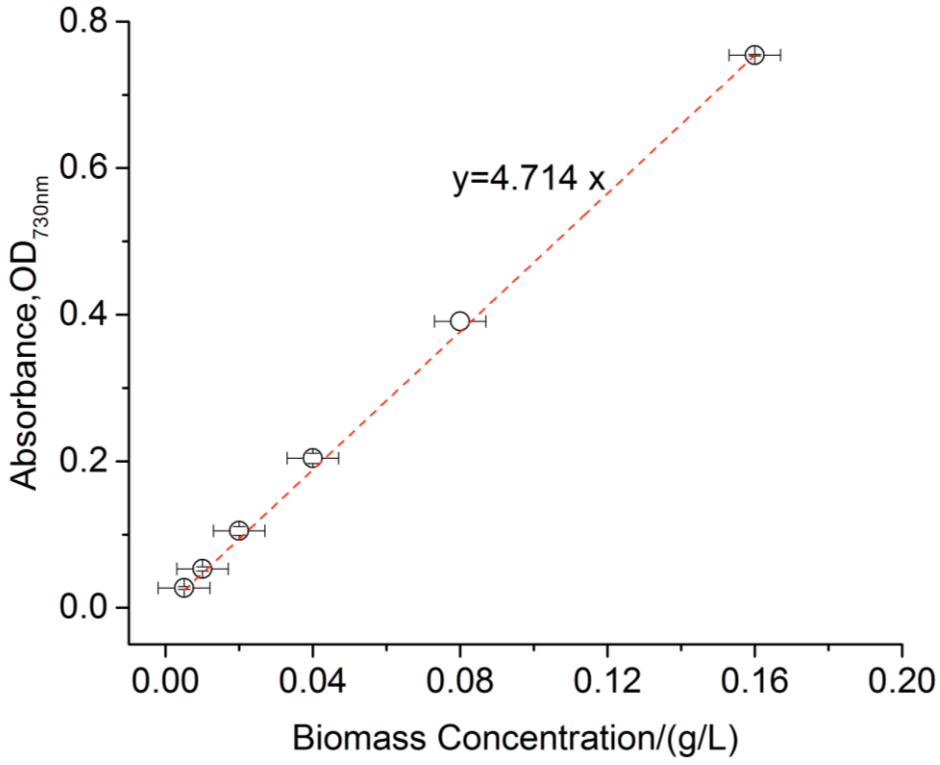

Figure 2-2: Calibration curve correlating absorbance at 730 nm and biomass concentration based on dry cell weight [the mean ± se is shown for each data set (n=6 for biomass concentration and n=3 for absorbance)]. The red dashed line is a straight-line fit passing through the origin. Biomass concentration/ (g/L) = (0.21 ± 0.01) x absorbance at OD_{730nm}. The equation is valid for absorbance between 0 and 1.

2.2 *Rhodopseudomonas palustris* ATCC® 17007™

2.2.1 Cell Cultivation

2.2.1.1 Bacterial Strain

The purple non-sulfur photosynthetic bacteria *Rhodopseudomonas palustris* (ATCC® 17007™) with strain designation ATH 2.1.37 [NCIB 11774] was obtained from Ning Xiao, a previous PhD student in Professor Nigel Slater's Laboratory (BioScience Engineering Group at the Department of Chemical Engineering and Biotechnology, University of Cambridge). The microorganism will be referred to as *R. palustris* onwards. Axenity of the bacterial culture was regularly monitored by plating some bacterial sample on tryptone soya agar. The agar plate was incubated in the dark at 30°C for at least a day to check for the sole presence of a single species.

2.2.1.2 Media Preparation

Cells of *R. palustris* were cultivated in a modified nitrogen fixing photosynthetic [PM(NF)] medium, based on a recipe described by Gosse et al.[67] All chemicals were obtained from Sigma Aldrich, UK and were of analytical grade. Table 2-3 and Table 2-4 detail the composition of solutions that constitute [PM(NF)] medium, which is shown in Table 2-5.

Table 2-3: Composition of trace element solution, Hutner's Metal 44[67]

Hutner's Metal 44 Solution	**per litre**
Ethylenediaminetetraacetic acid, $C_{10}H_{16}N_2O_8$	2.50 g
Zinc sulphate heptahydrate, $ZnSO_4.7H_2O$	11.0 g
Iron (II) sulphate heptahydrate, $FeSO_4.7H_2O$	5.0 g
Manganese (II) sulpahate monohydrate, $MnSO_4.H_2O$	1.50 g
Copper (II) sulphate pentahydrate, $CuSO_4.5H_2O$	392 mg
Cobalt nitrate hexahydrate, $Co(NO_3)_2.6H_2O$	250 mg
Sodium tetraborate decahydrate, $Na_2B_4O_7.10H_2O$	177 mg

The chemicals were dissolved in the order given and the next component was not added until the previous one had completely dissolved. After all the chemicals had been dissolved, a few drops of concentrated sulphuric acid (H_2SO_4) were added to retard precipitation. The solution was then made up to a final volume of 1 litre with deionised water, which gave a clear lime green colour. The bottle was wrapped in aluminium foil to protect it from light.

Table 2-4: Composition of concentrated base solution[67]

Concentrated Base Solution	**per litre**
Nitrilotriacetic acid (NTA), $C_6H_9NO_6$	20.0 g
Magnesium sulphate, $MgSO_4$	28.9 g
Calcium chloride dehydrate, $CaCl_2.2H_2O$	7.60 g
Ammonium molybdate tetrahydrate, $(NH_4)_6Mo_7O_{24}.4H_2O$	17.7 mg
Iron (II) sulphate heptahydrate, $FeSO_4.7H_2O$	0.198 g
Hutner's Metal 44 Solution	100 ml

NTA was dissolved separately in 600 ml deionised water and was neutralised with 14.6 g potassium hydroxide (KOH). The other components were then dissolved in the order given above. The pH of the solution was adjusted to 6.8 with approximately 100 ml of

1 M KOH. A precipitate formed from the acid side of 6.8 but it eventually dissolved on stirring. When the pH was near 6.8, the colour of the solution changed from a deep yellow to a straw colour. The solution was made to a final volume of 1 litre to be stored at 4˚C.

Table 2-5: Composition of PM(NF) medium[67]

PM(NF)	**per litre**
Potassium phosphate dibasic, K_2HPO_4	2.20 g
Potassium phosphate monobasic, KH_2PO_4	1.70 g
Sodium thiosulphate, $Na_2S_2O_3$	25.0 mg
4-aminobenzoic acid, $H_2NC_6H_4CO_2H$	2.00 mg
Concentrated Base Solution	1.00 ml

After the components were dissolved in the order given above, the solution was made to a final volume of 1 litre. The pH of the medium was adjusted to 7.0 with 30-35% hydrochloric acid (HCl) or 3 M sodium hydroxide (NaOH), after which it was autoclaved at 121˚C for 15 minutes at 1 bar.

The medium was supplemented with appropriate concentrations of nitrogen (N) and carbon (C) sources, depending on the mode of growth. The nitrogen source used was L-glutamic acid monosodium salt hydrate (Sigma Aldrich, UK), hereafter referred to as glutamate. 1 M solution of glutamate was prepared and autoclaved at 121°C for 15 minutes at 1 bar. 1 M solution of glycerol (Sigma Aldrich, UK) used as the carbon source was prepared and autoclaved at 121°C for 15 minutes at 1 bar.

2.2.2 Culture Conditions

Cell cultures of *R. palustris* were usually maintained with 5.4 mM glutamate and 10 mM glycerol in 500 ml Duran® bottles, with a working volume of 400 ml. The bottles were fitted with GL45 Omnifit® Q-series solvent bottle caps (Kinesis Ltd, UK), which has two sampling ports each with a built-in on/off valve. Each port was individually used to collect liquid and gas samples. The liquid sample port was fitted with a piece of polytetrafluoroethylene (PTFE) tubing (Cole Parmer), connected to a 0.20 μm

Sartorius™ Minisart™ syringe filter unit. Argon gas (Air Liquide) was bubbled through the cultures via the filter unit for 15 minutes to create an anaerobic environment, while maintaining sterility.

The culture bottles were housed in a custom-made bacterial culture cabinet of dimensions 53.5 cm x 49.0 cm x 69.5 cm (length x breadth x height). The cell cultures were continuously mixed using magnetic stirrer plates and were continuously illuminated by 6 x 60W incandescent/halogen light bulbs, giving about 124±17 µmol photons m^{-2} s^{-1} (Amprobe LM-120 Light Meter). The heat given out by the light bulbs maintained a temperature of 35 ± 2 °C.

Figure 2-3: Growth of *R. palustris* cultures in 500 ml Duran® bottles, with a working volume of 400 ml under illumination on magnetic stirrer plates.

2.2.3 Analytical Techniques

2.2.3.1 Dry Cell Weight Measurement

The biomass concentration of *R. palustris* was determined spectrophotometrically. A correlation between biomass dry weight of cells and absorbance values of the culture suspension measured at an optical density of 660 nm (OD_{660nm}) was developed. A wavelength of 660 nm was chosen as there is no pigment absorption at that value.[62]

Aliquots of 33 ml of a late exponential culture was spun down at 4696 x g for 10 minutes in a Thermo Scientific™ Heraeus™ Megafuge™ 16 centrifuge, with two washing steps using an isotonic solution of ammonium bicarbonate (Sigma Aldrich). After the final washing step, the supernatant was discarded and the pellet was re-suspended in 33 ml of ammonium bicarbonate.

30 ml of the bulk suspension was divided equally and placed in 6 pre-weighed aluminium-drying dishes. The latter were then dried in an oven at 105°C until a constant weight was obtained. The dry cell weight was the average of the 6 readings obtained after subtracting the weight of the empty dishes.

The 3 ml of culture left was divided equally into 3 mixing tubes. 6 x two-fold serial dilutions were carried out in triplicates with ammonium bicarbonate. The absorbance of each dilution was measured with a spectrophotometer (Thermo Scientific Evolution 201) at a wavelength of 660 nm against ammonium bicarbonate. The dry cell weight of each diluted solution was obtained by dividing the original average weight by the respective dilution factor. The biomass concentration is correlated to the absorbance as illustrated in Figure 2-4.

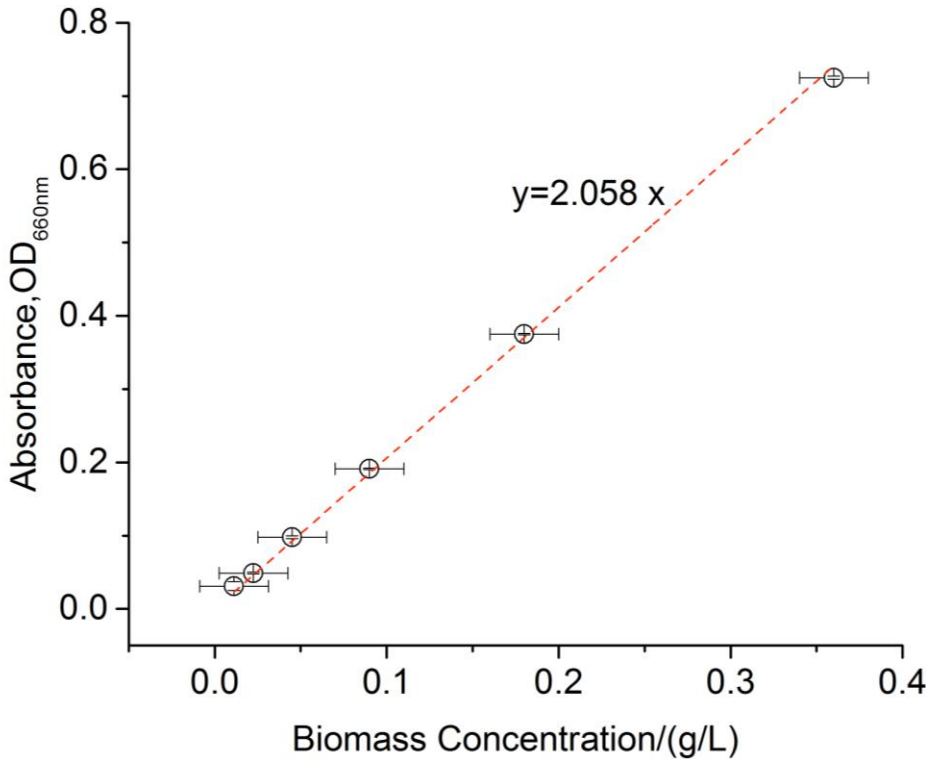

Figure 2-4: Calibration curve correlating absorbance at 660 nm and biomass concentration based on dry cell weight [the mean ± se is shown for each data set (n=6 for biomass concentration and n=3 for absorbance)]. The red dashed line is a straight-line fit passing through the origin. Biomass concentration/ (g/L) = (0.49 ± 0.02) x absorbance at OD_{660nm}. The equation is valid for absorbance between 0 and 1.

2.2.3.2 Gas Analysis using a Gas Chromatograph (GC)

The two gases of interest are hydrogen and carbon dioxide as they are the resulting products of the oxidation of glycerol during photofermentation. The composition of the off-gas was analysed by injecting the sample manually via the syringe into an Agilent 7890A gas chromatograph, fitted with a Thermal Conductivity Detector (TCD) and a 1.2 m Hayesep 13X 45/60 column with a molecular sieve. The carrier gas used to measure the retention time of hydrogen was nitrogen, which then switched to helium to gauge the retention times of carbon dioxide, argon and nitrogen. The retention times of the different components of the gas sample were then translated into percentage composition using the existing calibration database, as shown in Figure 2-5.

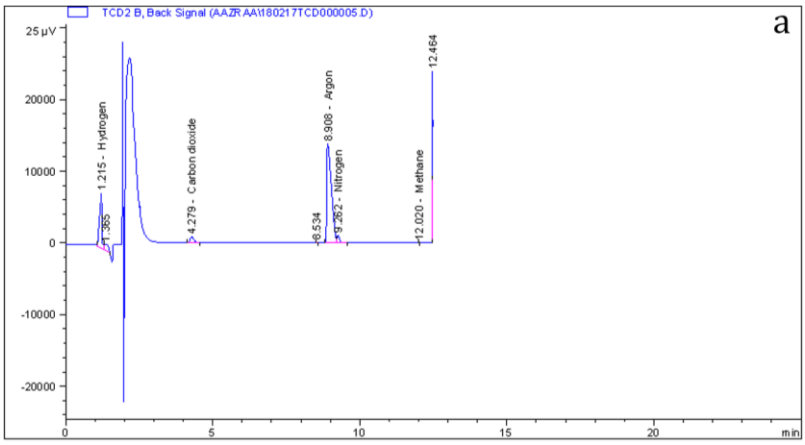

b

```
=====================================================================
                    External Standard Report
=====================================================================

Sorted By             :      Signal
Calib. Data Modified  :      25/05/2018 15:07:43
Multiplier:                   :      1.0000
Dilution:                     :      1.0000
Sample Amount:                :     10.00000  [%]   (not used in calc.)
Do not use Multiplier & Dilution Factor with ISTDs

Signal 1: TCD2 B, Back Signal

RetTime  Type     Area      Amt/Area    Amount   Grp   Name
 [min]          [25 µV*s]                 [%]
-------|------|----------|----------|----------|--|------------------
  1.215 BV     3.97921e4  8.37064e-4   33.30857    Hydrogen
  4.279 BB     7000.81641 5.40808e-4    3.78610    Carbon dioxide
  8.908 BV S   1.49343e5  4.67829e-4   69.86710    Argon
  9.262 VB S   6145.94678 5.53232e-4    3.40013    Nitrogen
 10.840           -          -           -        Carbon monoxide
```

Figure 2-5: (a) A typical example of a gas chromatograph showing retention times of the different gases present in the gas sample (b) A subsequent generated report showing the conversion of the retention times into % composition by using existing calibration methods.

2.2.3.3 Glycerol Assay

Glycerol concentration was measured using the periodate method, adapted from a technique developed by Bondioli and Della Bella.[125] The periodate oxidation of glycerol produces formaldehyde. The reaction between formaldehyde and two molecules of acetylacetone in the presence of ammonium acetate forms 3,5-diacetyl-1,4-hydrolutidine, usually known as Hantzsch's reaction. The final product formed has a very high specific absorption at a wavelength of 410 nm. The concentration of glycerol in the cultures can, thus, be correlated to the absorbance of 3,5-diacetyl -1,4-hydrolutidine.

To develop such a relationship, a 0.3 mM glycerol stock solution was made, with which 5 x two-fold serial dilutions were carried out. Enough volume was prepared for triplicates measurement. Reagent stock solutions of 1.6 M acetic acid and 4.0 M ammonium acetate were, then, prepared in water. These solutions can be stored at room temperature as they are stable over time. A 0.2 M solution of acetylacetone was

prepared by dissolving 200 µl of acetylacetone (Sigma Aldrich) in 5 ml of acetic acid stock solution and 5 ml of ammonium acetate stock solution. 10 mM sodium periodate solution was made by first completely dissolving 21 mg of sodium (meta)periodate (Sigma Aldrich, UK) in 5 ml of acetic acid stock solution. After dissolution, 5 ml of ammonium acetate stock solution was added. Acetylacetone solution and sodium periodate solution must be prepared on the day of the experiment.

2 ml of each of the prepared glycerol solution was placed in separate mixing tubes. 1.2 ml of periodate solution was added to each tube and the resulting solution was mixed for 30 seconds, after which 1.2 ml of acetylacetone solution was added. The mixing tubes were next placed in a water bath at 70°C for 1 minute, during which the tubes were continuously stirred. The tubes were then immediately placed and maintained in a water bath at 20°C, until they cooled down. The absorbance of each of the solution was then measured at 410 nm, as shown in Figure 2-6.

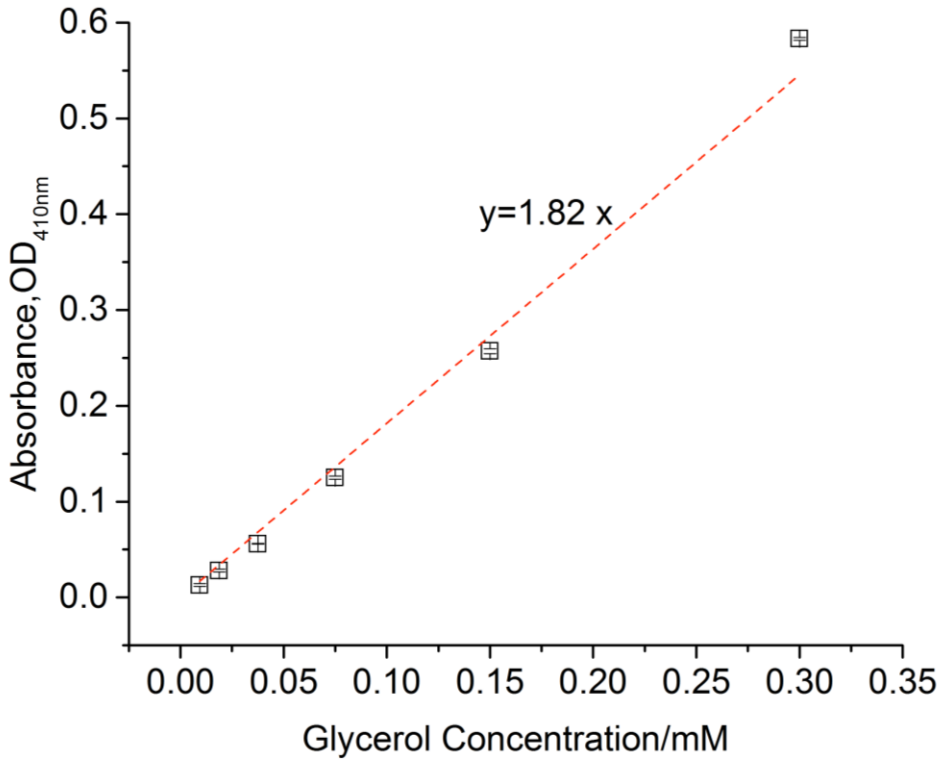

Figure 2-6: Calibration curve correlating absorbance at 410 nm and glycerol concentration [absorbance is the mean ± se for n=3]. The red dashed line is a straight-line fit passing through the origin. Glycerol concentration/mM= (0.55 ± 0.09) x absorbance at OD_{410nm}. The equation is valid for absorbance between 0 and 1.

To measure the concentration of glycerol in the cultures, an aliquot of 2 ml culture was obtained through the liquid port of the bioreactor. The liquid sample was filtered using a 0.45 μm syringe filter to remove cells and any debris. The same experimental steps used for the preparation of the calibration curve of the glycerol solution were applied to the filtrate.

The blank used to zero the spectrophotometer was PM(NF) media supplemented with glutamate, sodium periodate solution and acetylacetone solution. The blank was, also, used to dilute sample solutions if the absorbance exceeded the limits of the calibration curve.

2.2.3.4 Glutamate Assay

The ninhydrin colorimetric method, for the determination of the concentration of amino acids[126], was used to analyse the concentration of glutamate in the cell cultures. Ninhydrin, which is yellow in colour, reacts with a free alpha-amino group in five mechanistic steps to produce a final complex of ninhydrin, which is purple in colour. In essence, the reduced ninhydrin and ammonia that are produced in intermediate reactions provide the colour, which absorbs light at a wavelength of 570 nm. The test is adapted to detect glutamate as it contains an amino acid group. The concentration of glutamate can, thus, be associated with the absorbance of the final complex of ninhydrin.

The procedure was based on a protocol described by N.Wang.[127] An 8 mM stock solution of sodium glutamate was prepared, with which 4 x two-fold serial dilutions were carried out. Enough volume was prepared to perform the experiment in triplicates. Reagent stock solution of 0.35 g of ninhydrin (Sigma Aldrich, UK) in 100 ml of absolute ethanol (Fisher Scientific, UK) was prepared. The reagent solution is stable and can be kept indefinitely. 5 ml of each of the prepared glutamate solution was placed in different mixing tubes. 1 ml of ninhydrin solution was added to each tube and the resulting liquid was mixed. The tubes were, then, placed in a water bath at 80°C for 4 minutes, after which they were maintained in a water bath at 20°C, until they cooled down. The absorbance of each of the solution was measured at 570 nm, as shown in Figure 2-7.

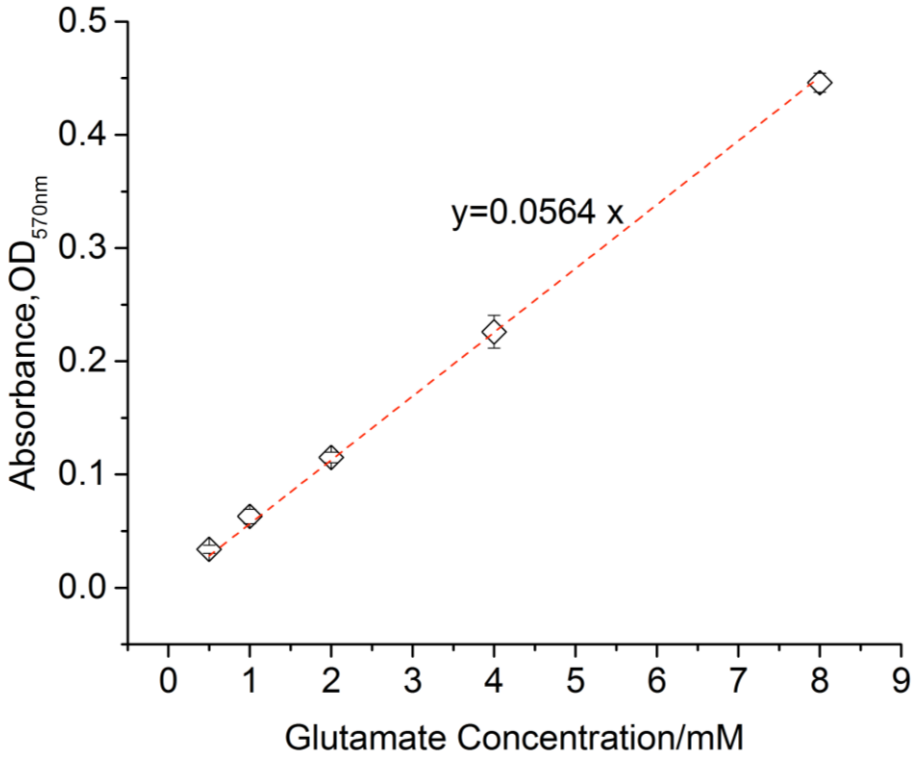

Figure 2-7: Calibration curve correlating absorbance at 570 nm and glutamate concentration [absorbance is the mean ± se for n=3]. The red dashed line is a straight-line fit passing through the origin. Glutamate concentration/mM= (17.730 ± 0.001) x absorbance at OD_{570nm}. The equation is valid for absorbance between 0 and 1.

To determine glutamate concentration in the cell culture, an aliquot of 5 ml was sampled. The latter was filtered using a 0.45 µm syringe filter to remove cells and any debris. The same procedure used to formulate the calibration curve was applied to the filtrate. The blank used to zero the spectrophotometer was PM(NF) media supplemented with glycerol and ninhydrin solution. The blank was, also, used to dilute sample solutions if the absorbance exceeded the limits of the calibration curve.

2.2.3.5 Bacteriochlorophyll *a* Measurement

The concentration of bacteriochlorophyll *a* (BChl *a*) was determined by solvent extraction using methanol and measuring its absorption spectrophotometrically at 770 nm. This is because BChl *a* posseses maximum light absorption at that wavelength in solvents.[128–131]

1 ml of bacterial culture was harvested and centrifuged at 15000 x g for 7 minutes in a Sigma 1-15 microcentrifuge. The supernatant was discarded and 1 ml of precooled methanol at 4°C was added. The sample was mixed by gently pipetting the solution up

and down. The sample was then incubated at 4°C in the dark for 20 minutes so as to extract the pigment from the cells. After the extraction period, the sample was centrifuged again at 15000 x g for 7 minutes to obtain a moss green supernatant.[132] The concentration of the pigment in the supernatant was, then, read in the spectrophotometer at 770 nm against methanol. An extinction coefficient of 11.8906 mg L^{-1} was used to determine the concentration of BChl *a*.[128]

2.3 Common Methodology for *S. elongatus* and *R. palustris*

2.3.1 Scanning Electron Microscope (SEM)

To observe the features of the biofilm, 1.5 ml of cultures with a concentration of 0.63 g L^{-1} and 1.47 g L^{-1} for *S. elongatus* and *R. palustris*, respectively were inoculated on the surface of the appropriate anode material. The latter was placed at the bottom of a transparent tube with a diameter of 10 mm. The biofilm was allowed to develop for a duration of 5 days. At the Cambridge Advanced Imaging Centre (CAIC), the samples were washed thrice with deionised water to oust any stray cells, following which they were quenched frozen by immersion into melting ethane in cooled liquid nitrogen. The biofilm on the substrates were, then, freeze dried in a Quorum/Emitech K775X for at least 8 hours. After the freeze-drying process, the samples were stuck onto SEM stubs by using carbon tape. For better electrical connection between the tape and the carbon paper, a dash of silver ink was added. All the substrates were then coated with 35 nm gold and 16 nm iridium in a Quorum/Emitech K575X sputter coater. The samples were then loaded into a FEI Verios 460L Scanning Electron Microscope (SEM) for imaging.

2.3.2 Electrochemical Measurements

The electrochemical measurements of cyclic voltammetry and double potential step chronoamperometry were carried out in a conventional three electrodes arrangement. The different bioanode materials acted as the working electrode, silver/silver chloride electrode in 3 M NaCl, +0.209 V vs. SHE at 25°C served as the reference electrode (RE-5B, BaSi) and 99.9% platinum gauze mesh was used as the counter electrode (Alfa Aesar). Cyclic voltammogram and chronoamperogram of the biofilms were obtained

by using a 4 channels potentiotstat (MultiEmStat[3], PalmSens) integrated with MultiTrace software.

A working device[133] was made of acrylic, which consisted of a 35 x 40 mm (inner diameter x length) cylindrical chamber chemically bonded to a square base of dimensions 70 x 70 x 10 mm (length x breadth x thickness). The base had a central hole of 18 mm diameter, which acted as a well. The working electrode (the different bioanode materials) with an active electrode area of 18 mm diameter was placed at the bottom of the well. A titanium strip was used to electrically connect the working electrode. The top of the chamber was covered with a PET disc which was sealed with an adhesive film. The PET disc had two holes on each end, each of 8 mm diameter, which were covered with nitrocellulose membrane (0.2 µm pore size) to allow sterile exchange of gas. Figure 1-28 illustrates a schematic diagram of the working device.

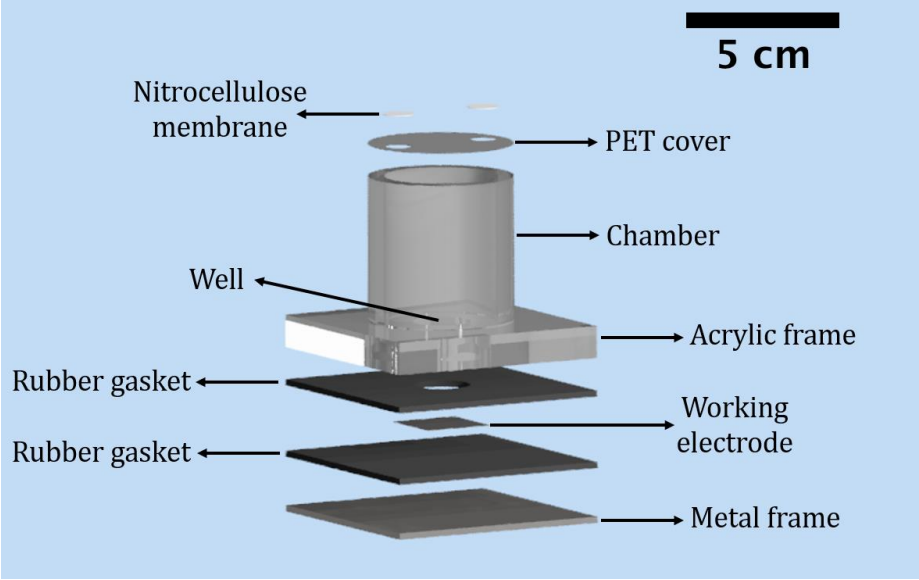

Figure 2-8: Schematic diagram of the working device holding the working electrode.

2.3.2.1 *S. elongatus*

After assembly, the working devices were autoclaved at 121°C for 15 minutes after which 4 ml of *S. elongatus* culture with a biomass concentration of 0.63 g L^{-1} was inoculated in the well of the working device. The top of the chamber was sealed with the PET disc. The cells were left to settle for 5 days to form a natural biofilm in an axenic manner at 30±1 °C under four cool white fluorescent light tubes with an intensity of 37±1 µmol photons m^{-2} s^{-1} under a 12:12 hours light-dark cycle. After 5 days, 30 ml of potassium phosphate buffer pH 7.0 was added as the electrolyte. The CV

scans were conducted at a scan rate of 1 mV s^{-1} in the potential range of -0.15 V to 0.35 V. The double potential step chronoamperometry was carried out in a set of 5 cycles at the potential steps of E_1=0.35 V and E_2=0 V with a time duration of 300 s for each potential step. The electrochemical analysis was performed at 30±1 °C and under illumination with the aforementioned intensity.

Figure 2-9 illustrates the experimental set-up for electrochemical measurements.

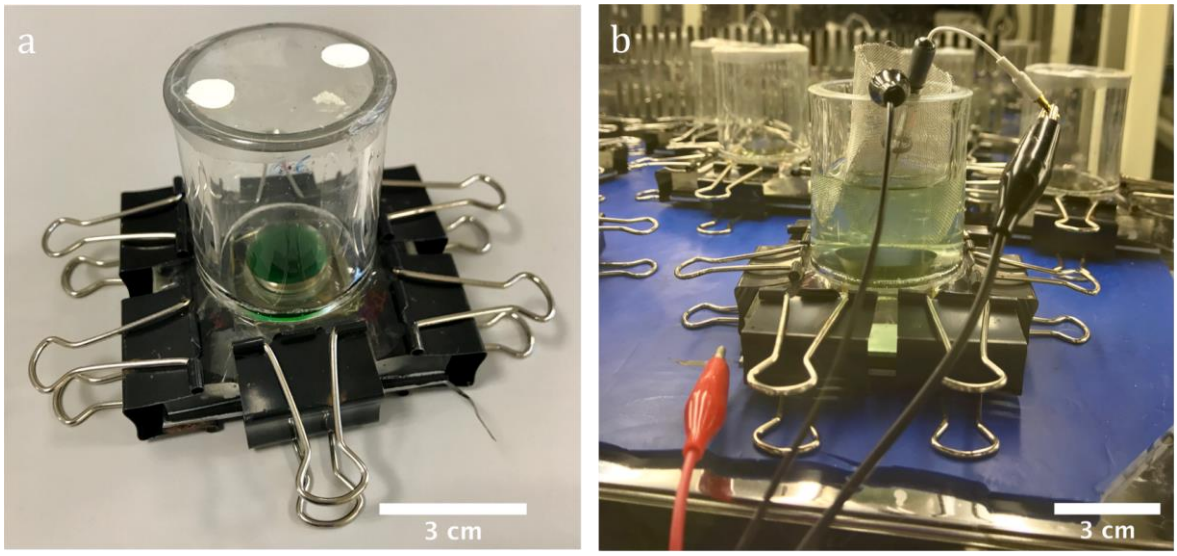

Figure 2-9: The experimental set-up for electrochemical measurements (a) Inoculation of the cell culture in the well of the working device for an axenic biofilm formation (b) working device connected in a three electrodes arrangement after 5 days.

2.3.2.2 *R. palustris*

After autoclaving, the well of the working devices was inoculated with 4 ml of *R. palustris* culture with a biomass density of 1.47 g L^{-1}.

The cells were left to settle for 5 days so as to form a natural biofilm on the working electrode, which is carbon paper. The biofilm was grown axenically both anaerobically and aerobically at 35±2 °C and under continuous illumination of 6 x 60W incandescent/halogen light bulbs, giving about 124±17 µmol photons m^{-2} s^{-1}. For an anaerobic set-up, the working device was placed in a system of automatic evacuation-replacement jar (Anoxomat, MART Microbiology b.v) using argon gas. After the 5 days, 30 ml of PM(NF) medium was added as the electrolyte. For the anaerobic condition, the working device was purged again with argon gas and CV measurements were carried out on the next day.

Figure 2-10 depicts the steps involved in measuring the CV for the anaerobic condition. The CV scans were conducted at a scan rate of 1 mV s^{-1} in the potential range of -0.8 V to 0.2 V. All electrochemical analyses were performed at a temperature of 35±2 °C and under illumination with the aforementioned intensity.

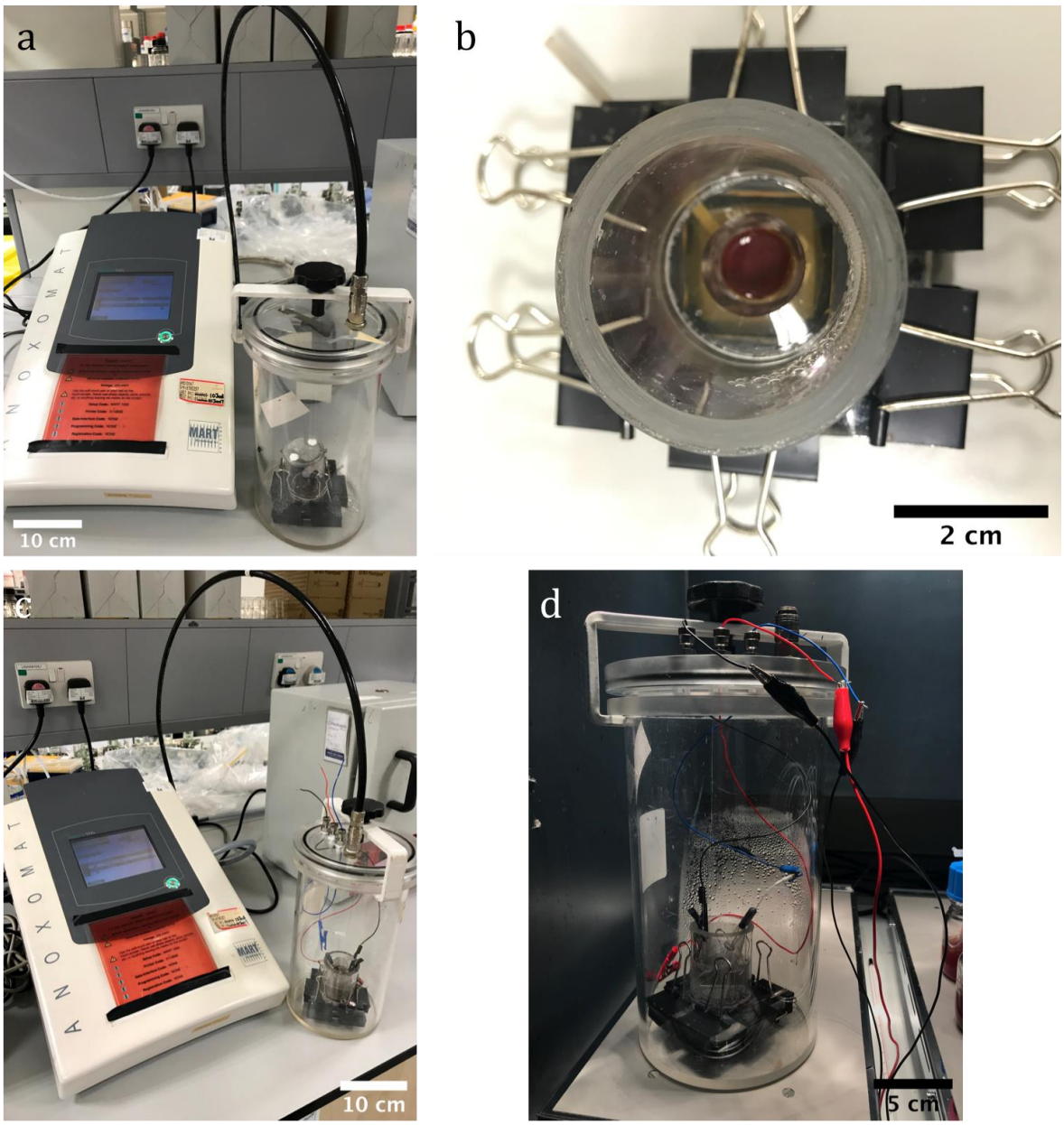

Figure 2-10: Steps involved in CV measurement for the anaerobic condition (a) Purging of working device with argon before incubation for 5 days (b) biofilm formed after 5 days (c) working device purged after adding electrolyte, reference and counter electrodes and (d) working device connected to potentiostat: red wire connects to the working electrode, black wire connects to the counter electrode and blue wire connects to the reference electrode.

2.3.3 Performance Analysis of BPVs and photoMFCs

Polarisation and power curves were determined by continuously monitoring and recording voltage drop using PicoLog ADC-24 data logger and PicoLog data acquisition software at an interval of two minutes. The voltage drop was induced by varying the external loads; the range of 32 MΩ to 33 kΩ, 10 MΩ to 33 kΩ and 5MΩ to 56 Ω was used for the single chamber BPV device, the MEA-type BPV device and the photoMFC devices respectively. The load was switched to a lower value once a pseudo-steady voltage value was obtained. This measurement allowed the analogous current and power of the devices to be calculated by using Ohm's law. The internal resistance of the devices was obtained from the slope of the linear part of the polarisation curve. Once satisfactory measurements were obtained, the devices were left to reach OCP, after which the load that gave the maximum power output was connected to the circuit to maintain a current flow.

3 Improving the Performance of ITO-coated Substrates by Enhancing Surface Roughness

3.1 Introduction

The nature of the anode is a key factor for the performance of the BPV device as it largely influences biofilm formation and electrochemical communication between the anode surface and the microorganisms. One of the strategies used to develop anodes that foster microbial interaction for high electrochemical reaction rates and low potential losses is to modify the geometric surface area or topography of the material, for instance by increasing surface roughness. This is usually carried out by modifying the surface of the anode materials with functional materials to enhance biofilm attachment and minimise electrochemical losses.[22,36,87,119,134] This chapter evaluates and optimises the design of graphene deposited on conventional indium tin oxide (ITO)-coated substrates for enhanced surface roughness and subsequent improved performance as bioanodes.

3.1.1 Topography and Surface Roughness

Topography, as defined by Abbott-Firestone,[86] is represented by the roughness parameters R_{rms} (mean roughness) and R_z (maximum roughness) as well as other parameters. Surface roughness can be measured at the nanometer scale using techniques like Atomic Force Microscopy (AFM), which helps in understanding the nanometre scale interactions in cell attachment. Besides the effects on bioadhesion, surface roughness also influences electrochemical activity as both activation and ohmic losses can be minimised.[22,99]

3.1.1.1 Biocompatibility

The scale of irregularities of a material surface can be identified by several degrees or grades of surface roughness. Each type of roughness has a defined effect on the behaviour and adherence of cells. Macroroughness is irregularities distinguished by the human eye, in the scale of at least 100 μm and seems to be supportive of cell adhesion and spreading. This is because the cells do not feel the large irregularities and they can, thus, spread easily. Microscale roughness is characterised by irregularities from 1 to 100 μm and it behaves more controversially. Some studies have proclaimed that microroughness improves cell adhesion and growth while the opposite has also been reported.[85] The dual mechanism of microroughness still remains unclear, as there is a lack of systematic study on this particular behaviour. This issue can be related to the way of defining surface roughness. The most common parameter used to represent surface roughness is R_a, which is the average peak-to-valley height. This measure does not reflect the type of surface topography, for example the spacing between the irregularities, their different shapes (pyramids, cones, ridges, grooves, round pores), the curvature of the valleys and especially the sharpness of the peaks on the material surface, which could hamper cell adhesion and spreading. Submicron surface roughness is defined by aberration in the range of 100 nm and 1 μm and it also exhibits dual effects on cell growth and attachment with improved bioadhesion being the most common occurrence. Nanoroughness is indicated by irregularities of less than 100 nm and it has unquestionably been considered as a beneficial factor for the growth and adhesion of cells as the nanostructure of the material resembles the nanoarchitecture of the natural extracellular matrix.[85]

Several research works have shown that increasing the surface roughness of the anode enhances the performance of bioelectrochemical cells. In one study, the use of acid treatment of anodes led to cracks being introduced on the surface, which improved the performance of the electrochemical cell.[22,119] Cao et al.[135] compared the attachment of cells on two types of surfaces of stainless steel. They have shown that algae preferred to attach to textured surfaces rather than smooth ones. Sekar et al.[136] evaluated the adhesion of *Chlorella vulgaris*, *Nitzschia amphibia and Chroococcus minutus* on different substrates. It was found that cells attachment was higher on rough surfaces than on smooth surfaces of both titanium and stainless steel substrates. However, these studies failed to define the degree of smoothness or roughness of the surfaces. Han

and Fukurawa[137] have demonstrated that carbon cloth coated with polyaniline (PANI) produced more power compared to uncoated ones. Moreover, carbon paint anodes without any polymer showed weak positive light response while the anodes coated with conductive polymers polyaniline and polypyrrole showed significantly higher light amplitude response. The difference between the bare and coated anodes can be based on improved efficiency in electron transfer from the biofilm to the modified anodes and the positive effects of the conductive polymers on biofilm formation. In terms of power output, the bare carbon anode produced 0.35 mW m^{-2} while polyaniline-coated anode produced 0.95 mW m^{-2} and polypyrrole-coated anode produced 1.3 mW m^{-2}.[35] Another investigation determined that carbon fibres coated with both granular and fibrillar polypyrrole showed higher light amplitude response compared to non-coated carbon fibres. This suggests that the conductive polymer enhances electron collection. From electrochemical impedance spectroscopic studies, the anodic interfacial charge-transfer resistance was the lowest with fibrillar polypyrrole (4.3 Ω) compared to granular polypyrrole (12.6 Ω) and bare carbon fibres (39.8 Ω). The conductive polymers helped to substantially improve the efficiency of electron transfer from the biofilm.[138] Since nanostructure of anodes is an area of interest, a study compared ITO-coated glass with polyaniline/ITO-coated glass in a MFC inoculated with rice paddy field soil. A 30-fold increase in current density was observed when the ITO conductive glass anode was coated with a polyaniline nanowire network (PANI-NN) of three dimensional nanosized porous structures as compared to a thin flat structure of polyaniline. The rough surface structure of PANI-NN improved the direct attachment of bacterial cells to the surface of the anode. The large surface area was mostly due to nanosized network structures with pores much smaller than microbial cells.[134]

3.1.1.2 Electrochemical Activity

A high electrochemical activity of the bioanode is important for the performance of the BPV device. It can be promoted by roughening the anode surface to obtain a large surface to geometric area ratio.[139] The increase in surface area decreases the resistance of the anode. The latter is proportional to ohmic losses and, thus, increasing the surface roughness of the anode decreases ohmic losses.[22] Moreover, activation

losses are minimised by an increase in surface area as when surface area is increased, the current density is reduced.[99]

The electrochemical performance of lithium-ion rechargeable batteries was evaluated by depositing thin film of amorphous silicon anode on two types of substrates: a normal copper foil and a roughened copper foil. It was found that the rough foil helped the silicon film to maintain electrical contact with the current collector during charging and discharging. More importantly, the rough foil assisted the silicon anode in reducing polarisation or internal resistance during subsequent cycles of charging and discharging.[139] Herraiz-Cardona et al.[140] assessed the effect of the surface roughness factor on the hydrogen evolution reaction (HER) by comparing three types of electrodes, namely rough pure nickel electrodeposits, smooth nickel-cobalt electrodeposits and smooth commercial nickel electrodes. The experimental study indicated that the rough nickel electrode had the highest electrocatalytic activity in HER. The increase in the surface area of the catalyst helped in minimising activation overpotentials.

3.1.2 ITO-coated Substrates as Bioanodes

Doped metal oxides are attractive transparent electrodes widely used in flat panel displays, solar cells, gas sensors and electronic applications. ITO-coated substrates are one of the best performing transparent electrode materials. Since they possess a large band gap, they are transparent to visible light and the high levels of tin doping help to retain a metal-like conductivity. Moreover, they were shown to be biocompatible.[141–143]

ITO-coated PET was used as a transparent and conductive anode in a single chamber BPV system to analyse the performance of green alga *Chlorella vulgaris* and *Dunaliella tertiolecta* and cyanobacteria *Synechocystis* sp. PCC 6803 and *Synechococcus* sp. WH 5701.[34] It was found that *Synechococcus* performed better than the other strains with a total maximum power output of 10.3 mW m^{-2}. The performance was attributed to its marine nature, as the medium used was higher in conductivity and contributed to the high power output. Bombelli et al.[36] compared the performance of various anodic materials, namely ITO-coated PET, stainless steel, polyaniline-coated glass and carbon paper in a mediatorless, multichannel and open-air BPV device using photosynthetic biofilms of *Pseudanabaena limnetica*. It was determined that ITO-coated PET had a

smooth and a highly homogenous surface, thus having the lowest average surface roughness. However, it outperformed the other materials in terms of maximum power density and internal resistance with a value of about 30 μW m^{-2} and 305.24 kΩ, respectively. Cyanobacteria *Arthrospira maxima* were inoculated in a BPV device containing ITO-coated glass as the anode. The study demonstrated that increasing the temperature and light intensity improved the peak power density with the highest value being 24.8 μW m^{-2} at an internal resistance of 1.2 MΩ.[144] Ng et al.[145] compared the unicellular *Chlorella* UMACC 313 and the filamentous *Spirulina* UMACC 159 on three types of surface structures; an unmodified smooth ITO-coated anode, etched ITO-coated anode with lines at 2.5 mm apart and etched ITO-coated anode with lines at 1 mm apart. Both modified surfaces had higher biofilm coverage than the unmodified bioanode. Moreover, the maximum relative electron transport rate was also higher with the etched surfaces. These results suggest that the increase in surface roughness improved the biofilm attachment resulting in a better electron transport rate. The performances of ITO-coated glass and reduced graphene oxide (RGO)-coated glass were compared using green alga *Chlorella* sp. (UMACC 313) with RGO-coated glass producing an improved peak power of 273 μW m^{-2} and a noticeable increase in efficiency. The enhanced performance of the BPV was attributed to the unique properties of RGO. The highly porous RGO film was said to increase surface area, which enhanced biofilm attachment and, thus, improved the efficiency of electron transfer.[142] Cyanobacteria *Nostoc punctiforme* and *Synechosystis* sp. PCC 6803 were used to assess the performance of microporous and nanoporous ITO on fluorine doped tin oxide (FTO)-coated substrates against non-porous ITO-coated PET. Both the microporous and nanoporous anodes outperformed the non-porous anode by producing a 300-fold increase in photocurrent from a value of 0.04 mA m^{-2}, with the microporous anode being better performing. The enhanced performance is linked to the large electrode surface area available for electrochemical interactions. The advantage of the microporous over the nanoporous anode was ascribed to the larger, more accessible electrode surface, a smaller average distance that self-mediated molecules have to travel to reach the anode and the fact that the biofilm can reach further into the microporous anode. However, the comparison was not carried out by using the same base electrode, as the non-porous anode was not doped with any FTO as the other two types of anodes. It would be further useful to have insight of the effects of the porous

anode materials on the internal resistance of the devices and the maximum power output. Moreover, the anode was at 0.2 V in all the experiments rather than exploiting the natural anode potential.[141] Thus, electrochemical losses were not taken into account and current densities were not limited by the architecture of the system, which may, therefore, be overestimated.[81]

3.2 Proposed Concept and Research Aim

The research aim of this chapter is to improve the performance of conventionally used ITO-coated substrates in BPVs by enhancing their surface roughness and surface topography. The following objectives were established to achieve the research goal.

1. Designing the configuration of the BPV device and bioanodes
    - A single chamber BPV device was designed, capitalising on the features of ITO-coated substrates with overall aim to maximise their performance.
    - In a first trial, ultrasonicated liquid phase exfoliated (LPE) graphene was cast on ITO-coated substrates.
    - A screen-printing process using microfluidised liquid phase exfoliated (LPE) graphene nanoplatelets cross-linked with carboxymethylcellulose (GNP-CMC ink) was optimised to obtain the appropriate design and features.
2. Surface characterisation was carried out to decipher the material surface chemistry and biofilm coverage was analysed by using the SEM technique.
3. SEM images and electrochemical methods, such as cyclic voltammetry and double potential step chronoamperometry were used to identify any electroactive traits of the biofilm. Chronoamperometry was used to further analyse and interpret the electrochemical interactions between the cells of *S. elongtaus* and the anode materials.
4. The performance of the BPV devices was analysed using the following four parameters: OCP, activation loss, internal resistance and maximum power output.

3.3 Materials and Methods

3.3.1 Ultrasonicated Graphene

The Cambridge Graphene Centre produced the ultrasonicated liquid phase exfoliated (LPE) graphene nanoplatelets that was cast on indium tin oxide (ITO)-coated glass (15-25 Ω/square, Sigma Aldrich UK) and indium tin oxide (ITO)-coated PET (60 Ω/square, Sigma Aldrich UK). Natural flake graphite was dispersed in 9 mg/ml sodium deoxycholate (Sigma Aldrich, UK) in water by using a sonication bath for 9 hours. The dispersion was centrifuged at 10 000 rpm for one hour to remove the unexfoliated graphite, before the supernatant could be collected. 0.5 ml of the supernatant was diluted with 1 ml deionised water and was vacuum filtered onto a nitrocellulose membrane (100 nm pore size). The dried film was, then, washed with 15 ml water and left to dry at room temperature. The membrane was, then, soaked in water until it was fully wet. The graphene side of the membrane was placed down onto the substrate. The film was compressed with clips between two glass slides and left to dry in an oven at 80˚C for 1 hour. The glass slides were removed and the substrate/graphene nitrocellulose was placed in a beaker, containing 100 ml acetone for 3 days to dissolve the nitrocellulose membrane. The substrate/graphene sample was transferred to a beaker of 100 ml isopropyl alcohol for 1 hour and, then, to a beaker of 100 ml water for 1 hour. The sample was, then, dried in an oven at 80˚C for 1 h.

The diameter of LPE graphene on ITO-coated glass was 16 mm whereas that on ITO-coated PET was 15 mm.

3.3.2 Microfluidised Graphene Nanoplatelets in Carboxymethylcellulose (GNP-CMC ink)

The preparation and screen-printing of GNP-CMC ink was carried out at the Cambridge Graphene Centre.

3.3.2.1 Preparation of GNP-CMC Ink

Graphene flake ink was produced by microfluidic processing as reported previously.[146] Timrex KS25 graphite flakes were used as a starting material, selected because their size is suitable for flow in microchannels of width of about 87 μm (D90 <27.2 μm).

Larger flakes would cause blockages. The flakes were used in conjunction with sodium deoxycholate (Sigma Aldrich, UK). The latter was first mixed in deionised water at a concentration of 5 g L^{-1} and the graphite flakes were then added at a concentration of 100 g L^{-1}. A microfluidic processor with a Z-type geometry interaction chamber (M-110P, Microfluidics) was used to process the mixture at the maximum pressure of the system (about 207 MPa) for 70 process cycles. The temperature increased from 20°C to 55°C after the liquid passed through the interaction chamber. A cooling system, then, reduced it to about 20°C. This is important as otherwise the temperature would keep on increasing and the solvent would eventually boil.

Following microfluidisation, carboxymethylcellulose sodium salt (CMC) (Molecular weight, M_W = 700.000, Sigma Aldrich No. 419338), a biopolymer, which is a rheology modifier, was added to the dispersion to stabilise the flakes against sedimentation. CMC was added at a concentration of 10 g L^{-1} over a period of 3 hours at room temperature. CMC was not easily dissolved and its preparation can be affected by factors including the CMC particle size, rotational speed of the mixer, the rate at which solutes are introduced and the temperature of the solution.[147] Heating of the graphene dispersion should be avoided as this may promote flocculation. CMC is water-absorbent and has very high water retention and, therefore, it clumps easily. To prevent this, CMC was added slowly over a period of 3 hours and in small (100 mg) portions until dissolved completely. The solution was stirred at slow speeds (about 300 rpm) and was left overnight. Vigorous stirring can cause air bubbles, especially as viscosity builds up. These must be removed prior to printing. If clumps of CMC do form, it may be necessary to use a spatula to grind them by hand so that they can dissolve.

Due to the application as an electrode in aqueous media, the inherent water solubility of CMC would cause the dissolution of the graphene flake electrode during operation. Therefore, a cross-linking agent, 1,4-Butanediol diglycidyl ether (≥95%, Sigma Aldrich UK), was added to fix the CMC in place, at a ratio of 10 ml ink to 40 µl cross-linker. Stirring was performed for at least 2 hours before the inks were used for printing/coating. The cross-linker contains two reactive epoxy end-groups that ring open to react with hydroxyl groups on the cellulose backbone. Upon addition of water to the dried films, there are different degrees of swelling of the electrodes but no observable dissolution.

3.3.2.2 Screen-printing of GNP-CMC Ink

Screen-printing was performed using a Kippax KPX2012 Semi-Automatic screen-printer. The screens, purchased from Mascoprint Ltd., UK, was an aluminium frame of dimensions 800 x 460 mm, covered in 90 polyester mesh, which is water-proof and hard. Prior to printing on ITO-coated PET substrates only, they were treated using UV-Ozone Cleaner UVC-1014 (NanoBioAnalytics) for 5 minutes to improve their wettability.

The steps involved in the screen-printing process are depicted in Figure 3-1. GNP-CMC ink was applied to the screen and the squeegee was lightly pressed over the screen to fill the mesh. The squeegee was, then, passed over the screen at a higher pressure such that the ink was pushed through the mesh onto the substrate. This step is known as a pass. The wet film was left to dry to produce the final design.

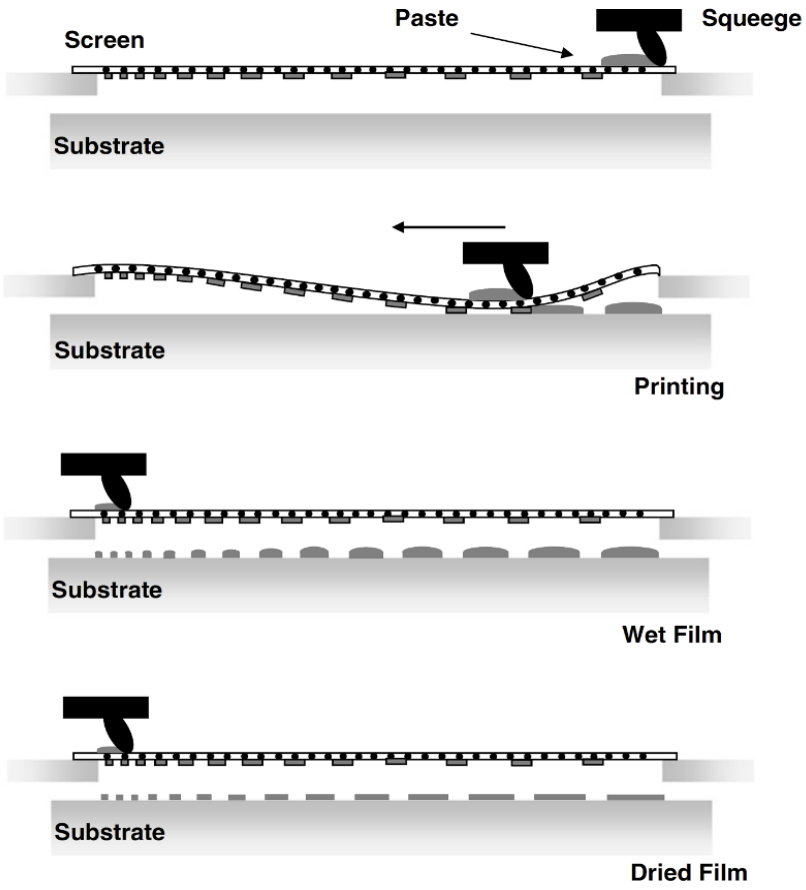

Figure 3-1: Schematic illustration of the steps involved in the screen-printing process. Reproduced from Lee at al.[148]

3.3.3 Characterisation of GNP-CMC Ink/ITO-coated Bioanodes

3.3.3.1 Optical Microscopy

Optical images of GNP-CMC ink on the ITO-coated substrates were obtained with a Nikon OPTIPHOT 300 microscope at the Cambridge Graphene Centre.

3.3.3.2 Profilometry

Profilometry was used to measure the thickness and roughness of the anodes. Measurements were performed using a DektakXT Stylus profilometer (Bruker) with a 12 μm diameter probe applying a 3 mg force during the scan. 3 line profiles were measured for each sample and an average was taken. Analysis was performed using Vision64 Operation and Analysis Software.

3.3.3.3 Atomic Force Microscopy

AFM topography images were acquired at the Material Imaging and Analysis (MIA) Centre with a Veeco Dimension 3100 Scanning Probe Microscope (Digital Instruments Veeco Metrology Group). The scanning was carried out in an area of 10 x 10 μm^2 in tapping mode. Quantitative material surface characteristics such as average surface roughness and surface area were obtained with the software NanoScope 6.14R1.

3.3.4 Single Chamber BPV Device

The single chamber BPV device houses both the electrodes and electrolyte in one single compartment. The device was constructed using two acrylic frames, each of dimension 50 x 50 x 5 mm (length x breadth x thickness). Both frames had a hole to provide an active electrode area of 18 mm diameter. The acrylic frames were tooled using an 80 W CO_2 laser cutter (HPC Laser Ltd). Two circular polydimethyl siloxane (PDMS) gaskets of about 1 mm thickness matching the design were positioned below each frame to seal the device. The ITO-coated substrates were cut into squares of length 25 mm. Each anode was placed on the bottom PDMS gasket-acrylic frame. A PDMS ring with a thickness of 6±1 mm was placed between the anode and cathode to create a cell chamber to accommodate about 1.5±0.1 ml of culture. The cathode used was Toray Carbon Paper TGP-H-60 coated with platinum mixed in carbon black (0.36-0.5 mg

Pt/cm^2, Alfa Aesar and Fuel Cell Earth LLC). A small hole was perforated in the middle of the cathode to allow access to the cell chamber. Titanium strips were used to make electrical contacts to both the anode and cathode. The whole system was held together by eight hex socket cap screws. Figure 3-2 illustrates the schematic structure and an actual photograph of the single chamber BPV device.

The devices were autoclaved, following which 1.5 ml of culture at an initial biomass concentration of 0.63 g L^{-1} was inoculated. A translucent, breathable and anti-bacterial adhesive film was used to seal the top of the device to maintain sterility and to minimise evaporation. The BPV devices were, then, incubated at 30±1°C on a light box emitting cool white fluorescent light with an intensity of 73±4 µmol photons m^{-2} s^{-1} under a 12:12 hours light-dark cycle. The cells were allowed to settle for 5 days so as to form a natural biofilm, before measurements were carried out.

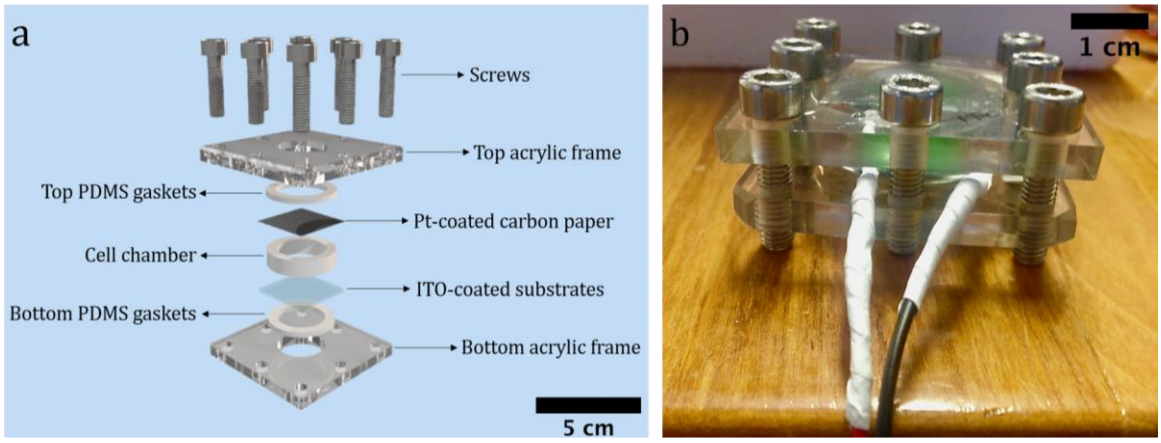

Figure 3-2: Illustration of a single chamber BPV device (a) a schematic diagram and (b) actual devices inoculated with *S. elongatus*. The device was designed by Gonzalez Aravena.[149]

3.4 Results and Discussion

3.4.1 Baseline Performance

The performance of indium tin oxide (ITO)-coated glass and indium tin oxide (ITO)-coated polyethylene terephthalate (PET) in the single chamber BPV devices was first determined to set the baseline against which the new designed bioanodes can be contrasted to.

Figure 3-3 illustrates the polarisation curves from which OCP values, activation and ohmic losses can be determined. The different regions of electrochemical losses are determined by the linear behaviour of the ohmic region (R^2 value) and by double-

checking the value of the ohmic loss with the external load that produces the maximum power output.

ITO-coated glass bioanodes had a slightly higher OCP value of 306±18 mV as compared to ITO-coated PET bioanodes with an OCP value of 243±1 mV. However, ITO-coated glass bioanodes suffered from a higher activation loss of 158 mV as compared to 106 mV for ITO-coated PET bioanodes. The ohmic losses would be identified in Figure 3-4.

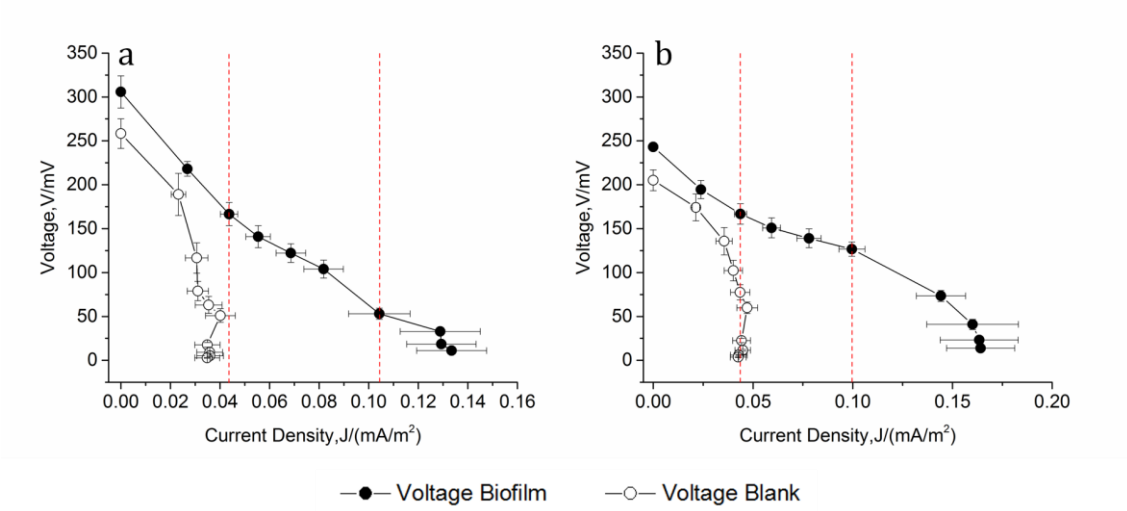

Figure 3-3: Polarisation curves of (a) ITO-coated glass and (b) ITO-coated PET [the mean ± se is shown for each data set (n=3)]. The lines shown are purely used to guide the eye. The additional red dash lines separate the different regions of electrochemical losses for the biofilm only.

As shown in Figure 3-4, ITO-coated PET bioanodes had a slightly better performance than ITO-coated glass bioanodes. The slightly lower internal resistance of devices containing ITO-coated PET bioanodes resulted in a marginally higher maximum power output of 13±2 μW m^{-2} as compared to 9±2 μW m^{-2} for ITO-coated glass bioanodes.

a

Bioanode Materials	Internal Resistance/MΩ
ITO-coated Glass	5.7±0.6
ITO-coated PET	4.9±0.3

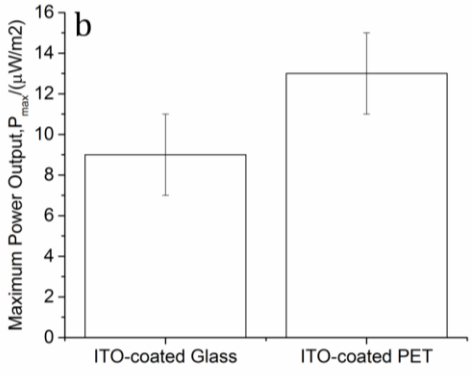

Figure 3-4: Data extracted from polarisation and power curves to compare the performance of ITO-coated substrates with regards to (a) internal resistance and (b) geometric maximum power output [the mean ± se is shown for each data set (n=3)].

The power densities produced by the devices were low with high internal resistances. One of the factors contributing to the poor performance was the design of the BPV device. With the absence of a membrane separator, the bioanode and the cathode were positioned within a significant distance of each other, which contributed to a substantial internal resistance. However, it is worth mentioning that since the transparent and non-porous anodes were positioned at the bottom of the devices and with light being shone from below, there was maximum light usage by the photosynthetic biofilm.

3.4.2 Optimisation of Graphene Deposition

The first attempt at improving the surface roughness of ITO-coated substrates was carried out using ultrasonicated graphene. A second approach included screen-printing a differently produced graphene, namely microfluidised GNP-CMC ink. Before any characterisation was carried out, the patterns to be cast were first optimised for enhanced BPV performances.

3.4.2.1 Ultrasonicated Graphene/ITO-coated Bioanodes

The graphene solution synthesised by ultrasonication contained nanoplatelets of lateral size of less than 500 nm and an approximate thickness of 3 nm. Ultrasonication is not an ideal method as a significant amount of graphite remains unexfoliated since the ultrasonic intensity is not uniformly applied.[146] The two-point resistance of graphene/ITO-coated glass was 130±0.2 Ω as compared to 37.3±0.2 Ω for bare ITO-coated glass. Graphene/ITO-coated PET had a two-point resistance of 136±0.5 Ω in

contrast to 340±0.4 Ω for bare ITO-coated PET. The resistivity of the modified ITO-coated substrates was of similar order but worsened for graphene/ITO-coated glass. Figure 3-5 illustrates ITO-coated substrates modified with ultrasonicated graphene.

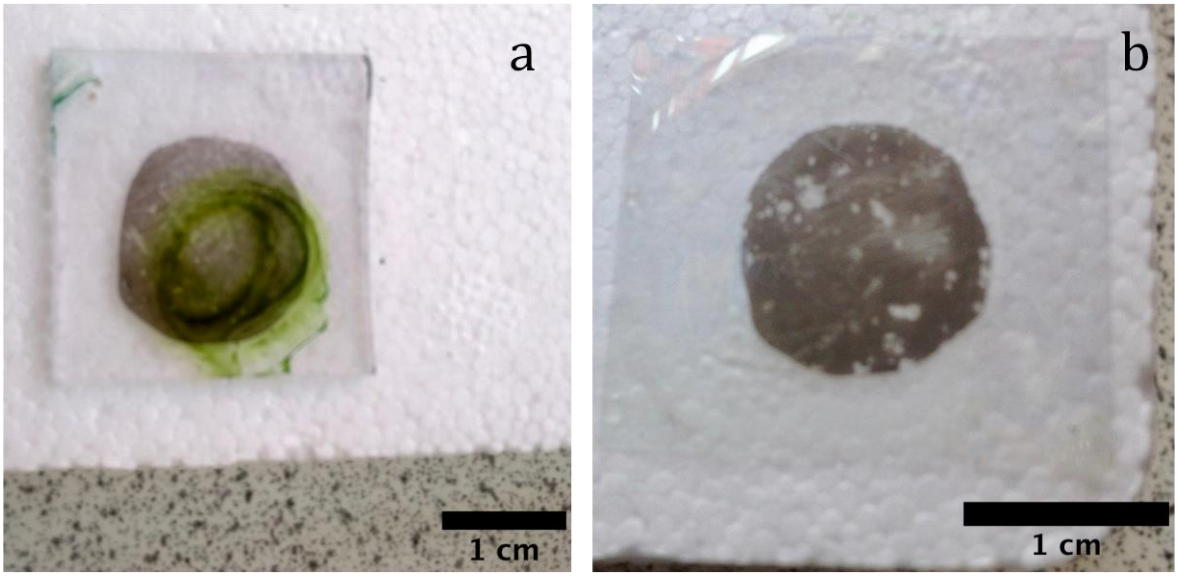

Figure 3-5: Ultrasonicated graphene cast on (a) ITO-coated glass (biofilm formation is shown) and (b) ITO-coated PET.

Figure 3-6 depicts their performance in BPV devices as compared to the baseline. The OCP values of the bare ITO-coated substrates were higher than graphene/ITO-coated substrates, with bare ITO-coated glass showing an apparent difference. This suggests that there was a better electrochemical interaction between the bare ITO-coated substrates and *S. elongtaus*. The internal resistance of BPV devices with graphene/ITO-coated glass was 5.0±0.1 MΩ, with relatively no change as compared to BPV devices with bare ITO-coated glass. However, the internal resistance of BPV devices with graphene/ITO-coated PET doubled to 10±1 MΩ. In terms of power output, there was no compelling disparity between the glass substrates. However, the power output of graphene/ITO-coated PET bioanodes was 2.2-fold lower than the bare counterparts. The two-fold increase in internal resistance explains the decrease in maximum power output.

There was barely any improvement in the performance of BPV devices with the modified bioanodes, which may be attributed to the fact that the casting of ultrasonicated graphene reduced access of light to the biofilm.

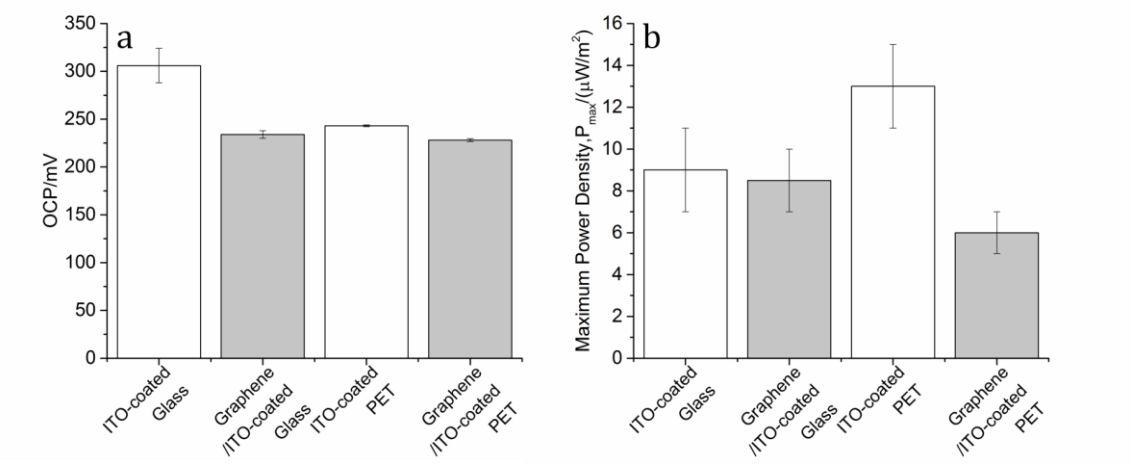

Figure 3-6: Data extracted from polarisation and power curves for comparison of the modified ITO-coated with ultrasonicated graphene against the baseline (a) OCP and (b) geometric maximum power output [the mean ± se is shown for each data set (n=3)].

3.4.2.2 GNP-CMC Ink/ITO-coated Bioanodes

The microfluidised graphene nanoplatelets were of better quality with lateral size of 1 μm and an average thickness of 7 nm. The technique is homogeneous as the shear rate is applied to the whole fluid and not just locally as in sonication. Additionally, GNP-CMC ink has much higher throughput and scalability.[146]

The graphene ink was transferred to the ITO-coated substrates by screen-printing. Screen-printing is a commonly used industrial technique for fast, inexpensive and reproducible deposition of films over large areas. It, also, allows patterning to define which areas of the substrate receive deposition.[150,151] The technology is additive, easy and simple; thus does not involve the complex transfer steps as with ultrasonicated graphene, which may alter the electrochemical characteristics of the substrates.[152–154]

A few designs were initially patterned onto ITO-coated glass substrates so as to assess their performance in BPV devices in order to obtain the optimal one. Unlike the first samples, the new layouts were made in a mesh style, so as to improve the usage of light. Two types of designs, namely a criss-cross pattern and hexagonal-shaped patterns with different amount of spacing were selected, as shown in Figure 3-7.

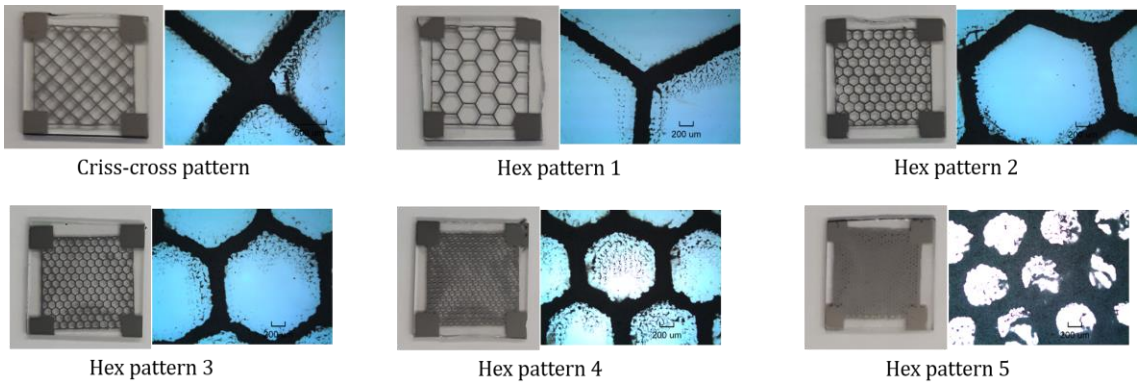

Figure 3-7: GNP-CMC ink screen-printed onto ITO-coated glass substrates with 4 passes, shown alongside their respective optical images with a scale bar of 200 µm.

The performance of the new screen-printed bioanodes in BPV devices was analysed in comparison with the baseline as shown in Figure 3-8.

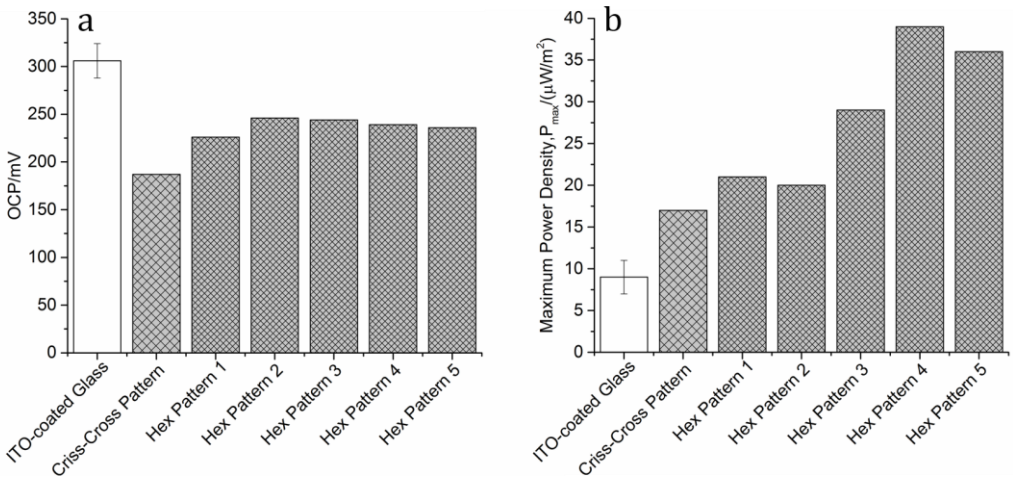

Figure 3-8: Data extracted from polarisation and power curves for comparison of the screen-printed GNP/CMC ink on ITO-coated glass substrates against the baseline (a) OCP and (b) geometric maximum power output [the mean ± se is shown for ITO-coated glass (n=3)].

The OCP value of bare ITO-coated glass bioanodes exceeded that of screen-printed bioanodes, with their values averaging 230 mV. BPV devices with Hex Patterns 1 and 2 had internal resistances of 3 and 4 MΩ, respectively while devices with the criss-cross pattern and Hex Patterns 3-5 bioanodes demonstrated a lower internal resistance of 2 MΩ. The latter halved the internal resistance of the BPV devices as compared to those containing bare ITO-coated glass bioanodes. Moreover, the screen-printed bioanodes superseded the bare ITO-coated glass bioanodes in terms of maximum power output. There was a 4.3-fold increase in maximum power output with Hex Pattern 4 bioanode. The decrease in internal resistance explains the increase in maximum power output

even though BPV devices with bare ITO-coated glass had a higher OCP value. Moreover, the results suggest that the graphene coating helped to substantially improve the efficiency of electron transfer from the biofilm to the bioanodes.

For the selection of the optimum bioanode, the performance in BPV devices and the ease of production were taken into consideration. The criss-cross pattern was chosen as the hexagonal-shaped mesh patterns are not easy to model. The spacing used in Hex Pattern 4 were, however, replicated with the criss-cross patterns as it was the bioanode which produced the highest maximum power output. However, having a much closer spacing would make the screen-printing process messier as was the case with Hex Pattern 5 and would, moreover, limit the extent of illumination.
The selected design was both screen-printed on ITO-coated glass and PET substrates and were first characterised before being assessed in BPV devices.

3.4.3 Surface Characterisation

The modification of the ITO-coated substrates was studied using optical microscopy to better observe the pattern printed. Moreover, AFM was used to characterise the surface of the bioanodes in terms of average surface roughness and increase in surface area. Eventually, the effect of surface roughness on biofilm formation was qualitatively assessed using SEM images.

3.4.3.1 Microscopic Images of New Bioanodes

The criss-cross patterns of GNP-CMC ink were screen-printed with three passes on ITO-coated substrates, as illustrated in Figure 3-9. The thickness of the graphene was 3-3.5 μm and 5 μm on ITO-coated glass and PET, respectively. The two-point resistance of graphene/ITO-coated glass was 31.3±0.3 Ω as compared to 37.3±0.2 Ω for bare ITO-coated glass. Graphene/ITO-coated PET had a two-point resistance of 73.8±0.3 Ω in contrast to 340±0.4 Ω for bare ITO-coated PET.

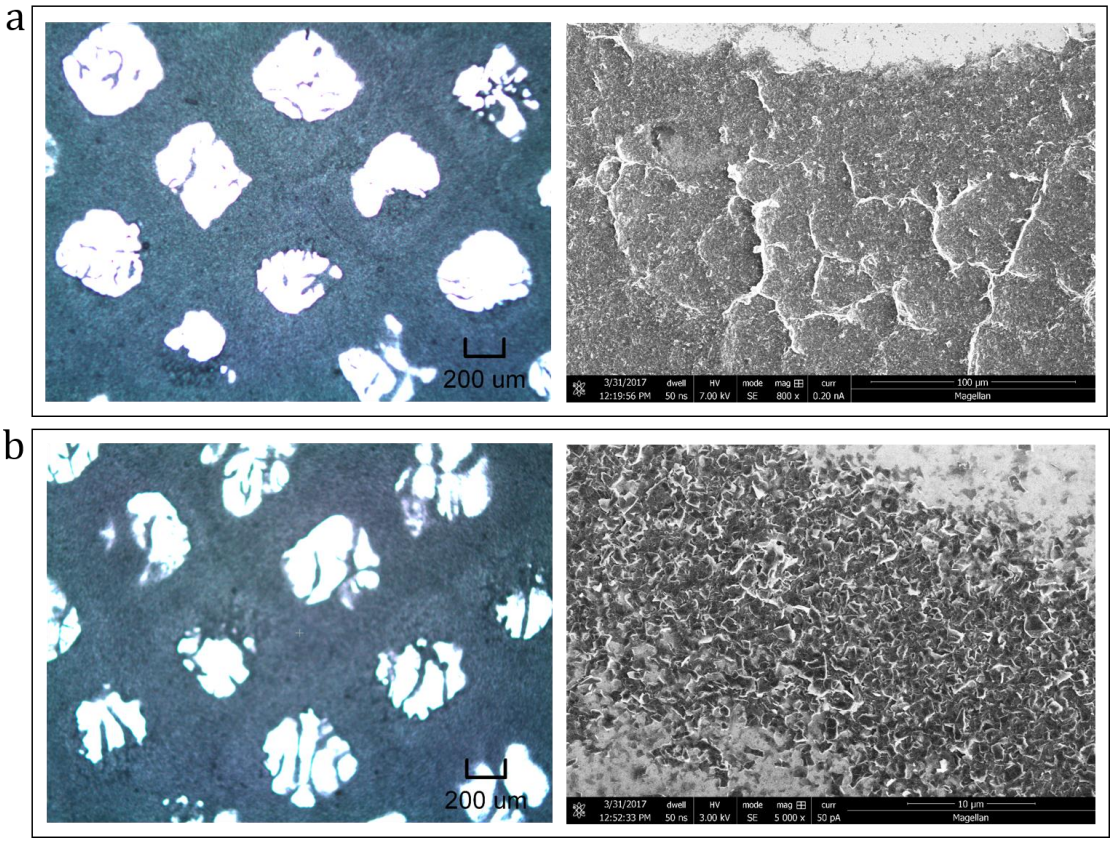

Figure 3-9: Optical and SEM images of GNP-CMC ink screen-printed on (a) ITO-coated glass and (b) ITO-coated PET.

3.4.3.2 Atomic Force Microscopy, AFM

The bioanodes were characterised by using Atomic Force Microscopy. The latter allows a surface to be seen in three-dimensional space, down to the nanometre scale as shown in Figure 3-10. Moreover, surface parameters of average surface roughness and increase in surface area can be analysed.

ITO-coated glass and PET indicated the presence of peaks mostly, with a maximum height of 10 nm. Therefore, their surfaces can be characterised as being smooth and homogeneous. However, both graphene/ITO-coated glass and PET displayed a mix of peaks and valleys, with the maximum height being 1 µm for graphene/ITO-coated glass and 1.7 µm for graphene/ITO-coated PET.

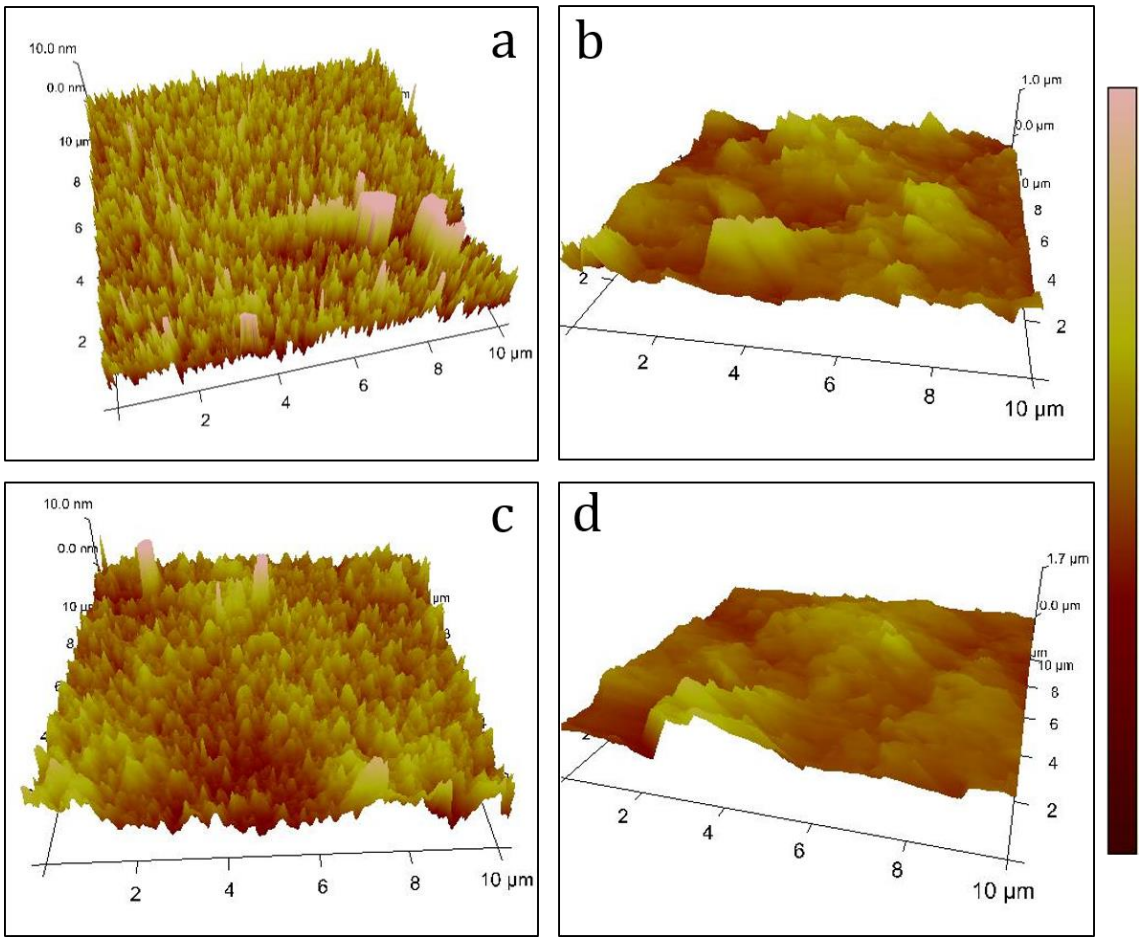

Figure 3-10: AFM 3D topographic scans of 100 µm² for (a) ITO-coated glass (b) graphene/ITO-coated glass (c) ITO-coated PET and (d) graphene/ITO-coated PET.

The average surface roughness and increase in percentage surface areas of the bioanode materials are detailed in Table 3-1. Of the surfaces measured, the average surface roughness was lowest with ITO-coated glass and highest with graphene/ITO-coated PET. The degree of surface roughness is qualified as nanoroughness for ITO-coated glass and PET and submicron surface roughness for graphene/ITO-coated glass and PET.

The increase in average surface roughness brought about a corresponding increase in surface areas of the materials. The lowest percentage increase in surface area was observed with ITO-coated glass and the highest percentage increase in surface area was seen with graphene/ITO-coated PET.

Table 3-1: Average surface roughness and increase in surface areas of the ITO-coated substrates generated by 100 μm^2 scans [the mean ± se is shown for each data set (n=2)].

Bioanode Material	**Average Surface Roughness, S_a/nm**	**% Increase in Surface Area**
ITO-coated Glass	7±2	0.28±0.02
Graphene/ITO-coated Glass	137±11	31±2
ITO-coated PET	25±13	0.76±0.01
Graphene ITO-coated PET	177±15	38±3

3.4.3.3 Biofilm Coverage

Bare ITO-coated substrates were faintly covered with cells of *S. elongatus* while graphene/ITO-coated substrates were fully covered. The biofilm coverage corroborates with the fact that high surface roughness promotes biofilm formation and adhesion.[85] Graphene/ITO-coated PET was more heavily covered, corresponding to the highest value of average surface roughness measured.

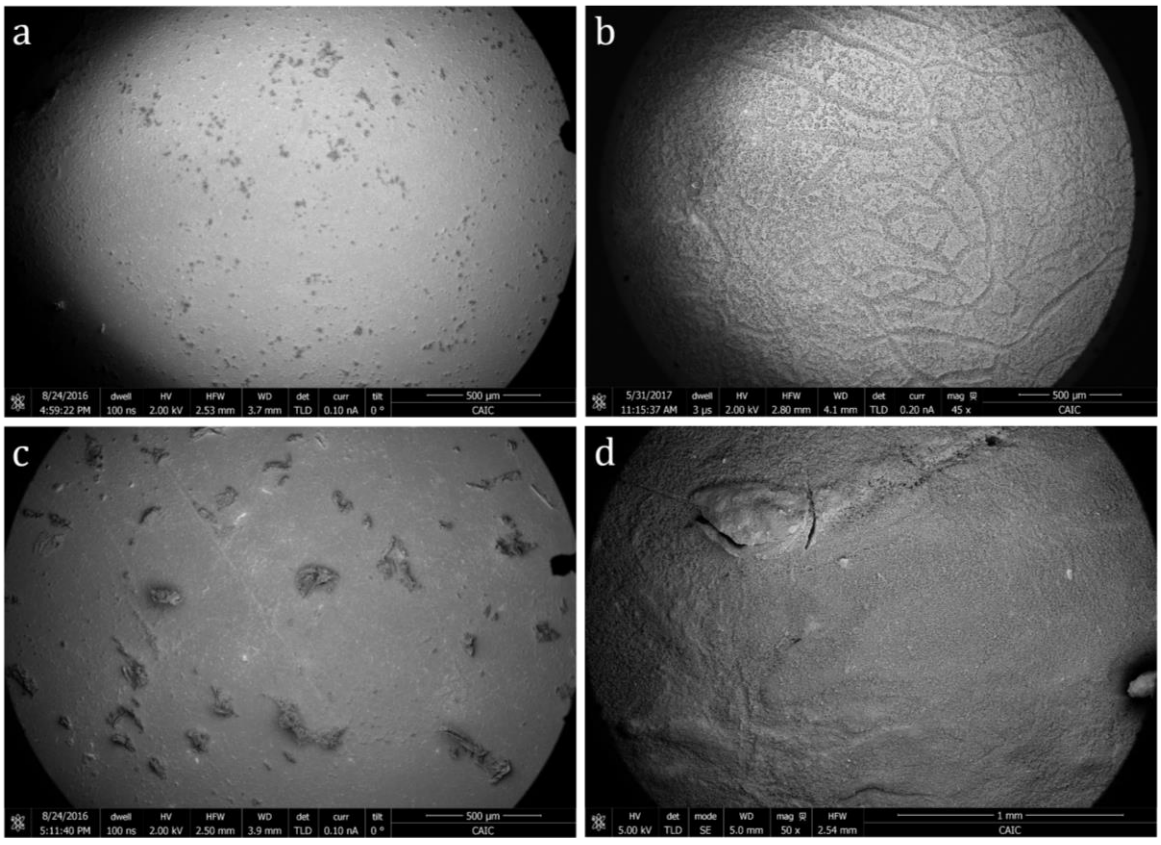

Figure 3-11: Biofilm coverage of *S. elongatus* on (a) ITO-coated glass (b) graphene/ITO-coated graphene (c) ITO-coated PET and (d) graphene/ITO-coated PET.

3.4.4 Exoelectrogenic Activity

SEM images were first analysed to detect any features that may participate in the extracellular electron transport. Electrochemical methods were, then, employed to assess the electroactivity of the biofilm. The exocellular electrons were, eventually, captured in BPV devices for bioelectricity generation.

3.4.4.1 Features of Biofilm

SEM images of the biofilm on the bioanodes reveal the presence of putative nanowires or pili. Figure 3-12 shows the examples of two different bioanodes where cells communicate with each other via the pili structures and also use them to connect to the anode surface.

It has been revealed that some microorganisms can produce electrically conductive pilus-like appendages, for example the oxygenic photosynthetic cyanobacteria *Microcystis aeruginosa* PCC 7806 and *Synechocystis* PCC 6803.[155] The purpose of these structures in *Synechocystis* PCC 6803 was linked to the cells channelling excess electrons that cannot be fixed into biomass during CO_2 fixation. It is, thus, hypothesised that these nanowires serve to facilitate electron transfer to the environment surrounding the cells.[156]

Based on the discovery of electron conducting nanowires in other microorganisms,[157,158] it can be conjectured that the presence of nanowires in the biofilm of *S. elongatus* may participate in the electron transfer mechanism. However, this is yet to be investigated.

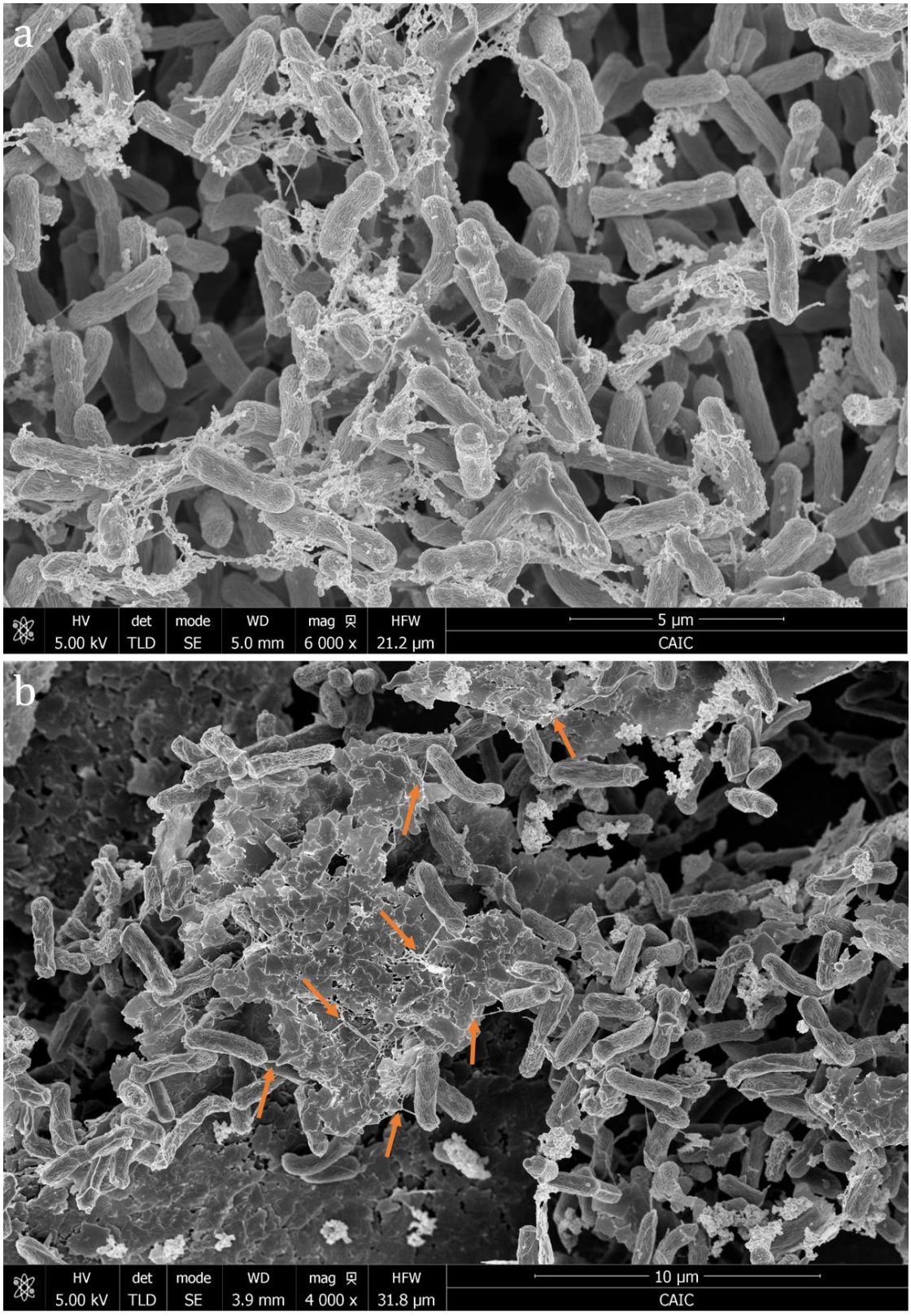

Figure 3-12: Interaction of cells of *S. elongatus* with (a) bare ITO-coated PET and (b) graphene/ITO-coated glass. Putative nanowires or pili in cells to cells and cells to anode communication can be observed. The orange arrows in (b) illustrate pili structures attached to graphene nanoplatelets.

3.4.4.2 Electrochemical Techniques

The electrochemical interactions between the biofilm of *S. elongatus* and the bionaodes were first evaluated by using cyclic voltammetry, followed by double potential step chronoamperometry. Moreover, double potential step chronocoulometry provided more clarity on the electrochemical interactions.

3.4.4.2.1 Cyclic Voltammetry

As illustrated in Figure 3-13, the biofilms on the different bioanodes appear to be electrochemically inactive as there is no presence of distinct redox peaks, even though there is an increase in current as compared to the control experiments. The biocatalytic activity of *S. elongatus* is known to be slow and it could not even be detected at a low scan rate of 1 mV s^{-1}. Graphs (a) and (c) even show characteristics of non-Faradaic currents, which may possibly mask the redox peaks.

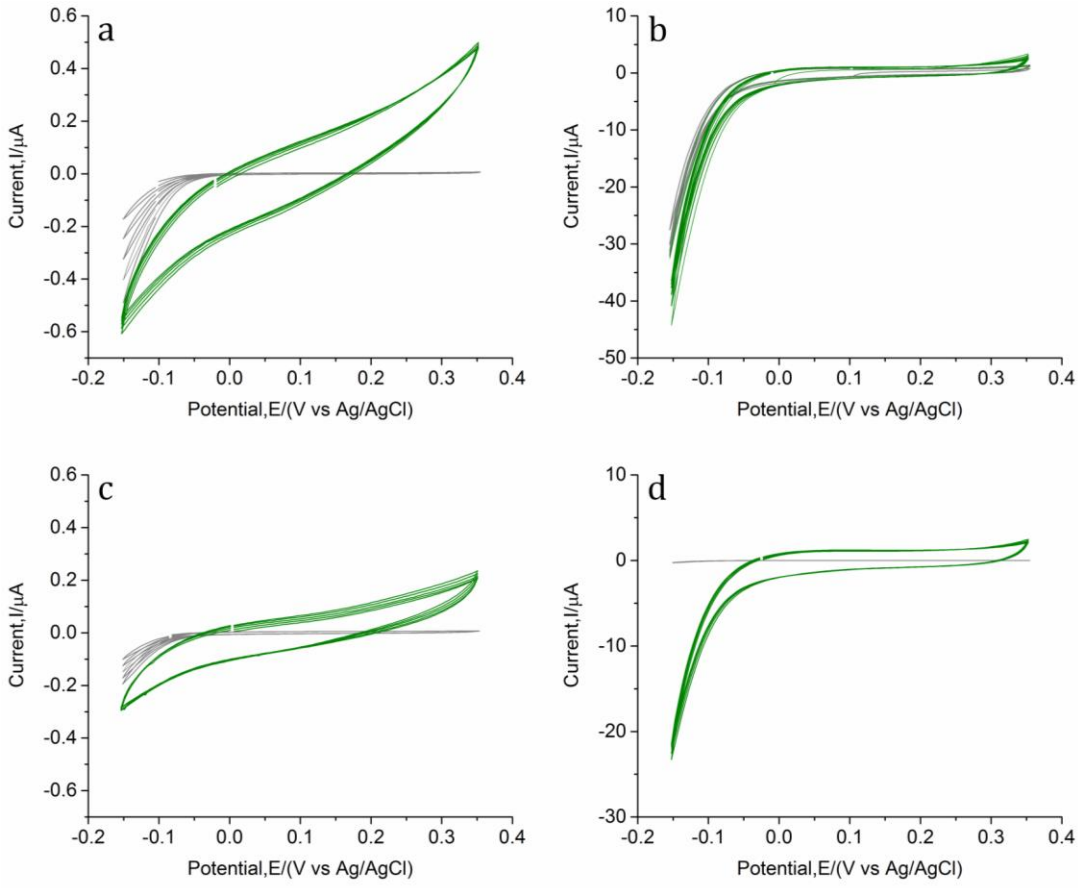

Figure 3-13: Cyclic voltammograms illustrating 5 consecutive scans at a scan rate of 1 mV s^{-1} for (a) ITO-coated glass (b) graphene/ITO-coated glass (c) ITO-coated PET and (d) graphene/ITO-coated PET.

Wenzel et al.[141] observed a similar behaviour with the interaction of *Synechocystis* with porous anodes. Even at a slow scan rate of 0.5 mV s^{-1}, the catalytic activity of *Synechocystis* could not be detected. The anode materials demonstrated strong surface charging, which led to high charging non-Faradaic currents that broaden the CV hysteresis curve, which ultimately masked the biocatalytic peaks. However, Gonzalez-Aravena et al.[133] managed to detect a clear electroactive region of *Synechococcus elongatus* PCC 7942 on ITO-coated glass anodes, with a midpoint potential of 0.22 V vs. Ag/AgCl in both iron limited and iron sufficient biofilms.

3.4.4.2.2 Double Potential Step Chronoamperometry

In regards to the unsuccessful detection of any electrochemical activity using cyclic voltammetry, a simpler electrochemical approach was used. Double potential step chronoamperometry, also, known as the current transient technique was used to analyse the electrochemical interactions between the biofilm of *S. elongatus* and the different bioanodes by detecting changes in electric current with Cottrell analysis.

The oxidising and reducing step potentials were selected based on the window potential used to generate the cyclic voltammograms in Figure 3-13. When the oxidising step potential was applied, there was a surge in current, followed by a decrease in current in a diffusion-limited manner. The sudden increase in current suggests that all the extracellular redox cofactors were instantaneously oxidised and the height of the peak current is said to be proportional to the instant concentration of the redox centres. The subsequent decrease in current is attributed to current being limited by the mass transfer of electrons across the hydrated biofilms. The reducing step potential was, then, applied, resulting in the instantaneous reduction of the redox cofactors. The similar heights of the peak currents in both the oxidising and reducing potential steps suggest that the same number of redox centres were subsequently oxidised and reduced.[118] The biofilms were consecutively oxidised and reduced in five cycles and the repeated patterns demonstrated the reproducibility, robustness and reversibility of the reactions as depicted in Figure 3-14.

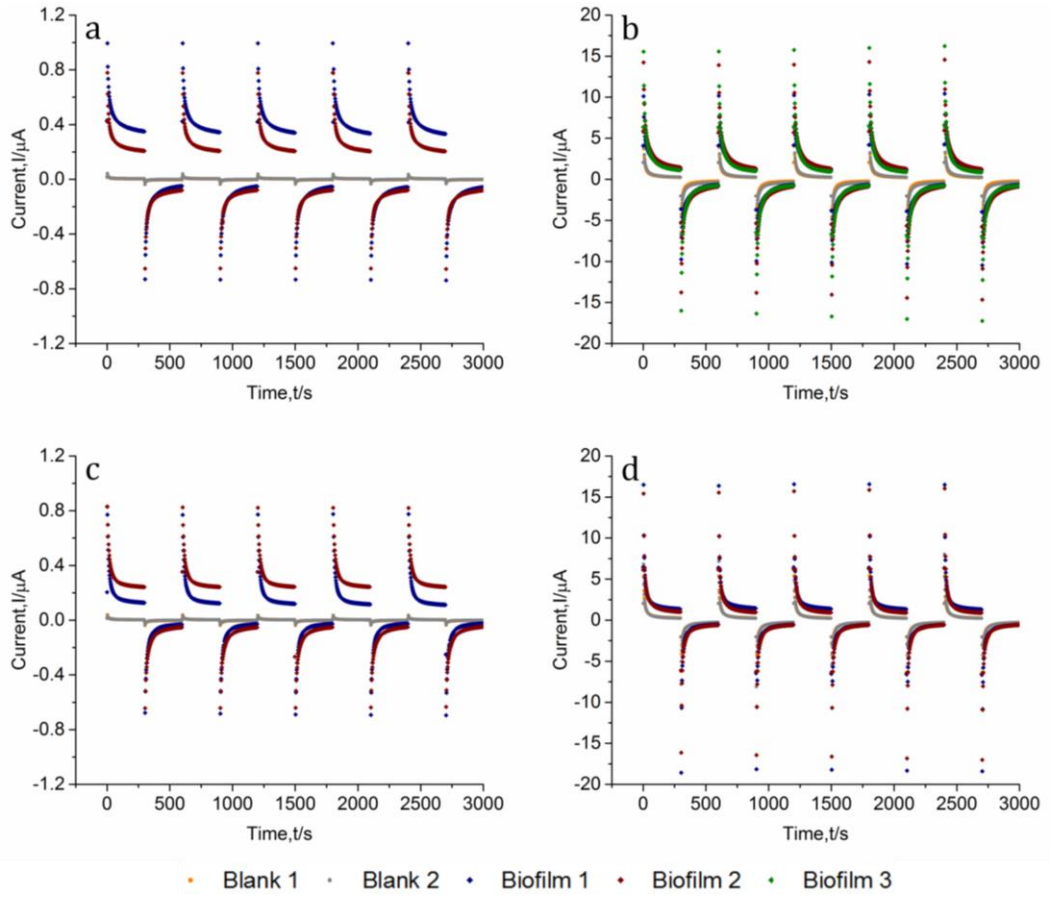

Figure 3-14: Chronoamperomograms depicting a set of 5 cycles obtained at E_1=0.35 V and E_2=0 V for 300 s at each applied potential for (a) ITO-coated glass (b) graphene/ITO-coated glass (c) ITO-coated PET and (d) graphene/ITO-coated PET.

Two main information can be extracted from the above plots; the peak current and the limiting current generated, which can be used to distinguish between the performances of the different bioanodes. All the values of the blanks were significantly lower than the biofilms and were hence omitted from Table 3-2.

On average, there was a 19.8-fold increase in peak current and a 3.6-fold increase in limiting current when the surface of ITO-coated glass was screen-printed with graphene. For ITO-coated PET, there was about a 20-fold increase in peak current and a 6.7-fold increase in limiting current when graphene was present on the surface. These results clearly indicate that graphene improves the electrochemical interaction of the biofilm with the bioanodes, which impact on the enhancement of the extracellular electron transport.

Table 3-2: Data extracted from the chronoamperomograms for the different bioanode materials in terms of peak and limiting currents [the mean ± se is shown for each data set (n=2, except for graphene/ITO-coated glass: n=3)]

Bioanode Material	**Peak Current/µA**	**Limiting Current/µA**
ITO-coated Glass	0.8±0.1	0.27±0.07
Graphene/ITO-coated Glass	15.8±0.1	0.97±0.04
ITO-coated PET	0.80±0.03	0.18±0.06
Graphene/ITO-coated PET	16.1±0.4	1.2±0.2

The differences between each biofilm for a specific anode, especially for the bare ITO-coated substrates [Figure 3-14 (a) and (c)], can be attributed to the different strength of biofilm attachment to the bioanodes. Even though the same amount of biomass was inoculated, the density of attached cells might defer. These results, further, suggest that graphene helps to produce more reliable and stronger biofilm attachment correlating to the high average surface roughness of the materials.

The corresponding Cottrell plots are illustrated in Figure 3-15. They illustrate an almost linear function, indicating the diffusion-controlled character of the current.

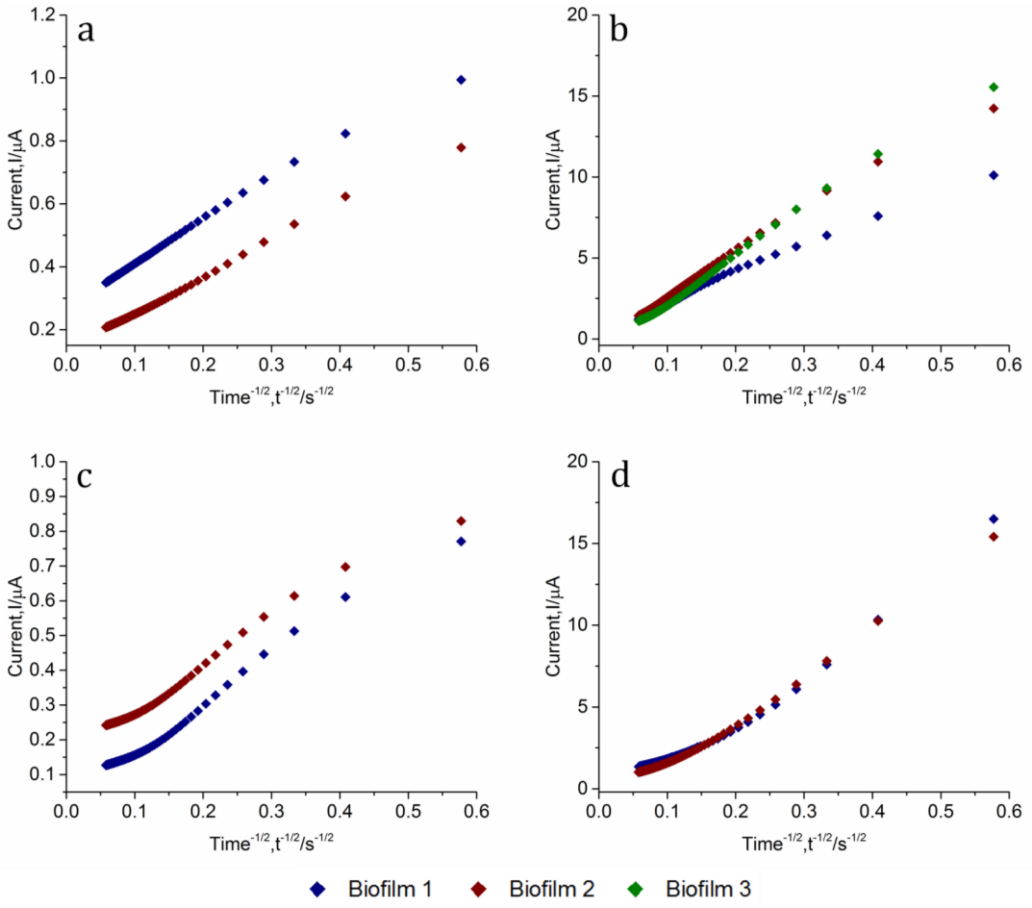

Figure 3-15: Corresponding Cottrell plots of Figure 3-14 for the first step cycle only of (a) ITO-coated glass (b) graphene/ITO-coated glass (c) ITO-coated PET and (d) graphene/ITO-coated PET.

Interpreting chronoamperomograms can sometimes be tricky and misleading. As a result, integrating the current using chronocoulometry can offer more insight into the systems.

As illustrated in Figure 3-16, there is a clear distinction between the blank and the biofilm for all the anodes unlike in the chronoamperomograms. Moreover, the charge produced by the biofilm on graphene-coated anodes in comparison to bare ITO-coated substrates are higher in magnitude, which suggest that they are better performing than bare ITO-coated anodes. As expected, the charge for the blank has a decreasing trend, as it cannot sustain current for long.

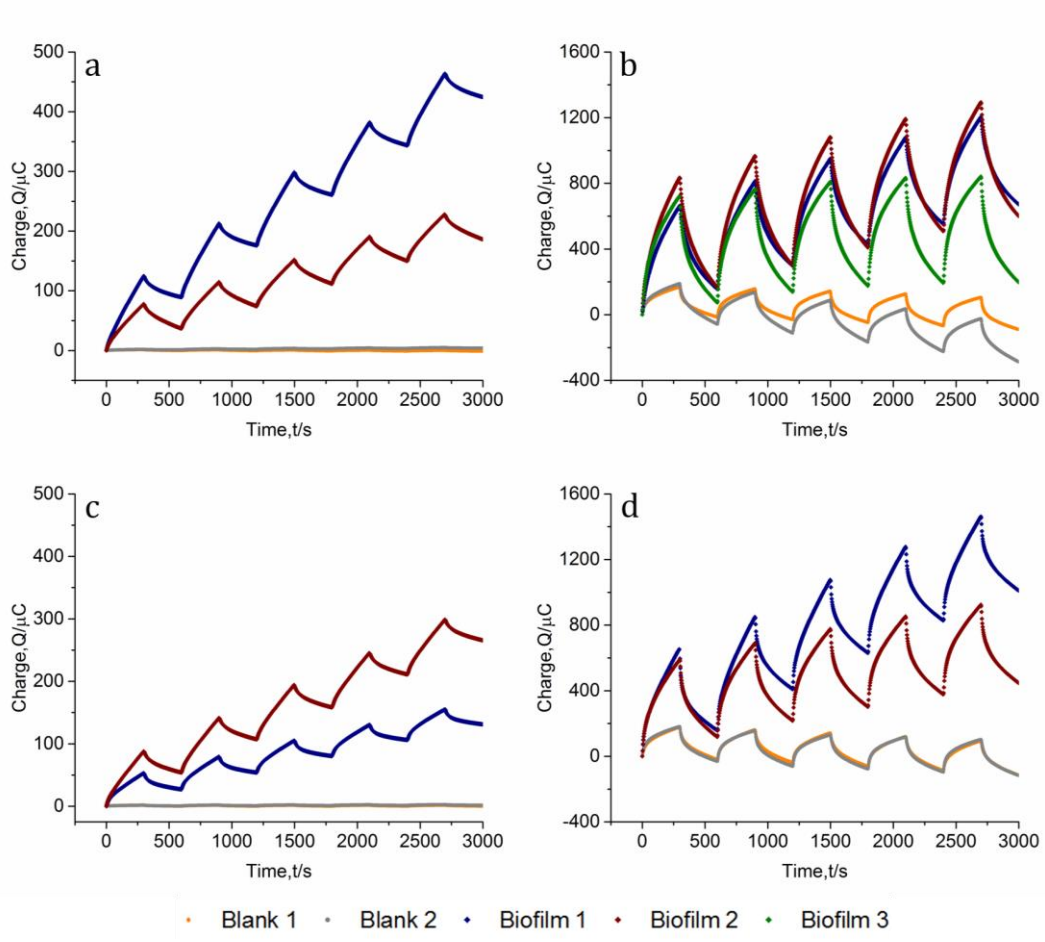

Figure 3-16: Corresponding chronocoulomograms of Figure 3-14 for (a) ITO-coated glass (b) graphene/ITO-coated glass (c) ITO-coated PET and (d) graphene/ITO-coated PET.

3.4.4.2.3 Performance Analysis of BPV Devices

After the analysis of the electrochemical interactions between the biofilms of *S. elongatus* and the bioanodes, the performance of the latter was evaluated in the single chamber BPV devices for bioelectricity generation.

As shown in Figure 3-17, the OCP values of graphene/ITO-coated glass and graphene/ITO-coated PET are 327±9 mV and 313±3 mV, respectively. Both values are higher than their bare counterparts, suggesting that graphene enhanced the anode-biofilm interaction. ITO-coated glass bioanodes had an OCP value of 306±18 mV while ITO-coated PET bioanodes had an OCP value of 243±1 mV. Moreover, the average surface roughness introduced by graphene significantly reduced the activation losses from 158 mV and 106 mV to of 32 mV and 87 mV for ITO-coated glass and ITO-coated PET bioanodes, respectively. Overall, graphene ITO-coated glass bioanodes suffered the least from activation polarisation.

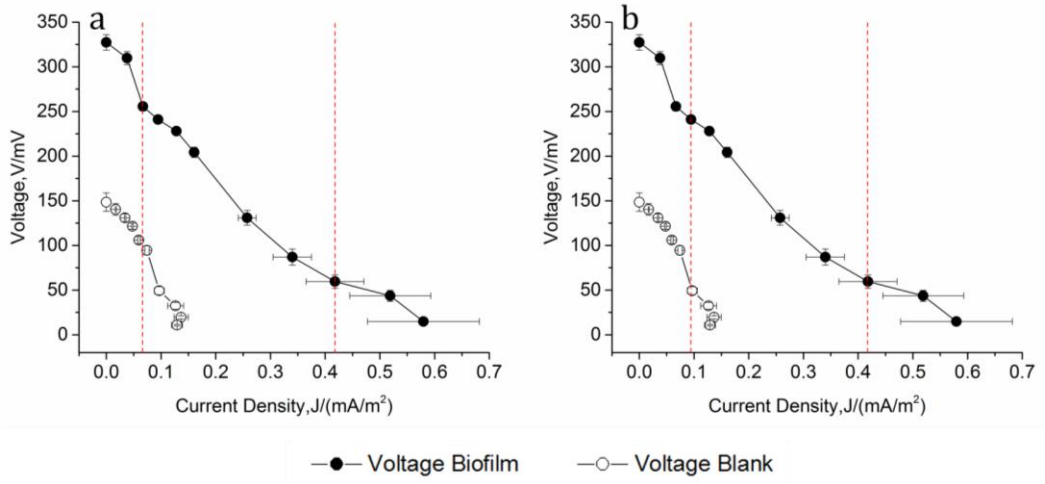

Figure 3-17: Polarisation curves of (a) graphene/ITO-coated glass and (b) graphene/ITO-coated PET [the mean ± se is shown for each data set (n=3)]. The lines shown are purely used to guide the eye. The additional red dash lines separate the different regions of electrochemical losses for the biofilm only.

As illustrated in Figure 3-18 (a), the internal resistance of BPV devices was almost halved as compared to BPV devices with bare ITO-coated substrates, as shown in Figure 3-4 (a). The average surface roughness and the increase in surface area of the graphene/ITO-coated substrates were beneficial in decreasing the internal resistance of the anodes and, hence, ohmic losses.

a

Bioanode Materials	Internal Resistance/MΩ
Graphene/ITO-coated Glass	2.3±0.1
Graphene/ITO-coated PET	2.7±0.2

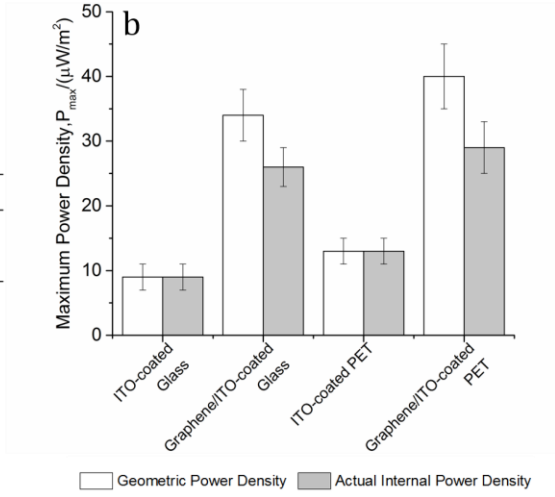

Figure 3-18: Data extracted from polarisation and power curves to compare the performance of ITO-coated substrates with regards to (a) internal resistance and (b) maximum power output [the mean ± se is shown for each data set (n=3)].

Figure 3-18 (b) depicts maximum power density in terms of both the geometric surface area and the actual internal surface area. The increase in surface area of the graphene/ITO substrates, as detailed in Table 3-1, decreased the geometric power density. The maximum power density of graphene/ITO-coated glass bioanodes dropped from 34±4 μW m^{-2} to 26±3 μW m^{-2}, while that of graphene/ITO-coated PET decreased from 40±5 μW m^{-2} to 29±4 μW m^{-2}. Modifying the surface of ITO-coated substrates with graphene brought a 2.9-fold and a 2.2-fold increase in maximum power density for ITO-coated glass and ITO-coated PET, respectively. The increase in OCP values and the drop in internal resistance have brought about the increase in maximum power output.

The effect of the changes in surface properties is correlated to the actual internal maximum power output as depicted in Figure 3-19. The actual maximum power density increases linearly with both average surface roughness and percentage increase in surface areas of the bioanode materials. These correlations, further, confirm that the graphene nanoplatelets improved the direct attachment of *S. elongatus* cells to the surface of the anodes and enhanced the efficiency of electron transfer from the biofilm to the anodes.

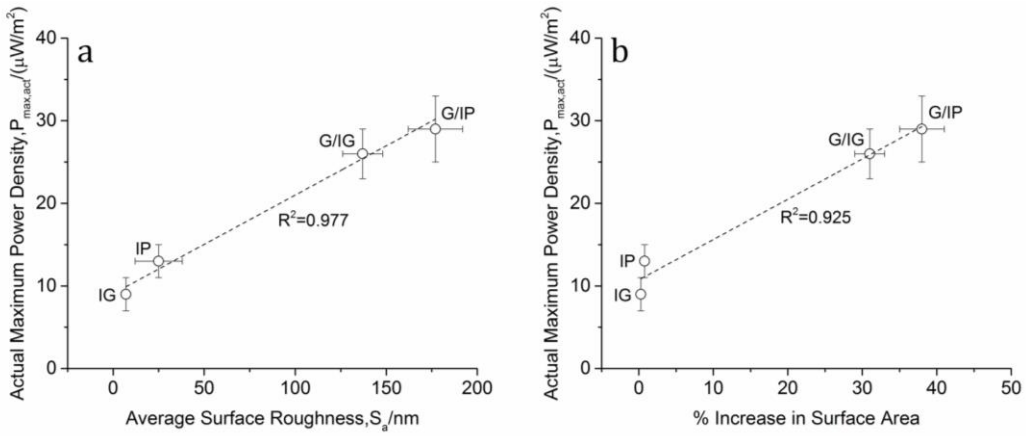

Figure 3-19: The influence of (a) average surface roughness and (b) % increase in surface area on actual maximum power density for the four types of bioanode materials [the mean ± se shown is representative of data sets shown in Table 3-1 and Figure 3-18]. IG: ITO-coated glass, IP: ITO-coated PET, G/IG: Graphene/ITO-coated glass and G/IP: graphene/ITO-coated PET.

3.5 Conclusions

The technique employed to improve the performance of conventional ITO-coated substrates in BPVs was to improve the surface roughness. The functional material used to modify the surface of the ITO-coated substrates was graphene. The first method involved casting ultrasonicated graphene on the surfaces. However, the performance of bare ITO-coated substrates in the BPV devices outperformed that of the ultrasonicated graphene-coated bioanodes in terms of both OCP and maximum power output. The reason for the poor performance was attributed to the graphene production method as well as to the fact that illumination was compromised. As a result, a new production method and a different way of casting graphene were used. Graphene nanoplatelets cross-linked in carboxymethyl cellulose was screen-printed on the ITO-coated substrates in a mesh-optimised design. The graphene improved both average surface roughness and surface area. Moreover, the surface characteristics enhanced biofilm formation and attachment. The OCP values were slightly improved and activation losses were considerably reduced. Additionally, there was about a 2-fold decrease in internal resistance of the BPV devices. As a result, there was a significant increase in maximum power output, with a 2.9-fold increase with graphene/ITO-coated glass and a 2.2-fold increase with graphene/ITO-coated PET. A linear correlation between average surface roughness and maximum power output and between increase in surface area and maximum power output were obtained. The modified bioanodes improved biofilm formation and improved the efficiency of electron transfer as well as enhanced the electrochemical activity by minimising activation and ohmic losses.

Graphene/ITO-coated PET was the anode with the highest average surface roughness and surface area and thus produced the highest maximum power output. These two surface characteristics overpowered the conductivity properties of ITO-coated glass, which is beneficial since ITO-coated PET has a lower cost of production.

4 Impact of the Wettability Property on the Performance of Carbonaceous Materials

4.1 Introduction

The performance of the bioanode is one of the important aspects in the design and performance of BPV devices. The surface chemistry property of wettability is one of the crucial properties of an electrode. It has been reported to improve bioadhesion and electrochemical activity, with a combined output of enhanced electron transfer mechanism.[118] The degree of wettability modulates the way in which cells form and attach to the bioanode as well as determine the extent of electrochemical losses.[157] This chapter evaluates an anodic surface modification technique to improve the wettability property of carbon paper and carbon felt and their subsequent performance in BPV devices. Moreover, an inherently hydrophilic carbon-based material, namely graphene paper, is assessed.

4.1.1 Carbonaceous Materials as Bioanodes

Carbon-based materials are by far the most common anode materials used in MFCs, namely graphite plates, rods, foils and brushes, reticulated vitreous carbon, carbon cloth, carbon paper and carbon felt.[22,87] They offer a good compromise in terms of the following requirements; they possess high electrical conductivity, large reactive surface area, biocompatibility, chemical stability and are low cost.[22,87,159] However, their use in BPV studies have not been extensively exploited.

Bombelli et al.[36] compared the performance of various anodic materials, namely ITO-coated PET, stainless steel, polyaniline-coated glass and carbon paper in a mediatorless, multichannel and open-air BPV device using photosynthetic biofilms of *Pseudanabaena limnetica*. Carbon paper was found to be the most hydrophobic with the highest average surface roughness. The experiments revealed that carbon paper

was outperformed by all the other anodic materials with the lowest power output of about 45 (pW(nmol Chl)$^{-1}$). This suggests that carbon paper may not be the most effective anode to be used in BPVs.[36] Legeay et al.[86] discovered that high roughness combined with hydrophobicity makes the movement of entrapped air energetically unfavourable. As a result, the formation of micro bubbles between the biofilm and the substrate limits bioadhesion or spreading. One study indicated that the presence of bubbles were enough to create an oxidative stress in *E. coli*.[86] This is a possible phenomenon that may have occurred with carbon paper used in the above study. Thorne et al.[37] investigated the biocompatibility of macroporous titanium dioxide ceramic coated with FTO against carbon felt and FTO-coated glass by using a ferricyanide-mediated cylindrical BPV device containing biofilms of *C. vulgaris*. By analysing SEM images, it was revealed that carbon felt was not an appropriate substrate for *C. vulgaris*. The carbon fibres were faintly covered with cells and no extensive extracellular matrix was observed. The cells seem to inhabit the interiors of the material rather than populating the surface of the carbon fibres. However, a dense biofilm with fibrous extracellular matrix was observed on the porous ceramic anode, with fibres attaching to the electrode surface. Carbon felt had the poorest performance in a BPV platform with a maximum power output of 0.04 mW m^{-2} while the FTO-coated glass had the highest maximum power output of 24 mW m^{-2}.[37] It is worth noting that even though a biofilm was allowed to develop, ferricyanide was still used as a mediator. As deduced from the above studies, carbon-based materials do not seem to be optimal anode materials. Their dense black structures only allow light to penetrate into the first layer of any biofilm growing on their surface. As a result, a major part of the internal surface area remains unused.[37] Another major drawback is their low electrochemical activity and poor wettability due to their hydrophobic nature, which result in substantial polarisation and poor energy efficiency during operation.[159]

4.1.2 Surface Wettability

It has been repeatedly demonstrated that cell attachment to a material and high electrochemical activity relies on the physico-chemical properties of the material surface.[85,159] For instance, the chemical composition of a surface material is a crucial factor in determining the surface energy, polarity, wettability and zeta potential of the material.

The material surface energy includes both polar and non-polar elements and is obtained from contact angle measurement between the material surface and various polar liquids.

A low contact angle between the material and water indicates good spreading of water, which means that the material is hydrophilic. Hydrophilic surfaces have high surface energy and a high polar component because of the presence of polar groups such as –OH (alcohol), $–NH_2$ (amine), –COOH (acid). It can, thus, form polar, ionic and acid-base bonds with the surrounding medium. Materials with such properties include glass, silicon wafer, poly(vinyl alcohol), cellulose derivatives, poly(ethylene glycol), polyamides, some polyurethanes, poly(vinylpyrrolidone).[85,86]

However, a high water contact angle, usually more than 90°, is a characteristic of a hydrophobic material. These surfaces have low energy with a negligible polar component. They are composed of chemical groups such as –C–H, C–C, –C–F, Si–O–Si. Hydrocarbon materials (polyolefins), fluorinated polymers and silicones are hydrophobic and surfaces coated with polycations are also characterised as moderately hydrophobic.[85,86] Figure 4-1 illustrates examples of degrees of wettability on a solid substrate.

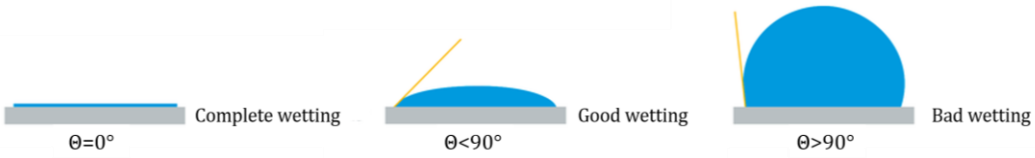

Figure 4-1: Illustration of hydrophilic and hydrophobic surfaces with different degrees of wettability.[160]

It is widely accepted that the surface wettability of electrodes can be promoted by introducing surface-active oxygen functional groups by using surface modification techniques, classified as physical, chemical and thermal. Physical treatments include plasma treatment, irradiation with ions, UV light and gamma-ray irradiation.[87,159,161] The chemical approach involves acid treatment with nitric acid and sulphuric acid, which facilitates the protonation of functional groups on the surface.[119,159,162] Other chemicals used include hydrogen peroxide, potassium and sodium hydroxides, ethylenediamine, ammoniumnitrate, ammonium persulfate, polyaniline, and 4(N,N-dimethylamino) benzene diazonium. The chemical treatments usually introduce nitrogen and oxygen containing groups[21] and electrochemical oxidation results in the

formation of carboxyl groups. Thermal treatment is usually carried out at 500°C in the presence of air for the mild oxidation of the electrode.[161,163]

4.1.2.1 Biocompatibility

Several studies have demonstrated that cell adhesion is hindered on hydrophobic substrates or substrates with low energy surfaces. High surface energy materials or moderately hydrophilic surfaces offer excellent biofilm formation and attachment.[36,138,164–166] Moreover, hydrophilic surfaces enhance the extracellular electron transfer rate between microbes and electrodes.[167] However, it is worth noting that on highly hydrophilic surfaces, cell attachment and spreading may be limited or completely disabled.[85] Glassy carbon and graphite felt anodes were pre-treated with either an oxygen or a nitrogen plasma before being used in a MFC with mixed microbial consortia. The surface of the anodic materials became hydrophilic and the generated anodic current was increased sharply. It was analysed that the plasma treatment improved the initial cell adhesion, which accelerated the biofilm development.[168] The electrochemical oxidation of graphite felts generated functional groups, such as carboxyl which helped to improve the electron transport from the microorganisms to the anode. These functional groups may generate peptide bonds between the anode surface and the microorganisms, which acted as a bridge for an effective electron transfer. Electrochemically modified graphite felts produced a 40% increase in current density as compared to the unmodified ones. After being treated with nitric acid, graphite felt anodes generated a 2-fold increase in power density.[163] Oxygen functional groups generated, increased the polar component of the surface free energy of the material surface, which makes it more wettable, stickier and more prone to cell adhesion.[85]

4.1.2.2 Electrochemical Activity

One of the factors affecting the performance of the BPV is the electrochemical activity of the anode. Ensuring good wetting properties between the bioanode and the liquid electrolyte minimises activation and ohmic losses.[169] This is because surface wettability has a substantial influence on electrolyte-wetting and redox electron transfer.[167] The non-polar nature of carbon-based materials hinders the wettability with aqueous electrolytes. However, the presence of oxygen functional groups

facilitates the interaction with the water molecules for a better penetration of ions through the porous structures of the carbon materials. Therefore, the wettability of carbon materials in aqueous electrolyte is governed by the interaction of the surface charge and the dipolar moment of water.[170]

Three types of surface modification techniques, such as mild oxidation, oxygen plasma and gamma-ray irradiation were used to enhance the electrochemical activity of carbon felt electrodes in vanadium redox flow batteries (VRFBs).[161] Even though carbon felt electrodes provide abundant redox reaction sites, it has poor wettability and electrochemical activity in aqueous solutions due to its hydrophobic nature. Therefore, poor kinetics related to the reduction and oxidation of vanadium ions results in low energy efficiency of VRFBs. All the three treatments introduced carbon-oxygen functional groups, such as carboxyl or carbonyl groups (C=O) and phenolic groups (C-O) groups. Mild oxidation and oxygen plasma reduced overpotential, leading to higher voltage efficiency while gamma-ray irradiation improved coulombic efficiency.[161] In another study, Kim et al.[159] coupled corona discharge with hydrogen peroxide to improve the electrochemical performance of carbon felt electrodes in VRFBs. The treatment generated a high concentration of oxygen functional groups on the surface of carbon felt which substantially improved the wettability of the electrodes. The effects of the surface treatment improved the energy efficiency of VRFBs by 7% via enhanced wetting and catalytic activity in the reaction with vanadium ions. These improvements likely resulted from the reduction of electrochemical polarisation of the vanadium redox pairs at the electrodes.[159] Hydrogen evolution electrodes (HEEs) made of platinum (Pt) particles and octadecyltrimethoxysilane (OTS) molecules on titanium dioxide nanotubes were hydrophilised by the photocatalytic decomposition of OTS molecules by ultraviolet light. It was revealed that hydrophilic HEEs exhibited a larger electrochemical active area of Pt and a lower adhesion force to a gas bubble as compared to the hydrophobic ones. The modified electrodes allow more protons to react at a lower overpotential so that a larger current can be produced. It was deduced that optimising the surface wettability is of prime importance in improving the electrocatalytic activity of the electrodes.[167]

4.2 Proposed Concept and Research Aim

The research aim of this chapter is to evaluate the effect of surface wettability on the performance of carbon-based materials in BPVs. The following objectives were set out to establish and achieve the following research goals.

1. Designing the configuration of the BPV device and bioanodes
    - A MEA-type BPV device was designed by taking into account the properties of the carbonaceous materials so as to maximise their performance.
    - Conventionally used carbon paper and carbon felt underwent surface modification with oxygen functional groups so as to overcome their hydrophobic nature.
    - A hydrophilic novel carbon material, namely graphene paper, was evaluated.
2. Surface characterisation was carried out to understand the material surface chemistry of the anodes and biofilm formation was analysed by using SEM technique.
3. SEM images and double potential step chronoamperometry were used to identify any electroactive features of the biofilm on the best performing anodes. Chronoamperometry was used to further analyse and interpret the electrochemical interactions between the cells of *S. elongatus* and the anodes.
4. The performance of the BPV devices was summarised by four parameters: OCP, activation loss, internal resistance and maximum power output.

4.3 Materials and Methods

4.3.1 Surface Functionalisation

Carbon paper (TGP-H-060, Toray Carbon Fibers Europe) and carbon felt (1.59 mm thick, Alfa Aesar) underwent surface functionalisation. Table 4-1 illustrates the characteristics of the carbon fibres.

Table 4-1: Properties of carbon paper and carbon felt taken from literature. Estimates of surface electrical resistivity was obtained through the equation $C_p = 1/(R_s \times t_m)$, C_p is in plane electrical conductivity in S m^{-1}, R_s is surface electrical resistivity in Ω/square and t_m is thickness of material in m.

Carbon Fibres	% Porosity	Specific Surface Area/m^{-1}	Electrical Resistivity/(Ω/square)
Carbon Paper[171]	78	20 000[172]	0.305
Carbon Felt[173]	98	22 400	1.70

The surface functionalisation included three treatments. The first treatment involved a plasma discharge (plasma treated, PT) using a Femto Electronic Diener Plasma Surface Technology apparatus. The dielectric barrier between the electrodes of the instrument and the samples was 15 mm. The generator was operated at a rating of 50 W and a frequency of 40 kHz. Each side of the electrode was exposed twice for about 16 s. The second treatment consisted of sonicating the electrodes in 30% aqueous hydrogen peroxide solution (Sigma Aldrich, UK) at 200 W for 1 hour (H_2O_2 treated, HT). The third treatment combined the first and second treatment; the electrodes were plasma treated followed by sonication with hydrogen peroxide (fully treated, FT). Bare carbon paper and carbon felt were used as controls (non-treated, NT). The experiment was designed by Arely Gonzalez and the studies were carried out jointly.

4.3.1.1 Contact Angle Analysis

The wettability property of carbon paper and carbon felt were determined by the water contact angle measurement with a Drop Shape Analyser (Kruss DSA100) integrated with the Drop Shape Analysis software.

4.3.1.2 Chemical Titration

To qualitatively assess the presence of oxygen functional groups, the bare and treated electrodes were immersed in 98% tetraethyl orthosilicate (TEOS, Sigma Aldrich UK) for 24 hours. The samples were washed with deionised water and were dried in an oven. At the Cambridge Advanced Imaging Centre (CAIC), the samples were stuck onto SEM stubs by using carbon tape. For better electrical connection between the tape and

the carbon paper, a dash of silver ink was added. All the substrates were then coated with 35 nm gold and 16 nm iridium in a Quorum/Emitech K575X sputter coater. The samples were then loaded into a FEI Verios 460L SEM for imaging at 5kV.

4.3.2 Graphene Paper

The Cambridge Graphene Centre provided the graphene paper, which was obtained from XG Sciences, Inc. Commercially, graphene paper is known as XG Leaf®, which is a unique family of thin sheets based on XG Sciences' graphene nanoplatelets, xGNP®.[174] Four different thicknesses of XG® Leaf B was used in the experiments, as detailed in Table 4-2.

Table 4-2: Surface electrical resistivity of the different thicknesses of graphene paper. They were obtained from XG Leaf® B information sheet, attached in Appendix B.

Thickness of Graphene Paper/μm	Surface Electrical Resistivity/(Ω/square)
50	0.070
75	0.040
120	0.030
240	0.014

Since the graphene papers were not sufficiently porous, patterned holes of 1 mm diameter were drilled into the papers to allow the electrolyte to flow through. As shown in Figure 4-2, graphene papers were placed in a mould to drill the required pattern. The papers were cut into a square form of length 22 mm and the diameter of the whole pattern was 18 mm.

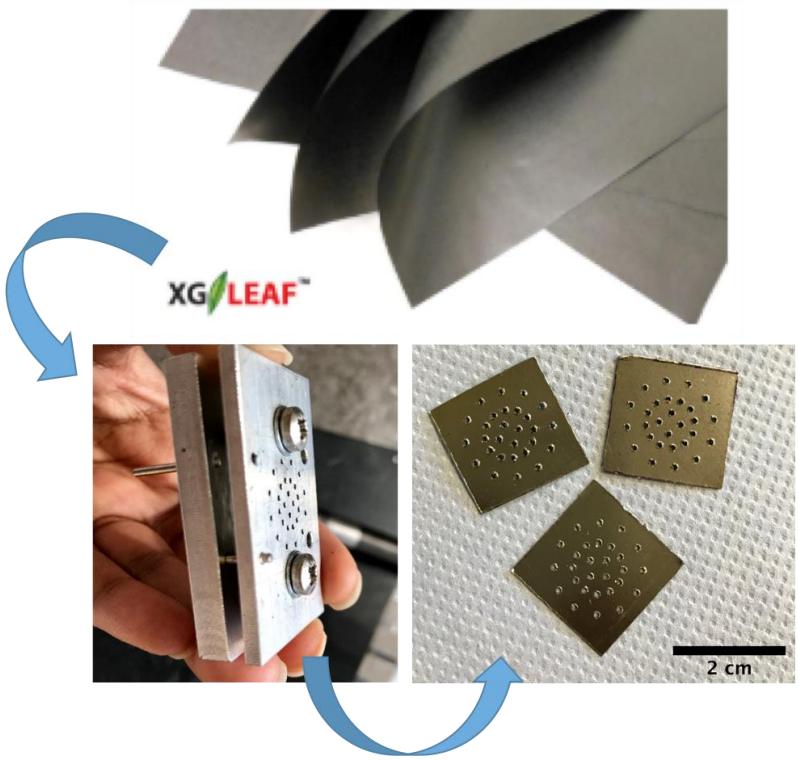

Figure 4-2: A schematic illustration of some of the processes involved before graphene paper could be used in BPV devices.

The contact angle analysis of the samples was performed using a FTA1000 B Class system (First Ten Angstroms) at the Cambridge Graphene Centre. This system has a Prosilica GC705 gigabyte Ethernet camera with a 752 x 480 pixel resolution at 62 frames per second. Drop Shape Analysis Software was used for imaging and analysis.

4.3.3 MEA-type BPV Device

The MEA was sandwiched between two acrylic frames, each of dimensions 50 x 50 x 5 mm (length x breadth x thickness). Both acrylic frames had a hole in the middle to provide an active electrode area of 18 mm diameter. The acrylic frames were tooled using an 80 W CO_2 laser cutter (HPC Laser Ltd). The two PDMS gaskets used to seal the device were square in shape with a length of 30 mm. A hole of 18 mm diameter was punched in the centre to match the design of the acrylic frames. The MEA consisted of the carbon-based materials as bioanodes separated by a non-ion exchange separator (Amersham™ Protran® nitrocellulose membrane of 0.2 µm pore size) from the cathode, which was Toray Carbon Paper TGP-H-60 coated with platinum mixed in carbon black (0.36-0.5 mg Pt/cm^2, Alfa Aesar and Fuel Cell Earth LLC). The cathode was placed on the bottom PDMS gasket, with the uncoated side exposed directly to air. The bioanode

faced the top frame, on which a cylindrical tube of dimensions 18 x 50 mm (inner diameter x length) was chemically bonded. The latter acted as the anodic chamber which held a working volume for the cell culture. Titanium strips were used to make electrical contacts to both the anode and cathode. The whole system was held together by eight hex socket cap screws. Figure 4-3 illustrates the schematic and an actual photograph of the MEA-type BPV device.

The devices were autoclaved, following which 5 ml of culture at an initial biomass concentration of 0.63 g L^{-1} was inoculated. The top of the chamber was covered with a PET disc which was sealed with an adhesive film. The PET disc had a central hole of 4 mm diameter, which was covered with nitrocellulose membrane (0.2 µm pore size) to allow sterile exchange of gas. The BPV devices were, then, placed in an incubator at 30±1°C under four cool white fluorescent light tubes with an intensity of 37±1 µmol photons m^{-2} s^{-1} under a 12:12 hours light-dark cycle. The cells were allowed to settle for 5 days so as to form a natural biofilm, before measurements were carried out.

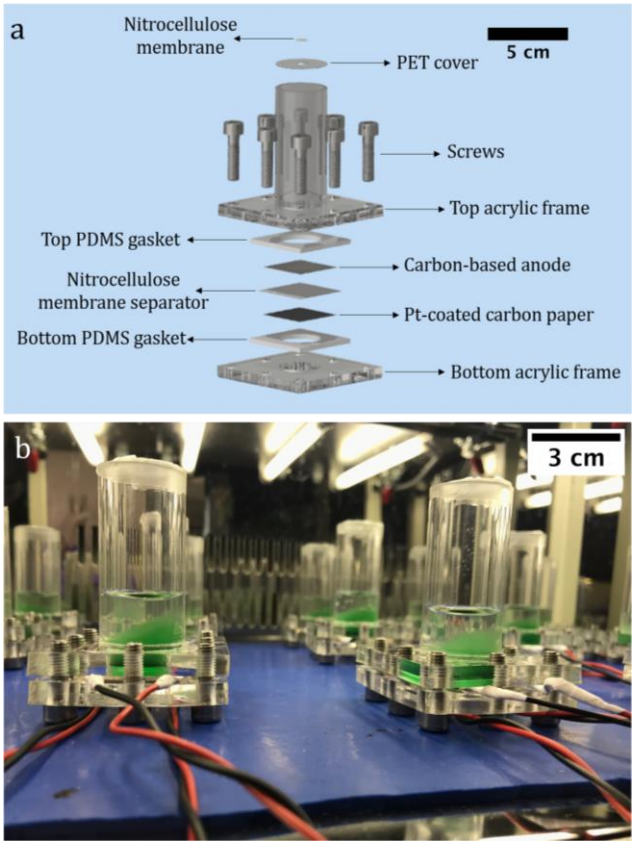

Figure 4-3: Illustration of a MEA-type BPV device (a) a schematic diagram and (b) actual devices inoculated with cultures of *S. elongatus*. The device was designed by Gonzalez Aravena.[149]

4.4 Results and Discussion

4.4.1 Conventional Carbon Fibres Bioanodes

4.4.1.1 Surface Functionalisation and Characterisation

To overcome the hydrophobic nature of both carbon paper and carbon felt, a surface treatment that introduced oxygen functional groups was employed. Plasma discharge introduced unstable free radicals on the surface of the electrodes while the sole use of peroxide treatment added oxygen-based functional groups.[159,175] Combining these two treatments is said to further increase the number of oxygen functional groups, where the free radicals were transformed into surface-active oxygen functional groups by the subsequent peroxide treatment. Figure 4-4 depicts a schematic diagram of the combined treatment strategy.

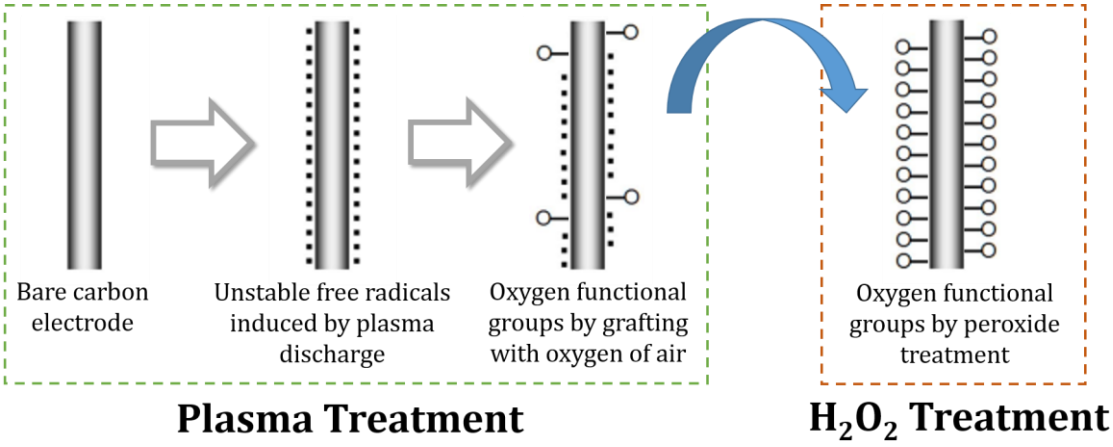

Figure 4-4: A schematic illustration of a combined plasma and hydrogen peroxide treatment, termed as fully treated (FT). Modified from Kim et al.[159]

4.4.1.1.1 Surface Wettability

Figure 4-5 illustrates the effects of surface functionalisation on the wettability of carbon paper and carbon felt. Plasma treatment completely changed the surface of both carbon paper and carbon felt from a hydrophobic one to a hydrophilic one as both electrodes became entirely soaked. However, there was no alteration in the hydrophobicity of peroxide treated and fully treated electrodes, with a slight decrease in the degree of hydrophobicity. Moreover, it can be observed that fully treated samples behave similarly to peroxide treated electrodes, indicating that the oxygen

groups formed during plasma treatment may have been lost in the subsequent peroxide treatment.

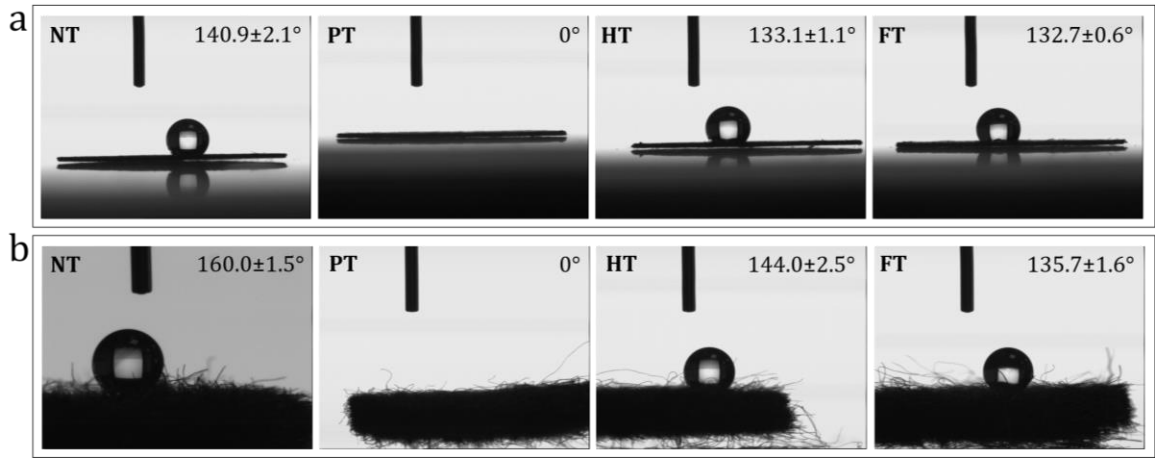

Figure 4-5: Photographs of water contact angle measurements for all surface treatments of (a) carbon paper and (b) carbon felt [the mean ± se is shown for each data set (n=3)]. Modified from Kim et al.[159]

4.4.1.1.2 Chemical Titration

Chemical titration with tetraethylorthosilicate (TEOS) was used as an approximate qualitative method for gauging the presence of oxygen functional groups. TEOS is known to react with oxygen functional groups to form orthosilicate.

As shown in Figure 4-6, there is sparse formation of orthosilicate clusters on the treated carbon paper fibres with almost none on the bare carbon paper. If observed closely, an abundance of TEOS clusters can be found behind the treated carbon fibres in the background. Figure 4-7 further emphasises on the difference in the background of non-treated and plasma treated carbon paper samples. Both samples have clusters of TEOS, with a higher proportion in the plasma treated one. Thus, this method may not be appropriate for assessing the presence of oxygen functional groups on the fibres of carbon paper. This experimental method has previously been used with carbon felt samples by Kim et al.[159] Although carbon paper and carbon felt are of the same material, the morphology and surface chemistry may differ.

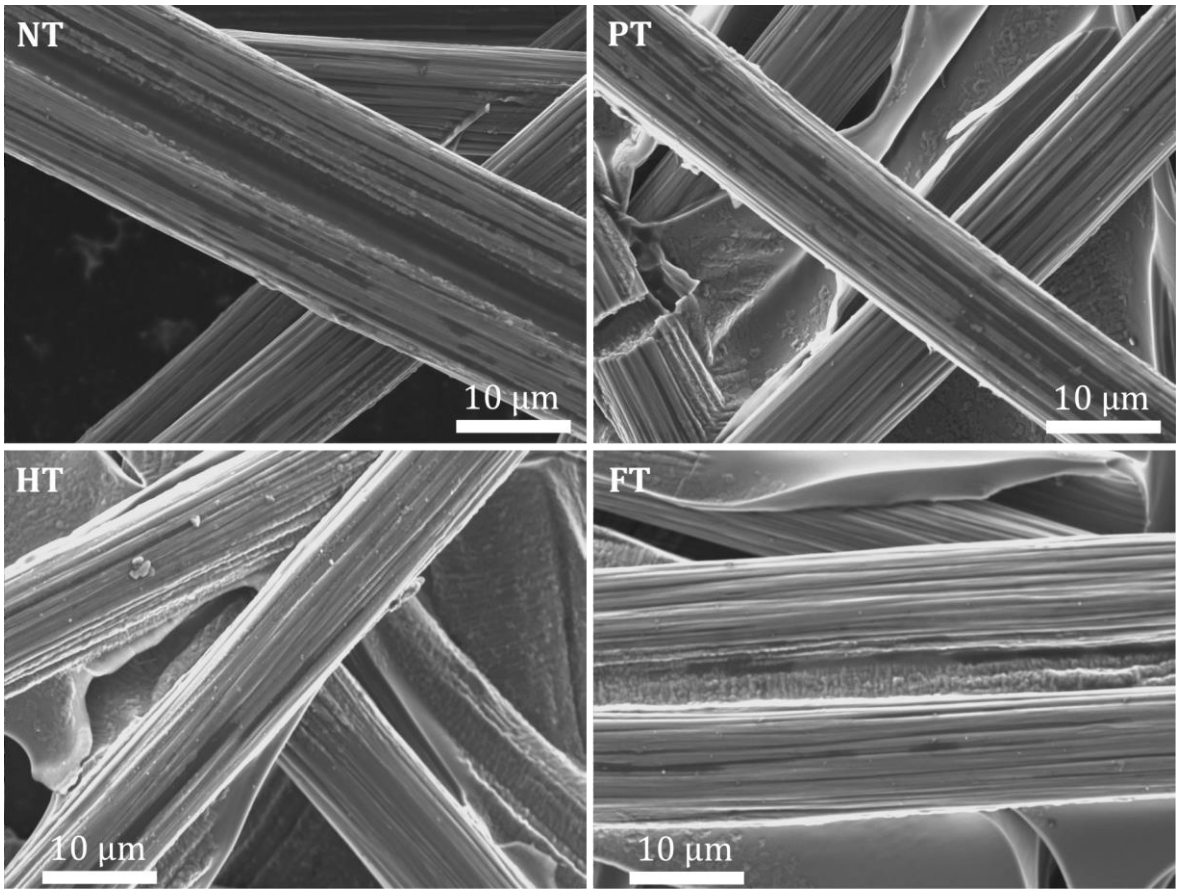

Figure 4-6: SEM images of carbon paper fibres post chemical titration with TEOS.

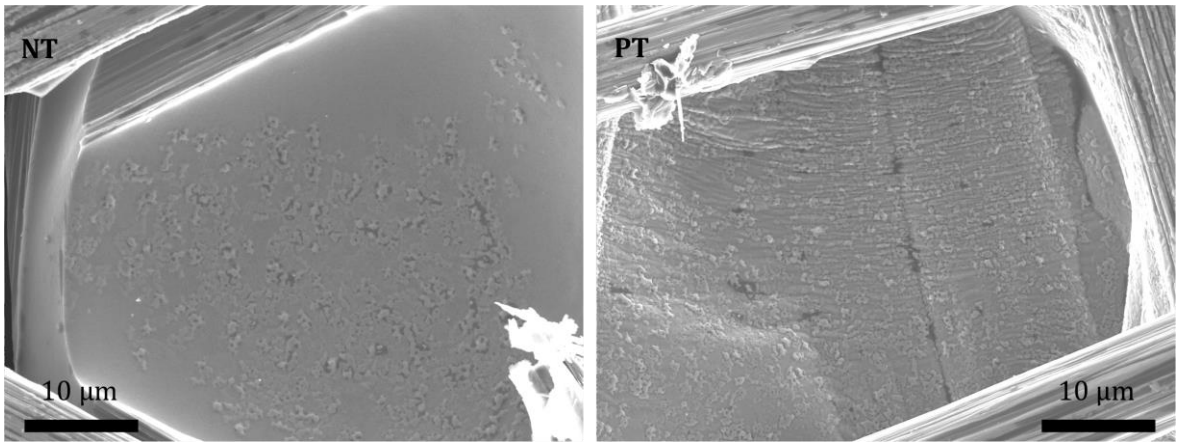

Figure 4-7: SEM images of carbon paper showing the background populated with clusters of TEOS.

The presence of orthosilicate can be detected in all samples of carbon felt as depicted in Figure 4-8. Peroxide treated carbon felt has a much higher proportion of TEOS clusters, followed by fully treated, plasma treated and non-treated carbon felt samples. This disparity may be attributed to the presence of different oxygen functional groups in accordance to the treatment used. For instance, plasma treatment is more likely to

generate carbonyl groups (C=O) and phenolic groups (C-O).[161] Peroxide treatment alone can effectively introduce hydroxyl groups (C-OH) and phenolic groups (C-O) while the combined treatment (FT) is more likely to generate carboxyl groups (COOH) together with phenolic groups (C-O).[159]

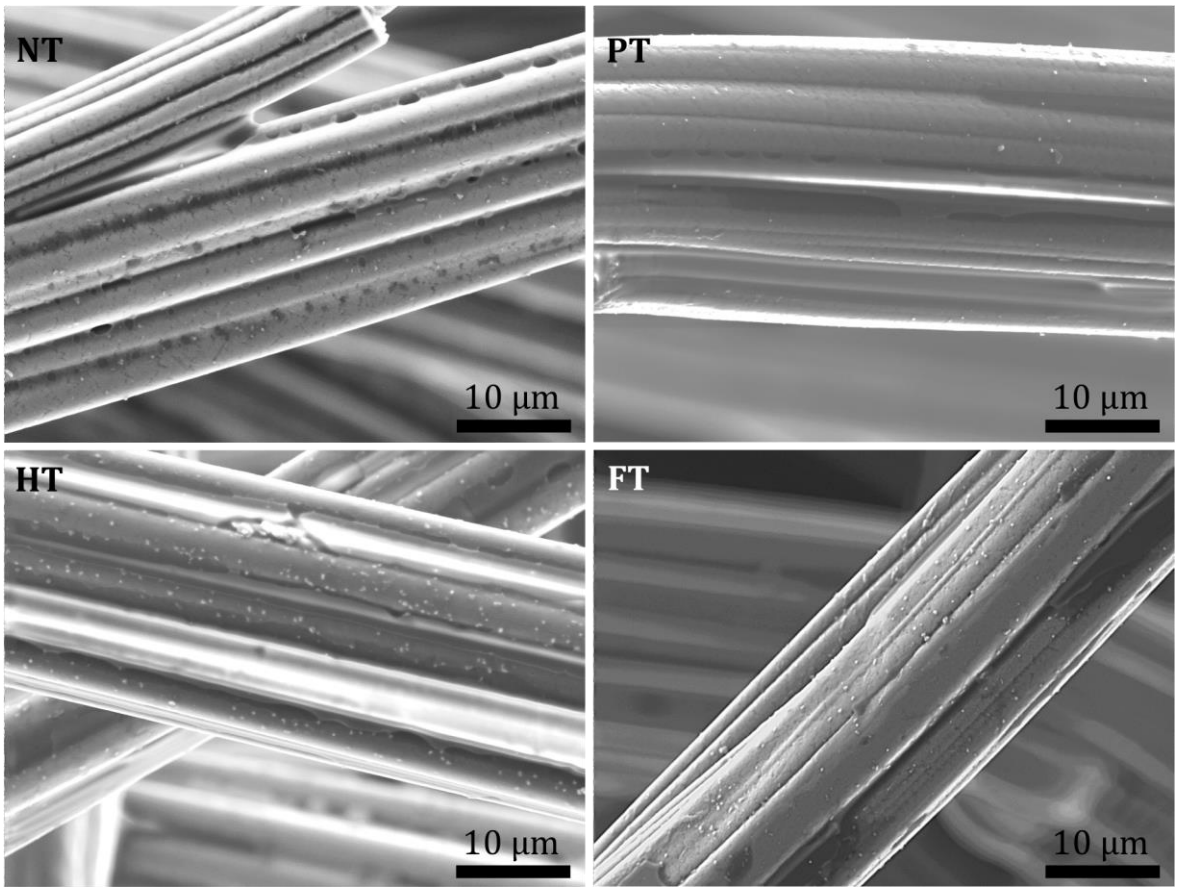

Figure 4-8: SEM images of carbon felt fibres after chemical titration with TEOS.

The results with TEOS are in contradiction with the water contact angle measurements. Peroxide and fully treated carbon felt samples were found to be hydrophobic, even though they have a higher proportion of TEOS clusters, indicating a higher number of oxygen functional groups. This can again be explained by the affinity of TEOS to react with particular oxygen groups and as mentioned earlier, TEOS is only an approximate analysis to detect the presence of functional oxygen groups.

4.4.1.1.3 Biofilm Coverage

Wettability may have an effect on biofilm formation and attachment and, thus, SEM images were used for a qualitative assessment. As shown in Figure 4-9, biofilm formation is similar on all the surfaces of carbon paper samples. The hydrophobic samples of non-treated, peroxide treated and fully treated carbon paper did not hinder

biofilm formation or adhesion. Some studies have reported that some microorganisms have the ability of modifying their cell surfaces to allow direct hydrophobic-hydrophobic interactions with the substrates.[176,177]

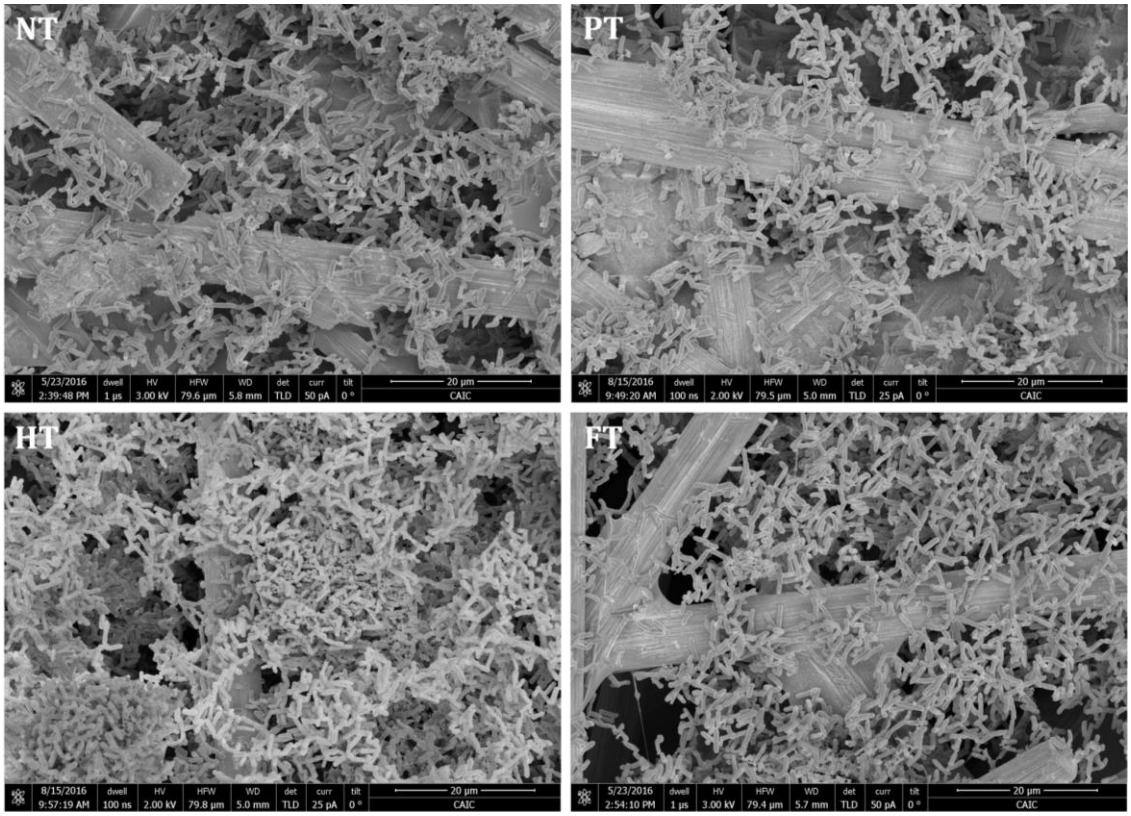

Figure 4-9: SEM images of biofilm of *S. elongatus* on the different treated samples of carbon paper.

Similarly, as illustrated in Figure 4-10, all the surface treated samples of carbon felt produced about the same density of biofilm, except for fully treated carbon felt, where a less dense biofilm was formed. Fully treated carbon felt may be exhibiting the case, where a hydrophobic surface deters biofilm formation and attachment.

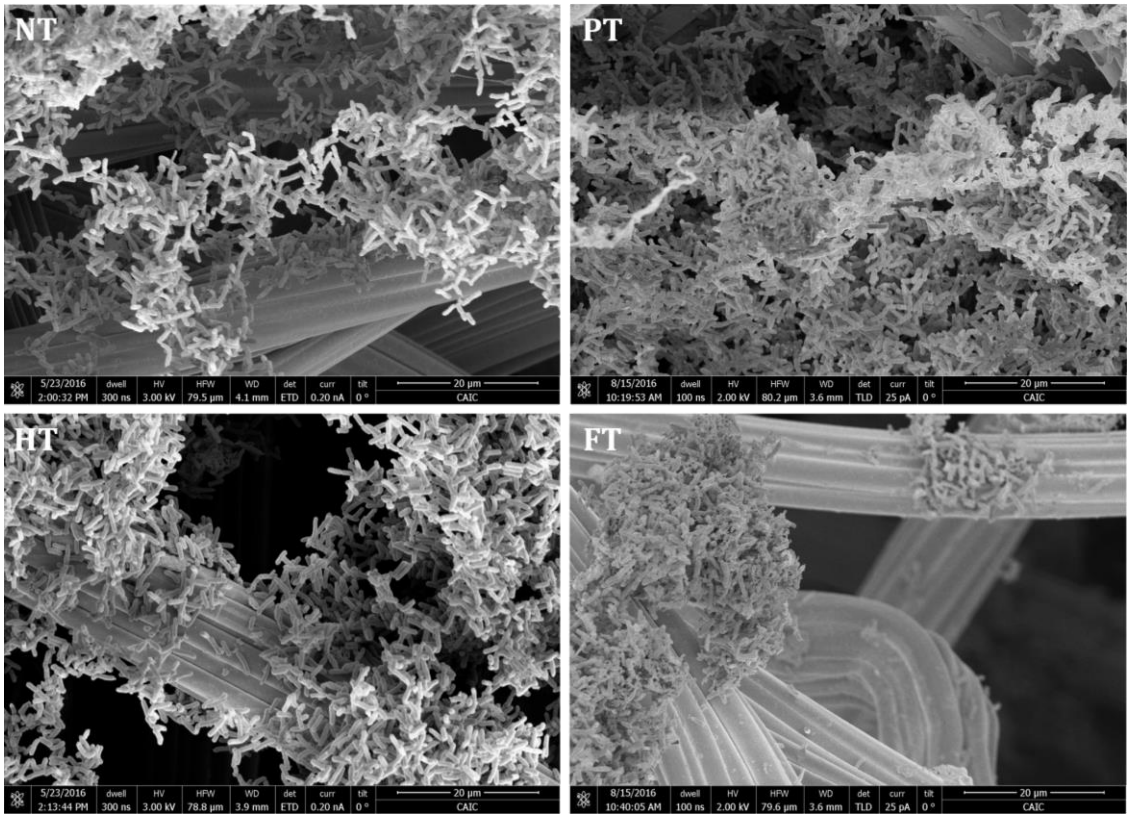

Figure 4-10: SEM images of biofilm of *S. elongatus* on the different treated samples of carbon felt.

4.4.1.2 Performance Analysis of BPV Devices

All the samples of carbon paper and carbon felt were used as bioanodes in MEA-type BPV devices to analyse the effects of the surface treatment on their electrochemical performances.

In Figure 4-11, it can be seen that all the samples of carbon paper have similar OCP values, averaging 300 mV, suggesting that a similar affinity exists between the cells of *S. elongatus* and the carbon fibres of carbon paper. Non-treated carbon paper suffered an activation loss of 133 mV, while plasma treated, peroxide treated and fully treated carbon paper samples experienced a loss of 106 mV, 88 mV and 86 mV, respectively. The surface treatment, thus, improved the electrochemical activity of the bioanodes by reducing activation losses. The ohmic losses, also, obtained from the polarisation plot will be analysed in Figure 4-13 (a).

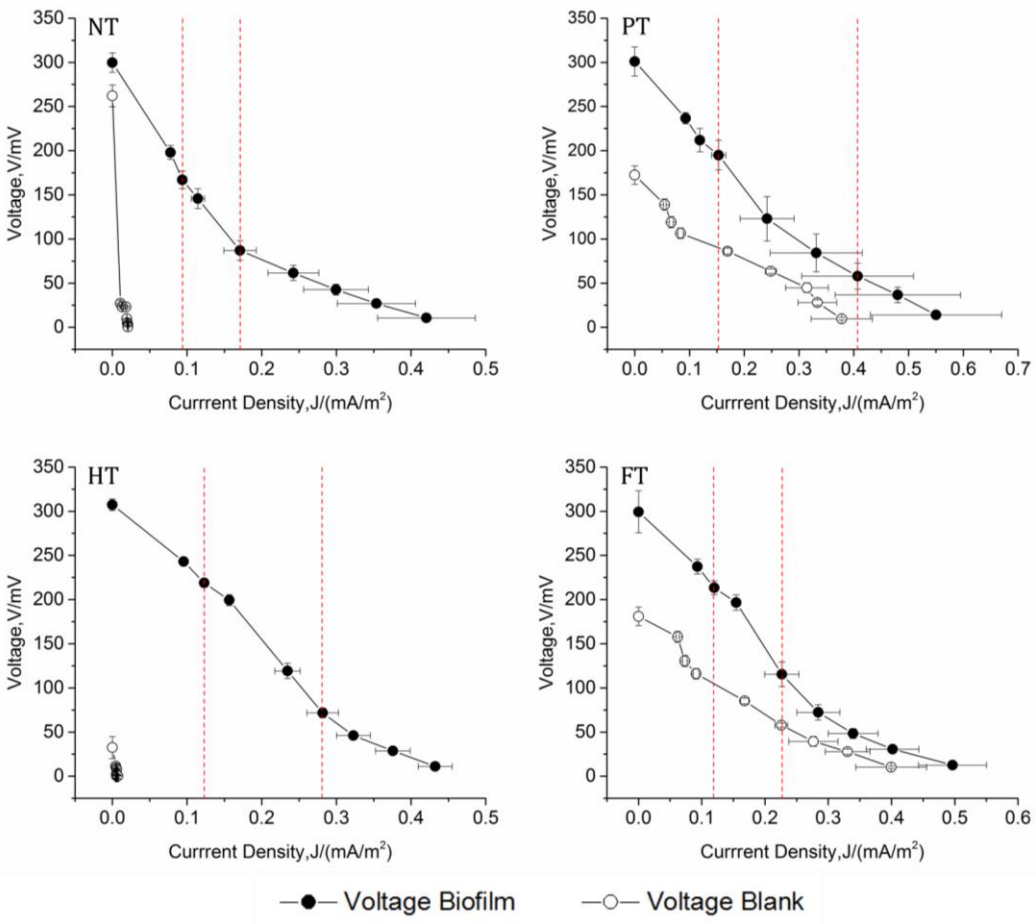

Figure 4-11: Polarisation curves of the different treated samples of carbon paper [the mean ± se is shown for each data set (n=3)]. The lines shown are purely used to guide the eye. The additional red dash lines separate the different regions of electrochemical losses for the biofilm only.

The OCP values of the different samples of carbon felt averaged at around 300 mV, suggesting similar interactions of the biofilm with the anodes. As observed in Figure 4-12, non-treated carbon felt bioanodes suffer from high irreproducibility as represented by the large error bars. Moreover, the systems suffered from high activation overpotential of 233 mV. Plasma treated, peroxide treated and fully treated carbon felt bioanodes exhibited activation polarisation of 77 mV, 103 mV and 66 mV, respectively. Similarly to the carbon paper bioanodes, the introduction of active oxygen functional groups minimised the electrochemical loss of activation. Ohmic losses will be discussed in Figure 4-13 (a).

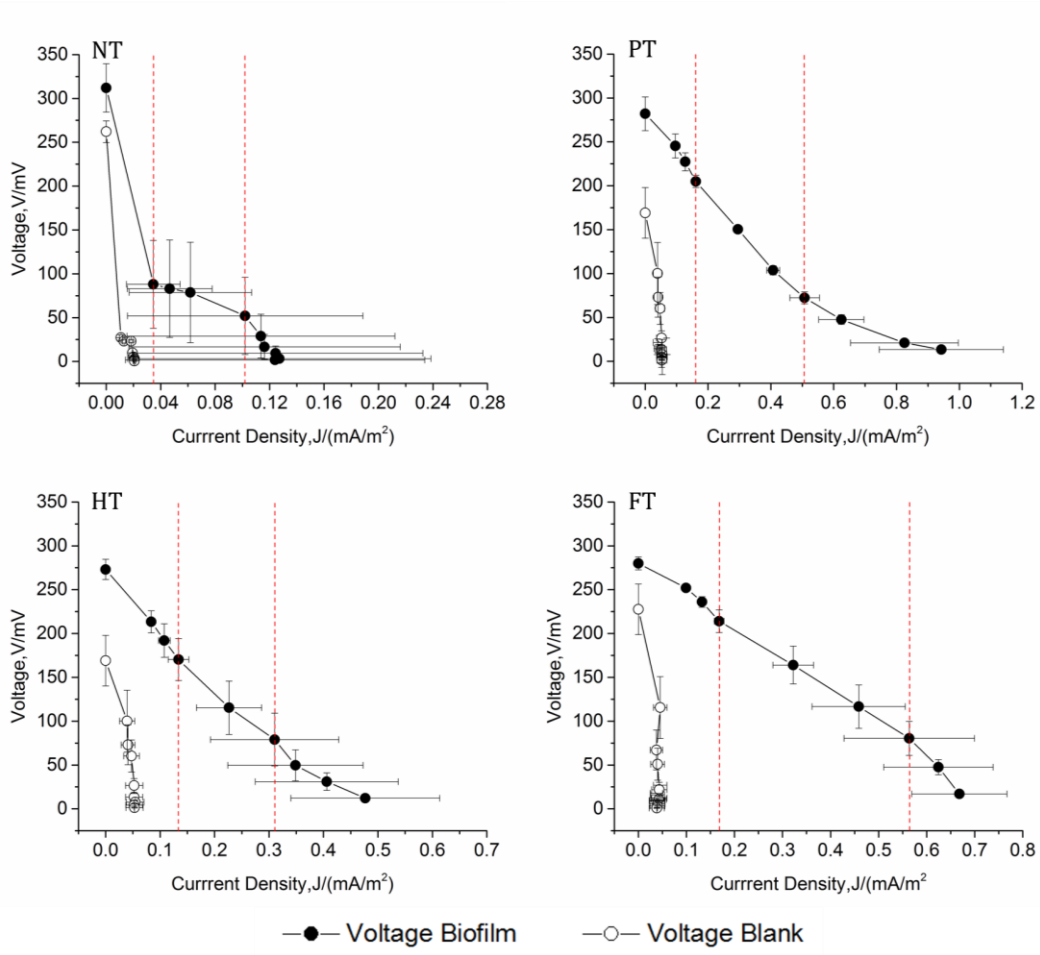

Figure 4-12: Polarisation curves of the different treated samples of carbon felt [the mean ± se is shown for each data set (n=3)]. The lines shown are purely used to guide the eye. The additional red dash lines separate the different regions of electrochemical losses for the biofilm only.

a

Bioanode Materials	Internal Resistance/MΩ			
	NT	PT	HT	FT
Carbon Paper	4.1±0.5	2.1±0.5	3.7±0.2	3.7±0.2
Carbon Felt	51±61	1.60±0.03	2±1	1.3±0.4

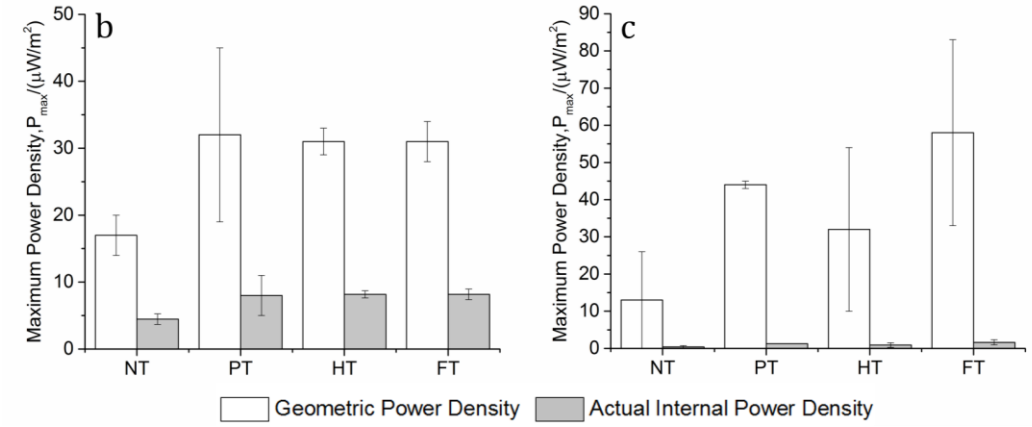

Figure 4-13: Data extracted from polarisation and power curves to compare the performance of the treated carbon fibres (a) internal resistance and (b) maximum power output of carbon paper and (c) maximum power output of carbon felt [the mean ± se is shown for each data set (n=3)].

There is a positive effect of the surface treatments on ohmic losses, as illustrated in Figure 4-13 (a). The internal resistance of devices with plasma treated carbon paper bioanodes was halved as compared to devices with non-treated carbon paper bioanodes while the internal resistances of devices with peroxide and fully treated carbon paper bioanodes were only slightly lower. Taking into consideration the specific surface area of carbon paper, the actual maximum power output was considerably lower than the geometric maximum power density. The treated bioanodes had about a 2-fold increase in actual maximum power density as compared to the non-treated carbon paper bioanode with an actual maximum power density of 4.47±0.79 μW m^{-2}. Peroxide and fully treated carbon paper bioanodes had similar degree of irreproducibility while plasma treated carbon paper was slightly more irreproducible.

Non-treated carbon felt bioanodes behaved volatilely as the error in the resistance was even bigger than the actual resistance. They proved to be highly resistive and were, also, the more hydrophobic among all the samples. Their highly hydrophobic nature

hinders the wettability with the aqueous electrolyte and, hence, its diffusion. However, devices with treated carbon felt bioanodes exhibited about a 32-fold average decrease in internal resistance, suggesting that there was a better interaction and diffusion with the electrolyte. The actual maximum power density was substantially lower than the geometric maximum power density. Only plasma treated and fully treated carbon felt bioanodes had slightly apparent maximum power output of values 1.23±0.03 μW m^{-2} and 1.63±0.70 μW m^{-2}, respectively.

It is worth highlighting that within the treated samples, there is no marked difference between internal resistance and actual maximum power output achieved, even though plasma treatment makes the bioanodes completely hydrophilic. It had been observed that plasma treatment does not always last for long and, thus, the similarities amongst the treatments. Moreover, other factors may play an important role. BG11, the electrolyte, used for the freshwater *S. elongatus*, is known to have poor conductivity. The latter already imposed an initial resistivity for the diffusion of ions. Moreover, limitations could be in the form of electron transfer at the anode-biofilm interface.
Taking into account irreproducibility, overall, the best performing bioanode was peroxide treated carbon paper, with an actual maximum power density of 8.16±0.53 μW m^{-2}.

A MEA-type BPV device was used as it is suitable for opaque and porous materials. Moreover, the membrane being sandwiched between the anode and cathode reduces the distance the electrolyte has to travel and, hence, a lower internal resistance is expected as compared to the single chamber device used in Chapter 3. In comparison to the best performing bioanode in a single chamber BPV device, graphene/ITO-coated PET outperformed peroxide treated carbon paper bioanode in terms of OCP, internal resistance and actual maximum power density. Graphene/ITO-coated PET had an OCP value of 313±3 mV, an internal resistance of 2.7±0.2 MΩ at an actual maximum power output of 29±4 μW m^{-2}. Graphene/ITO-coated PET is a better bioanode as the hydrophobicity of peroxide treated carbon paper hindered its performance, even though a better configuration of the device was used.

The chemical titration with TEOS and the contact angle measurements do not strictly correlate to the performance of the bioanodes in the BPV devices. As a result, a novel

carbon-based material, graphene paper, was investigated with the overall aim to bridge the shortcomings of the carbon fibres.

4.4.2 Graphene Paper as Novel Bioanode

XG Leaf® is a new product line and has high potential as electrodes. Currently, it is being explored as electrodes in supercapacitors and in lithium-ion batteries.[174] It is electrically conductive with high mechanical strength. Moreover, it is said to be inherently hydrophilic.

4.4.2.1 Surface Characterisation

The wettability of the different thicknesses of graphene paper was assessed by measuring the water contact angle. Subsequently, the effect of wettability on biofilm formation is qualitatively analysed using SEM images.

4.4.2.1.1 Surface Wettability

The surface wettability of the different thicknesses of graphene paper is illustrated in Figure 4-14. All the contact angle measurements were below 90°, suggesting that the graphene papers were indeed hydrophilic. The first three thicknesses of graphene paper had similar degrees of wettability at approximately 60°, while that of 240 μm thick graphene paper was considerably lower at 42±2°. Overall, the hydrophilicity increases with the thickness of the paper, with 75 μm thick graphene paper being an outlier.

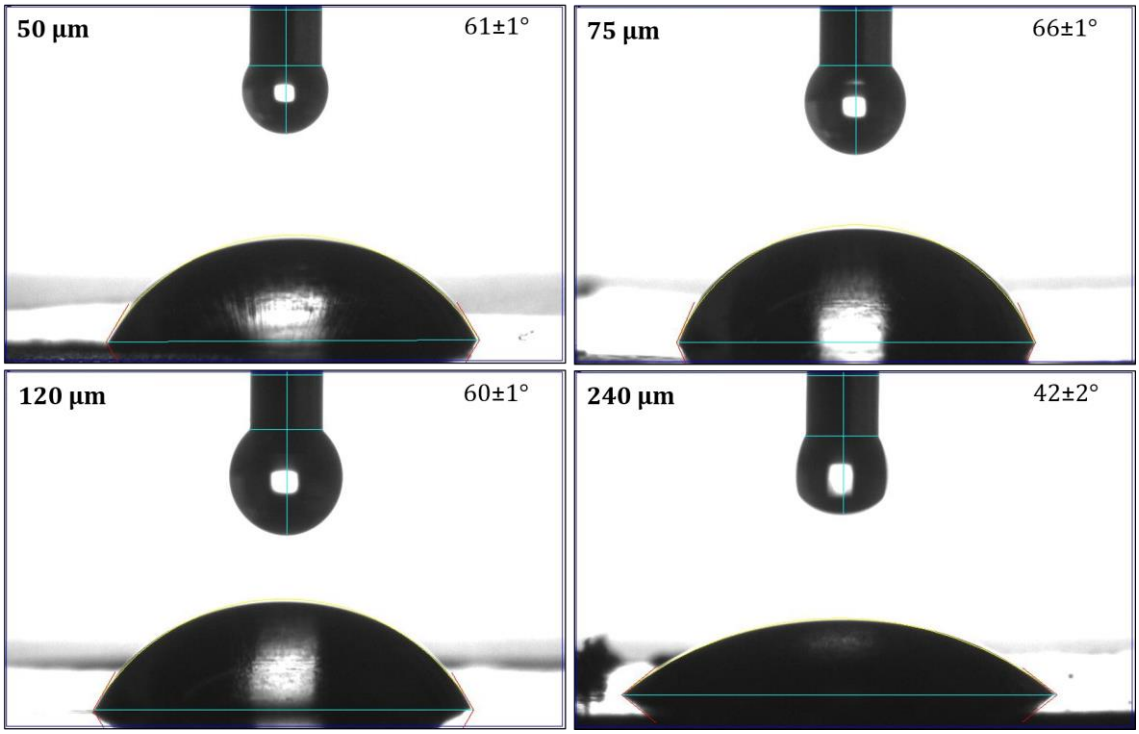

Figure 4-14: Photographs of the water contact angle measurements for the four different thicknesses of graphene paper [the mean ± se is shown for each data set (n=3)].

4.4.2.1.2 Biofilm Coverage

The biofilm coverage on all samples of graphene paper was similar and, thus, two examples only are shown in Figure 4-15. It is quite intricate to compare biofilm formation with samples of carbon fibres as the latter are porous and, hence, the cells will inhabit the interiors as well.

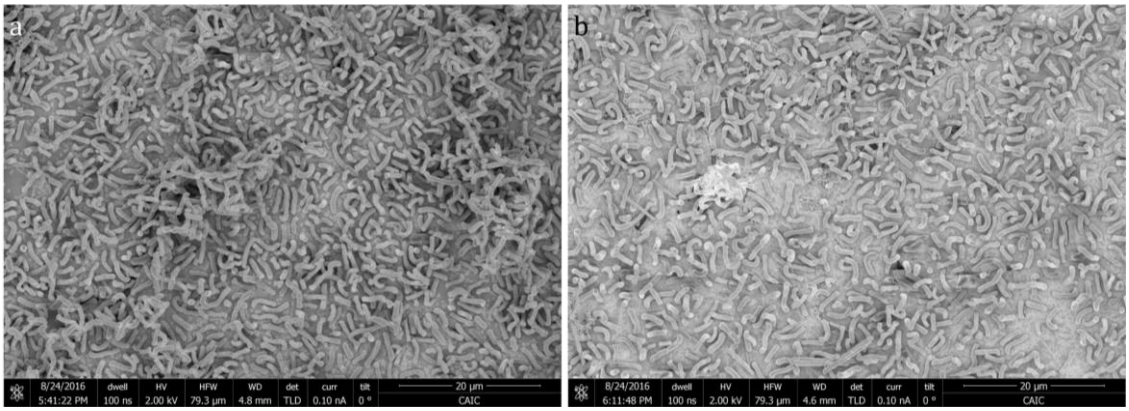

Figure 4-15: Examples of SEM images of biofilm of *S. elongatus* on (a) 75 µm thick graphene paper and (b) 240 µm thick graphene paper. The other two thicknesses had a similar coverage.

4.4.2.2 Exoelectrogenic Activity

The mechanism of *S. elongatus* to export electrons in an extracellular manner was first determined by SEM images of biofilm and using the electrochemical method of double potential step chronoamperometry. These electrons were, then, harvested in BPV devices for bioelectricity generation.

4.4.2.2.1 Features of Biofilm

SEM images of biofilm of *S. elongatus* revealed the presence of putative nanowires or pili as well as extracellular matrix, as shown in Figure 4-16. As explained in Chapter 3, the pili may possibly be part of the exoelectrogenic structure of *S. elongatus*.

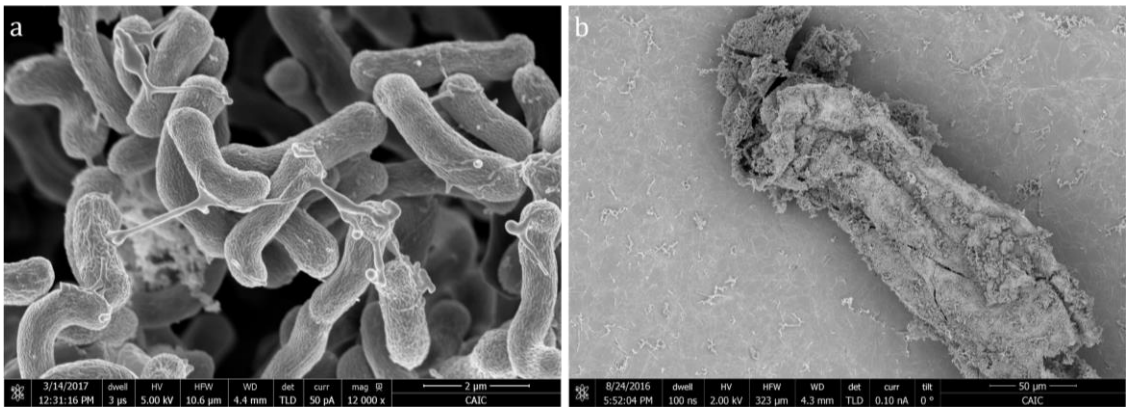

Figure 4-16: Interaction of cells of *S. elongatus* with 120 μm thick graphene paper (a) putative nanowires or pili in cells to cells interactions and (b) presence of extracellular matrix.

4.4.2.2.2 Double Potential Step Chronoamperometry

As mentioned in Chapter 3, the biocatalytic activity of *S. elongatus* is quite slow and thus its electrochemical activity was not easily detected by cyclic voltammetry. Thus, double potential step chronoamperometry was employed to analyse the electrochemical interactions between the biofilm of *S. elongatus* and the different thicknesses of graphene paper.

The biofilms were consecutively oxidised and reduced in 5 cycles and the repeated patterns demonstrated the reproducibility, robustness and reversibility of the reactions as depicted in Figure 4-17. The similar heights of the peak currents in both the oxidising and reducing potential steps suggest that the same number of redox centres were subsequently oxidised and reduced.

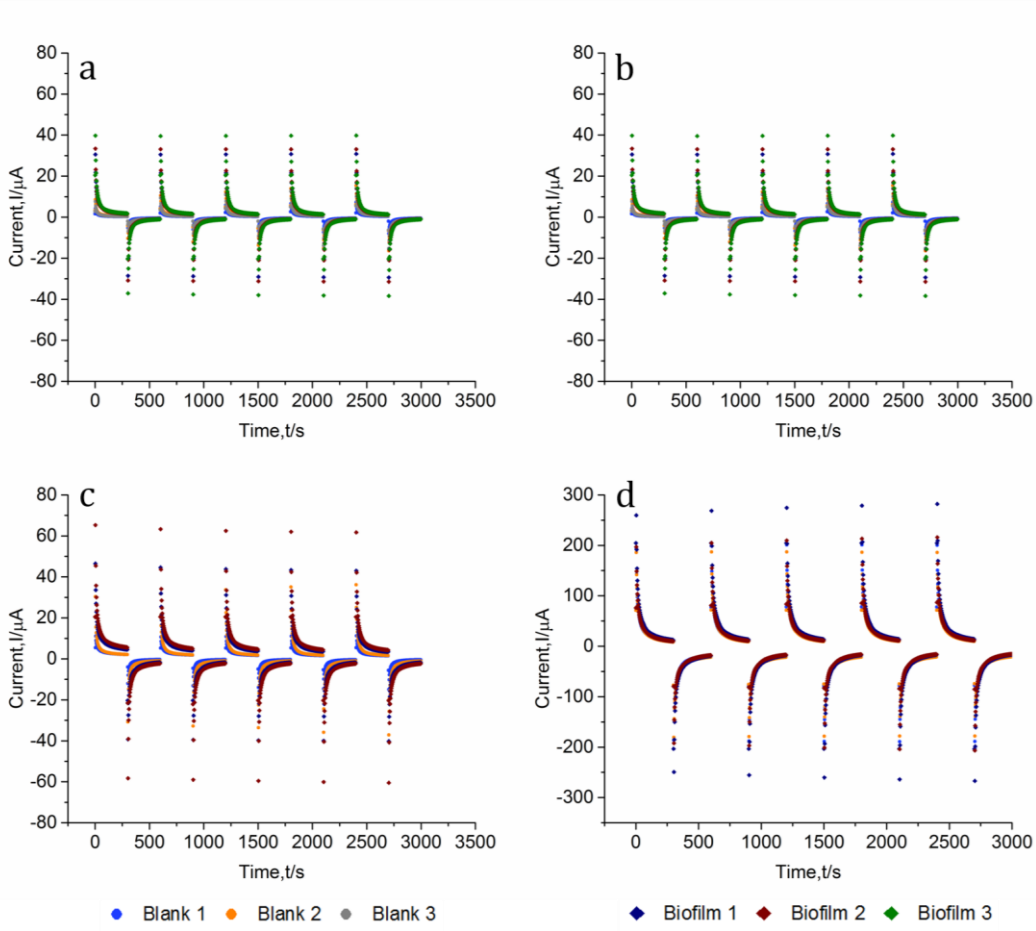

Figure 4-17: Chronoamperograms showing sets of 5 cycles obtained at E_1=0.35 V and E_2=0 V for 300 s at each applied potential for graphene papers of thickness (a) 50 μm (b) 75 μm (c) 120 μm and (d) 240 μm.

The peak current and the limiting current generated were analysed to distinguish between the performances of the different thicknesses of graphene paper, as shown in Table 4-3.

The values of the blanks were lower than the biofilms. Overall, there is an increase in peak current and limiting current as the thickness of graphene paper increases, except for 75 μm thick graphene paper, which seems to be an outlier. 240 μm thick graphene paper displayed a significant increase in both peak and limiting currents as compared to 50 μm thick graphene paper, namely a 6-fold and an 8-fold increase, respectively. The results indicate that 240 μm thick graphene paper is the best performing anode.

Table 4-3: Data extracted from the chronoamperograms for the different thicknesses of graphene paper in terms of peak current and limiting current [the mean ± se is shown for each data set (n=3 for 50 μm and 75 μm and n=2 for 120 μm and 240 μm)].

Thickness of Graphene Paper/ μm	Peak Current/μA		Limiting Current/μA	
	Blank	Biofilm	Blank	Biofilm
50	12±1	39.7±0.1	0.55±0.09	1.5±0.1
75	9.4±0.2	29.0±0.1	0.86±0.03	1.17±0.03
120	33±1	63.0±0.6	1.84±0.06	4.7±0.2
240	185±2	240±3	9.8±0.2	12.1±0.3

The corresponding Cottrell plots are illustrated in Figure 4-18. They illustrate linearity for the whole cycle, indicating the diffusion-controlled character of the current. The differences between the three devices containing the biofilms may be attributed to the fact that the growth of biofilm could not be minutely controlled. Though the same initial biomass was used, it would be different as the biofilm proceeds through the growth phase. Thus, its attachment may also be different in each device.

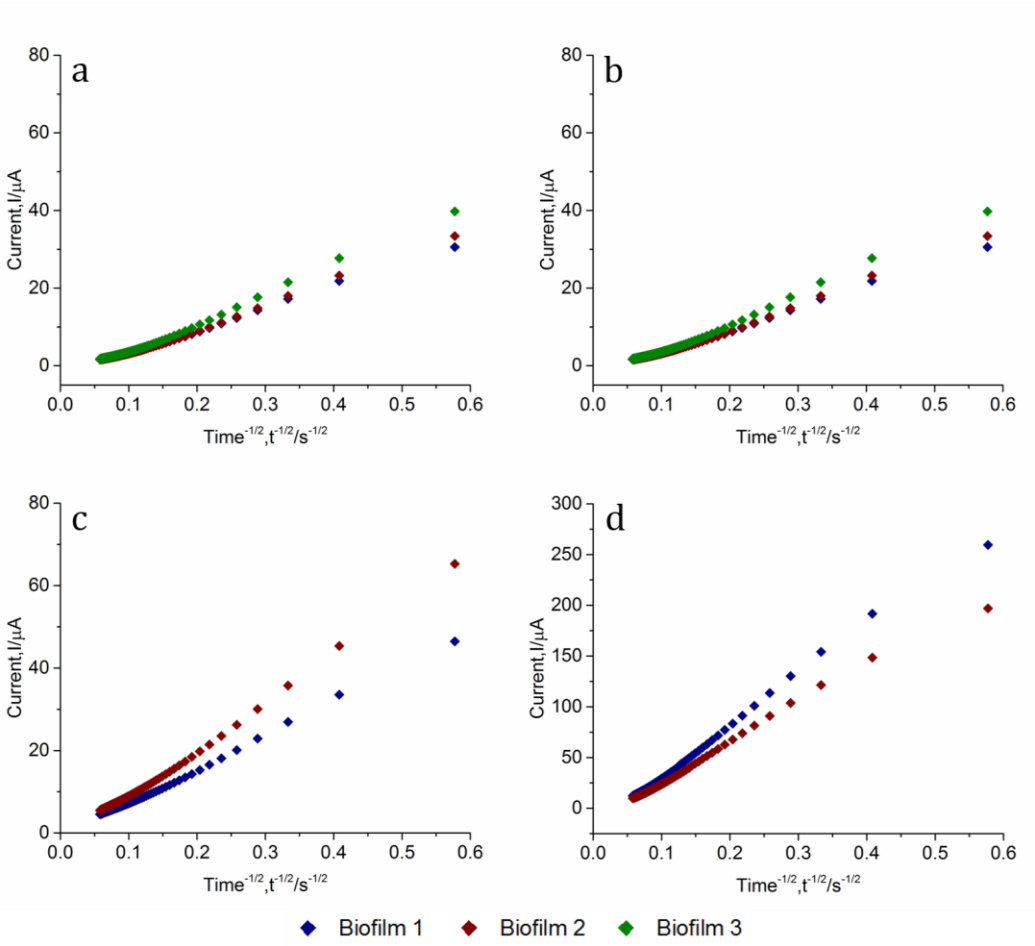

Figure 4-18: Corresponding Cottrell plots of Figure 4-17 shown only for the first step cycle of thicknesses (a) 50 µm (b) 75 µm (c) 120 µm and (d) 240 µm.

Since the difference between the blanks and the biofilms were not strikingly apparent in the chronoamperomograms of Figure 4-17, the integrated charge was plotted in Figure 4-19 for better analysis. The charge over biofilms of 50 µm and 75 µm thick graphene paper has a smaller increasing rate and have highly reproducible behaviour with the three independent biofilms. The charge on all the biofilms has an increasing trend, except for 240 µm thick graphene paper. The decreasing trend may be attributed to the surface chemistry of the graphene paper as it had the highest degree of hydrophilicity. However, the charges are of higher magnitude in comparison to the other thicknesses. All the blanks have a decreasing trend, except for 120 µm thick graphene paper but were still lower than the biofilms.

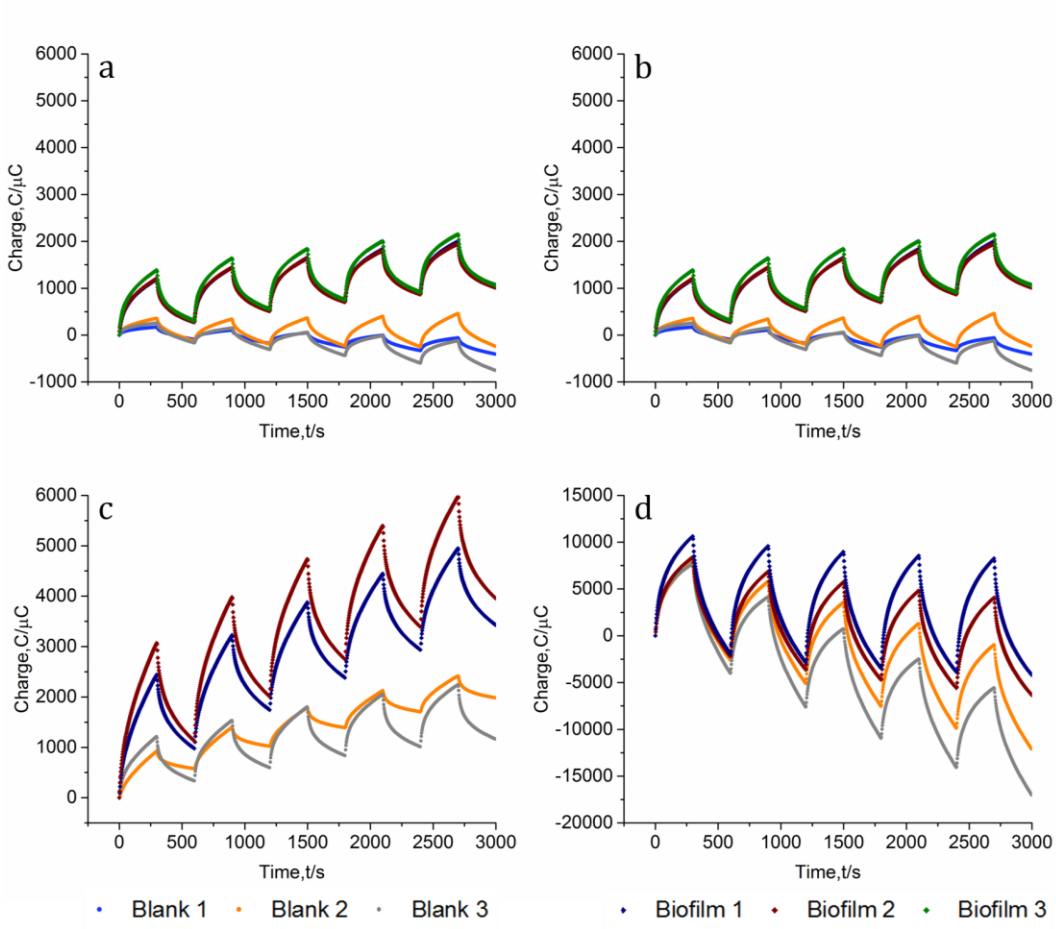

Figure 4-19: Corresponding chronocoulomograms of Figure 4-17 for the thicknesses of (a) 50 μm (b) 75 μm (c) 120 μm and (d) 240 μm.

4.4.2.2.3 Performance Analysis of BPV Devices

The performance of the four different thicknesses of graphene paper was analysed in the MEA-type BPV devices.

Figure 4-20 illustrates polarisation curves, from which OCP values, activation and ohmic losses can be determined. 50 μm and 75 μm thick graphene papers have similar OCP values, averaging 250 mV. 120 μm and 240 μm have lower OCP values at 219 mV and 200 mV, respectively. Overall, there is no significant difference between the OCP values, suggesting similar interaction of the biofilm with the anode materials. However, there was a significant difference in activation overpotentials. 50 μm thick graphene paper suffered an activation loss of 38 mV, while 75 μm, 120 μm and 240 μm thick graphene papers experienced a loss of 75 mV, 30 mV and 17 mV, respectively. 75 μm thick graphene paper was again an outlier as in the studies of double potential step chronoamperometry. The OCP of carbon fibres bioanodes were higher than those of

graphene papers but suffered from substantial activation losses. 240 µm thick graphene paper was the highest performing bioanode with minimal polarisation, which corresponds to its more hydrophilic nature. The ohmic losses will be analysed in Figure 4-21 (a).

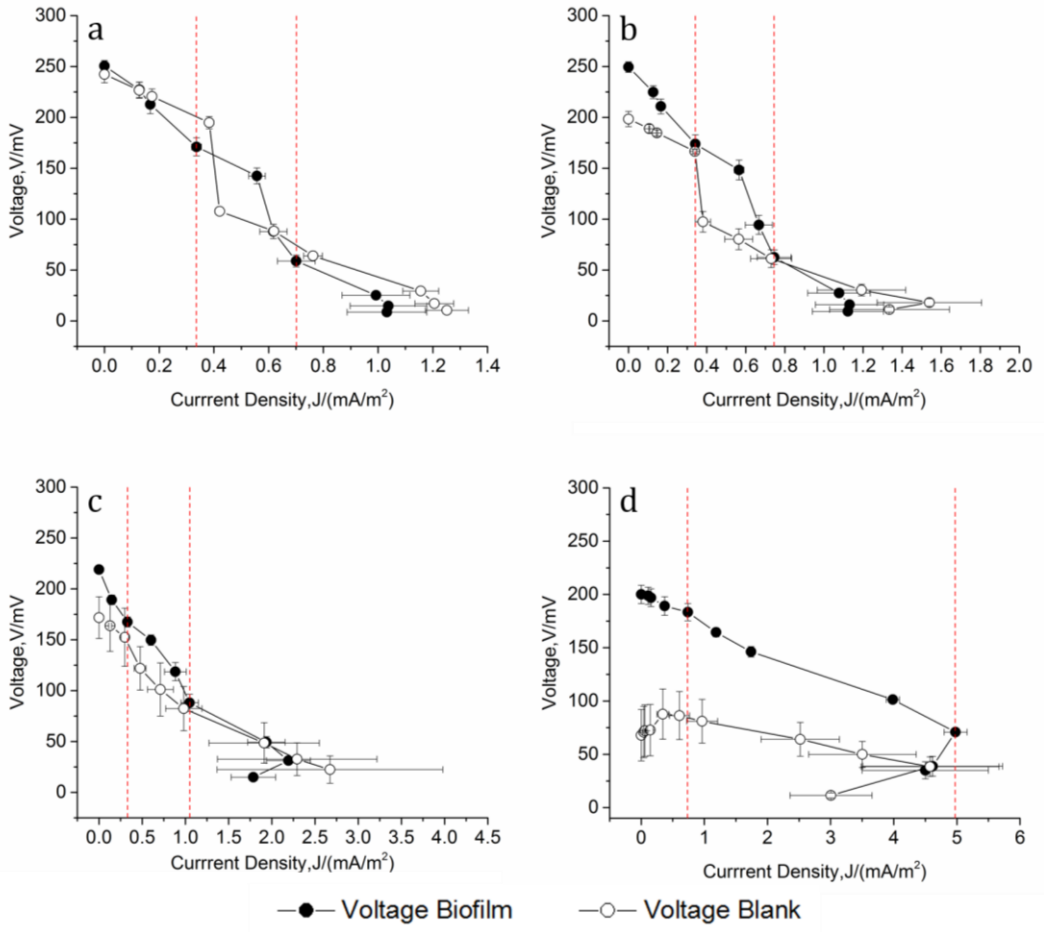

Figure 4-20: Polarisation curves of the different thicknesses of graphene paper (a) 50 µm (b) 75 µm (c) 120 µm and (d) 240 µm [the mean ± se is shown for each data set (n=3)]. The lines shown are purely used to guide the eye. The additional red dash lines separate the different regions of electrochemical losses for the biofilm only.

As depicted in Figure 4-21 (a), the internal resistance of the devices decreases with the increasing thickness of the graphene paper. The order of internal resistances decreased to kΩ as compared to carbon fibres. Similarly to activation loss, 240 µm thick graphene paper had the lowest internal resistance of 97±4 kΩ. This further translated into the highest actual maximum power output achieved at 393±20 µW m^{-2}. Additionally, the actual maximum power output produced by devices of the first three thicknesses of graphene paper was substantially higher than those containing the

carbon fibres, with values of 72±8 μW m^{-2}, 80±7 μW m^{-2} and 126±33 μW m^{-2} for 50 μm, 75 μm and 120 μm thick graphene paper respectively. Overall, the maximum power output increased with increasing thickness of the bioanode, as illustrated in Figure 4-21 (b).

a

Thickness of Graphene Paper/μm	Internal Resistance/kΩ
50	944±73
75	826±65
120	337±54
240	97±4

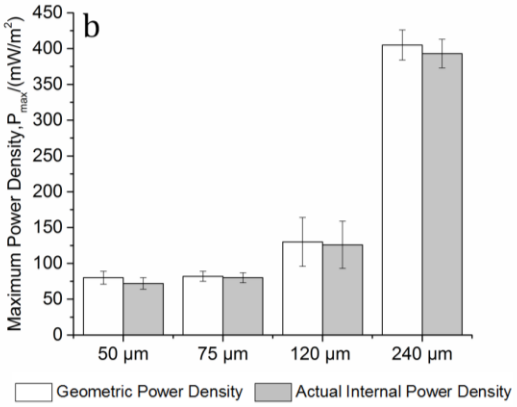

Figure 4-21: Data extracted from polarisation and power curves to compare the performance of the different thicknesses of graphene paper with regards to (a) internal resistance and (b) maximum power output [the mean ± se is shown for each data set (n=3)].

The hydrophilic graphene papers contributed to low activation and ohmic losses, which resulted in higher maximum power output, as compared to the carbon fibres. Hydrophilicity ensures excellent wetting properties between the bioanode and the electrolyte and facilitates its diffusion. Moreover, it is probable that the interaction between the biofilm and the anode was enhanced for better electron transfer.

4.5 Conclusions

This study focused on examining the effect of the wettability property of carbon-based materials, namely carbon paper, carbon felt and graphene paper on the performance of BPV devices. Carbon paper and carbon felt are known to be highly hydrophobic materials. As a result, surface modification techniques, which included plasma treatment and hydrogen peroxide treatment, were used to introduce oxygen-functional groups with the aim of improving the wettability of the materials. Only plasma-treated fibres were completely transformed from a state of hydrophobicity to hydrophilicity. The only benefit of the treatment was the reduced activation losses and internal resistance of the devices. Moreover, the decrease in internal resistance was more obvious in the treated carbon felt samples, with only plasma treated carbon

paper showing a marked improvement amongst treated carbon paper samples. In comparison to carbon felt bioanodes, carbon paper bioanodes produced slightly more significant maximum power densities. Taking into account irreproducibility, peroxide treated carbon paper bioanode was better performing with the highest maximum power output of 8.16±0.53 μW m^{-2}. The performance of the single chamber BPV device unexpectedly outperformed the MEA-type BPV device in terms of OCP, internal resistance and maximum power output by comparing the best performing bioanodes. The highly hydrophobic hydrogen peroxide treated carbon paper bioanode overpowered the advantageous design of the MEA-type BPV device. Since the surface treatments were not completely successful, a novel carbonaceous bioanode material was tested. While all the thicknesses of graphene paper were hydrophilic, 240 μm thick graphene paper had a higher degree of hydrophilicity. As a result, it was the best performing bioanode and all the experimental results corroborated. It produced the highest maximum power output of 393±20 μW m^{-2} at the lowest internal resistance of 97±4 kΩ and suffered from the lowest activation losses. Moreover, it generated the highest peak and limiting currents in double potential step chronoamperometry and had higher charge magnitude as displayed in the chronocoulomogram. However, further analysis is required to decipher its decreasing trend as compared to the other thicknesses of graphene paper. It can be concluded that, in this study, biofilm formation was not hindered by hydrophobicity but the anode-microbe interaction was probably not effective. The major improvement of surface wettability was in terms of activation and ohmic losses.

5 Performance Analysis of Graphene-coated and Carbon Nanotubes-coated Bioanodes

5.1 Introduction

Based on the highly promising performance of carbon-based nanomaterials, a proof of concept study was designed to investigate the potential use of some newly designed nano-based bioanodes in MEA-type BPV devices. Nitrocellulose membranes were coated with graphene (GNP-CMC ink) while 3D-printed bioanodes were functionalised with multi-walled carbon nanotubes (MWCNTs). The overall aim of the proposed proof of concept study presented in this chapter is to establish the future challenges and opportunities when using the newly designed bioanodes. Such a strategy will indeed generate preliminary data that will form the basis of future work, beyond the scope of the current research work.

5.1.1 Graphene as Bioanodes

Graphene is considered as a material of interest and potentially has numerous technological applications in catalysis, environment remediation, and energy storage and conversion, such as in lithium ion batteries, fuel cells, solar cells and electrochemical supercapacitors. The potential use of graphene in renewable energy-related devices is due to its unique one atom thick two-dimensional layer of sp^2-bonded carbon structure. Its extraordinary properties include high surface area, high conductivity, excellent mechanical strength, thermal conductivity, intrinsic flexibility and electrocatalytic activities. Graphene possesses rapid ion diffusion characteristics and offers multi-dimensional continuous electron-transport pathways.[83,178–180] Electron measurements have revealed that graphene has notable electron mobility.[181] Graphene has more often been used in MFCs than in BPVs. Graphene-based anodes improved the performance of MFCs by increasing the electron transfer efficiency, the

specific surface area and the microbe-electrode-electrolyte interaction.[182,183] Carbon cloth modified with graphene improved both the power density and the energy conversion efficiency of a *Pseudomonas aeruginosa*-catalysed mediatorless microbial fuel cell by about 3-fold.[184] The enhancement was attributed to the biocompatibility of graphene which promoted bacterial growth for improved direct electron transfer. Moreover, higher peak current and smaller peak separation in cyclic voltammograms were observed with the modified carbon cloth. It was even suggested that exoelectrogens incorporate graphene into their extracellular pathways.[184] Graphene modified stainless steel bioanode had an 18-fold increase in maximum power density as compared to plain stainless steel. SEM images indicated that the increase in maximum power output was due to the high surface area of the material and the increase in number of bacteria attached.[178]

Reduced graphene oxide (RGO) produced by the Langmuir-Blodgett method was cast onto glass substrates.[185] The modified bioanode produced a 2-fold increase in peak power output in comparison to ITO-coated glass bioanode.[142] The enhanced performance of the BPV was attributed to the unique properties of RGO. The highly porous RGO film was said to increase surface area, which enhanced biofilm attachment of green alga *Chlorella* sp. (UMACC 313) and, thus, improved the efficiency of electron transfer.[142] The power densities were quoted as a function of the geometric surface area, which can be misleading. Since an increase in surface area was described as one of the reasons for the enhanced performance, the actual power density per active anode area would be considerably lower. Improvement in photocurrent generation was observed when photosystem I (PSI) was adsorbed onto a monolayer graphene in an electrochemical cell. The enhanced performance was explained to be due to the unique properties of graphene.[186,187]

5.1.2 Carbon Nanotubes as Bioanodes

Carbon nanotube, an allotrope of carbon, is a promising anode material because of its unique electrical conductivity, chemical stability, biocompatibility, high specific surface area and catalytic properties. It has been reported that CNTs promote growth of cells, cell adhesion and cell attachment.[188,189] Another research work[190] addressed the fact that microorganisms grown over CNTs produce excellent charge transfer properties as electrons can be transferred through microbial nanowires to the π-π

stacking between the carbon atoms of graphite. It was observed that the spaces between grown CNTs on stainless steel mesh provided room for microbial growth and the minimum amount of amorphous carbon offered excellent charge interaction.[22] Moreover, the charge transfer capabilities of CNT electrodes were confirmed by using cyclic voltammetry and electrochemical impedance spectroscopy techniques.[119]

A novel technique of digitally printing cyanobacterium *Synechocystis* sp. PCC 6803 on top of a conducting surface composed of carbon nanotubes was conducted in a series of feasibility studies. Nink-100: multiwall inkjet, consisting of CNTs in aqueous dispersion, was printed on a paper substrate for the conductive anode pattern. The cyanobacteria was printed and grown directly onto the surface of the CNTs. The printed cyanobacteria were able to sustain an electric current both in light and in the dark. With a platinum-coated carbon paper as cathode, a maximum current density of about 4 mA m^{-2} and 3 mA m^{-2} were generated in light and in the dark respectively. These values were about 3 to 4-fold higher when the cells of the same cyanobacteria were deposited by gravity on the surface of ITO-coated PET from a liquid culture. However, the power outputs were comparable to liquid culture-based BPV devices. As part of the same study[191], a semi-dry thin film BPV system was fabricated, where the cathode was also printed on the paper. Both the anode and the cathode were printed side by side in CNTs ink on a paper substrate in a zigzag manner. A water-absorbent gel was used to cover the electrodes and to act as a salt bridge and a source of nutrients to the cells. In terms of performance, the power output was smaller than the first case and literature values of common BPV systems. The decrease in power was correlated to the increase in ink resistivity. Nonetheless, the new design system has potential as a disposable and environmentally friendly power supply.[191]

The ability for electron transfer from freshwater cyanobacterium *Nostoc* sp. was investigated by immobilising the cells on CNT modified carbon paper anode and a l*accase*/CNT modified carbon paper cathode. Without any mediator, the maximum current and power densities achieved were 250 mA m^{-2} and 35 mW m^{-2} respectively. However, by adding the redox mediator 1,4-benzoquinone, the current and power densities were significantly improved with values attaining 2300 mA m^{-2} and 100 mW m^{-2} respectively. Sekar et al.[52] claimed that wiring the cells of cyanobacteria on CNTs for electricity generation has not been reported previously.

Alternative research work from the former authors involved using carbon paper modified with MWCNTs as working electrode in amperometric studies. The abilities of extracellular electron transfer of wild type *S. elongatus* PCC 7942 and a genetically engineered *S. elongatus* PCC 7942 containing a foreign outer membrane cytochrome S (OmcS) were compared. A 9-fold higher photocurrent generation was obtained with the engineered cyanobacteria as compared to the wild-type.[192]

5.1.3 3D Printing

Additive manufacturing or 3D printing is a burgeoning technology and has been used in various fields, including industrial prototyping, lightweight machines, medical implants, drug delivery, tissue engineering and building industry. More recently, it is being used in the research area of bioelectrochemical systems (BES).[101,193] 3D printing provides a high degree of design freedom. Besides the ability to produce various geometries, 3D printing offers the simplicity in fabrication that is of compact structures and can be made without any fixtures like screws, clips or clamps. As a result, the manufacturing and assembly of BES can considerably be made simpler and faster. The individual components of a BES can be optimised for a cost-effective, consistent and stable performance. Moreover, 3D printing would be beneficial in a scale-up scenario by building stacks of multiple units.[101,193] 3D printing has mostly been used in MFC systems.

You et al.[193] investigated three 3D printed polymer membranes against the commercially available cation exchange membrane (CEM) CMI-7000. It was found that Gel-Lay had the best performance, producing a maximum power output of 240±1 μW, 1.4 fold higher than that of CEM. Gel-Lay consists of rubber elastomeric polymers, polyvinyl acetate and the functional group polyamide. A 3D printed anode material in the shape of a rectangular mesh was also designed. However, it had a poor performance in comparison to a plain carbon veil. It was attributed to the low conductivity of the material.[193] 3D printed anodic chamber, cathodic chamber and the anode were also investigated in a separate study.[101] The MFC chamber was designed so that it could be opened with a unique non-assembly mechanism. The aluminium alloy anode was also structured as a 3D macroporous cellular lattice with low density, high specific surface area and surface roughness to promote bacterial proliferation. Moreover, a new technique, namely spray coating was used to deposit bacteria on the

anode in a uniform manner. A cation exchange membrane was used to isolate the anode from a carbon felt cathode in contact with ferricyanide. The maximum power density achieved was 816 mW m^{-2}. The system was able to recover a total energy of 3 kWh m^{-3} per day, which can be used to power sensors and low power appliances.[101] The performance of 3D printed copper anodes were compared to copper mesh anode, where the former showed 8.3 and 12.3-fold increase in OCP and power density, respectively. However, it underperformed in comparison to carbon cloth.[194] A BPV study used 3D printing to manufacture only the devices in order to have a compact and shareable design. More importantly, the hollow walls design facilitated temperature control via a circulating water bath.[141]

5.2 Proposed Proof of Concept Study and Research Aim

The research aim of this chapter is to further improve the performance of MEA-type BPV devices by evaluating graphene-coated and multi-walled carbon nanotubes-coated bioanodes, as part of a proof of concept study. The following objectives are set out to generate preliminary data.

1. Designing the configuration of the bioanodes through an optimisation process
    - Nitrocellulose membranes were coated with an ink of graphene nanoplatelets in carboxymethyl cellulose (GNP/CMC ink) by using two techniques, namely blade coating and screen-printing.
    - Five different thicknesses of 3D-printed bioanodes were produced. The bioanodes were made conductive by coating them with multi-walled carbon nanotubes (MWCNTs).
2. Surface characterisation was carried out to decipher the material surface chemistry using AFM.
3. SEM images and double potential step chronoamperometry were used to identify any electroactive features of the biofilm. Chronoamperometry was used to further analyse and interpret the electrochemical interactions between the cells of *S. elongtaus* and the anode materials.

4. The performance of the MEA-type BPV devices was summarised by four parameters: OCP, activation loss, internal resistance and maximum power output.

5.3 Materials and Methods

5.3.1 GNP/CMC Ink-coated Bioanodes

The microfluidised graphene nanoplatelets in carboxymethyl cellulose (GNP-CMC ink) as described in Section 3.3.2, was used to directly coat the non-ion exchange separator (Amersham™ Protran® nitrocellulose membrane of 0.2 µm pore size), which isolates the cathode.

Initial studies included varying the volume of the cross-linking agent, 1,4-Butanediol diglycidyl ether at a ratio of 10 ml ink: x µl (x=20, 30, 40) to give different levels of cross-linking, as illustrated in Figure 5-1. The higher the concentration of the cross-linker, the smaller are the pores and the lesser the swelling of the ink. One coating of GNP-CMC ink was deposited on the nitrocellulose membranes by the method of blade coating using a K Lox Proofer (RK PrintCoat Instruments Ltd, UK).

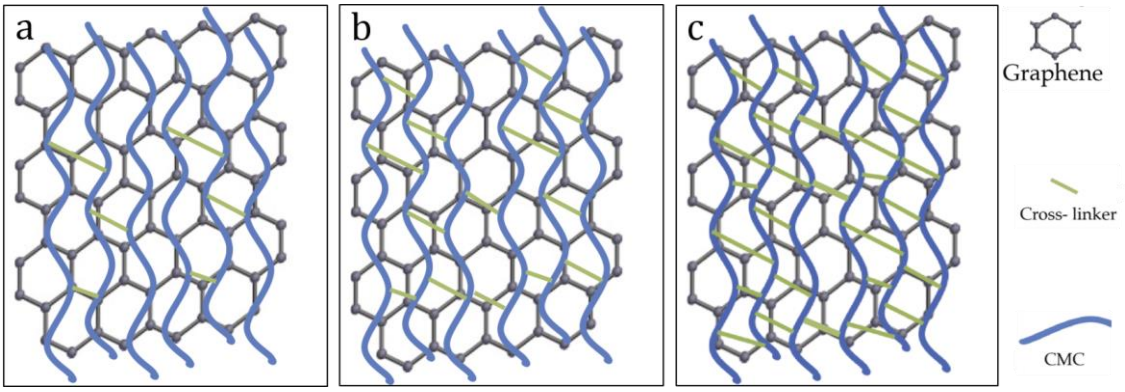

Figure 5-1: A schematic illustration of the GNP-CMC ink at different cross-linker volume of (a) 20 µl (b) 30 µl and (c) 40 µl.

As part of an optimisation process, the GNP-CMC ink was, then, screen-printed directly onto the nitrocellulose membranes using the optimal volume of cross-linker determined by the performance of the blade-coated membranes. Two patterns were screen-printed using a Kippax KPX2012 Semi-Automatic screen-printer. They are distinguished as a smooth pattern (3 passes) and a rough pattern (3 passes+ 2 passes for the square pattern), as depicted in Figure 5-2.

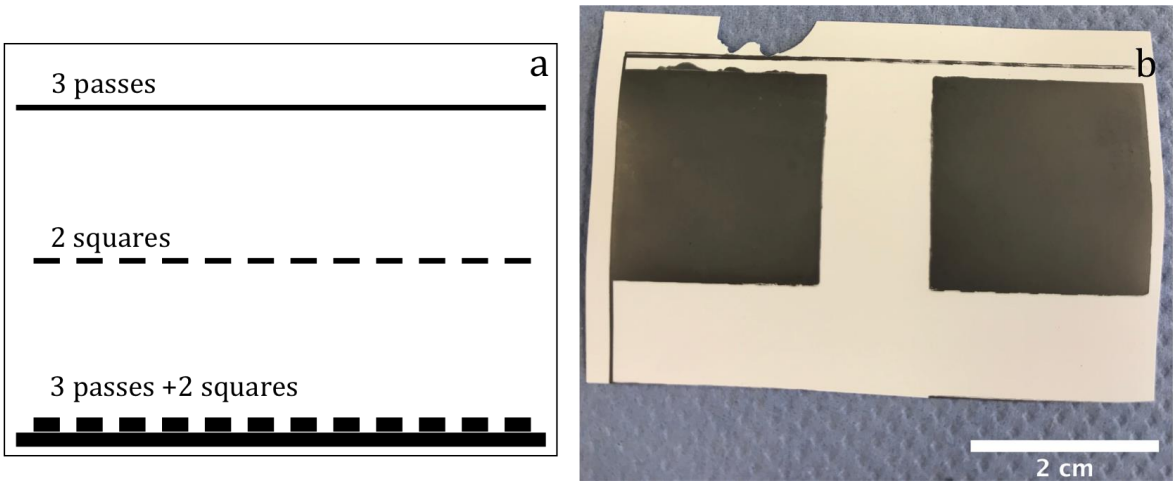

Figure 5-2: Schematic diagram of the screen printed designs (a) 3 passes (smooth) and 3 passes+2 squares (rough) and (b) 3 passes of GNP-CMC ink screen-printed on nitrocellulose membrane.

5.3.2 MWCNTs-coated 3D-printed Bioanodes

The anodes were designed as a flat disc of 22 mm diameter with five different thicknesses, namely 0.2 mm, 0.4 mm, 0.6 mm, 0.8 mm and 1.0 mm by using Autodesk Inventor Professional 2018. The designed models were 3D-printed using DurusWhite-RGD430 commercial ink (Stratasys, USA) and a soluble support material SUP706 (Stratasys, USA). The samples were printed with OBJET30 (Stratasys, USA) commercial printer in a glossy mode. Since the printing material is not porous, a concentric pattern of holes of 1 mm diameter was added to the design. After printing, the support material was removed by immersing the printed objects in a base solution of 2% sodium hydroxide (NaOH) and 1% sodium metasilicate (Na_2SiO_3) solution heated to 40^0C, followed by thorough cleaning and washing with soap and water.

Aqueous dispersion of multi-walled carbon nanotubes (MWCNTs) was prepared by mixing 1 wt% of MWCNTs, NC7000™, (Nanocyl S.A, Belgium), 2 wt% of polymeric dispersant SOLSPERSE®46000 (Lubrizol, USA) and 0.1 wt% of a wetting agent (Byk 348; Byk-Chemie GmbH, Germany) with deionised water. The MWCNTs were dispersed using a horn sonicator (Vibra-Cell, Sonics & Materials Inc., USA) for 30 min at 637.5 W to form a stable and uniform ink (the samples were cooled in an ice water bath during the sonication process). The 3D-printed anodes were then coated by a simple dipping and drying method. The samples were dipped in the CNT dispersion so that the entire sample was coated. After dipping, the sample was placed in a 500°C heated oven in order to dry the wet layer. The process was repeated three more times

to achieve a total of four layers of MWCNTs.[195] Figure 5-3 illustrates the designed 3D-printed anode.

The 3D-printing and MWCNTs coating were carried out at The Casali Centre of Applied Chemistry, Institute of Chemistry and the Centre for Nanoscience and Nanotechnology at the Hebrew University of Jerusalem, as part of a collaboration.

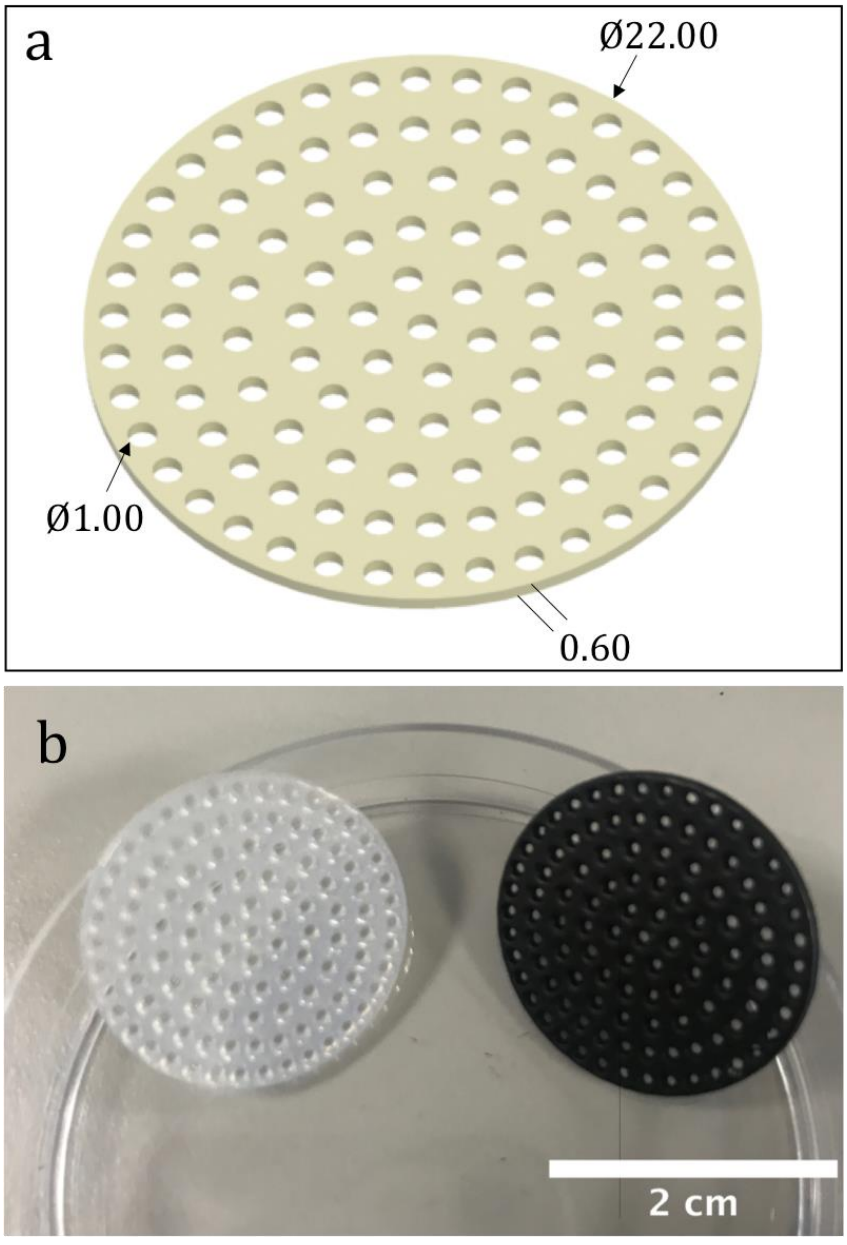

Figure 5-3: Illustration of 0.60 mm thick anode (a) schematic diagram with dimensions in mm and (b) uncoated and MWCNTs-coated anodes.

5.3.3 MEA-type BPV Device

The MEA-type BPV device, as described in Chapter 4, was used to analyse the performance of the new bioanodes. After assembly, the devices were autoclaved, following which 5 ml of culture at an initial biomass concentration of 0.63 g L^{-1} was inoculated. The top of the chamber was covered with a PET disc which was sealed with an adhesive film. The PET disc had a central hole of 4 mm diameter, which was covered with nitrocellulose membrane (0.2 µm pore size) to allow sterile exchange of gas. The BPV devices were, then, placed in an incubator at 30±1°C under four cool white fluorescent light tubes with an intensity of 37±1 µmol photons m^{-2} s^{-1} under a 12:12 hours light-dark cycle. The cells were allowed to settle for 5 days so as to form a natural biofilm, before measurements were carried out.

5.4 Results and Discussion

5.4.1 Optimisation of Graphene Deposition

This research work builds up on the studies in the previous chapters, which evaluated the performance of graphene-based bioanodes in BPV platforms. In order to further improve the performance of the MEA-type BPV device, the thickness of the bioanode was significantly reduced to minimise ohmic losses. Hence, the anode was directly coated on the nitrocellulose membrane separator.

5.4.1.1 Blade Coated GNP-CMC Ink Bioanodes

Blade coating produced a graphene film of up to a thickness of 30 µm per coating, with a two-point resistance of about 100 Ω.

The performance of the blade-coated bioanodes cross-linked at different cross-linker volume was analysed in MEA-type BPV devices to verify the stability of the ink in relation to the membrane and the cell culture of *S. elongatus*, as shown in Figure 5-4.

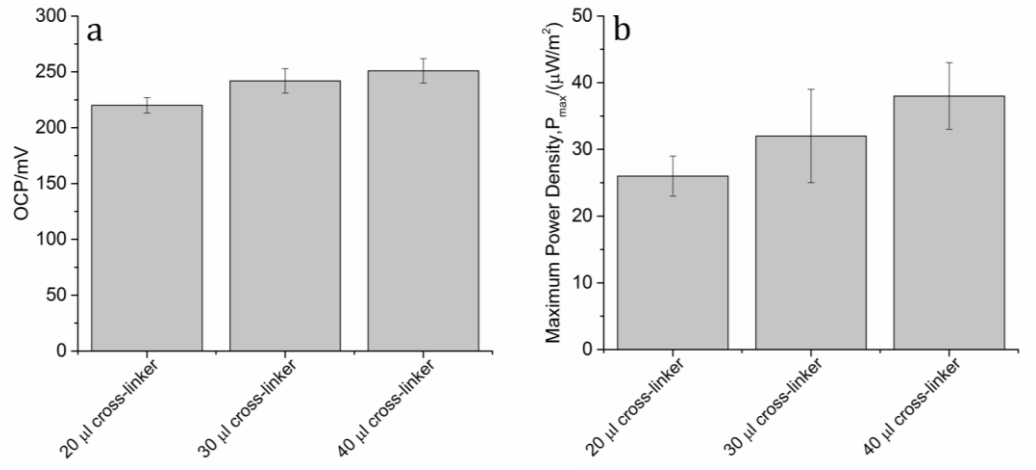

Figure 5-4: Data extracted from polarisation and power curves to evaluate the impact of varying the cross-linker volume on (a) OCP and (b) geometric maximum power output [the mean ± se is shown for each data set (n=3)].

Varying the volume of the cross-linker showed no significant difference in the performance of the BPV devices, suggesting that GNP-CMC ink was stable. The OCP values had an increasing trend with values of 220±7 mV, 242±11 mV and 251±11 for 20 µl, 30 µl and 40 µl of cross-linking agent, respectively. The different devices had similar internal resistance, averaging 2.5±0.3 MΩ and the maximum power densities were of similar order at 26±3 µW m^{-2}, 32±7 µW m^{-2} and 38±5 µW m^{-2} for 20 µl, 30 µl and 40 µl of cross-linking agent, respectively. The performance of the BPV devices did not improve in comparison to the different thicknesses of graphene paper, with a considerably higher internal resistance and lower maximum power density. The probable reason would be the high resistivity of the graphene nanoplatelets in comparison to the graphene paper.

5.4.1.2 Screen-printed GNP-CMC Ink Bioanodes

In an attempt to resolve the resistivity issues of the graphene nanoplatelets, the screen-printing technique was used, where 1 pass produced a film thickness of about 1 µm. Moreover, screen-printing allows the patterning of intricate designs down to75 µm resolution unlike blade coating which gives just continuous films.

Based on the above evaluation, a volume of 40 µl cross-linking agent was used to fix the CMC ink. The '3 passes' design had a two-point resistance of about 88 Ω while the '3 passes+2 squares' had a two-point resistance of about 42 Ω. The latter structure was

specifically designed so as to increase the surface roughness to provide more anchor points for cells to attach to.

5.4.1.2.1 Surface Characterisation

The functionalisation of the nitrocellulose membrane was studied using optical microscopy to better observe the printed pattern. Moreover, AFM was used to characterise the surface of the bioanodes in terms of average surface roughness and increase in surface area. Eventually, the effect of surface roughness on biofilm formation was qualitatively assessed using SEM images.

5.4.1.2.1.1 Microscopic Images of Screen-printed Bioanodes

The two screen-printed designs were observed under an optical microscope and the structure of the graphene was observed using SEM, as illustrated in Figure 5-5.

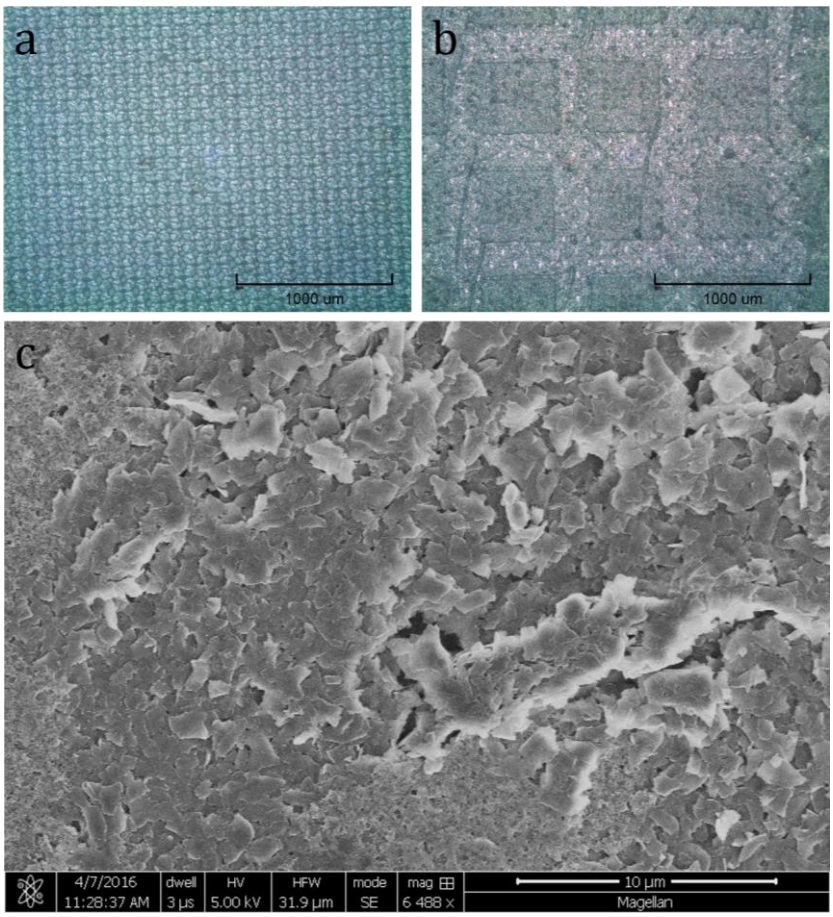

Figure 5-5: Microscopic images of screen-printed bioanodes (a) 3 passes (b) 3 passes+2 squares and (c) SEM image of screen-printed graphene nanoplatelets

5.4.1.2.1.2 Atomic Force Microscopy

The surface morphologies of the two screen-printed bioanodes were characterised by AFM, as illustrated in Figure 5-6. Both designs displayed a mix of peaks and valleys, suggesting a rough surface. The maximum height of the peaks averaged around 1 µm.

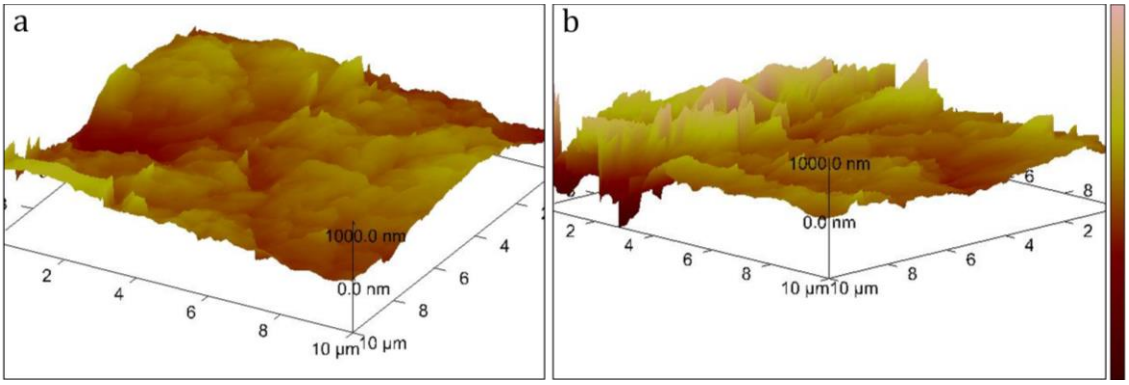

Figure 5-6: AFM 3D topographic scans of 100 µm^2 for (a) 3 passes bioanodes and (b) 3 passes+2 squares bioanodes.

The analysis of the AFM images produced parameters of average surface roughness and increase in surface area. The addition of the square pattern, expectedly, increased both the average surface roughness and the surface area of the material, as detailed in Table 5-1.

Table 5-1: Average surface roughness and increase in surface areas of the bioanode materials generated by AFM surface scans of 100 µm^2 [the mean ± se is shown for each data set (n=2)].

Bioanode Material	Average Surface Roughness, S_a/nm	% Increase in Surface Area
3 passes	107±5	22±3
3 passes+2 squares	145±4	127±15

5.4.1.2.1.3 Biofilm Coverage

3 passes bioanode had a slightly better biofilm coverage as compared to the 3 passes+2 squares bioanodes, even though the latter had a rougher surface. The increase in surface roughness did not promote cell growth and seems to reflect the influence of submicron surface roughness, which may or may not promote bioadhesion.[85] The results indicate that a trade-off exists between biofilm formation and surface roughness.

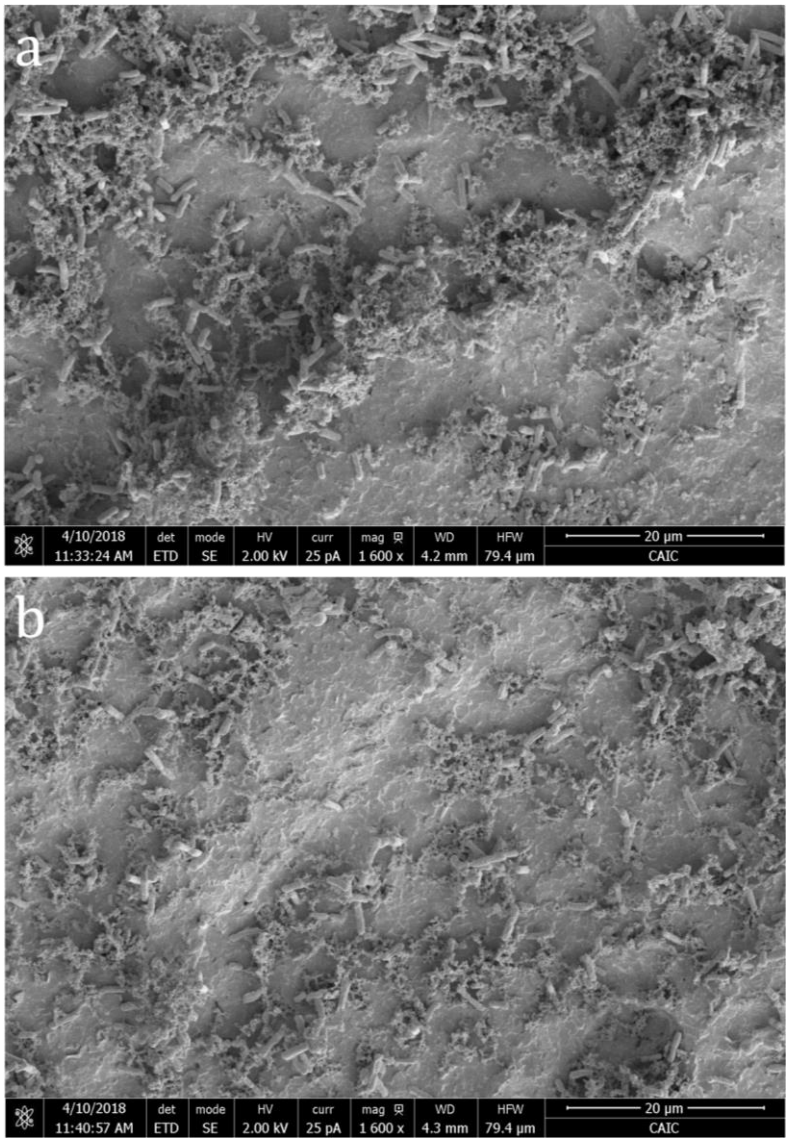

Figure 5-7: Biofilm coverage of *S. elongatus* on (a) 3 passes bioanode and (b) 3 passes+2 squares bioanode.

5.4.1.2.2 Exoelectrogenic Activity

The mechanism of *S. elongatus* to export electrons in an extracellular manner was first determined by SEM images of biofilm and using the electrochemical method of double potential step chronoamperometry. These electrons were, then, harvested in BPV devices for bioelectricity generation.

5.4.1.2.2.1 Features of Biofilm

Figure 5-8 illustrates some exoelectrogenic features of *S. elongatus* on the surface of the two types of bioanodes. Extracellular matrix containing pili or putative nanowires surrounded the cells and helped in potentially relaying electrons from the cells to the anode and from cells to cells.

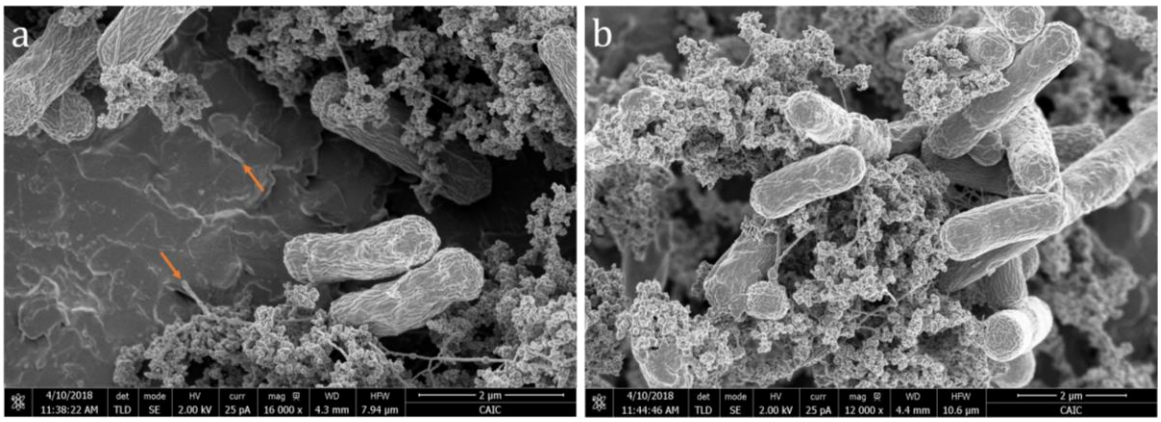

Figure 5-8: SEM images of biofilm of *S. elongtaus* on the surface of the two types of bioanodes (a) 3 passes bioanode illustrating pili attaching to the surface and (b) cell to cell communication via the extracellular matrix, containing pili structures on 3 passes+2 squares bioanode.

5.4.1.2.2.2 Double Potential Step Chronoamperometry

The double potential step chronoamperometry was employed to analyse the electrochemical interactions between the biofilm of *S. elongatus* and the two screen-printed bioanodes.

The biofilms were consecutively oxidised and reduced in 5 cycles and the repeated patterns demonstrated the reproducibility, robustness and reversibility of the reactions as depicted in Figure 5-9.

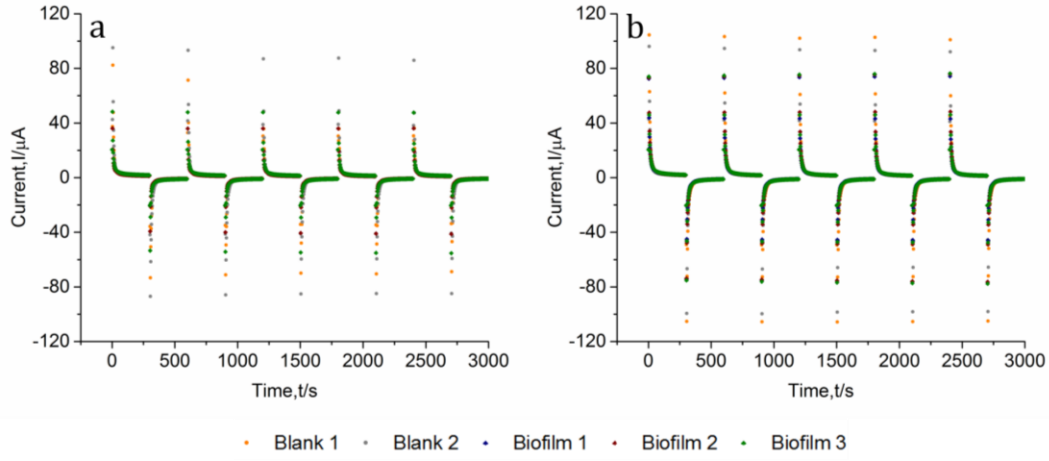

Figure 5-9: Chronoamperomograms showing sets of 5 cycles obtained at E_1=0.35 V and E_2=0 V for 300 s at each applied potential for (a) 3 passes bioanode and (b) 3 passes+2 squares bioanode.

The peak current and the limiting current generated were analysed to distinguish between the performances as shown in Table 5-2.

The peak current of the blank was higher than the peak current of the biofilm. However, the limiting current of the biofilm was higher than the blank. Amongst the biofilm, the 3 passes+ 2 squares bioanode was better performing, but not significantly enough.

Table 5-2: Data extracted from the chronoamperograms for the two screen-printed bioanodes in terms of peak current and limiting current [the mean ± se is shown for each data set (n=2 for 3 passes and n=3 for 3 passes+2 squares)].

Screen-printed Bioanode / µm	**Peak Current/µA**		**Limiting Current/µA**	
	Blank	**Biofilm**	**Blank**	**Biofilm**
3 passes	71±19	42±6	1.23±0.07	1.34±0.37
3 passes+2 squares	98±2	75.3±0.4	1.35±0.04	1.68±0.09

Since the blank of the peak current interfered with the performance of the biofilm, double potential step chronocoulometry was used to offer clearer analysis, as illustrated in Figure 5-10. The blanks have higher charging capacity in the initial cycles, which may be due to conditioning. However, they become lower as time progresses. The blanks have a decreasing trend while the biofilms have an increasing trend, as expected. Moreover, the charge produced by the biofilm on 3 passes+2 squares bioanodes is of higher magnitude than the 3 passes bioanodes. This, further, confirms that the 3 passes+2 squares is a better bioanode.

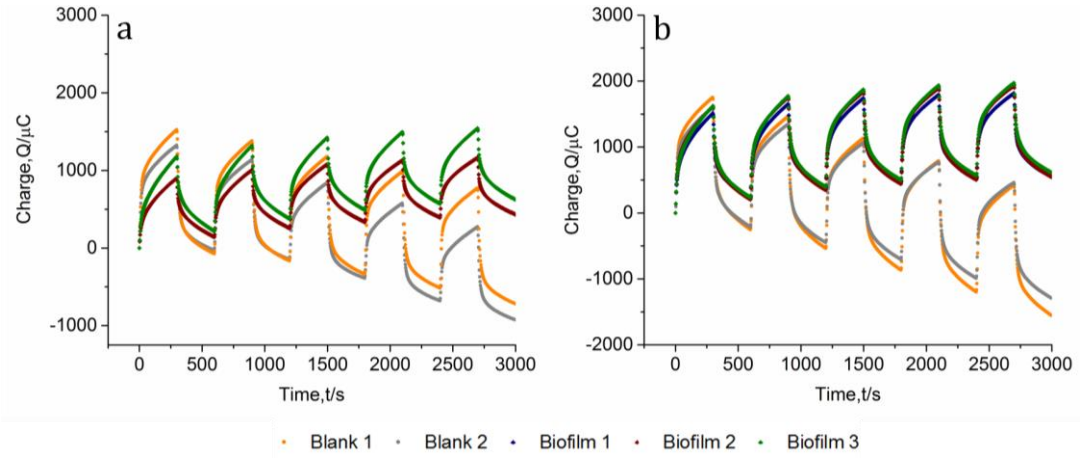

Figure 5-10: Corresponding chronocoulomograms of Figure 5-9 for bioanodes (a) 3 passes and (b) 3 passes+2 squares.

5.4.1.2.2.3 Performance Analysis of BPV Devices

The performance of the two screen-printed bioanodes was analysed in the MEA-type BPV devices. As depicted in Figure 5-11, the OCP values of the two bioanodes are similar with values of 227±4 mV and 230±3 mV for 3 passes and 3 passes+2 squares, respectively. Moreover, 3 passes and 3 passes+2 squares bioanodes suffered from similar activation losses of 20 mV and 19 mV, respectively.

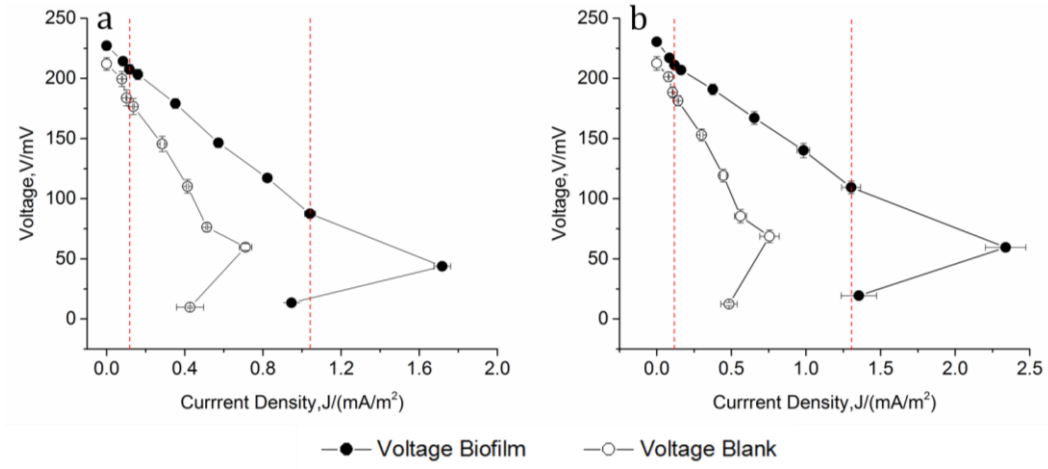

Figure 5-11: Polarisation curves of the screen-printed bioanodes (a) 3 passes and (b) 3 passes+2 squares [the mean ± se is shown for each data set (n=6)]. The lines shown are purely used to guide the eye. The additional red dash lines separate the different regions of electrochemical losses for the biofilm only.

As shown in Figure 5-12 (a), both devices have similar internal resistances, averaging 333 kΩ, which is significantly lower than devices containing 50 μm, 75 μm and 120 μm thick graphene paper. Since there was an increase in surface area of the bioanodes, the

maximum power densities obtained from the power curves were corrected to reflect the actual internal surface area, as illustrated in Figure 5-12 (b). The power densities decreased from 97±4 μW m^{-2} to 80±10 μWm^{-2} for 3 passes bioanode and from 144±10 μW m^{-2} to 64±10 μW m^{-2} for 3 passes+2 squares bioanode. There was a significant decrease in power density for the latter, with no major difference in comparison to the 3 passes bioanodes.

By correlating the surface properties of the bioanodes to their performance in the BPV devices, the general trend indicates that with an increase in average surface roughness and surface area, the maximum power density decreases. The type of surface roughness obtained is characterised as submicron surface roughness, which is said to have dual effects on cell growth and adhesion.[85] This study is a prime example showing that an increase in surface roughness is not beneficial for the performance of the bioanode.

a

Screen-printed Bioanode	Internal Resistance/kΩ
3 passes	332±13
3 passes+2 squares	334±23

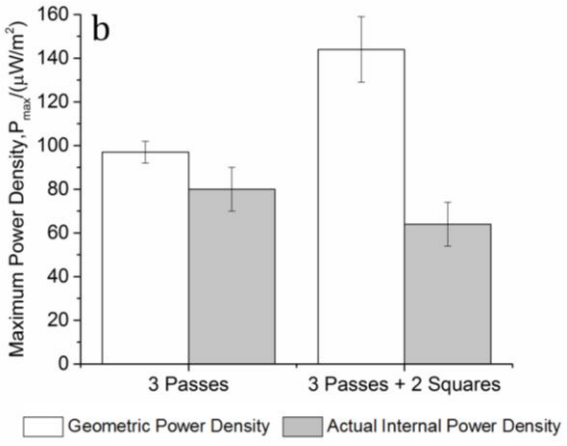

Figure 5-12: Data extracted from polarisation and power curves to compare the performance of the two screen-printed bioanodes with regards to (a) internal resistance and (b) maximum power output [the mean ± se is shown for each data set (n=6)].

Based on geometric power density, BPV device with screen-printed 3 passes+2 squares bioanode had a 7.5-fold decrease in internal resistance and a 3.8-fold increase in maximum power density in comparison to blade-coated bioanode (40 μl cross-linker). Changing the technique of coating the nitrocellulose membranes significantly impacted their performances. The thinner film thickness reduced the resistivity of the bioanodes as confirmed by the 2-point resistance measurement. The resistivity of the bioanodes highly influenced the ohmic losses of the devices.

5.4.2 MWCNTs-coated 3D-printed Bioanodes

Since the performance of the screen-printed bioanodes did not improve with respect to 240 µm thick graphene paper, a 3D structure of the bioanode was designed for performance analysis. Moreover, the 3D-printed bioanodes are a first step towards the fabrication of a monolithic BPV platform. In an initial stage, the performance of five different thicknesses of the bioanodes was evaluated in the current design of the MEA-type BPV device.

5.4.2.1 Surface Characterisation

The structure of the MWCNTs-coated 3D-printed bioanodes was first characterised using AFM. All thicknesses of the bioanodes had a mean average surface roughness of 217±16 nm and an average increase in surface area of 70±14%. Since all the plots were similar, Figure 5-13 depicts a typical AFM scan whereby a 0.8 mm thick bioanode is used as an example.

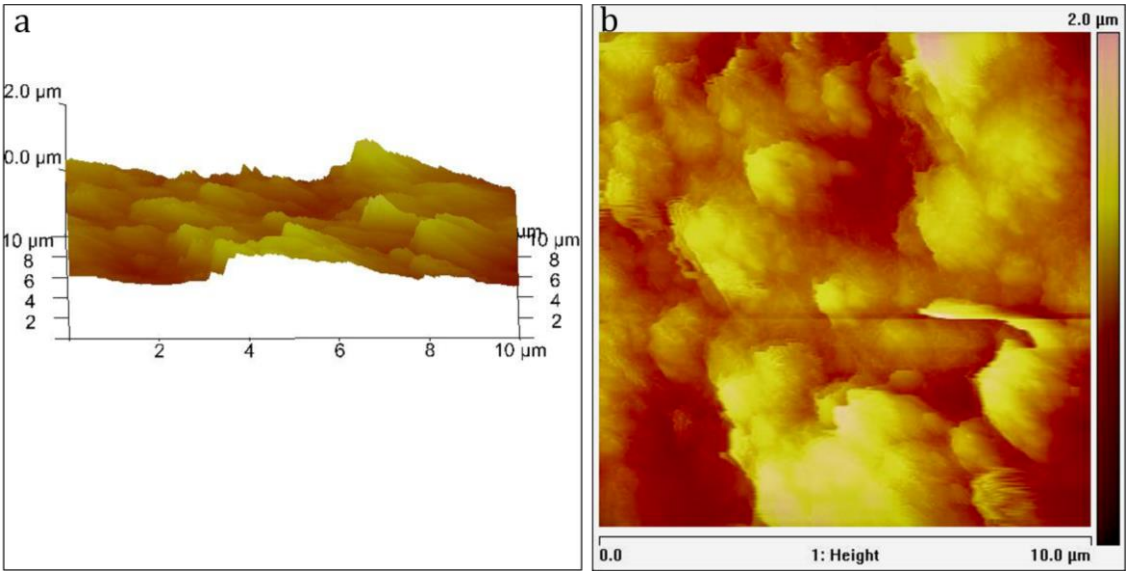

Figure 5-13: Example of an AFM topographic scan of 100 µm^2 for 0.8 mm MWCNTs-coated 3D-printed bioanode (a) 3D plot and (b) top view of plot.

5.4.2.2 Exoelectrogenic Activity

SEM images were first analysed to detect any features that may participate in the extracellular electron transport. Double potential step chronoamperometry was, then, employed to assess the electroactivity of the biofilm. The exocellular electrons were, eventually, captured in BPV devices for bioelectricity generation.

5.4.2.2.1 Features of Biofilm

The biofilm generated on all the surfaces of the MWCNTs-coated 3D-printed bioanodes was analysed by SEM imaging technique and Figure 5-14 illustrates a rich fibrous extracellular matrix. The same dense biofilms can be seen on the surfaces of the different thicknesses of the anodes. Pilus-like appendages are seen to connect cells to cells as well as connect cells to the surface of the anode. Such a biofilm has not been observed with the other bioanodes previously studied (ITO-coated substrates, carbon fibres, graphene paper and screen-printed GNP-CMC-coated membrane). As mentioned in the earlier chapters, these pili or putative nanowires may play a role in external electron transfer from the cells to the anode material.

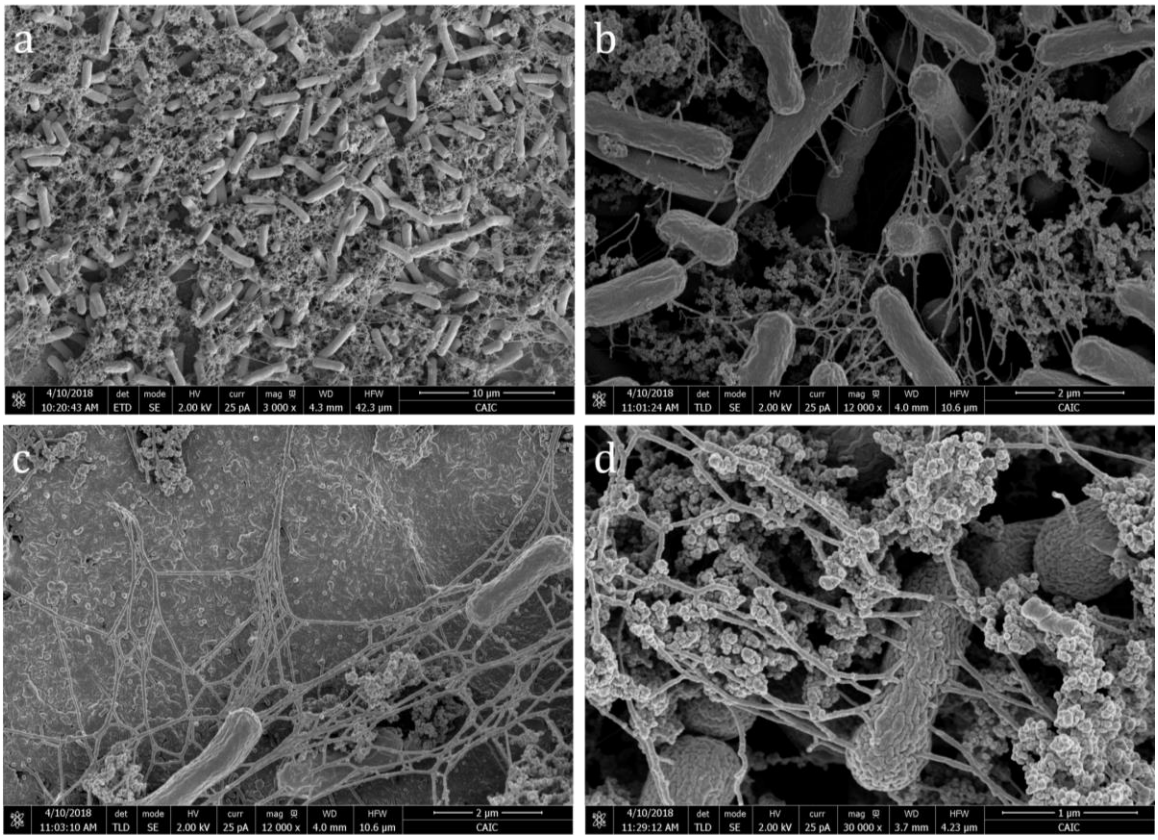

Figure 5-14: SEM images of the biofilm of *S. elongatus* on the surface of the MWCNTs-coated anodes illustrating (a) a fibrous extracellular matrix (b) pili structures in cell to cell communication (c) putative nanowires or pili attaching to the surface and (d) pilus-like appendages extending from a cell to the environment.

5.4.2.2.2 Double Potential Step Chronoamperometry

The electrochemical activity of the biofilm on the different thicknesses of the MWCNTs-coated 3D-printed anodes was analysed, as illustrated in Figure 5-15. Both the peak

and limiting current of the blanks were higher than that of the biofilms, except for the limiting current of 0.40 mm thick bioanode. Therefore, further investigations are needed to establish the potential effect generated by the biofilm. Double potential step chronocoulometry was used to make the distinction between the blank and the biofilm as shown in Figure 5-16.

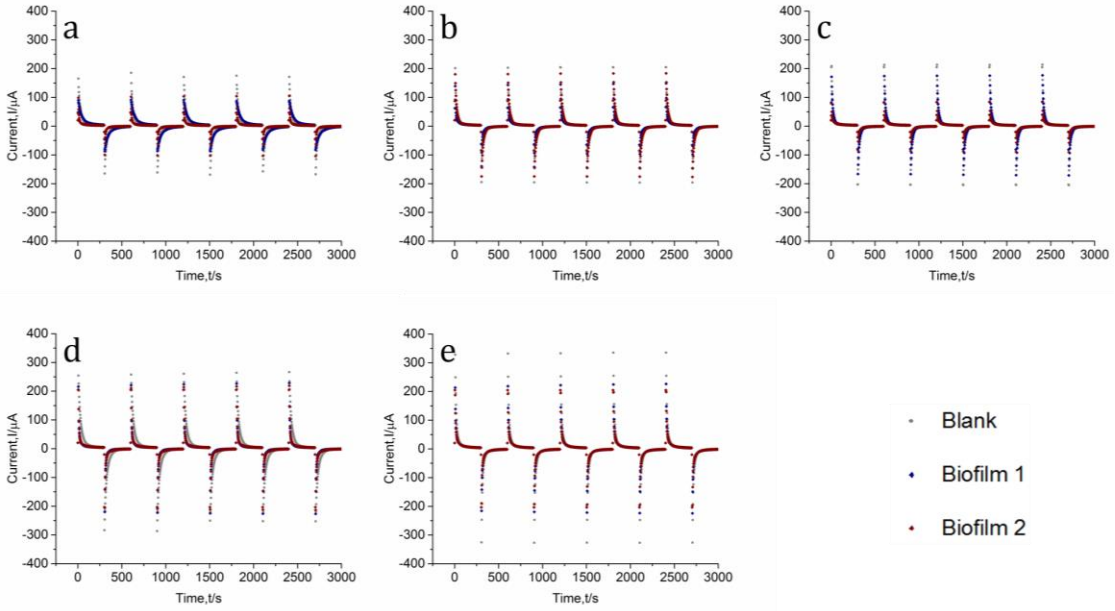

Figure 5-15: Chronoamperomograms depicting sets of 5 cycles obtained at E_1=0.35 V and E_2=0 V for 300 s at each applied potential for MWCNTs-coated 3D-printed bioanodes of thicknesses (a) 0.20 mm (b) 0.40 mm (c) 0.60 mm (d) 0.80 mm and (e) 1.0 mm.

The chronocoulomograms are in agreement with the chronoamperometric results. All the charges produced by the blanks were higher than the biofilms, except for one biofilm on 0.40 mm thick anode. One possible reason for the low electrochemical activity of the biofilms could be that the holes of the anode materials were clogged by cells of *S. elongatus*, resulting in the significant reduction of the electrochemical reaction surface. Therefore, a much decreased electrocatalytic activity of the electrode microbial reactions could be observed.

The explanation can, further, be validated by SEM images in Figure 5-17 that show that the holes in the anode material were completely covered with cells of *S. elongatus*.

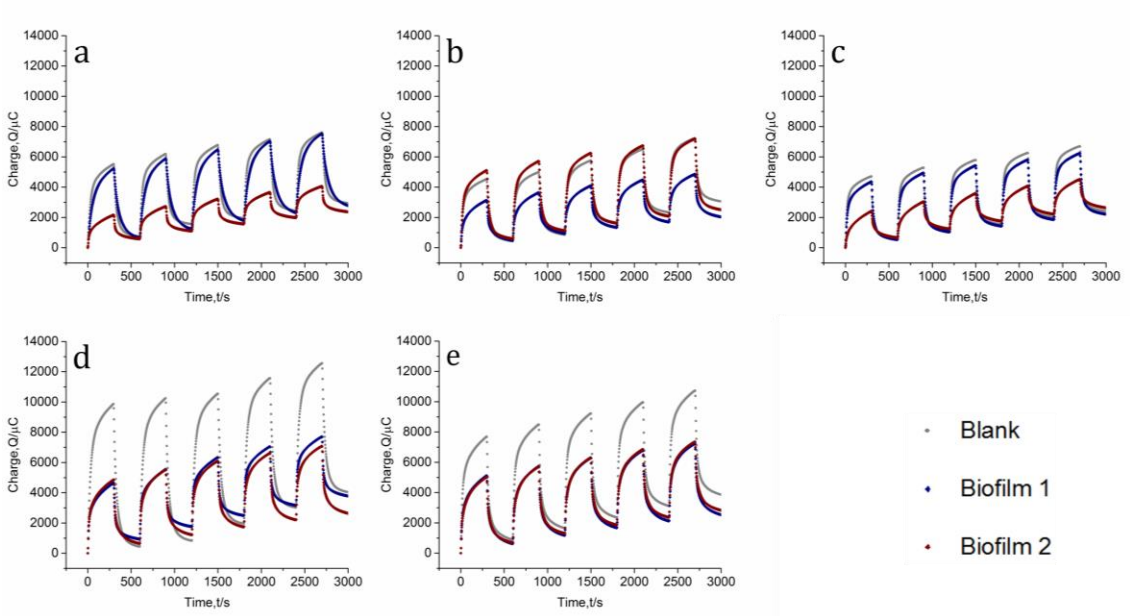

Figure 5-16: Corresponding chronocoulomograms of Figure 5-15 for MWCNTs-coated 3D-printed bioanodes of thicknesses (a) 0.20 mm and (b) 0.40 mm (c) 0.60 mm (d) 0.80 mm and (e) 1.0 mm.

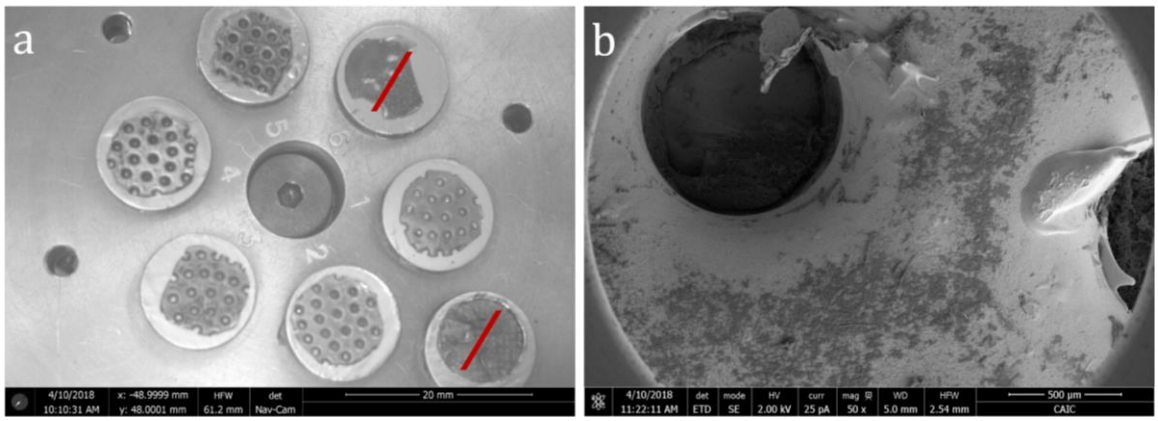

Figure 5-17: SEM images of (a) the different thicknesses of MWCNTs-coated 3D-printed bioanodes seen with the patterned holes (1-5) and (b) the holes mostly covered with the biofilm of *S. elongatus*.

5.4.2.2.3 Performance Analysis of BPV Devices

The OCP values of the different thicknesses of the MWCNTs-coated 3D-printed bioanodes are obtained from Figure 5-18. The experiments were carried out in triplicates but some of the devices were not functional due to short-circuiting or evaporation. There is a general increasing trend in the OCP values with the thickness of the bioanode. 0.2 mm and 0.4 mm thick bioanodes had OCP values of 291±9 mV and 286±19 mV, respectively. 0.60 mm, 0.80 mm and 1.00 mm thick bioanodes clustered

around 311±1 mV, 328±6 mV and 336 mV, respectively. There was no significant variation in the OCP values, suggesting similar interaction between the anode and the biofilm. The activation losses followed a decreasing trend with the increase in the thickness of the bioanode. 0.20 mm, 0.40 mm, 0.60 mm, 0.80 mm and 1.00 mm thick bioanodes suffered activation polarisation of 67 mv, 49 mV, 41 mV, 34 mV and 32 mV, respectively. So far, 1.00 mm thick bioanode seems to be better performing.

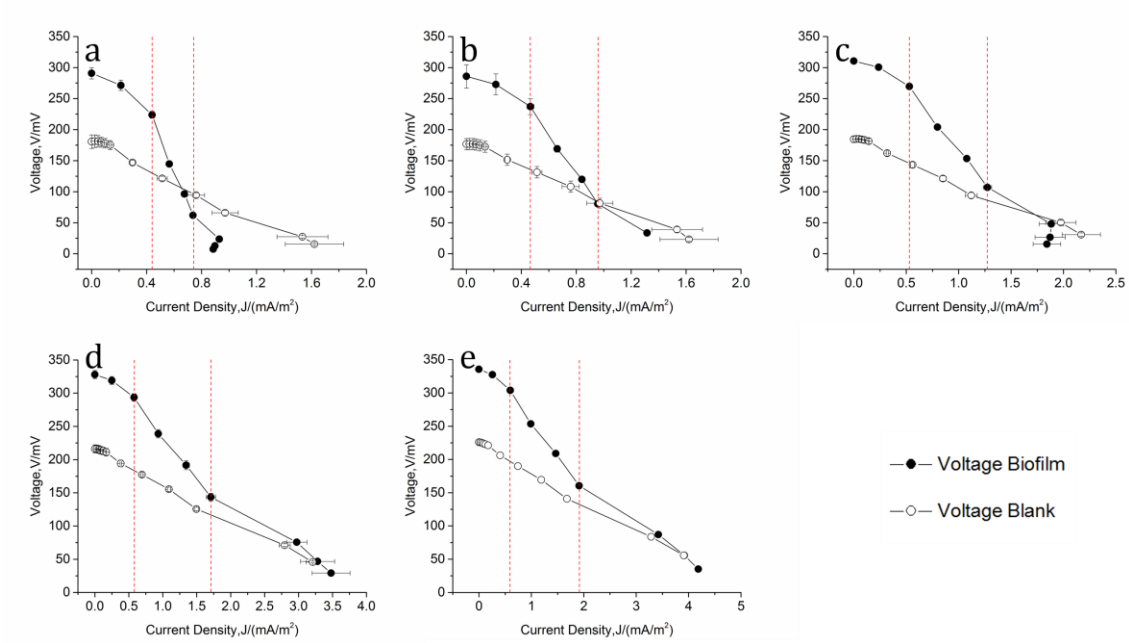

Figure 5-18: Polarisation curves of the different thicknesses of MWCNTs-coated 3D-printed bioanodes (a) 0.20 mm (b) 0.40 mm (c) 0.60 mm and (d) 0.80 mm and (e) 1.00 mm [the mean ± se is shown for each data set (n=3 for 0.20 mm and 0.40 mm; n=2 for 0.60 mm and 0.80 mm; n=1 for 1.00 mm)]. The lines shown are purely used to guide the eye. The additional red dash lines separate the different regions of electrochemical losses for the biofilm only.

The internal resistance of the devices followed the same trend as activation losses. There was significant improvement in ohmic losses, as the thickness of the biaonode increased, decreasing from 2.1±0.1 MΩ to 217 kΩ. However, as observed in Figure 5-19 (a), the blanks have lower internal resistance than the biofilms, except for 0.20 mm thick anode. The results indicate that the biofilms imposed a larger resistivity, which can be attributed to the holes being clogged, as described in Section 5.4.2.2.2. Thus, a resistance to the movement of the electrolyte was created, which contributed to the high internal resistance of the devices.

a

Thickness of Bioanode/mm	Internal Resistance/kΩ	
	Blank	Biofilm
0.20	4233±379	2100±75
0.40	403±47	1234±54
0.60	256±25	841±21
0.80	202±10	514±26
1.00	166	217

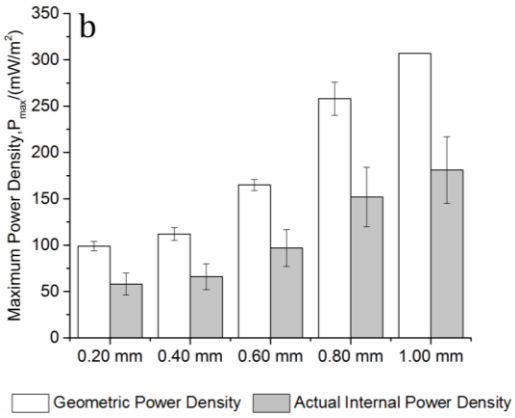

Figure 5-19: Data extracted from polarisation and power curves to compare the performance of the different thicknesses of MWCNTs-coated 3D-printed bioanodes with regards to (a) internal resistance and (b) maximum power output [the mean ± se is shown for each data set (n=3 for 0.20 mm and 0.40 mm; n=2 for 0.60 mm and 0.80 mm; n=1 for 1.00 mm)].

The power densities are represented as a function of their actual internal surface areas, as shown in Figure 5-19 (b). Overall, there is a general trend which correlates the increase in actual maximum power density to the increase in the thickness of the bioanode. There was a significant improvement as 0.20 mm thick bioanode produced an actual maximum power density of 58±12 μW m^{-2} while 1.00 mm thick bioanode generated an actual maximum power density of 181±36 μW m^{-2}. An explanation for the increase in actual maximum power density with the thickness of the bioanode is due to the fact that as the holes become deeper, the cells have more space to inhabit and a large contact area is provided.

Based on OCP values, activation and ohmic losses and maximum power output, 1.00 mm thick bioanode is better performing. However, chronoamperometric and chronocoulometric studies have shown that the holes get clogged with the cells, reducing the effective electrochemical surface area. Therefore, the design of the bioanode should be optimised so as to eliminate this effect.

5.5 Conclusions

This chapter investigated the performance of nano-based carbon materials, as a follow-up from the previous chapters. It is worth highlighting that the bioanodes developed in this study are at the initial phase of research and development and further studies are needed to improve their performances in BPV systems. However, they do provide enough preliminary data to be considered as an initial working prototype.

In order to significantly reduce the thickness of the bioanodes for minimum resistance, GNP-CMC ink was coated directly onto the membrane separator. By switching the technique of depositing GNP-CMC ink from blade coating to screen-printing, there was a significant improvement in the performance of the BPV device. Two patterns were screen-printed to create the effect of a smooth (3 passes) and a rough surface (3 passes+2 squares). Chronoamperometric and chronocoulometric studies indicated that 3 passes+2 squares bioanodes might produce better performance. Moroever, chronocoulometric analysis helped to clearly distinguish between the blank and the biofilm. Based on actual internal surface area, 3 passes bioanodes produced a higher maximum power density of 80±10 μW m^{-2}. A correlation between surface properties and actual maximum power density indicated that as average surface roughness and surface area increase, the actual maximum power density decreases. Based on geometric power density, BPV devices with screen-printed 3 passes+2 squares bioanodes had a 7.5-fold increase in internal resistance and a 3.8-fold increase in maximum power density as compared to blade-coated bioanodes. For future work, the correlation between the surface properties and maximum power density should be taken into account. A trade-off between these properties and the performance of the bioanodes in the BPV devices should be determined.

Since the performance of the screen-printed bioandes was still lower than that of 240 μm thick graphene paper, MWCNTs-coated 3D-structured bioanodes were designed with five different thicknesses. However, the blanks overpowered the biofilms in both chronoamperometric and chronocoulometric studies. SEM images of the biofilm on the bioanodes helped in explaining the electrochemical results. It was observed that the biofilm covered most of the holes in the anode materials, which may lead to clogging. Hence, the effective electrochemical surface area was reduced. Furthermore, the internal resistance of the BPV devices with blanks were higher, suggesting a

resistance to the movement of ions. However, amongst the five thicknesses, 1.00 mm thick bioanode had the lowest internal resistance of 217 kΩ with a high actual maximum power density of 181±36 μW m^{-2}. Nonetheless, these results need to be confirmed as only one device containing the 1.00 mm thick bioanode was operational. Based on the electrochemical results, the 3D-printed bioanodes have to be redesigned due to the clogging issue. The MWCNTs-coated 3D-printed discs present promising function as bioanodes as they induced a rich biofilm with fibrous extracellular matrix that has not been observed with the other bioanodes. The dimensions of the 3D-printed bioanodes should be redesigned to take into account the issue of clogging.

6 Improving the Performance of *R. palustris* for Enhanced Exoelectrogenic Activity

6.1 Introduction

The second strategy employed, besides improving the performance of the bioanode, is to improve the performance of the microorganism. In this study, *R. palustris* is used as a model organism. Common experiments involving *R. palustris* include optimising biohydrogen production by varying the nitrogen to carbon ratio. Therefore, the same approach would be used to assess whether the exoelectrogenic activity of *R. palustris* is improved. This chapter, thus, focuses on two important aspects of *R. palustris*; firstly its ability to generate biohydrogen by photofermentation and secondly its exoelectrogenic capacity. These two attributes are, then, captured in a novel platform, known as a hybrid hydrogen-photoMFC, to generate bioelectricity.

Nitrogenase mediated biohydrogen production relies on the transfer of electrons from organic electron donors to electron carriers. Hydrogen production by *R. palustris* has mostly been reported with substrates, such as acetic, lactic, butyric or malic acids. However, there are early reports of the ability of *R. palustris* to use glycerol as a carbon source.[61] As such, Sabourin-Provost and Hallenbeck have demonstrated that photofermentation of glycerol into hydrogen is possible with about 6 moles H_2 per mole glycerol obtained equivalent to 86% of the maximum stoichiometric conversion.[196] Pott et al.[197] compared the maximum growth rate of *R. palustris* on a wide variety of carbon sources, such as acetate, butyrate and lactate. It was found that *R. palustris* grew by metabolising all the substrates, with the highest maximum specific growth rate obtained with glycerol at a value of $0.07 \pm 0.01\ h^{-1}$. Moreover, glycerol is currently generated as a waste stream from biodiesel production. Its mass production makes it no longer feasible for sale. As a result, an attractive option would be to use it as a substrate in the photofermentative production of biohydrogen by *R. palustris*.[196–

[198] In the experiments carried out, pure glycerol was used as part of a fundamental study.

Since hydrogen production is catalysed by nitrogenase, it is crucial to have a medium that allows its biosynthesis. *R. palustris* can tolerate many sources of nitrogen but sodium glutamate is well-known to promote satisfactory nitrogenase synthesis and activity.[69,196,199]

6.1.1 Photofermentation Process in Photobioreactors

6.1.1.1 Product Formation Kinetics

Hydrogen is the main microbial product that is linked to the bacterial growth of *R. palustris*. Microbial products are usually classified into three major categories based on their relation with microbial growth. The first type is growth associated product, where the product is formed along with the growth of the microbial cells and the concentration of the product is almost directly proportional to microbial growth rate. The second category is non-growth associated product, where product formation is unrelated to growth rate of microbial cells but is rather a function of cell concentration. The third class is known as mixed mode product formation, where product formation is a combination of both microbial growth rate and microbial cell concentration. Many biochemical processes fall under this third category.[200–202] Figure 6-1 illustrates the three modes of product formation.

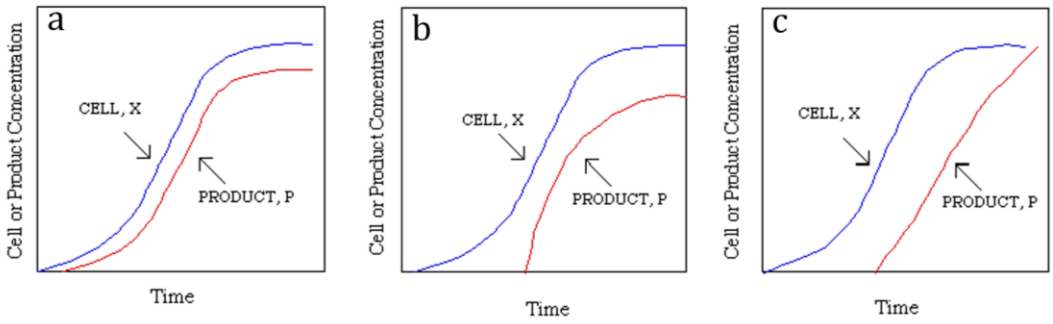

Figure 6-1: Product formation kinetics can be classified into three categories (a) growth associated product formation (b) non-growth associated product formation and (c) mixed mode product formation. X represents microbial cell concentration and P represents hydrogen concentration. Reproduced from Mutharasan.[202]

6.1.1.2 Hydrogen Yield

One of the important parameters used to assess the photofermentation process of biohydrogen is hydrogen yield. The latter is defined as a percentage of glycerol conversion to biohydrogen. The theoretical maximum hydrogen yield is expressed as the maximum amount of biohydrogen generated when the organic substrate is fully oxidised to carbon dioxide.[69] As shown in Equation 6-1 and Equation 6-2, the theoretical maximum conversion of glycerol is 7 moles of hydrogen generated per mole of glycerol consumed, if all glycerol is used for hydrogen production.

$$C_3H_8O_3 + 3H_2O \rightarrow 7H_2 + 3CO_2$$

Equation 6-1

$$Hydrogen\ yield = \frac{number\ of\ moles\ of\ H_2\ produced}{7\ \times\ number\ of\ moles\ of\ glycerol\ consumed}$$

Equation 6-2

6.1.1.3 Effects of Different Limiting Nitrogen Regimes

The biosynthesis of nitrogenase and the subsequent biohydrogen generation is mainly determined by the nitrogen to carbon ratio (N:C). The initial N:C ratio greatly modulates the performance of the bacterial cultures, in terms of growth rate, biohydrogen production and glycerol conversion efficiency.[196] Glycerol is the main carbon source for cell growth in the presence of sodium glutamate and is the main driving force for biohydrogen production and bacterial maintenance in the absence of glutamate. Selecting an appropriate N:C ratio is quite intricate. A high N:C ratio facilitates cell growth and increases biomass density. The high biomass density would lead to higher total biohydrogen production. However, when initial N:C ratio is high, electrons obtained from glycerol are diverted mainly towards biomass growth instead of biohydrogen generation. Therefore, a high N:C ratio decreases or limits the conversion efficiency of glycerol into average biohydrogen production.[203]

Cultures containing both a nitrogen and carbon source are termed to be in a growing state, where the CO_2-fixing Calvin cycle competes with nitrogenase for electrons. Thus, in this condition, the main process competing for electrons against biohydrogen production is biosynthesis. However, cultures that are nitrogen-deprived are known to be in a non-growing state, where the bacteria dissociate their metabolism from

biosynthesis and divert their metabolic flow to use electrons for the exclusive generation of biohydrogen.[69].

Various studies have been carried out on nitrogen-limited conditions for the photofermentation production of biohydrogen. Sabourin-Provost and Hallenbeck[196] analysed two sources of nitrogen, namely ammonium sulphate and sodium glutamate in the presence of 10 mM glycerol. The biomass density increased monotonically with the increase in concentrations of both nitrogen sources. It was found that gas production was severely reduced at a concentration of 4 mM ammonium sulphate. The biohydrogen yield, antagonistically to biomass concentration, increased with decreasing concentration of ammonium sulphate. 4.9 moles H_2/mole glycerol, 2.9 moles H_2/mole glycerol and 1.7 moles H_2/mole glycerol were obtained for concentrations of 0 mM, 2 mM and 4 mM ammonium sulphate, respectively. The concentration of sodium glutamate was studied at 0 mM, 2 mM, 4 mM and 6 mM and the optimum hydrogen yield of 6.2 moles H_2/mole glycerol was obtained at 2 mM of sodium glutamate, namely, 88.6% of the theoretical maximum conversion (7moles H_2/mole glycerol). 5.2 moles H_2/mole glycerol, 5.6 moles H_2/mole glycerol and 3.7 moles H_2/mole glycerol were obtained for concentrations of 0 mM, 4 mM and 6 mM sodium glutamate, respectively. The hydrogen yield of the growing conditions of 2 mM and 4 mM exceeded that of the non-growing condition.[196] It can, thus, be deduced that nitrogen depletion was counterproductive for biohydrogen generation. It is worth mentioning that *R. palustris* wild type strain CGA009 was used in the above experiments, which is defective in uptake hydrogenase.[66,69] Hydrogen utilisation is normally mediated by uptake hydrogenases, which catalyse the oxidation of hydrogen. Thus, it is expected that more hydrogen would be generated in its absence.

Zhang et al.[203] constructed dynamic models to simulate the effects of initial N:C ratio on hydrogen yield and glycerol conversion efficiency. For an initial biomass concentration of 0.1 g L^{-1}, an optimal initial N:C ratio for hydrogen production was found to be 0.27 with a glycerol conversion efficiency estimated to be at 3.30 moles H_2/mole glycerol, corresponding to 47.1% of the theoretical maximum conversion. The simulated optimum N:C ratio was close to the experimental result of 0.20 reported by Sabourin-Provost and Hallenbeck[196] but the glycerol conversion efficiency was lower. However, when the initial biomass concentration was increased to 0.8 g L^{-1}, the computational value of glycerol conversion efficiency increased to 64.4%, much closer

to the experimental value obtained by Sabourin-Provost and Hallenbeck.[196] If the initial biomass density is low, an important fraction of glycerol is needed for bacterial growth instead of hydrogen production, contrary to the case of high initial biomass concentration. It can be deduced that the conversion efficiency of glycerol increases with increasing initial biomass concentration.[203] For cultures containing 10 mM glycerol and 5 mM sodium glutamate, Pott et al.[197] achieved 80-85% of the stoichiometric maximum conversion of glycerol, with some cultures even reaching values as high as 90%. In another study, Pott et al.[198] compared the maximum specific hydrogen production achieved with glycerol to other sources of carbon. The maximum specific hydrogen production was explained as being the slope of the linear part of a plot of hydrogen production (ml g biomass^{-1}) against time. The data points in the linear region lay between the time ranges of 150-250 h for a hydrogen production range of 1-4 ml g biomass^{-1}. However the reported values of the maximum specific hydrogen production were of the order of 30 ml g biomass^{-1} h^{-1} when mathematically they should have been of the order 0.03 ml g biomass^{-1} h^{-1}. These reported values were misleading.[197,198] Xiao[204] compared the growing and non-growing phases of *R. palustris*. For the growing condition, 10 mM glycerol and atmospheric nitrogen were used as carbon and nitrogen sources respectively. For the non-growing condition, 10 mM glycerol was used as the carbon source and argon gas was sparged to create an anaerobic and nitrogen-free atmosphere. The maximum specific hydrogen production of both conditions were reported to be similar at values of 1.06 ml L^{-1} h $^{-1}$ for the growing phase and 1.04 ml L^{-1} h^{-1} for the non-growing phase. However, a significant increase in the hydrogen yield of the non-growing condition was observed at 77% of the theoretical maximum conversion, while only 10% of the maximum stoichiometric conversion was obtained for the growing condition. However, the initial biomass density for the non-growing condition (0.563 g L^{-1}) was significantly higher than that of the growing condition (0.108 g L^{-1}), explaining the high theoretical maximum conversion. Initial biomass density is of paramount importance in biohydrogen production as explained above and, thus, for a comparative analysis, the same initial biomass density should have been used.

6.1.2 Photosynthetic Microbial Fuel Cells

There have been limited applications of *R. palustris* in a photoMFC for direct electricity generation and practically no study of further converting the biohydrogen produced to bioelectricity.

Xing et al.[205] isolated a strain, called *R. palustris* DX-1 from an anode of a MFC. The exoelectrogenic bacteria were used with two different anodes; carbon paper and a graphite fibre brush, which were both treated with a high-temperature ammonia gas to increase surface area. A carbon cloth coated with platinum was used as an air cathode. With the graphite fibre brush, a maximum power density of 2720±60 mW m^{-2} was obtained with acetate as the electron donor. An internal resistance of 8 Ω was measured using electrochemical impedance. The high power density was obtained when the concentration of phosphate buffer solution (PBS) in the medium was changed from 50 mM to 200 mM. The high power density was attributed to the higher conductivity of the electrolyte. The above research paper claimed that the maximum power output is the highest yet achieved in any MFC with a pure culture under the circumstances where the anode potential was not set using a potentiostat.

Strain DX-1 was, also, used to metabolise nine other different carbon sources. A power density of about 200 mW m^{-2} was obtained with glycerol as the electron donor at an external resistance of 1000 Ω, with 50 mM PBS in the growing medium. There was no mention of the experiment being carried out anaerobically. Moreover, the performance of *R. palustris* ATCC® 17001™ was, also, analysed for comparison. However, it failed to generate any current over a period of 500 h with acetate as the electron donor.[205] However, the present work will investigate the performance of the same strain in converting biohydrogen into bioelectricity, thus assessing its performance.

Morishima et al.[206] used wild-type *R. palustris* CGA009 as the biocatalyst for bioelectricity generation with succinate as the carbon source. Anode and cathode were made by coating carbon paper or cloth with polyaniline. Both the electrodes were separated by PEM, Nafion® 117, and hot pressed to form a membrane electrode assembly (MEA). The aim of the study was to improve electron generation efficiency by using genetic engineering. It was assumed that quenching biohydrogen production would make more reducing equivalents available to be captured in a MFC. Thus, the performance of the wild type *R. palustris* was compared to two mutants, nifHD1d0941

(inactivated *nif* gene, encoding nitrogenase) and hupSL1d1518 (inactivated *hup* gene, encoding hydrogenase). The power generated by the MFC was measured by applying an external voltage. The mutant, nifHD1d0941, produced a slightly higher power density of 159 mW m^{-2} compared to 126 mW m^{-2} and 113 mW m^{-2} for the wild type and the strain hupSL1d1518, respectively. The mutant without nitrogenase produced more power, confirming that more reducing equivalents were available for extracellular export rather than for biohydrogen production. The wild type and the mutant without hydrogenase produced about the same power, which could be due to the fact that the wild type is already defective in hydrogenase uptake as mentioned by other works.[66,69] The research paper mentioned that the devices were assembled in an argon environment but that the experiments were carried out in air. Instabilities of the devices were reported; the culture suspensions were continuously stirred as a drop in power was observed, which questions the mechanism of electron transfer if a biofilm was not formed. Moreover, the fuel cell life was only about 8 hours, with fresh medium being added only after 2 hours of operation.[206]

Since, *R. palustris* can metabolise a wide range of substrates, Inglesby et al.[207] studied the performance of three types of MFCs with three different sources of electron donors, namely acetate, glycerol and cyanobacteria *Arthrospira maxima* (dried powder). The highest maximum power density was observed with *A. maxima*. In a micro-MFC, the highest maximum power density of 0.025 mW m^{-2} at an internal resistance of 15 MΩ was achieved. The low power output was attributed to the high internal resistance of the device. A flat plate MFC, operated in a fed batch mode, produced the highest maximum power density of 0.29 mW m^{-2} at an internal resistance of 1 MΩ. When the flat plate MFC was operated in continuous mode, the maximum power density obtained was 0.18 mW m^{-2}. From the experimental procedure, it was deduced that the devices were operated in air.

Venkidusamy and Megharaj[208] isolated a different strain of *R. palustris* from anodic biofilms of a microbial electrochemical remediation system (MERS), which is known to be electrophototrophic and hydrocarbonoclastic. The strain was identified as RP2 and its staple features are direct electrode respiration, dissimilatory metal oxide reduction, spore formation, anaerobic nitrate reduction, free-living diazotrophy and the capability to degrade n-alkane constituent of petroleum hydrocarbons in an anaerobic and photic environment. In acetate-fed bottle MFCs, a maximum power density of 200

mW m^{-2} at an external load of 1000 Ω was obtained when the concentration of PBS in the medium was changed from 50 mM to 200 mM. The anodic chamber was flushed with nitrogen.

With regards to generating electricity from the biohydrogen produced, most work has been carried out by Scholz and colleagues. Green alga *Chlamydomonas reinhardtii*, mesophilic anaerobe *Clostridim cellulolyticum*, thermophilic anaerobe *Clostridium thermocellum* and purple non-sulfur bacterium *Rhodobacter sphaeroides* were used for the in situ electrooxidation of hydrogen by polymer-coated electrocatalytic electrodes. The measurements were carried out using a conventional three-electrode arrangement. To measure the bioelectricity generated, a permanent potential of 0.2 V was applied to the working electrode for the in situ oxidation of biohydrogen produced in the microbial fuel cells. These studies also focused on the development of an electrocatalytic anode which is resistant against biofouling and deactivation in the complex microbial environment.[209–211] Using fuel cell analysis, a maximum power output of 182.5 mW m^{-2} at an external load of 100 Ω was obtained for *R. sphaeroides*.[209] These studies, however, failed to evaluate the contribution of the exoelectrogenic microorganisms towards electrical power generated. Another research study looked into diverting the biohydrogen produced by green alga *Chlamydomonas reinhardtii* to a fuel cell stack. 100 m^3 of algal culture was able to generate an average power of 240 W for 100 h, taking into consideration the fuel cell efficiency.[212]

6.2 Proposed Concept and Research Aims

The aims of this chapter are to maximise both biohydrogen production and exoelectrogenesis by manipulating the nitrogen to carbon ratio. A novel and sustainable platform is designed to harvest both biohydrogen and exocellular electrons for bioelectricity generation. The following objectives are set out to achieve the research aims.

1. The photofermentation process of biohydrogen production was investigated in photobioreactors.
    - Three limiting concentrations of the nitrogen source were studied as shown in Figure 6-2. Various parameters, including biomass density, biohydrogen production, concentrations of glycerol and glutamate were analysed to

determine which condition strikes the right balance between biomass production and biohydrogen production.

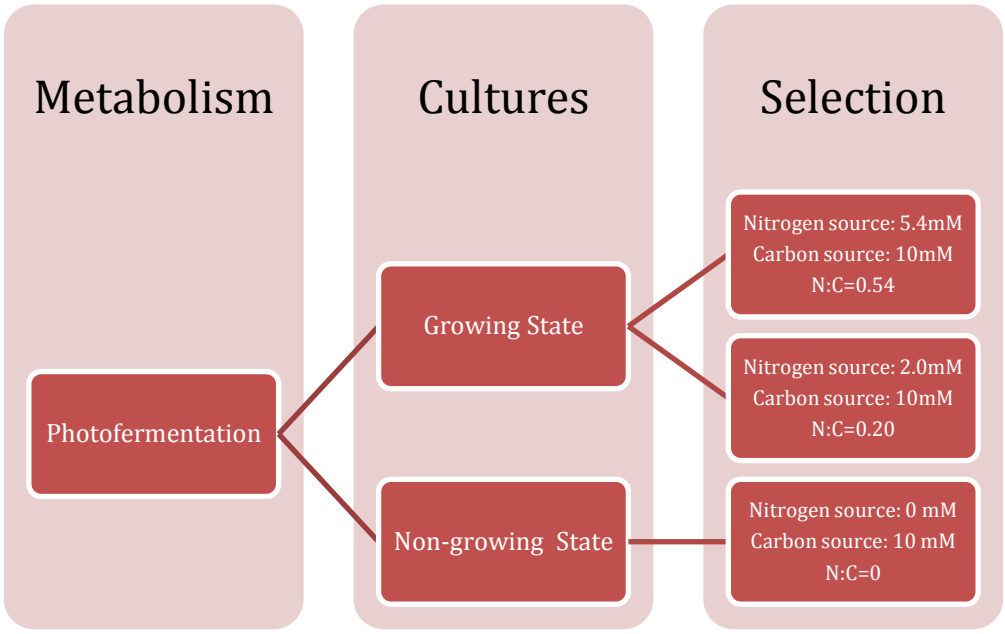

Figure 6-2: A schematic illustration of the different nitrogen limiting regimes under study for biomass and hydrogen production.

2. The biomass generated in the photobioreactors was inoculated in photoMFCs for bioelectricity generation from both exocellular electrons and biohydrogen generated.
   - SEM images of the biofilm of *R. palustris* were analysed for any specific features that could be involved in an electron transfer mechanism.
   - Cyclic voltammetry were used to identify any electroactive regions of the biofilm in both aerobic and anaerobic conditions.
   - Two types of photoMFCs were designed. The first prototype was based on a suspension culture and is termed as planktonic photoMFC. The second prototype was designed to house both a photoMFC and a hydrogen fuel cell and is, hence, named as a hybrid hydrogen-photoMFC. The photoMFC part was conceived for a biofilm framework.

Figure 6-3 illustrates a schematic of the two main parts involved in achieving the research aim.

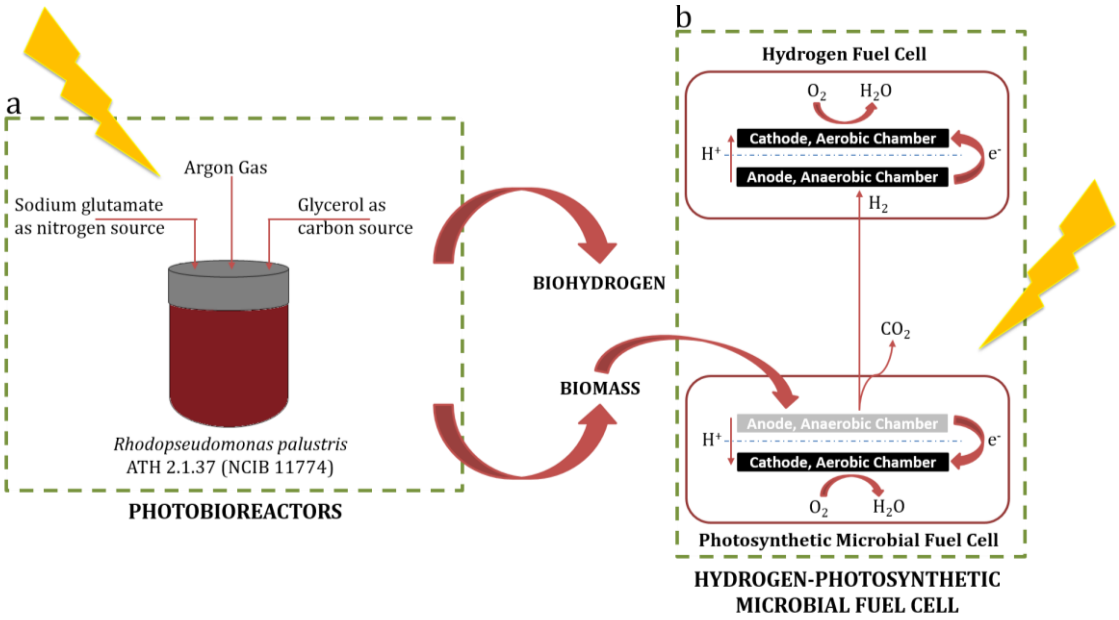

Figure 6-3: A schematic illustration summarising the two phases of the research chapter (a) photofermentation process in photobioreactors and (b) utilisation of the biomass generated in photoMFCs. The schematic of the second prototype is shown as an example.

6.3 Materials and Methods

6.3.1 Experimental Set-up for Photobioreactors

For the experimental studies, the precultures (as described in Chapter 2), were harvested and centrifuged in a Thermo Scientific™ Heraeus™ Megafuge™ 16 centrifuge at 4696 x g for 10 minutes, with two washing steps with PM(NF) medium, supplemented with the appropriate concentrations of glutamate and glycerol. The cultures were grown anaerobically in 500 ml Duran® bottles, with a working volume of 400 ml. They were incubated in the same bacterial culture cabinet as the precultures. Separate bottles were used for the measurement of volume and concentration of gas generated. For volume measurement, the gas sample port was connected to a long PTFE tubing which was then fitted to a water tank. Inverted 100 ml-graduated burettes were immersed in the water tank and the volume of gas produced was measured by water displacement. For gas composition measurement, a 20 ml luer lock syringe was fitted to the gas port to collect gas samples accumulated in the headspace of the bioreactors for injection into a gas chromatograph. For all experiments, the medium, the bottles, the tubing and the fittings were autoclaved

before inoculation. Figure 6-4 illustrates the set-up designed for the photofermentation experiments.

Figure 6-4: Experimental set-up of photobioreactors with *R. palustris*: (1) custom-made culture cabinet fitted with incandescent/halogen bulbs (2) arrangement of burettes in a water tank for gas collection (3) connections from the gas sampling port to the water tank (4) fittings to the liquid sampling port (5) a tubing connection to the gas port to collect gas samples in a syringe for measurement in a GC. The bottle caps and all fittings were made of PTFE and PEEK™ (polyarylethe-retherketone) to minimise hydrogen permeation and leakage.

6.3.2 Experimental Set-up for photoMFCs

6.3.2.1 Membrane Electrode Assembly (MEA)

The first step in the preparation of a MEA is the treatment of the membrane to remove impurities and to activate it with respect to proton numbers. Nafion® 115 (Sigma Aldrich) was cut into squares of 25 mm x 25 mm. They were placed in a lightly boiling

(about 80°C) 3% hydrogen peroxide solution (Sigma Aldrich) for 1 hour. The Nafion® membranes were, then, rinsed with deionised water before lightly boiling them in deionised water for 2 hours. The membranes were then immersed in lightly boiling 0.5M sulphuric acid for 1 hour, after which they were rinsed for about 2 to 3 times in lightly boiling (about 80-90°C) deionised water. They were stored in deionised water at all time to prevent them from drying.

The second step involved hot pressing the three layers. The hot plates of the hydraulic hot press (JBT Engineering) were heated to 140°C. The electrodes were cut into squares of 22 mm x 22 mm. The anode used was Toray Carbon Paper, TGP-H-60 (Toray Carbon Fibers Europe), unless a catalyst layer was required for the reactions studied. The cathode had Toray Carbon Paper, TGP-H-60 as the GDL, which was coated with platinum mixed in carbon black (0.36-0.5 mg Pt/cm^2, Alfa Aesar and Fuel Cell Earth LLC) to form the catalyst layer. Between two sheets of baking paper, the electrodes were aligned on each side of the membrane, with the catalyst layer preferably facing the membrane. The MEA layers sandwiched between the two pieces of baking paper were placed on the bottom plate and the jaws were closed without adding any pressure. The plates were left in this condition for 5 minutes to allow the temperature to equilibrate, after which a pressure of 10 MPa was applied for 1.5 minutes. The plates were unclamped and the single piece MEA was allowed to cool down to room temperature.[213,214]

6.3.2.2 Prototype 1: Planktonic photoMFC

A first prototype of the photoMFC was developed and it was called the planktonic photoMFC, as illustrated in Figure 6-5. Each bottle has a side flange, between which the MEA was sandwiched and sealed with polydimethyl siloxane (PDMS) ring gaskets. The whole assembly were held together with the help of fold-back clips. One end of the titanium strips (Ti-Shop.com) was used to make electrical contact with the electrodes while the other end was crimped to electrical wires. The glass flange provided an active electrode area of 18 mm in diameter. The side of the bottle with the Omnifit® blue cap was used as the anodic chamber while the other side with the red cap was the cathodic chamber, which was exposed to air. The red cap with aperture sealed a PET disc, which consisted of a 0.20 μm filter membrane to allow sterile gas

exchange. After assembly, the devices were sterilised by autoclaving at 121°C and 1 bar for 15 minutes.

80 ml of bacterial culture at an initial biomass concentration of 1.47 g L^{-1} was inoculated in the anodic chamber. The latter was kept anaerobic by purging air with argon. The presence of the Nafion® membrane in the MEA prevented any ingress of air into the anaerobic chamber. The devices were incubated under 6 x 60W incandescent/halogen light bulbs for continuous illumination with an intensity of 124±17 µmol photons m^{-2} s^{-1} at 35±2°C. Since the devices have a side flange, the bacterial culture had to be stirred continuously to prevent any cells from settling at the bottom of the bottle. Mixing the culture helped to keep the cells in contact with the anode. The devices were incubated for 5 days to allow a biofilm to develop on the anodes, after which their performance analysis was carried out. The control experiment was carried out with PM(NF) medium in the same devices before inoculation of bacterial cells.

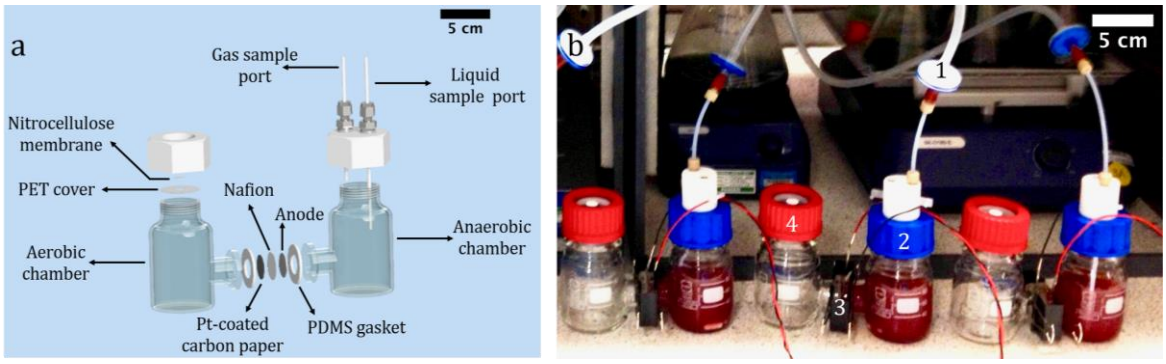

Figure 6-5: (a) Schematic diagram of the planktonic photoMFC (b) A triple set of the photoMFC devices undergoing purging with argon gas: (1) flushing of argon through the liquid sample port (2) anaerobic anodic chamber (3) side flanges holding MEA with the help of clips (4) aerobic cathodic chamber.

6.3.2.3 Prototype 2: Hybrid Hydrogen-photoMFC

The hybrid hydrogen-photoMFC was designed to generate bioelectricity from both the exoelectrogenic biofilm and the biohydrogen produced, with no agitation unlike the planktonic photoMFC.

The different parts of the device are illustrated in Figure 6-6. The MEA at the bottom of the device was used for biofilm formation while the top part was used for hydrogen reaction. Thus, the anode in the top MEA was of the same material as the cathode. Each

MEA was sealed and clamped between the glass flange and a metal disc with the help of PDMS ring gaskets and fold-back clips. Both the flange and the metal disc allowed for an electrode active area of 18 mm. Electrical contact to the electrodes was made by using titanium strips, with the other end crimped to electrical wires.

The devices were inoculated with 80 ml of bacterial culture at an initial biomass concentration of 1.47 g L^{-1}. The devices were kept anaerobic by sparging argon through the Omnifit® blue caps. The presence of Nafion® on both ends of the device also prevented any air to penetrate through. The bacterial cultures were incubated for 5 days under 6 x 60W incandescent/halogen light bulbs for continuous illumination of light intensity of 124±17 µmol photons m^{-2} s^{-1} and at a temperature of 35±2 °C to allow a natural biofilm to form. After the 5 days, performance analysis of the devices was carried out. The control experiment was carried out with PM(NF) medium in the same devices before inoculation of bacterial cells.

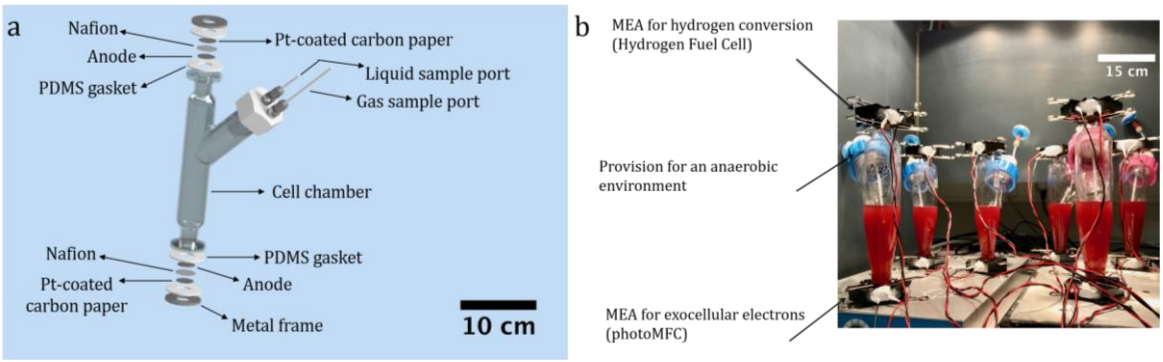

Figure 6-6: (a) Schematic diagram of the hybrid hydrogen-photoMFC and (b) actual photograph of the devices inoculated with cultures of *R. palustris* with no agitation.

6.4 Results and Discussion

6.4.1 Photofermentation Process in Photobioreactors

Three different limiting nitrogen regimes were evaluated, namely N:C=0.54, N:C=0.20 and N:C=0. The first two initial ratios were selected as the literature suggests that there is an optimal initial N:C ratio to obtain a high glycerol conversion efficiency. Moreover, N:C=0 is, often, referred to as the non-growing phase. The theory suggests that more hydrogen is generated in a nitrogen-starved environment.[196,203]

An initial average biomass density of about 0.70 g L^{-1} was used to study several parameters, such as biomass density, hydrogen production, concentration of glycerol, concentration of sodium glutamate, bacteriochlorophyll *a* concentration and pH. Bacteriochlorophyll *a* and pH of cultures are not extensively monitored in current literature. However, these two parameters provide a good insight of the physiological state of the cells.[132]

6.4.1.1 Growing Phase, N:C=0.54

At the beginning of the photofermentation process, hydrogen production increases as the biomass density increases, as shown in Figure 6-7 (a). However, at about 200 h, the biomass density decreases after peaking at a maximum value of about 2.60 g L^{-1}, while the cumulative hydrogen production keeps increasing to eventually level out at around 145 ml. Between 0 and 200 h, hydrogen is being generated simultaneously with growth of cells, thus the particular time period is characterised by growth associated product formation. Since hydrogen was still being generated after growth had ceased after 200 h, that phase is defined by non-growth associated product formation. As a result, the whole fermentation process can be described as a mixed mode product formation as hydrogen production was dependent on both cell growth rate and amount of biomass present.

The concentration of glycerol keeps decreasing over time but does not plateau, with a concentration of 0.5 mM at the end of the photofermentation reaction, achieving a total consumption of 94.5%. The concentration of glutamate levels up quickly at 0.37 mM after 50 h of reaction. This suggests that the bacterial cells used the bulk of glycerol as a carbon source for growth. Bacteriochlorophyll *a* concentration increases drastically around 100 h to then remain constant at around 23 mg L^{-1}. This seems to be a reasonable value as a similar concentration was observed by Carlozzi.[215] The pH of the culture decreases from a value of 7.04 to level up to about 6.75 for times in excess of 200 h. *R. palustris* usually shows excellent growth in a pH range of 6.0 to 8.5.[61]

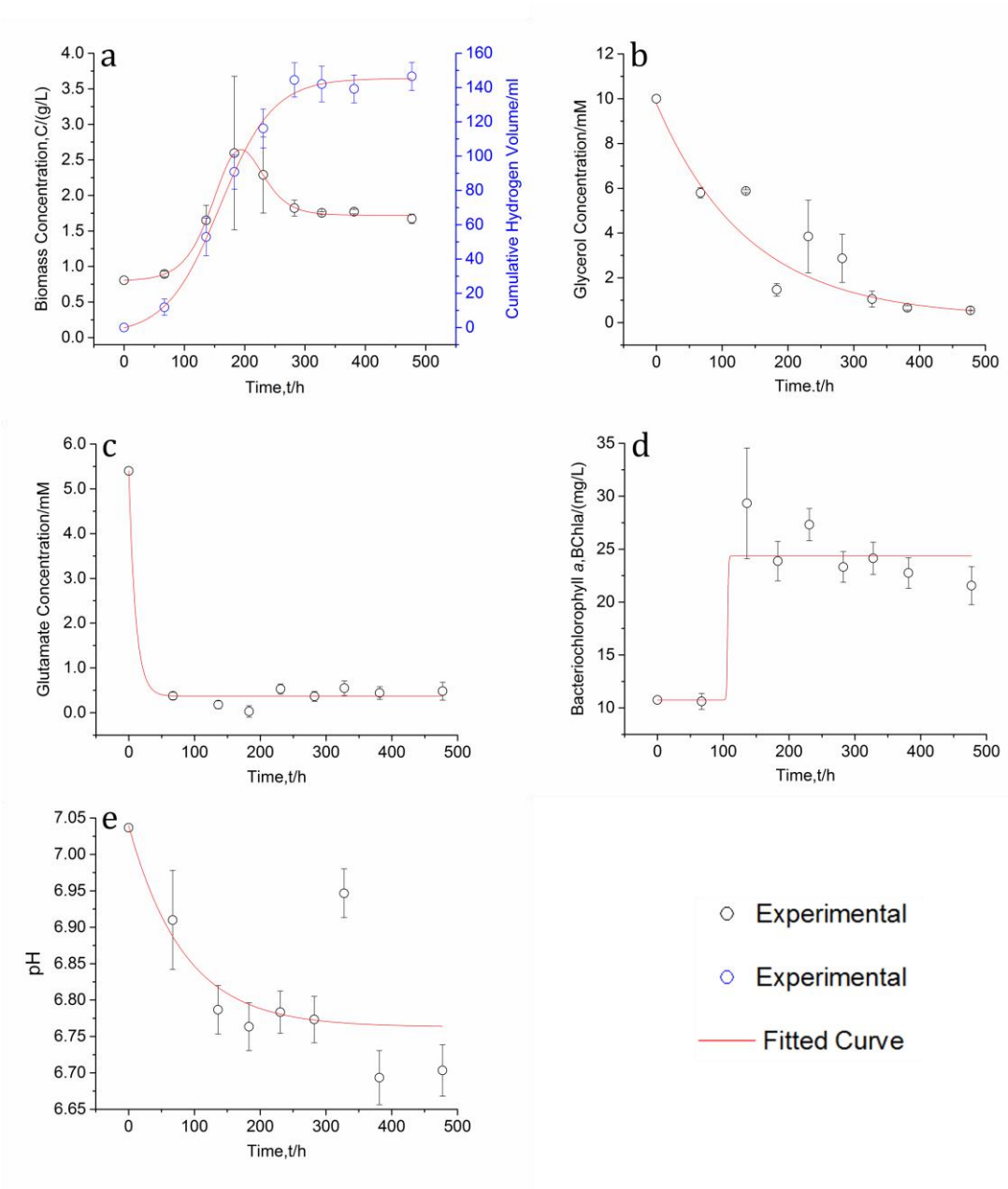

Figure 6-7: Experimental results showing the effects of growing cultures with a N:C=0.54 on parameters studied over a period of 20 days. (a) Bacterial growth curve of *R. palustris* is in black and cumulative hydrogen production is in blue (b) Glycerol consumption (c) Glutamate depletion (d) Bacteriochlorophyll *a* concentration (e) pH evolution [the mean ± se is shown for each data set (n=3)]. The red lines are lines of best fit generated using OriginPro 2016.

6.4.1.2 Growing, N:C=0.20

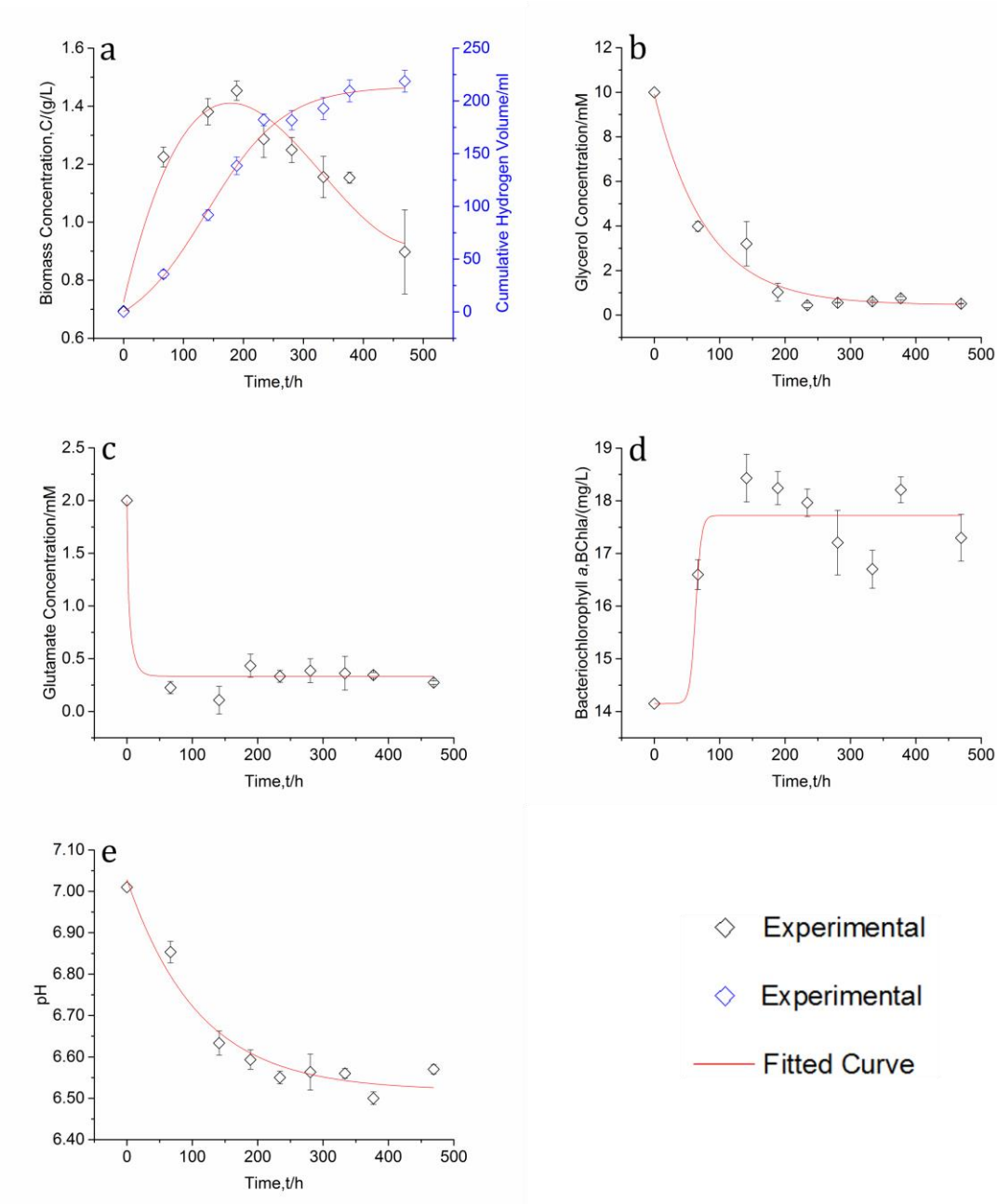

Figure 6-8: Experimental results showing the effects of growing cultures with a N:C=0.20 on parameters studied over a period of 20 days. (a) Bacterial growth curve of *R. palustris* in black and cumulative hydrogen production in blue (b) Glycerol consumption (c) Glutamate depletion (d) Bacteriochlorophyll *a* concentration (e) pH evolution [the mean ± se is shown for each data set (n=3)]. The red lines are lines of best fit generated using OriginPro 2016.

As illustrated in Figure 6-8 (a), the growth curve of the bacterial cells lacks a lag phase. The bacteria grew exponentially, reaching a maximum biomass concentration of 1.41 g L^{-1} within an incubation period of 200 h. The production of hydrogen is not

proportional to the microbial growth rate. It follows the trend of non-growth associated product as was illustrated in Figure 6-1. Biohydrogen production is, thus, dependent on the amount of biomass present, rather than cell growth. Even though the biomass density starts decreasing, the cumulative hydrogen production keeps increasing to reach a constant volume of about 213 ml. Unlike the first scenario, glycerol concentration depletes to a pseudo-constant value of about 0.5 mM, giving a total consumption of 94.9%. Glutamate concentration decreases within the first 50 h to a steady value of 0.3 mM.

Bacteriochlorophyll *a* concentration increases sharply at around 50 h to a constant value of 17.7 mg L^{-1}. The pH of the culture decreases from a value of 7.01 to about 6.53.

6.4.1.3 Non-growing, N:C=0

As observed in Figure 6-9 (a), there is minimal growth as the biomass density reaches a peak value of 0.84 g L^{-1} after 200 h from an initial biomass density of 0.70 g L^{-1}. Overall, the photofermentation process can be characterised as a mixed mode product formation as the generation of biohydrogen is both dependent on the microbial cell growth as well as amount of cells present. This indicates that the initial biomass density was probably not high enough as the cells barely grew. The cumulative volume of hydrogen keeps increasing to reach a value of 38 ml at the end of the reaction. Glycerol concentration drops drastically before a reaction time of 50 h to a steady value of 5.4 mM, which corresponds to a low consumption value of 46.9%. Due to the absence of a nitrogen source, cell growth and hydrogen generation compete for glycerol utilisation. In the above two case studies, glycerol was being consumed slowly with time as glutamate was balancing its utilisation. Moreover, severely less hydrogen is generated. This opposes the hypothesis, which describes that the complete removal of the nitrogen source will direct all substrate and energy towards hydrogen production as cell growth will slow down.[69] In this experiment, even though cell growth was not significant, hydrogen production was not improved. This suggests that a minimum biomass concentration must be available to sustain a higher hydrogen production.

Bacteriochlorophyll *a* concentration increases from 10.1 mg L^{-1} to peak a concentration of 11.2 mg L^{-1} within the first 200 h of the reaction, after which the concentration drops back to its initial value. The pH value of the cultures keeps dropping from its initial

value of 7.00 to 6.74. The pH does not settle at a constant value during the photofermentation reaction. These two parameters suggest that the cultures were not in an appropriate physiological state for the photofermentation process.

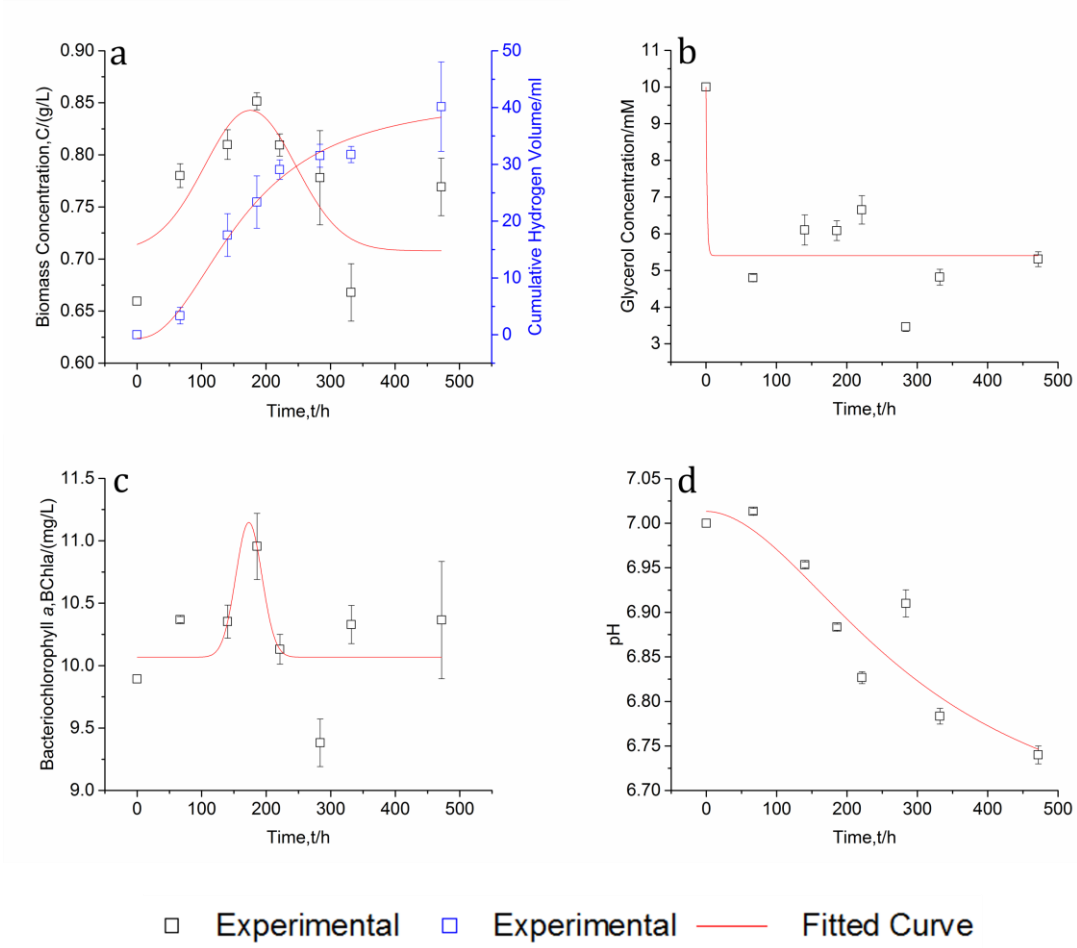

Figure 6-9: Experimental results showing the effects of non-growing cultures on parameters studied over a period of 20 days. (a) Bacterial growth curve of *R. palustris* in black and cumulative hydrogen production in blue (b) Glycerol consumption (c) Bacteriochlorophyll *a* concentration (d) pH evolution [the mean ± se is shown for each data set (n=3)]. The red lines are lines of best fit generated using OriginPro 2016.

6.4.1.4 Comparative Analysis of the Nitrogen Limited Regimes

The results from the above case studies can be summarised into normalisation elements of specific growth rate, specific hydrogen production and glycerol conversion efficiency for a better comparison and understanding of the effects of varying the concentration of glutamate.

The specific growth rate of the biomass was obtained from the slope of a straight-line fit to the exponential phase of a plot of the natural logarithm of the biomass concentration against time, as shown in

Figure 6-10 (a) for the case of N:C=0.54.[216] Similarly, the maximum specific hydrogen production is obtained from the slope of a linear fit to the exponential phase of a graph of hydrogen production (volume H_2/biomass concentration) against time, as illustrated in Figure 6-11 (a).[62]

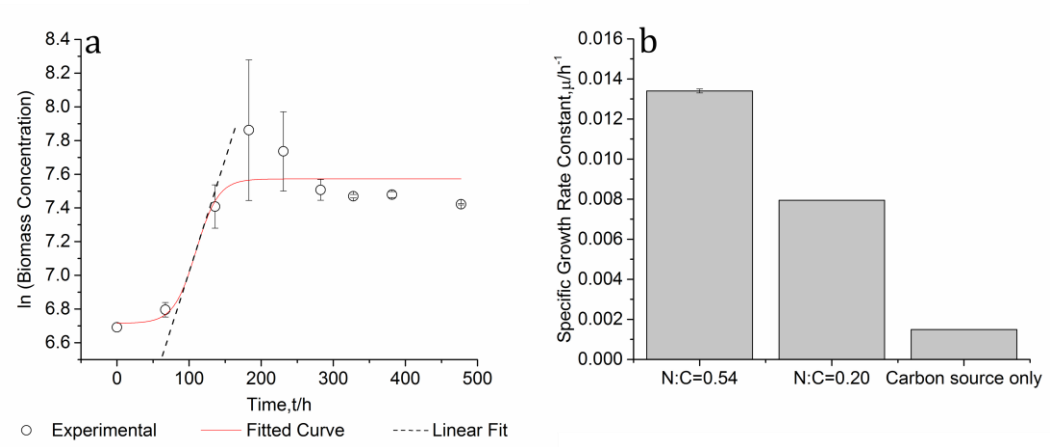

Figure 6-10: (a) The natural logarithm of biomass concentration (mg/L) against time for N:C=0.54 to show a sample example of obtaining the specific growth rate constant (b) The specific growth rate constant for all three scenarios of the nitrogen source [the mean ± se is shown for each data set (n=3)]. The error bars could not be seen because of their low magnitude.

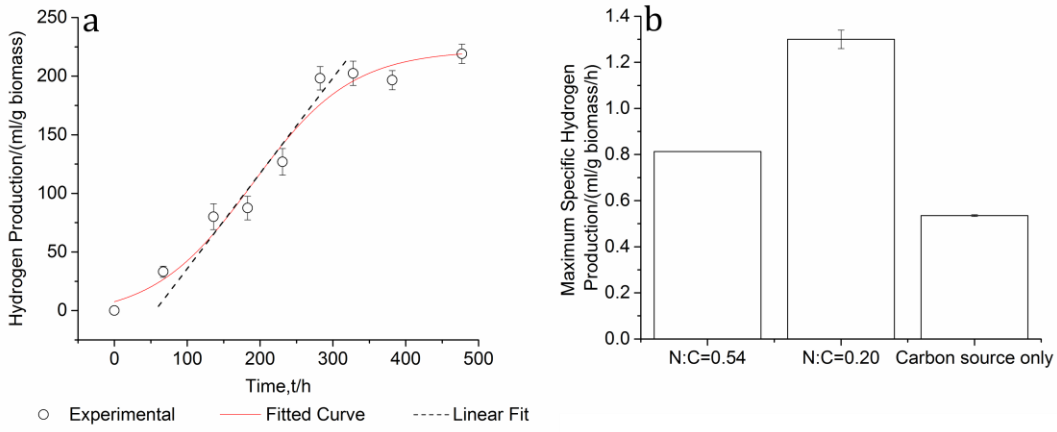

Figure 6-11: (a) Hydrogen production against time for N:C=0.54 to show a sample example of obtaining the maximum specific hydrogen production (b) The maximum specific hydrogen

production for all three concentrations of the nitrogen source [the mean ± se is shown for each data set (n=3)]. The error bars could not be seen because of their low magnitude.

The percentage values shown in Figure 6-12 represent an achievable conversion of the theoretical maximum conversion of glycerol, which is 7 moles of hydrogen generated per mole of glycerol consumed, if all glycerol is used for hydrogen production.

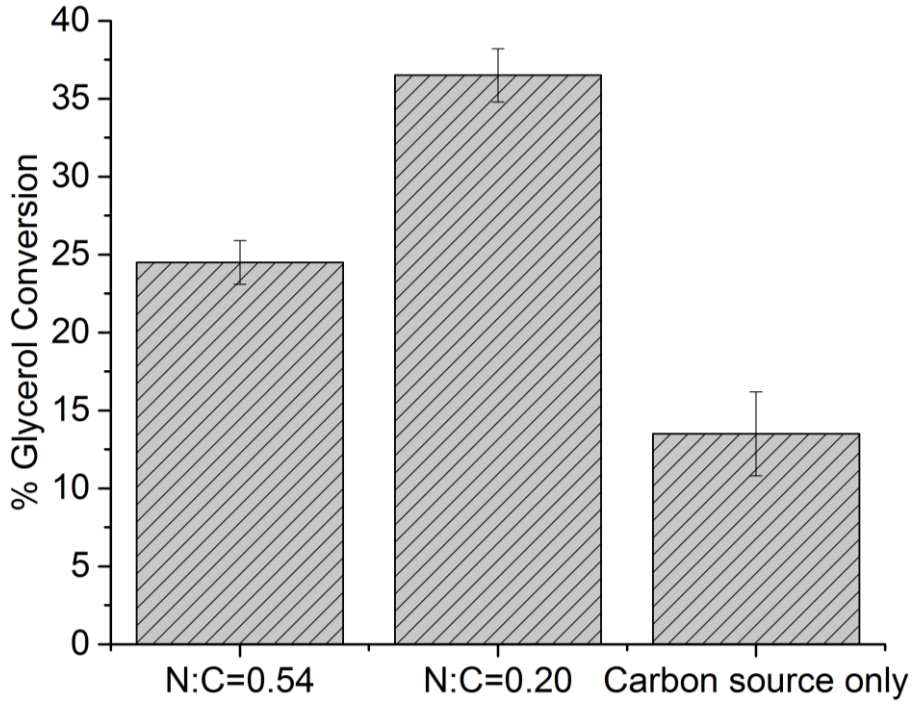

Figure 6-12: Hydrogen yield is shown as a percentage of glycerol conversion to hydrogen for the three nitrogen limiting regimes [the mean ± se is shown for each data set (n=3)].

As illustrated in Figure 6-10 (b), the specific growth constant increases with increasing nitrogen concentration: 0.0015 h^{-1} (N:C=0), 0.008 h^{-1} (N:C=0.20) and 0.013 h^{-1} (N:C=0.54), which is a reflection of the trend observed with maximum biomass density achieved: 0.84 g L^{-1} (N:C=0), 1.45 g L^{-1} (N:C=0.20) and 2.60 g L^{-1} (N:C=0.54). Limited growth occurs in the absence of nitrogen due to the possible carry over of nitrogen with the inoculum and also the cells can consume the nitrogen quota, which is the intracellular nitrogen source.

However, a completely different scenario is depicted in Figure 6-11 (b). Considering the growing conditions first, it can be observed that as the nitrogen concentration increases, the maximum specific hydrogen production decreases: 1.30 ml g $biomass^{-1}$ h^{-1} (N:C=0.20) and 0.81 ml g $biomass^{-1}$ h^{-1} (N:C=0.54). These values follow the

tendency observed with the cumulative volume of hydrogen generated: 218.7 ml (N:C=0.20) and 146.5 ml (N:C=0.54). Concurrently, the glycerol conversion efficiency increases as the nitrogen concentration decreases as shown in Figure 6-12. 2.55 moles H_2/mole glycerol is obtained for a concentration of 2.0 mM glutamate, namely 36.5±1.7% of the theoretical maximum conversion. For 5.4 mM glutamate, 1.72 moles H_2/mole glycerol is obtained, specifically 24.5±1.4% of the theoretical maximum conversion.

In the case of N:C=0.54, an excess presence of glutamate allows the photofermentation process to progress to the primary growth stage, where most of the electrons donated by glycerol are used for cell growth rather than hydrogen production. Thus, there is a low production of hydrogen, which ultimately results in low glycerol conversion efficiency. Moreover, the decrease in hydrogen yield may partially be due to the inefficient use of light as increasing biomass concentration may increase self-shading.

In the case of N:C=0.20, enough glutamate is present to sustain bacterial growth, while there is a remarkable increase in hydrogen production. The photofermentation process is dominated by the primary growth phase, which is crucial for a high biomass concentration. At the end of the photofermentation process, glycerol is almost completely consumed, substantiating that both hydrogen production and glycerol conversion efficiency are much higher than in the case of N:C=0.54.

For the growing condition, it can be said that biomass concentration and hydrogen production, each sits on either side of a lever, with the N:C ratio acting as the fulcrum. Varying the N:C ratio determines the dominance of either the biomass concentration or the hydrogen production.[217]

Taking into account the non-growing condition, it can be observed that limited bacterial growth did not translate into higher hydrogen production. On the contrary, the lowest maximum specific hydrogen production was obtained, correlating to a cumulative hydrogen volume of only 40.2 ml. The low hydrogen production corresponds to a low hydrogen yield of 0.95 mole H_2/mole glycerol, which is 13.5±2.7% of the theoretical maximum conversion. These results differ to the previous work[69], which dictates that completely suppressing the nitrogen source results in directing all substrate and energy towards hydrogen production without cell growth. The non-growing condition in this experiment seems to follow the case of a low N:C ratio. The initial biomass concentration is too low and hence, there was not enough

biomass to consume the glycerol, leading to a low glycerol conversion efficiency and hence a low production of hydrogen. The initial biomass to be used has to be optimised for a satisfactory hydrogen production.

6.4.2 Exoelectrogenic Activity of *R. palustris*

The ability of *R. palustris* to export electrons in an extracellular manner was first determined by analysing SEM images of the biofilm. Moreover, cyclic voltammetry was used to differentiate the electroactivity of aerobic and anaerobic grown biofilms. Eventually, the exocellular electrons were harvested in photoMFC devices for bioelectricity generation.

6.4.2.1 Features of Biofilm

A qualitative way of assessing cell to cell or cell to electrode interaction is to evaluate the features of formed biofilms. Figure 6-13 shows the SEM image of *R. palustris* biofilm grown on carbon paper. Two modes of communication can be observed; firstly the cells develop putative nanowires or pili and secondly the cells grow in clusters in a chain-like structure. It has been documented that some microorganisms can transfer electrons through nanowires or pili. Protein filaments in *Geobacter* spp. develop pili that are anchored in the cell envelope. They are required for the transfer of electrons between cells of *G. sulfurrenducens* PCA to Fe (III) oxides or oxyhydroxides and for many other purposes.[80] *Shewanella oneidensis* MR-1 is known to develop electrically conductive pilus-like appendages in direct response to electron-acceptor limitation. The study also emphasised that electrically conductive nanowires may not solely be developed in dissimilatory metal-reducing bacteria but may be a natural bacterial strategy for efficient electron transfer and energy distribution as observed in the oxygenic phototrophic cynaobacterium *Synechosystis* PCC6803.[156] Joining these groups of microorganisms is the metabolically versatile photosynthetic Fe (III) respiring bacterium, *R. palustris* strain RP2. The latter develops nanofilaments that are phylogenetically diverse inducible extracellular appendages, which have the possibility of acting like organic electronic conductors. The electrical properties of these nanowires were measured by using scanning probe and nanofabricated electrode measurements. A direct charge transfer along the length and radius of the nanofilaments were detected.[218] It can be deduced that the nanowires observed in the

SEM image may also contribute in the extracelluar electron transfer mechanism between the cells and the carbon paper electrode.

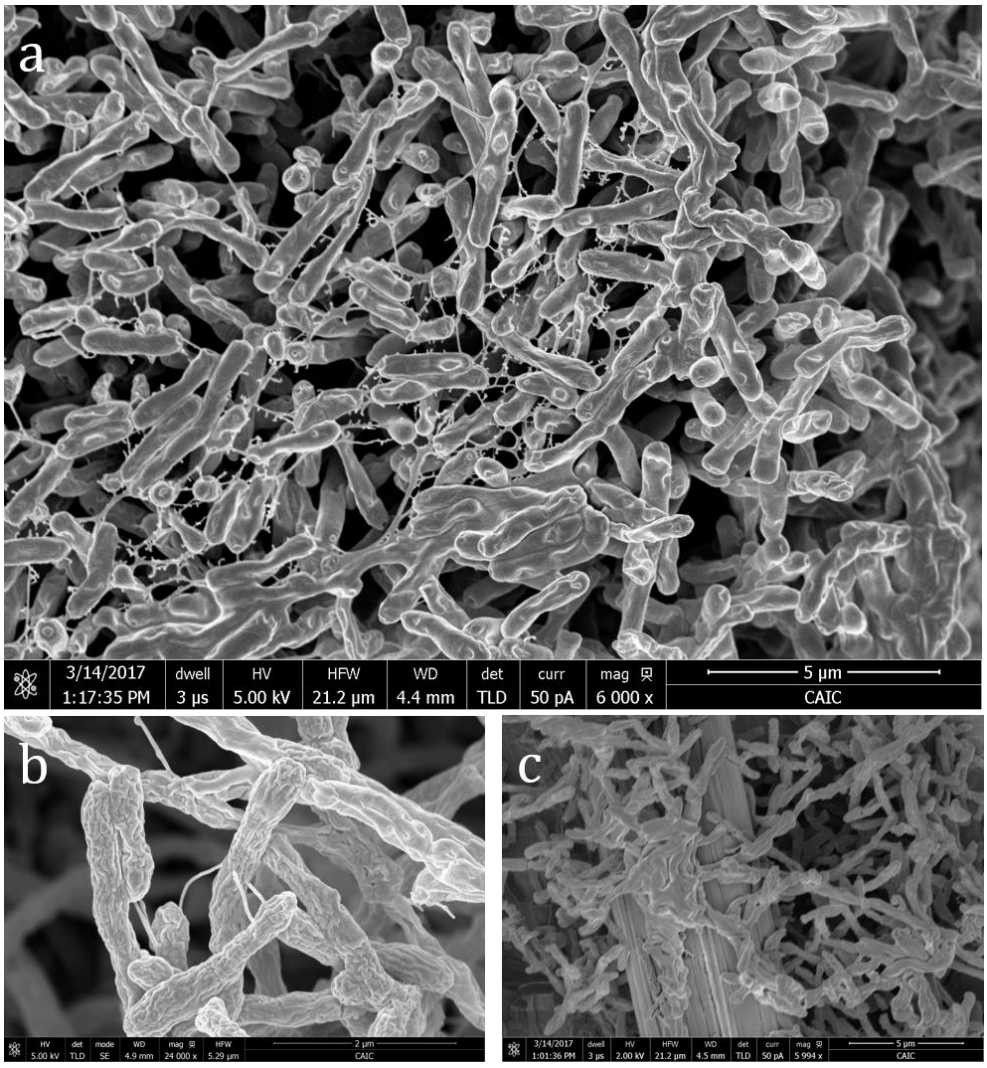

Figure 6-13: SEM image of biofilm of *R. palustris* showing two types of cell communication (a) a network of cells connected by putative nanowires or pili (b) magnified image of a cell anchoring on other cells by extending three putative nanowires like antennae (c) cells enveloping the carbon fibre, connecting with each other in a chain-like fashion

6.4.2.2 Cyclic Voltammetry

The electrochemical technique of cyclic voltammetry was used to determine the electrochemical activity of *R. palustris* both in anaerobic and aerobic conditions, namely to provide insight about the redox active region of the biofilm in electron transfer between the cells and the electrode.

As shown in Figure 6-14, anaerobically grown cells are electrochemically active unlike aerobically grown cells in all the three nitrogen conditions. Moreover, all three

conditions have an oxidation peak at -110 mV (vs Ag/AgCl) at a maximum current of 2.2 μA, 3.8 μA and 2.5 μA for N:C=0.54, N:C=0.20 and only glycerol, respectively. They exhibit about the same midpoint potentials of -160 mV, -130 mV and -150 mV with about the same starting potentials of -210 mV, -180 mV and -210 mV for N:C=0.54, N:C=0.20 and only glycerol, respectively. Expectedly, this indicates that the same redox compound was involved in the exocellular electron transfer for the three conditions. Several multi-heme cytochromes are known to be involved in exchanging electrons directly and reversibly with electrodes. The midpotential values obtained resemble the ones obtained for *D. africanus* cytochrome c_3 and *Desulfuromonas acetoxidans* cytochrome c_7.[219] The CV of *R. palustris* strain RP2 biofilm with Fe(III) oxide revealed midpoint potentials that are similar to the outer membrane cytochromes (OmcA) of *Shewanella oneidensis* MR, *Geobacter* and *Desulfuromonas acetoxidans*, with values around -240 to -320 mV.[208]

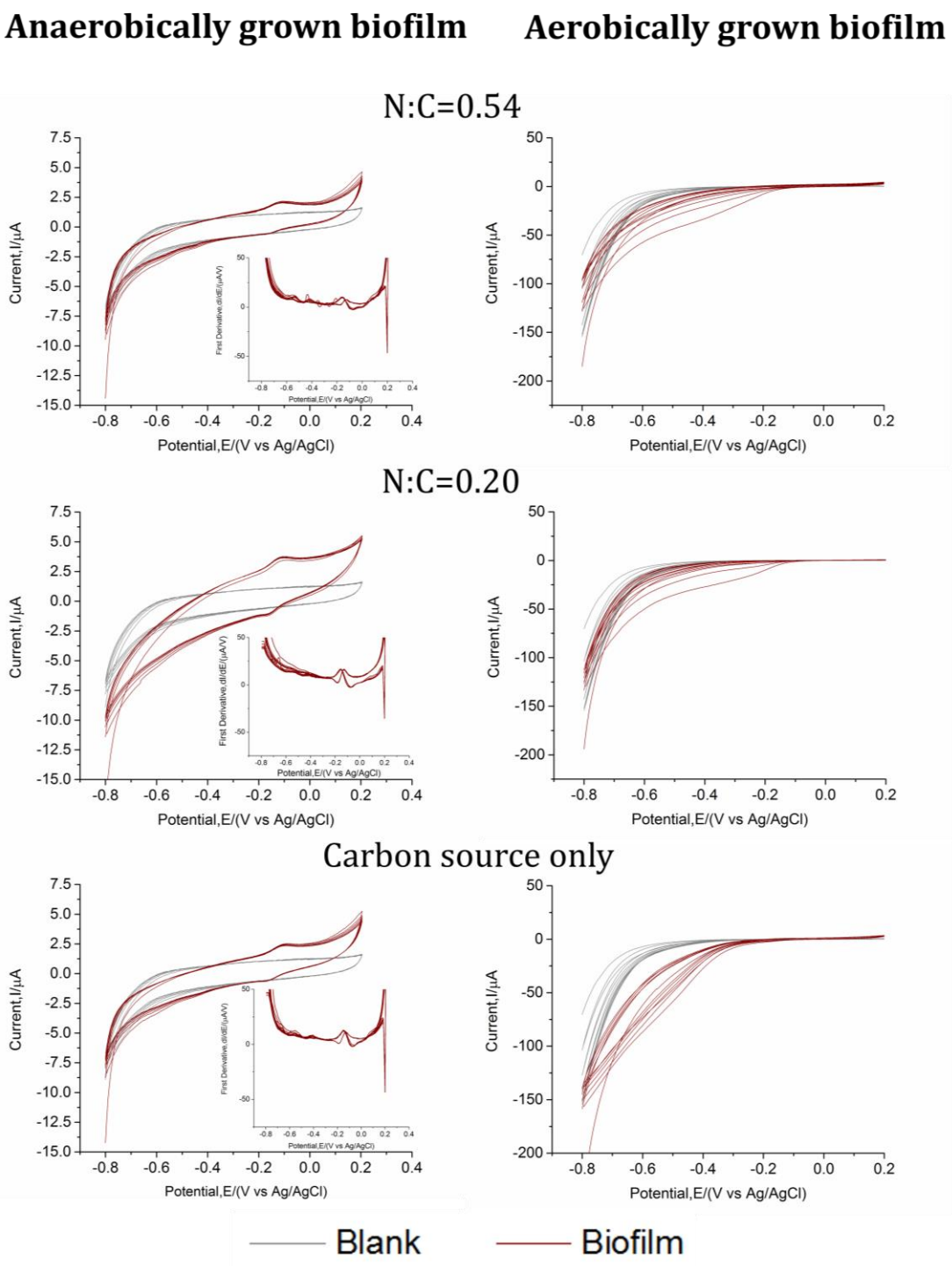

Figure 6-14: Cyclic voltammograms of anaerobically and aerobically grown biofilms for the three nitrogen regimes at 6 consecutive scans and a scan rate of 1 mV s^{-1}. The insets indicate the first derivative plots, showing midpoint potentials.

6.4.2.3 Performance Analysis of photoMFCs

The conditions used for the photofermentation process of hydrogen were replicated in photoMFCs to evaluate the exoelectrogenic activity of *R. palustris* for bioelectricity generation.

6.4.2.3.1 Prototype 1: Planktonic photoMFC

The planktonic photoMFCs were studied as two separate functional systems, under agitation. The first system focused solely on capturing electrons from the exoelectrogenic biofilm, and, thus, performed purely as a photoMFC. Therefore, the anode in this system did not contain a catalyst layer.

The second system was designed to capture electrons from the biofilm as well as harvesting the hydrogen generated into bioelectricity. The second system had a dual function, both as a photoMFC and a hydrogen fuel cell. As a result, the gas diffusion layer would require an additional layer of catalyst, to speed up the oxidation of hydrogen.

A first evaluation of the performance of the planktonic photoMFC devices was carried out using an initial biomass concentration of 1.47 g L^{-1} and an initial ratio of N:C=0.54. Figure 6-15 illustrates the polarisation and power curves of the two systems.

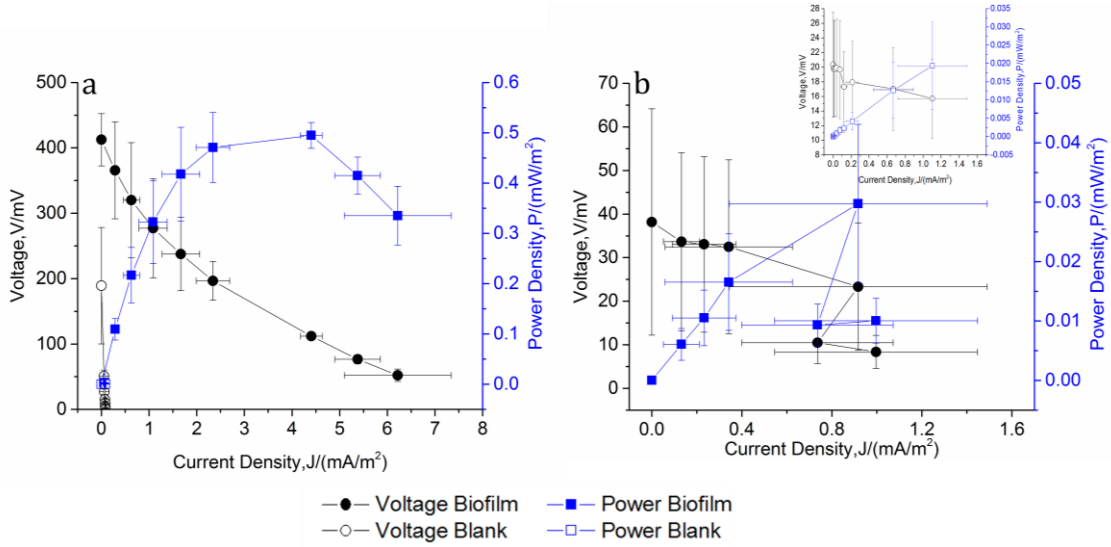

Figure 6-15: Polarisation and power curves for (a) System 1 with only biofilm of *R. palustris* and (b) System 2 used with both biofilm *R. palustris* and hydrogen generated, the blank is shown in an inset [the mean ± se is shown for each data set (n=2)]. The lines shown are purely used to guide the eye.

The first case as shown in Figure 6-15 (a) proves to be a much more stable system as compared to the second case in Figure 6-15 (b). Large error bars were obtained, undermining its performance. Moreover, insignificant activation and concentration losses were experienced with Figure 6-15 (a). The minimal activation loss may be due to a good interaction of the cells with the anode, facilitating the electron transfer mechanism. The system was typically characterised by ohmic losses. Contrarily, the second system suffers from all three types of polarisation losses. It even experienced an overshoot as the demand for electrons was greater than what the cells could provide. Figure 6-16 summarises the two parameters that can be observed in Figure 6-15.

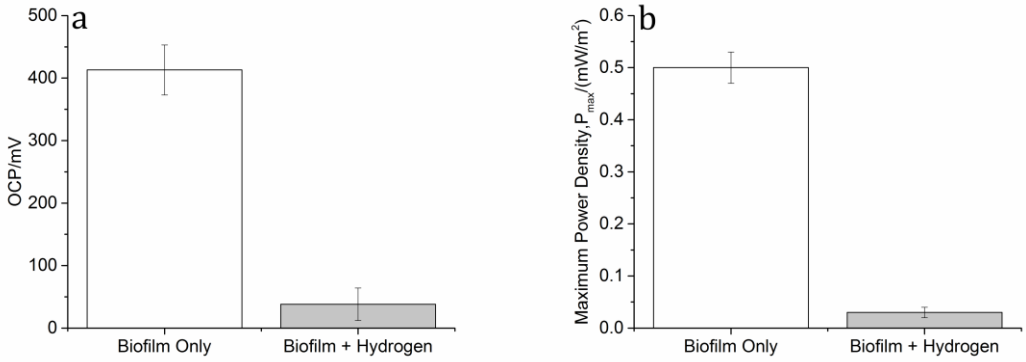

Figure 6-16: Data extracted from polarisation and power curves to show the performance of both systems in terms of (a) OCP and (b) maximum power output [the mean ± se is shown for each data set (n=2)].

An OCP of 413±40 mV was obtained for the first system and a significantly lower OCP of 38±26 mV was achieved for the second system. The OCP achieved by the first system are similar to literature values.[205,207,208] Not only was the second system marked by a low OCP value but it was also highly volatile. The low OCP value could be due to the poor stability of biofilm formation or its poor interaction with the anode. The same trend was observed for maximum power output. The first system achieved a power output of 0.50±0.03 mW m^{-2} at an internal resistance of 130±10 kΩ compared to only 0.03±0.01 mW m^{-2} at an internal resistance of 58±51 kΩ for the second system. The low power output of the second system was due to the substantially low OCP and the volatility of the internal resistance of the device. The main difference between the two systems was the presence of platinum catalyst particles in the anode of the second

system for the in situ conversion of hydrogen to bioelectricity. There have been reports that the aggressive microbial environment deactivates the platinum catalyst and even causes biofouling.[209–211] As a result, the electroactive anode was coated with a conductive polymer to prevent poisoning. It can be deduced that the inactivation of the anode in the second system compromised its performance. It is worth highlighting that the power output obtained from even the first system is low compared to reported values of MFCs in literature.[81] A possible reason is that the continuous stirring of the cultures may have perturbed the biofilm and, hence, the low power densities.

6.4.2.3.2 Prototype 2: Hybrid Hydrogen-photoMFC

Since the second system of the first prototype failed to encompass both features of *R. palustris*, a second prototype was designed with two main objectives: (1) improving the power output by switching to a complete biofilm mode and (2) to successfully convert the hydrogen generated into bioelectricity. Since hydrogen could not be electrically harvested in situ in the cultures, two electron collection points were implemented. The photoMFC was designed to have the bottom MEA for biofilm to settle naturally on and the top MEA for hydrogen to be harvested, as it rises due to its lower density. The bottom of the device therefore functions as a photoMFC and the top part operates as a hydrogen fuel cell. Thus, this device was named as a hybrid hydrogen-photoMFC.

The anode on which the biofilm settled had no presence of catalyst. However, both the anode and cathode for the hydrogen reaction had a catalyst layer (CL). The CL for the anode faced the membrane, while the CL for the cathode faced the outside environment. This arrangement was found to be ideal as it reduced short circuits. A layer of water was added on top of the cathode so as to create a capillary force for protons movement.

The first test with the hybrid hydrogen-photoMFC was carried out with the same initial biomass concentration of 1.47 g L^{-1} and an initial ratio of N:C=0.54 as shown in Figure 6-17. This lays a common ground for comparison between the two prototypes.

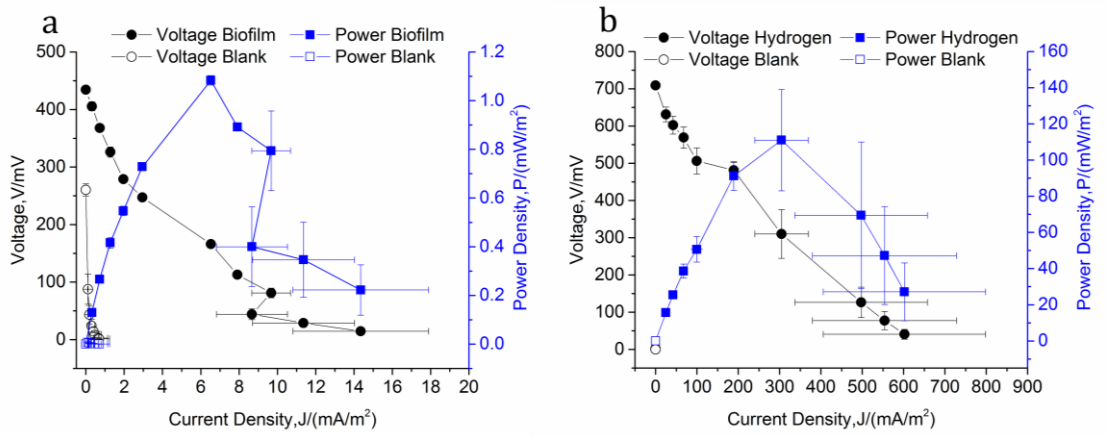

Figure 6-17: Polarisation and power curves for (a) the bottom part of the device, biofilm and (b) top part of the device, hydrogen. The blanks are shown for each condition [the mean ± se is shown for each data set (n=2)]. The lines shown are purely used to guide the eye.

An OCP of 434±3 mV and a maximum power output of 1.08±0.02 mW m^{-2} at an internal resistance of 103±1 kΩ were obtained for the biofilm part of the device while an OCP of 709±4 mV and a maximum power output of 111±28 mW m^{-2} at an internal resistance of 4±1 kΩ was attained by the hydrogen reaction. The performance of the biofilm was characterised by all the three types of polarisation losses and even suffered from an overshoot. The hydrogen reaction suffered from initial activation losses, followed by ohmic lossess with negligible concentration losses. The OCP of the first system of the first prototype was similar to the one observed in Figure 6-17 (a). This is because both systems utilised the same anode and the same biocatalyst. However, there was about a two-fold increase in the maximum power output achieved and a 1.3-fold decrease in internal resistance. These experimental results confirm that a good biofilm formation is important for increased power output as there is direct contact between the cells and the anode. Moreover, the design of the second prototype provided the added value of capturing the energy stored in the biohydrogen generated.

6.4.2.3.2.1 Hybrid Hydrogen-photoMFC at Different N:C Ratios

Since the second design demonstrated a performance improvement, the other two conditions of photofermentation were used in the hybrid hydrogen-photoMFC to verify the observations made in Section 6.4.1. Figure 1-18 shows a comparison between the three conditions.

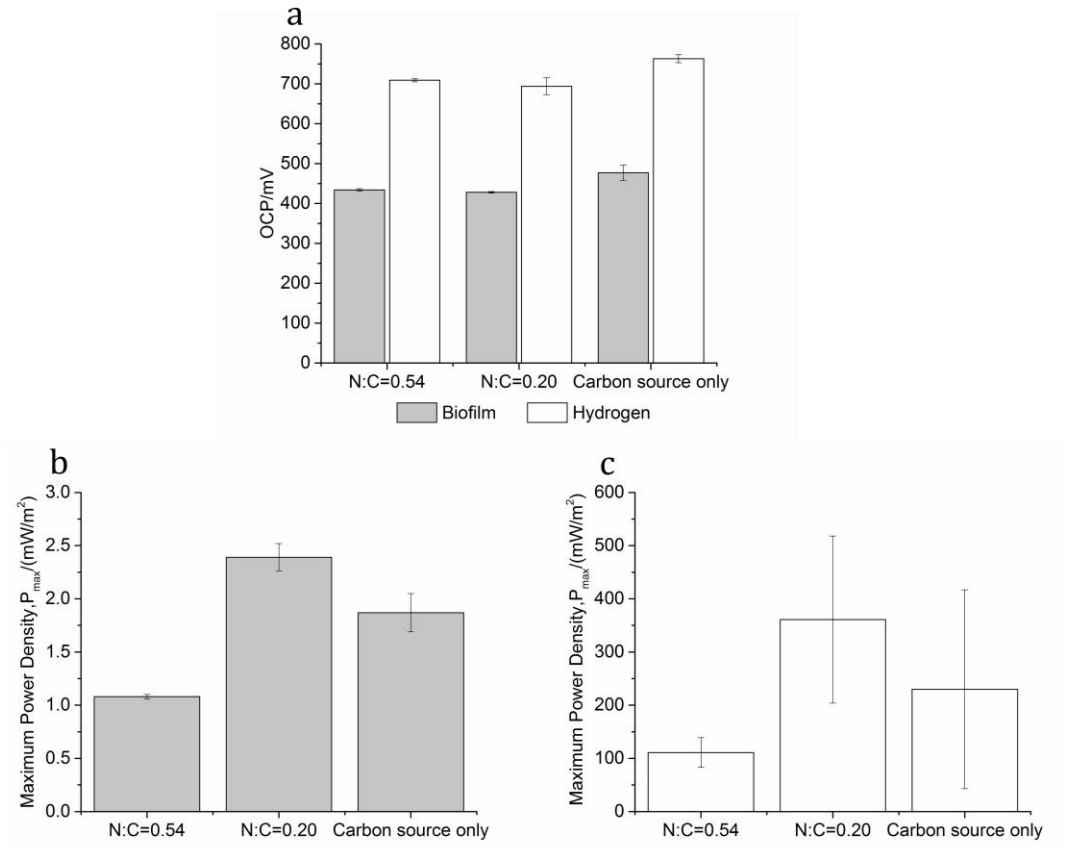

Figure 6-18: Data extracted from polarisation and power curves for the three initial ratios of N:C previously studied in photobioreactors (a) the comparison of OCP values obtained for the biofilm and biohydrogen (b) the maximum power output obtained from the exoelectrogenic biofilm and (c) the maximum power output obtained from the oxidation of biohydrogen [the mean ± se is shown for each data set (n=2)].

From Figure 6-18 (a), the OCP values of the biofilm in the three different nitrogen-limiting conditions are of equivalent order, as expected. Moreover, they are similar to values reported in literature.[205,207,208] Similarly, the OCP values of the biohydrogen are also within the same limits between each other, which are comparable to conventional hydrogen fuel cells. The theoretical voltage for a hydrogen fuel cell is 1.23 V, however, typical potentials such as 0.6 to 0.7 V are obtained due to thermodynamic overpotential losses.[220] Therefore, it can be deduced that the biohydrogen produced was successfully harvested in the designed prototype.

As depicted in Figure 6-18 (b), the exoelectrogenic activity of the biofilm produced a maximum power output of 2.39±0.13 mW m^{-2} at an internal resistance of 50±1 kΩ for the condition of N:C=0.20 while a maximum power output of 1.87±0.18 mW m^{-2} at an

internal resistance of 78±8 kΩ was reached by devices inoculated with only glycerol. It can clearly be gathered that the case with N:C=0.20 generated the highest maximum power output with the lowest internal resistance, followed by the nitrogen starved condition. The lower internal resistances of the devices with these two conditions compared to N:C=0.54 explained the difference in the maximum power output achieved. More intrinsically, when the nitrogen concentration was high, most of the electrons were used for cell growth. Therefore, in the two cases, where concentration of glutamate was low and 0, a larger pool of electrons was available for hydrogen production. Remarkably, these results indicate that a fraction of those electrons was diverted towards extracellular export; therefore nitrogen starvation also induces higher exoelectrogenic activity. The nitrogen starved condition performed better than the condition of N:C=0.54 as a higher biomass concentration was used compared to the one in the photobioreactors (Section 6.4.1), suggesting that there was enough biomass to consume the glycerol in the nitrogen-starved condition.

Figure 6-18 (c) illustrates the maximum power achieved from the electrooxidation of hydrogen in the devices at the three different conditions. A maximum power output of 361±157 mW m^{-2} at an internal resistance of 1.6±0.8 kΩ was obtained for devices with N:C=0.20 while a maximum power output of 230±187 mW m^{-2} at an internal resistance of 1.4±1.2 kΩ was produced with devices containing nitrogen-starved cultures. The maximum power output followed the same trend as shown in Figure 6-18 (b). The higher maximum power outputs obtained for cultures with N:C=0.20 and N:C=0 are due to the fact that more electrons are used for hydrogen production. However, the high irreproducibility of devices with nitrogen-starved cultures undermine their performance with respect to devices with N:C=0.54. Possible reasons could include the malfunctioning of the MEA and hydrogen leakage.

In general, the hydrogen fuel cell part of the devices face high instabilities due to the main issue of hydrogen leakage. A more rigorous design and engineering approach are needed to retain the hydrogen. However, this is a novel approach to harvesting bioelectricity from the exoelectrogenic biofilm and the direct electrochemical depletion of biohydrogen in a single device. Furthermore, for the first time it has been shown that varying the N:C ratio could help in increasing electron availability for the exoelectrogenic pathways.

6.4.2.3.2.2 Comparison of Hybrid Hydrogen-photoMFC to Photobioreactors

To better understand parameters, such as biomass concentration, specific hydrogen production and hydrogen yield, in the hybrid hydrogen-photoMFCs, photofermentation processes in photobioreactors using the same conditions were characterised simultaneously. The only difference was that the cultures were continuously mixed in the photobioreactors whereas a biofilm was allowed to form in the electrochemical cells. Therefore, the experimental results obtained from the photobioreactors were termed as ideal values.

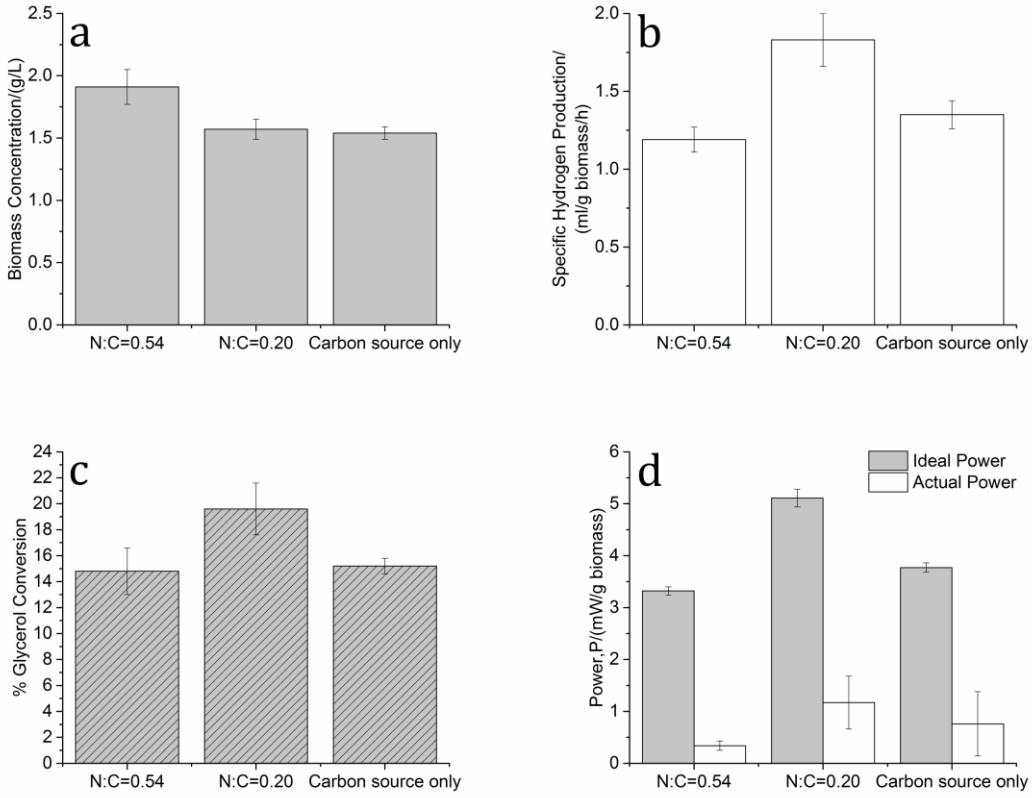

Figure 6-19: Analysis of some critical parameters to understand the performance of *R .palustris* in the photoMFCs, 5 days after inoculation (a) final biomass concentration (b) specific hydrogen production (c) % glycerol conversion to hydrogen as a percentage of the theoretical maximum conversion (d) actual power obtained from the hybrid hydrogen-photoMFCs as compared to the power that can be harvested from the hydrogen generated in the photobioreactors [the mean ± se is shown for each data set (n=3)].

As illustrated in Figure 6-19(a), the final biomass concentration of cultures with initial N:C=0.54 is slightly higher than the other two conditions, corroborating with the explanation in Section 6.4.1. The trend observed for hydrogen production was an

inverse of that of biomass concentration for conditions N:C=0.54 and N:C=0.20. In this specific study, slightly more hydrogen was produced by nitrogen-starved cultures in relation to cultures with N:C=0.54, as a higher initial biomass concentration was used. These experimental results reflect the performance of the hybrid hydrogen-photoMFCs. Figure 6-19 (c) shows the glycerol conversion as a percentage of the theoretical maximum conversion; 14.8 %, 19.6% and 15.2% for cultures with N:C=0.54, N:C=0.20 and for N:C=0, respectively, which reflects the trend of specific hydrogen production.

Another interesting evaluation is comparing how much actual power was obtained in relation to the power that can be harvested from the hydrogen produced in the photobioreactors. As shown in Figure 6-19 (d), the actual power obtained from the hybrid hydrogen-photoMFCs is normalised by the biomass concentration. Thus, the ideal power that can be obtained per g biomass was calculated by using the specific hydrogen and the low heating value (LHV) of hydrogen as the energy density. The actual power that can be produced is only 10.3%, 22.9% and 20.2% of the potential energy of hydrogen produced in the photobioreactors for conditions of N:C=0.54, N:C=0.20 and N:C=0, respectively.

6.5 Conclusions

This chapter is divided into two main sections: the study of the photofermentation process of biohydrogen production in photobioreactors and the utilisation of the biomass produced in photoMFCs. In the first phase, three nitrogen-limiting conditions were evaluated: N:C=0.54, N:C=0.20 and N:C=0. It was found that N:C=0.20 provided the ideal situation of enough generation of biomass for a better yield of biohydrogen, with a specific growth constant of 0.008 h^{-1} with a maximum specific hydrogen production of 1.30±0.04 ml g $biomass^{-1}$ h^{-1} at a glycerol conversion efficiency of 36.5±1.7% of the theoretical maximum conversion. The next step involved assessing the exoelectrogenic activity of *R. palustris*. SEM images of the biofilm showed the presence of putative nanowires or pili that may potentially contribute to the electron transfer mechanism as described by some other works. The next step involved analysing the performance of *R. palustris* in photoMFCs. CV scans showed that aerobically grown cells did not exhibit any electrochemical activity, unlike anaerobically grown biofilm. The midpoint potentials obtained for the three nitrogen-

limiting conditions were similar and they correspond to outer membrane cytochromes of other microbial species. As a result, it can be inferred that there is direct electron transfer from *R. palustris* to the electrode, thus cytochromes in the outer membrane were involved in the extracellular electron transfer.

The first prototype of the photoMFC failed to capture both the exocellular electrons from the biofilm as well as the biohydrogen produced into an electric current. As a result, a novel device was designed, which housed both a photoMFC and a hydrogen fuel cell. No other work in the literature had explored this perspective. The initial ratio of N:C=0.20 again provided the best performance in terms of power output obtained from both the biofilm and the biohydrogen. A power output of 2.39±0.13 mW m^{-2} at an internal resistance of 50±1 kΩ was obtained from the biofilm while the electrooxidation of hydrogen generated a maximum power output of 361±157 mW m^{-2} at an internal resistance of 1.6±0.8 kΩ. Moreover, for the first time it has been shown that varying the N:C ratio could help in increasing electron availability for the exoelectrogenic pathways. The hybrid hydrogen-photoMFC performed satisfactorily as a first prototype but a more rigorous design has to be engineered to mainly prevent the volatility of the hydrogen fuel cell caused by hydrogen leakage.

7 Concluding Remarks

7.1 Conclusions

Alternative sustainable sources of energy with zero-CO_2 emissions are of prime importance for our society. An emerging and sustainable platform for the capture of solar energy, namely photo-bioelectrochemical systems (photo-BESs) was assessed in this research work. These systems utilise photosynthetic microorganisms as biocatalysts to generate bioelectricity. Although the microorganisms are inexpensive and easily available, they are not naturally conceived for electron capture in an electrochemical cell. As a result, two strategies were adopted to improve the exoelectrogenic activity and electron transfer of the microorganisms. In Case Study 1, the performance of bioanode materials was analysed to improve the electron transfer efficiency of *S. elongatus* in BPV platforms, while in Case Study 2, the performance of *R. palustris* was improved for both enhanced biohydrogen production and exoelectrogenesis for conversion into bioelectricity in photoMFCs.

The electrochemical interaction between *S. elongatus* and ITO-coated substrates was improved by modifying their surfaces with graphene so as to increase average surface roughness and surface area. Liquid phase exfoliated graphene was synthesised using two different synthesis methods, namely ultrasonication and microfluidisation. The performance of ITO-coated substrates coated with ultrasonicated graphene was outperformed by the bare ITO-coated substrates. It was attributed to the poor quality of graphene produced and the limitation of light by the coating. However, microfluidised graphene could easily be screen-printed on the ITO-coated substrates, which helped in optimising a criss-cross mesh pattern so as to best utilise light. The ITO-coated bioanodes were used in a single chamber BPV device that inherently had a high internal resistance due to the large gap between the anode and cathode. It was found that graphene helped to significantly improve the maximum power output while halving the internal resistance of the BPV devices. A linear correlation was obtained between average surface roughness and maximum power output and between increase in surface area and maximum power output. Graphene/ITO-coated PET was

the best performing bioanode with the highest maximum power output of 29±4 μW m^{-2} at an internal resistance of 2.7±0.2 MΩ as it promoted a much denser biofilm coverage while minimising ohmic losses. The electroactivity of the biofilm on each anode material was assessed using double potential step chronoamperometry as cyclic voltammetry failed to detect any redox peak. The results confirmed that the surface roughness characteristics overpowered the conductivity property of the ITO-coated substrates, as ITO-coated glass is more conductive. Additionally, ITO-coated PET has a lower cost of production as compared to ITO-coated glass.

Carbon fibres, namely carbon paper and carbon felt are highly hydrophobic in nature. A surface functionalisation technique introducing oxygen functional groups on the surface of the materials was employed. Only plasma treatment initiated the change from hydrophobicity to hydrophilicity. Since the carbon fibres are porous and black, they were used in MEA-type BPV devices, where the anode and cathode are in close proximity, separated by just a membrane. Even though the surface treatment reduced the internal resistance of the devices, only hydrogen peroxide treated carbon paper produced a significant performance. In comparison to the single chamber BPV device, the performance of the MEA-type BPV device was outperformed in terms of OCP, internal resistance and maximum power output. It demonstrates that the highly hydrophobic hydrogen peroxide treated carbon paper overpowered the advantageous configuration of the MEA-type BPV device. Since the surface treatment was not completely successful, an inherently hydrophilic novel carbon-based material was analysed. Four thicknesses of graphene paper, 50 μm, 75 μm, 120 μm and 240 μm, were assessed for their performance as bioanodes. 240 μm thick graphene paper had a higher degree of hydrophilicity than the other three thicknesses of graphene paper, which translated into the highest maximum power output of 393±20 μW m^{-2} at the lowest internal resistance of 97±4 kΩ. The improvement in performance was mainly attributed to electrochemical polarisation, such as activation and ohmic losses. Double potential step chronoamperometry confirmed a more electroactive biofilm on the surface of 240 μm thick graphene paper. However, the blank was in close limits and had the potential of introducing ambiguities. Double potential step chronocoulometry helped in better understanding the role of the biofilm.

In a proof of concept study, the performance of a graphene-coated membrane was studied with the aim of reducing the thickness of the anode material for a better performance. Blade-coating GNP/CMC ink on nitrocellulose membranes was not as efficient as screen-printing it. Two screen-printed designs of GNP/CMC ink were made, to improve surface roughness. However, it was found that power density decreased with increasing average surface roughness and surface area. Bioanodes with 3 passes of graphene produced the highest maximum power output of 80±10 μW m^{-2} at a slightly higher internal resistance of 313±13 kΩ as compared to devices with 3 passes+ 2 squares bioanodes. Since the planar anode did not improve performance as compared to the 240 μm thick graphene paper, a 3D-printed bioanode coated with multi-walled carbon nanotubes (MWCNTs) was designed. Five different thicknesses were tested but 1 mm thick bioanode produced a maximum power density of 181±36 μW m^{-2} with the lowest internal resistance of 217 kΩ. However, the double potential step chronoamperometry study of the graphene-coated and multi-walled carbon nanotubes-coated bioanodes provided conflicting results as the peak and limiting currents of the blank were higher than the biofilm, even though a dense biofilm with extensive fibrous extracellular matrix was formed on the multi-walled carbon nanotubes-coated bioanodes. However, chronocoulometric studies helped in distinguishing the performance of the blank and the biofilm for graphene-coated bioanodes. However, the blank of the multi-walled carbon nanotubes-coated bioanodes was still higher due to the fact that the biofilm clogged the holes of the bioanodes leading to reduced electrochemical surface areas.

The performance of the microorganism is also an important part of the photo-BES and therefore, the ratio of nitrogen to carbon sources was manipulated to improve the performance of *R. palustris*. Three ratios were selected, namely N:C=0, N:C=0.20 and N:C=0.54. The study was broken into two phases: the evaluation of the photofermentation process of biohydrogen in photobioreatcors and the exoelectrogenic study in photoMFCs. It was found that the ratio N:C=0.20 was ideal for sufficient biomass production for a high hydrogen productivity of 1.30±0.04 ml g $biomass^{-1}$ h^{-1} at a glycerol conversion efficiency of 36.5±1.7% of the theoretical maximum conversion. The performance of *R. palustris* conditioned at the three different ratios was then analysed in photoMFCs, with carbon paper as the bioanode. A first prototype of the photoMFC consisted of capturing exocellular electrons and

biohydrogen at the same bioanode, which failed to function due to the inactivation of the catalyst. Thus, a second prototype, a hybrid hydrogen-photoMFC was designed, which housed both a photoMFC and a hydrogen fuel cell in one system. Similarly to the photobioreactors, cultures with N:C=0.20 provided the best performance in terms of power output for both the biofilm and the biohydrogen. A power output of 2.39±0.13 mW m^{-2} at an internal resistance of 50±1 kΩ was obtained from the biofilm while the oxidation of hydrogen generated a maximum power output of 361±157 mW m^{-2} at an internal resistance of 1.6±0.8 kΩ. The device performed satisfactorily as a first prototype but a more rigorous design has to be engineered to mainly prevent the volatility of the hydrogen fuel cell caused by hydrogen leakage. The exoelectrogenic activity was, further confirmed by cyclic voltammograms of the biofilm, which showed regions of electroactivity.

The following points summarise the findings in this thesis:

- Increasing the surface roughness of ITO-coated substrates resulted in a linear increase in maximum power output.
- A surface treatment introducing oxygen functionalisation groups failed to improve the hydrophilicity of carbon fibres. Inherently hydrophilic graphene paper helped to bridge the shortcomings of carbon fibres and displayed significant improved performance in MEA-type BPV devices.
- Screen-printed graphene on the membrane separator demonstrated a decrease in maximum power output with increase in surface roughness.
- MWCNTs-coated 3D-printed bioanodes were clogged with biofilm and thus the effective electrochemical surface area was significantly reduced, impacting on the electrochemical performance.
- The exoelectrogenic activity of *R. palustris* was improved by employing the same strategy that enhanced biohydrogen production; by varying the ratio of nitrogen to carbon sources. N:C=0.20 resulted in combined higher biohydrogen generation and higher exoelectrogenic activity.

Novel approaches adopted were successful in improving the efficiency of electron transfer of both *S. elongatus* and *R. palustris*. Considering both case studies, 240 µm thick graphene paper was a better performing bioanode, in terms of activation and ohmic losses as well as maximum power output and *R. palustris* conditioned at N:C=0.20 was a better exoelectrogenic bacteria.

Investigating the effect of the performance of the bioanode material as well as the performance of the microorganism on the operation of photo-BESs helped to provide a better understanding of the complex structure of the system, especially at the anode-biofilm interface.

7.2 Future Work

Electrochemical methods, such as cyclic voltammetry and double potential step chronoamperometry, were used to determine the electrochemical activity of the biofilm. However, these two methods did not always provide clear analysis. Conversely, double potential step chronocoulometry helped to remove ambiguities in some of the studies. Therefore, other pulse techniques, such as differential pulse voltammetry and square wave voltammetry, should be used to further elucidate the complex anode-biofilm interface. Moreover, a more sensitive method of electrochemical impedance spectroscopy could also be used.

The proof of concept study of the performance of both graphene-coated membrane and 3D-printed bioanodes coated with MWCNTs is at an initial phase. Therefore, further studies are required to improve their performances. The design of the 3 passes bioanodes should be further improved to obtain a trade-off between surface properties and maximum power output. Since the electrochemical active surface area of the MWCNTs-coated 3D-printed bioanodes was reduced due to clogging, the design has to be changed to take into account this issue. The performance of the 1.00 mm thick bioanode may not be relevant anymore. After optimising the performance of the bioanode, the whole system can be 3D-printed for a more compact and smart system.

In the case of *R. palustris*, the hybrid hydrogen-photoMFC is just a first working prototype. As seen by the irreproducibility in the power generated by the oxidation of hydrogen, a more rigorous design has to be engineered to prevent hydrogen leakage. Additionally, a continuous stream of biohydrogen generated in the photobioreactors

can be fed to the hybrid hydrogen-photoMFC to overcome irreproducibility. Furthermore, carbon paper bioanode should be replaced by the 240 μm thick graphene paper as it was the better performing bioanode. Combining the better bioanode with the most exoelectrognic condition of *R. palustris* should result in a better performance compared to what have been reported previously in this work.

Besides the anode material and the microorganism, the cathode material is an important part of the system. All the studies have been carried out with a platinum-based cathode. However, platinum has high cost of production and, thus, alternative materials should be sought. Transition metal-based catalyst, such as iron, cobalt and manganese are being evaluated as potential candidates for cathodic materials.[22] However, for a complete low cost and sustainable system, a biocathode would be more appropriate. Microorganisms or enzymes can be used as biocatalysts for the oxygen reduction reaction. The performance of the selected biocatalyst should be compared against a system with platinum-based cathode to identify the extent of any shortcomings.

8 References

1. Logan, B. E. Extracting Hydrogen and Electricity from Renewable Resources. *Environ. Sci. Technol.* **38,** 160A–167A (2004).
2. BP Energy Economics. *2018 BP Energy Outlook*. (2018).
3. World Energy Council. World Energy Issues Monitor 2018. 1–128 (2018). Available at: https://www.worldenergy.org/data/issues/. (Accessed: 2nd August 2018)
4. World Energy Council. World Energy Resources 2016. *World Energy Resources 2016* 1–33 (2016). doi:http://www.worldenergy.org/wp-content/uploads/2013/09/Complete_WER_2013_Survey.pdf
5. IRENA Coalition for Action. Working together to drive the global energy transition. *IRENA* 1–2 (2018). Available at: http://coalition.irena.org/-/media/Files/IRENA/Coalition-for-Action/IRENA-Coalition-for-Action_June-2018_v1.pdf. (Accessed: 4th August 2018)
6. European Commission. Renewable Energy. 1–3 (2018). Available at: https://ec.europa.eu/research/bioeconomy/index.cfm?pg=policy. (Accessed: 16th August 2018)
7. ExxonMobil. *The Outlook for energy: a view to 2040*. (2016). doi:10.1080/01998595.2012.10491656
8. Agency for Natural Resources and Energy. *Key World Energy Statistics 2017*. *IEA International Energy Agency* (2017). doi:10.1017/CBO9781107415324.004
9. Kruse, O., Rupprecht, J., Mussgnug, J. H., Dismukes, G. C. & Hankamer, B. Photosynthesis: a blueprint for solar energy capture and biohydrogen production technologies. *Photochem. Photobiol. Sci.* **4,** 957–970 (2005).
10. Blankenship, R. E. *et al.* Comparing Photosynthetic and the Potential for Improvement. *Science (80-.).* **332,** 805–809 (2011).
11. Royal Society of Chemistry. Solar Fuels and Artificial Photosynthesis. 1–26 (2012). Available at: http://www.rsc.org/globalassets/04-campaigning-outreach/policy/research-policy/global-challenges/solar-fuels-2012.pdf. (Accessed: 10th December 2018)
12. Steinfeld, A. & Meier, A. Solar fuels and materials. *Encycl. energy* **5,** 623–637 (2004).
13. Gust, D., Moore, T. a & Moore, A. L. Solar fuels via artificial photosynthesis. *Acc. Chem. Res.* **42,** 1890–8 (2009).
14. Schröder, U. Anodic electron transfer mechanisms in microbial fuel cells and their energy efficiency. *Phys. Chem. Chem. Phys.* **9,** 2619–2629 (2007).
15. McCormick, A. J. *et al.* Biophotovoltaics: oxygenic photosynthetic organisms in the world of bioelectrochemical systems. *Energy Environ. Sci.* **8,** 1092–1109 (2015).

16. Soni, R.A; Sudhakar, K and Rana, R. . Biophotovoltaics and Biohydrogen through artificial photosynthesis : an overview. **15,** 313–325 (2016).

17. Pant, D. *et al.* Bioelectrochemical systems (BES) for sustainable energy production and product recovery from organic wastes and industrial wastewaters. *RSC Adv.* **2,** 1248 (2012).

18. Potter, M. C. Electrical Effects Accompanying the Decomposition of Organic Compounds. *Proc. R. Soc. B Biol. Sci.* **84,** 260–276 (1911).

19. Bajracharya, S. *et al.* An overview on emerging bioelectrochemical systems (BESs): Technology for sustainable electricity, waste remediation, resource recovery, chemical production and beyond. *Renew. Energy* **98,** 153–170 (2016).

20. Wang, H. & Ren, Z. J. A comprehensive review of microbial electrochemical systems as a platform technology. *Biotechnol. Adv.* **31,** 1796–1807 (2013).

21. Santoro, C. *et al.* Influence of anode surface chemistry on microbial fuel cell operation. *Bioelectrochemistry* **106,** 141–149 (2015).

22. Mustakeem. Electrode materials for microbial fuel cells: Nanomaterial approach. *Mater. Renew. Sustain. Energy* **4,** 1–11 (2015).

23. Zhou, M., Chi, M., Luo, J., He, H. & Jin, T. An overview of electrode materials in microbial fuel cells. *J. Power Sources* **196,** 4427–4435 (2011).

24. Rosenbaum, M., He, Z. & Angenent, L. T. Light energy to bioelectricity: Photosynthetic microbial fuel cells. *Curr. Opin. Biotechnol.* **21,** 259–264 (2010).

25. Berk, R. S. & Canfield, J. H. Bioelectrochemical Energy Conversion. *Appl. Microbiol.* **12,** 10–12 (1964).

26. Bajracharya, S. *et al.* Long-term operation of microbial electrosynthesis cell reducing CO2to multi-carbon chemicals with a mixed culture avoiding methanogenesis. *Bioelectrochemistry* **113,** 26–34 (2017).

27. Christodoulou, X., Okoroafor, T., Parry, S. & Velasquez-Orta, S. B. The use of carbon dioxide in microbial electrosynthesis: Advancements, sustainability and economic feasibility. *J. CO2 Util.* **18,** 390–399 (2017).

28. Rabaey, K. & Rozendal, R. A. Microbial electrosynthesis - Revisiting the electrical route for microbial production. *Nat. Rev. Microbiol.* **8,** 706–716 (2010).

29. Saeed, H. M. *et al.* Microbial desalination cell technology: A review and a case study. *Desalination* **359,** 1–13 (2015).

30. Sophia, A. C. & Bhalambaal, V. M. Utilization of coconut shell carbon in the anode compartment of microbial desalination cell (MDC) for enhanced desalination and bio-electricity production. *J. Environ. Chem. Eng.* **3,** 2768–2776 (2015).

31. Cao, X. *et al.* A New Method for Water Desalination Using Microbial Desalination Cells. *Environ. Sci. Technol.* **43,** 7148–7152 (2009).

32. Driver & Bombelli, P. Biophotovoltaics Energy from algae. *Catal. Second. Sci. Rev.* **21,** 13–15 (2011).

33. Bradley, R. W., Bombelli, P., Rowden, S. J. L. & Howe, C. J. Biological photovoltaics: intra- and extra-cellular electron transport by cyanobacteria. *Biochem. Soc. Trans.* **40,** 1302–7 (2012).

34. McCormick, A. J. *et al.* Photosynthetic biofilms in pure culture harness solar energy in a mediatorless bio-photovoltaic cell (BPV) system. *Energy Environ. Sci.* **4,** 4699 (2011).

35. Zou, Y., Pisciotta, J., Billmyre, R. B. & Baskakov, I. V. Photosynthetic microbial fuel cells with positive light response. *Biotechnol. Bioeng.* **104,** 939–946 (2009).

36. Bombelli, P. *et al.* Surface morphology and surface energy of anode materials influence power outputs in a multi-channel mediatorless bio-photovoltaic (BPV) system. *Phys. Chem. Chem. Phys.* **14,** 12221–9 (2012).

37. Thorne, R., Hu, H., Schneider, K. & Bombelli, P. Porous ceramic anode materials for photo-microbial fuel cells. *J. Mater. Chem.* **21,** 18055 (2011).

38. Davis, J. . & Yarbrough, H. F. J. Preliminary Experiments on a Microbial Fuel Cell. *Science (80-.).* **137,** 615–616 (1962).

39. De Caprariis, B., De Filippis, P., Di Battista, A., DiPalma, L. & Scarsella, M. Exoelectrogenic activity of a green microalgae, chlorella vulgaris, in a bio-photovoltaic cells (bpvs). *Chem. Eng. Trans.* **38,** 523–528 (2014).

40. European Commission. Bioeconomy. 1–3 (2018). Available at: https://ec.europa.eu/research/bioeconomy/index.cfm?pg=policy. (Accessed: 16th August 2018)

41. Bombelli, P., Müller, T., Herling, T. W., Howe, C. J. & Knowles, T. P. J. A High Power-Density, Mediator-Free, Microfluidic Biophotovoltaic Device for Cyanobacterial Cells. *Adv. Energy Mater.* n/a-n/a (2014). doi:10.1002/aenm.201401299

42. Bradley, R. W., Bombelli, P., Lea-Smith, D. J. & Howe, C. J. Terminal oxidase mutants of the cyanobacterium Synechocystis sp. PCC 6803 show increased electrogenic activity in biological photo-voltaic systems. *Phys. Chem. Chem. Phys.* **15,** 13611–8 (2013).

43. Oster, U., Bauer, C. E. & Rüdiger, W. Characterization of chlorophyll a and bacteriochlorophyll a synthases by heterologous expression in Escherichia coli. *J. Biol. Chem.* **272,** 9671–9676 (1997).

44. Michigan State University. Introductory Microbiology: Photosynthesis. Available at: https://msu.edu/course/mmg/301/Lec21.pdf. (Accessed: 23rd May 2018)

45. Björn, L. O., Papageorgiou, G. C., Blankenship, R. E. & Govindjee. A viewpoint: Why chlorophyll a? *Photosynth. Res.* **99,** 85–98 (2009).

46. Weigl, J. W. Concerning the Absorption Spectrum of Bacteriochlorophyll. *J. Am. Chem. Soc.* **75,** 999–1000 (1953).

47. Okubo, Y., Futamata, H. & Hiraishi, A. Characterization of phototrophic purple nonsulfur bacteria forming colored microbial mats in a swine wastewater ditch. *Appl. Environ. Microbiol.* **72,** 6225–6233 (2006).

48. Hanada, S. Anoxygenic Photosynthesis —A Photochemical Reaction That Does Not Contribute to Oxygen Reproduction—. *Microbes Environ.* **31,** 1–3 (2016).

49. European Commission. FUTURE BRIEF : Bioelectrochemical systems Bioelectrochemical systems : Wastewater treatment , bioenergy and valuable. *Sci. Environ. Policy* (2013).

50. Gault, P. M. & Marler, H. J. *Handbook on cyanobacteria:Biochemistry, Biotechnology and Applications*. (Nova Science Publishers, Inc, 2009).

51. Yu, J. *et al.* Synechococcus elongatus UTEX 2973, a fast growing cyanobacterial chassis for biosynthesis using light and CO_2. *Sci. Rep.* **5,** 8132 (2015).

52. Sekar, N., Umasankar, Y. & Ramasamy, R. P. Photocurrent generation by immobilized cyanobacteria via direct electron transport in photo-bioelectrochemical cells. *Phys. Chem. Chem. Phys.* **16,** 7862–7871 (2014).

53. Nevo, R. *et al.* Thylakoid membrane perforations and connectivity enable intracellular traffic in cyanobacteria. *EMBO J.* **26,** 1467–1473 (2007).

54. Lea-Smith, D. J., Bombelli, P., Vasudevan, R. & Howe, C. J. Photosynthetic, respiratory and extracellular electron transport pathways in cyanobacteria. *Biochim. Biophys. Acta - Bioenerg.* **1857,** 247–255 (2015).

55. Flores, E. & Herrero, A. *The Cell Biology of Cyanobacteria*. (Caister Academic Press, 2014).

56. Bryant, D. A. *The Molecular Biology of Cyanobacteria*. **I,** (Springer-Science+Business Media, B.V, 1994).

57. Mielke, S. P., Kiang, N. Y., Blankenship, R. E., Gunner, M. R. & Mauzerall, D. Efficiency of photosynthesis in a Chl d-utilizing cyanobacterium is comparable to or higher than that in Chl a-utilizing oxygenic species. *Biochim. Biophys. Acta - Bioenerg.* **1807,** 1231–1236 (2011).

58. Govindjee. in *Chlorophyll Fluorescence: A signature of Photosynthesis* (ed. Papageorgiou, G. C.) 1–42 (Kluwer Academic Publishers, 2004). doi:10.1007/978-1-4020-6682-5

59. Senge, M. O., Ryan, A. A., Letchford, K. A., MacGowan, S. A. & Mielke, T. Chlorophylls, symmetry, chirality, and photosynthesis. *Symmetry (Basel).* **6,** 781–843 (2014).

60. Larimer, F. W. *et al.* Complete genome sequence of the metabolically versatile photosynthetic bacterium Rhodopseudomonas palustris. *Nat. Biotechnol.* **22,** 55–61 (2004).

61. van Niel, C. B. The Culture, General Physiology, Morphology, and Classification of the Non-Sulfur Purple and Brown Bacteria. *Bacteriol. Rev.* **8,** 1–118 (1944).

62. Pott, R. W. M. The Bioconversion of Waste Glycerol into Hydrogen by Rhodopseudomonas palustris. (University of Cambridge, 2013).

63. McKinlay, J. B. in *Microbial Bioenergy: Hydrogen Production* (eds. Zannoni, D. & De Philippis, R.) 155–176 (Springer, 2014). doi:10.1007/978-94-017-8554-9

64. Adessi, A. & De Philippis, R. in *Microbial Technologies inAdvanced Biofuels* (ed. Hallenbeck, P. C.) 53–76 (Springer Science+Business Media, 2012). doi:10.1007/978-1-4614-1208-3

65. Qi, X., Ren, Y., Liang, P. & Wang, X. New insights in photosynthetic microbial fuel cell using anoxygenic phototrophic bacteria. *Bioresour. Technol.* **258,** 310–317 (2018).

66. Rey, F. E., Heiniger, E. K. & Harwood, C. S. Redirection of metabolism for

biological hydrogen production. *Appl. Environ. Microbiol.* **73,** 1665–1671 (2007).

67. Gosse, J. L. *et al.* Hydrogen production by photoreactive nanoporous latex coatings of nongrowing Rhodopseudomonas palustris CGA009. *Biotechnol. Prog.* **23,** 124–130 (2007).

68. Parlevliet, D. & Moheimani, N. R. Efficient conversion of solar energy to biomass and electricity. *Aquat. Biosyst.* **10,** 4 (2014).

69. McKinlay, J. B. *et al.* Non-growing rhodopseudomonas palustris increases the hydrogen gas yield from acetate by shifting from the glyoxylate shunt to the tricarboxylic acid cycle. *J. Biol. Chem.* **289,** 1960–1970 (2014).

70. Varga, A. & Staehelin, L. A. Spatial Differentiation in Photosyntetic and Non-photosynthetic Membranes of Rhodopseudomonas palustris. *J. Bacteriol.* **154,** 1414–1430 (1983).

71. Bruslind, L. in *Microbiology* 1–10 (Pressbooks.com: Simple Book Production, 2018).

72. Roszak, A. W. *et al.* Crystal structure of the RC-LH1 core complex from *Rhodopseudomonas palustris*. *Science* **302,** 1969–1972 (2003).

73. McKinlay, J. B. & Harwood, C. S. Carbon dioxide fixation as a central redox cofactor recycling mechanism in bacteria. *Proc. Natl. Acad. Sci.* **107,** 11669–11675 (2010).

74. Arnon, D. I., Tsujimoto, H. Y. & McSwain, B. D. Photosynthetic Phosphorylation and Electron Transport. *Nature* **208,** 239–241 (1965).

75. Koku, H., Erolu, I., Gunduz, U., Yucel, M. & Turker, L. Aspect of the metabolism of hydrogen production by Rhodobacter sphaeroides. *Int J Hydrog. Energy* **27,** 1315–1329 (2002).

76. Kim, D. H. & Kim, M. S. Hydrogenases for biological hydrogen production. *Bioresour. Technol.* **102,** 8423–8431 (2011).

77. Basak, N., Jana, A. K., Das, D. & Saikia, D. Photofermentative molecular biohydrogen production by purple-non-sulfur (PNS) bacteria in various modes: The present progress and future perspective. *Int. J. Hydrogen Energy* **39,** 6853–6871 (2014).

78. Gabrielyan, L., Sargsyan, H. & Trchounian, A. Novel properties of photofermentative biohydrogen production by purple bacteria Rhodobacter sphaeroides: effects of protonophores and inhibitors of responsible enzymes. *Microb. Cell Fact.* **14,** 131 (2015).

79. Kadier, A. *et al.* Recent advances and emerging challenges in microbial electrolysis cells (MECs) for microbial production of hydrogen and value-added chemicals. *Renew. Sustain. Energy Rev.* **61,** 501–525 (2016).

80. Shi, L. *et al.* Extracellular electron transfer mechanisms between microorganisms and minerals. *Nat Rev Microbiol* **14,** 651–662 (2016).

81. Logan, B. E. Exoelectrogenic bacteria that power microbial fuel cells. *Nat. Rev. Microbiol.* **7,** 375–381 (2009).

82. Patil, S. A., Hägerhäll, C. & Gorton, L. Electron transfer mechanisms between

microorganisms and electrodes in bioelectrochemical systems. *Bioanal. Rev.* **1,** 71–129 (2014).

83. Yuan, Y., Zhou, S., Zhao, B., Zhuang, L. & Wang, Y. Microbially-reduced graphene scaffolds to facilitate extracellular electron transfer in microbial fuel cells. *Bioresour. Technol.* **116,** 453–458 (2012).

84. Bensaid, S., Ruggeri, B. & Saracco, G. Development of a photosynthetic microbial electrochemical cell (PMEC) reactor coupled with dark fermentation of organic wastes: Medium term perspectives. *Energies* **8,** 399–429 (2015).

85. Bacakova, L., Filova, E., Parizek, M., Ruml, T. & Svorcik, V. Modulation of cell adhesion, proliferation and differentiation on materials designed for body implants. *Biotechnol. Adv.* **29,** 739–767 (2011).

86. Legeay, G., Coudreuse, A., Poncin-Epaillard, F., Herry, J. M. & Bellon-Fontaine, M. N. Surface engineering and cell adhesion. *J. Adhes. Sci. Technol.* **24,** 2301–2322 (2010).

87. Schneider, K., Thorne, R. J. & Cameron, P. J. An investigation of anode and cathode materials in photomicrobial fuel cells. *Philos. Trans. A* **374,** 20150080 (2016).

88. Therdthianwong, A., Manomayidthikarn, P. & Therdthianwong, S. Investigation of membrane electrode assembly (MEA) hot-pressing parameters for proton exchange membrane fuel cell. *Energy* **32,** 2401–2411 (2007).

89. Pak, C., You, D. J., Choi, K. H. & Chang, H. in *Hydrogen Energy-Challenges and Perspectives* (ed. Minic, D.) 259–278 (IntechOpen, 2012). doi:http://dx.doi.org/10.5772/53683

90. Park, S., Lee, J. W. & Popov, B. N. A review of gas diffusion layer in PEM fuel cells: Materials and designs. *Int. J. Hydrogen Energy* **37,** 5850–5865 (2012).

91. Gasik, M. Materials for fuel cells. *Mater. Fuel Cells* 1–498 (2008). doi:10.1533/9781845694838

92. Nandy, A. *et al.* Performance evaluation of microbial fuel cells: Effect of varying electrode configuration and presence of a membrane electrode assembly. *N. Biotechnol.* **32,** 272–281 (2015).

93. Koraishy, B., Meyers, J. & Wood, K. Manufacturing of membrane electrode assemblies for fuel cells. *Researchgate.Net* 1–13 (2010).

94. Stolten, D. & Emonts, B. *Fuel Cell Science and Engineering: Materials, Processes, Systems and Technology*. **1,** (Wiley-VCH, 2012).

95. Modin, O. & Wilén, B. M. A novel bioelectrochemical BOD sensor operating with voltage input. *Water Res.* **46,** 6113–6120 (2012).

96. Chouler, J. *et al.* Towards effective small scale microbial fuel cells for energy generation from urine. *Electrochim. Acta* **192,** 89–98 (2016).

97. Logan, B. E. *et al.* Microbial fuel cells: Methodology and technology. *Environ. Sci. Technol.* **40,** 5181–5192 (2006).

98. Logan, B. E. *Microbial Fuel Cells*. (John Wiley & Sons, Inc., 2008).

99. Rabaey, K., Angenent, L. T., Schröder, U. & Keller, J. in *Bioelectrochemical systems : from extracellular electron transfer to biotechnological application* 119–132

(IWA Publishing, 2010).

100. Benziger, J. B., Satterfield, M. B., Hogarth, W. H. J., Nehlsen, J. P. & Kevrekidis, I. G. The power performance curve for engineering analysis of fuel cells. *J. Power Sources* **155,** 272–285 (2006).

101. Calignano, F., Tommasi, T., Manfredi, D. & Chiolerio, A. Additive Manufacturing of a Microbial Fuel Cell—A detailed study. *Sci. Rep.* **5,** 17373 (2015).

102. Aelterman, P., Rabaey, K. & Verstraete, W. Continuous Electricity Generation at High Voltages and Currents using Stacked Microbial Fuel Cells. *Environ. Sci. Technol.* **40,** 3388–3394 (2006).

103. Winfield, J., Ieropoulos, I., Greenman, J. & Dennis, J. The overshoot phenomenon as a function of internal resistance in microbial fuel cells. *Bioelectrochemistry* **81,** 22–27 (2011).

104. Ieropoulos, I., Winfield, J. & Greenman, J. Effects of flow-rate, inoculum and time on the internal resistance of microbial fuel cells. *Bioresour. Technol.* **101,** 3520–3525 (2010).

105. Compton, Richard G, Laborda,E, Ward, K. . *Understanding Voltammetry: Simulation of Electrode Processes*. (Imperial College Press, 2014).

106. Bard, A. J. & Faulkner, L. R. *Electrochemical Methods Fundamentals and Applications*. (John Wiley & Sons, Inc., 2001). doi:10.1016/B978-0-08-098353-0.00003-8

107. Zhao, F., Slade, R. C. T. & Varcoe, J. R. Techniques for the study and development of microbial fuel cells: An electrochemical perspective. *Chem. Soc. Rev.* **38,** 1926–1939 (2009).

108. Pyun, S.-I., Shin, H.-C., Lee, J.-W. & Go, J.-Y. in *Electrochemistry of Insertion Materials for Hydrogen and Lithium* (Springer, 2012). doi:10.1007/978-3-642-29464-8

109. Fisher, A. C. *Electrode Dynamics*. (Oxford University Press, 1996).

110. Harnisch, F. & Freguia, S. A basic tutorial on cyclic voltammetry for the investigation of electroactive microbial biofilms. *Chem. - An Asian J.* **7,** 466–475 (2012).

111. Marsili, E., Rollefson, J. B., Baron, D. B., Hozalski, R. M. & Bond, D. R. Microbial biofilm voltammetry: Direct electrochemical characterization of catalytic electrode-attached biofilms. *Appl. Environ. Microbiol.* **74,** 7329–7337 (2008).

112. Babauta, J., Renslow, R., Lewandowski, Z. & Beyenal, H. Electrochemically active biofilms: facts and fiction. A review. *NCBI* **28,** 789–812 (2012).

113. Fricke, K., Harnisch, F. & Schröder, U. On the use of cyclic voltammetry for the study of anodic electron transfer in microbial fuel cells. *Energy Environ. Sci.* **1,** 144 (2008).

114. Klymenko, O. V., Evans, R. G., Hardacre, C., Svir, I. B. & Compton, R. G. Double potential step chronoamperometry at microdisk electrodes: Simulating the case of unequal diffusion coefficients. *J. Electroanal. Chem.* **571,** 211–221 (2004).

115. Fourmond, V., Infossi, P., Giudici-Orticoni, M. T., Bertrand, P. & Léger, C. 'Two-

Step' chronoamperometric method for studying the anaerobic inactivation of an oxygen tolerant nife hydrogenase. *J. Am. Chem. Soc.* **132,** 4848–4857 (2010).

116. Owens, J. L., Marsh, H. A. & Dryhurst, G. Electrochemical Oxidation of Uric Acid and Xanthine: An Investigation by Cyclic Voltammetry, Double Potential Step Chronoamperometry and Thin-layer Spectroelectrochemistry. **91,** 231–247 (1978).

117. Ryan, D. Lecture 8: Chronoamperometry. *Univ. Massachusetts Lowell* (2005).

118. Zhang, X. *et al.* Rapid and Quantitative Assessment of Redox Conduction Across Electroactive Biofilms by using Double Potential Step Chronoamperometry. *ChemElectroChem* **4,** 1026–1036 (2017).

119. Wei, J., Liang, P. & Huang, X. Recent progress in electrodes for microbial fuel cells. *Bioresour. Technol.* **102,** 9335–9344 (2011).

120. Meher Kotay, S. & Das, D. Biohydrogen as a renewable energy resource-Prospects and potentials. *Int. J. Hydrogen Energy* **33,** 258–263 (2008).

121. Hallenbeck, P. C. Fermentative hydrogen production: Principles, progress, and prognosis. *Int. J. Hydrogen Energy* **34,** 7379–7389 (2009).

122. Hallenbeck, P. C., Abo-Hashesh, M. & Ghosh, D. Strategies for improving biological hydrogen production. *Bioresour. Technol.* **110,** 1–9 (2012).

123. Das, D. & Veziroglu, T. N. Advances in biological hydrogen production processes. *Int. J. Hydrogen Energy* **33,** 6046–6057 (2008).

124. Culture Collection of Algae and Protozoa. BG11 (Blue--Green Medium). (2014).

125. Bondioli, P. & Della Bella, L. An alternative spectrophotometric method for the determination of free glycerol in biodiesel. *Eur. J. Lipid Sci. Technol.* **107,** 153–157 (2005).

126. Moore, B. Y. S. & Stein, H. Photometric Ninhydrin Method for Use in the Chromatography of Amino Acids. *J. Biol. Chem.* **176,** 367–388 (1948).

127. Wang, N. S. Amino Acid Assay by Ninhydrin Colorimetric Method. 1–4 (2009). Available at: https://eng.umd.edu/~nsw/ench485/lab3a.htm. (Accessed: 22nd May 2018)

128. Stal, L. J., van Gemerden, H. & Krumbein, W. E. The simultaneous assay of chlorophyll and bacteriochlorophyll in natural microbial communities. *J. Microbiol. Methods* **2,** 295–306 (1984).

129. Namsaraev, Z. B. Application of extinction coefficients for quantification of chlorophylls and bacteriochlorophylls. *Microbiology* **78,** 794–797 (2009).

130. Frigaard, N. U., Larsen, K. L. & Cox, R. P. Spectrochromatography of photosynthetic pigments as a fingerprinting technique for microbial phototrophs. *FEMS Microbiol. Ecol.* **20,** 69–77 (1996).

131. Permentier, H.P, Schmidt, K.A, Kobayashi, M, Akiyama, M, Hager-Braun, C, Neerken, S, Miller, M, Amesz, J. Composition and optical properties of reaction centre core complexes from the green sulfur bacteria Prosthecochloris aestuarii and Chlorobium tepidum. *Photosynth. Res.* **64,** 27–39 (2000).

132. Zavrel, Tomas, Sinetova, M.A, Cerveny, J. Measurement of Chlorophyll a and

Carotenoids Concentration in Cyanobacteria. *Bio-protocol* **5,** 1–5 (2015).

133. Gonzalez-Aravena, A. C., Yunus, K., Zhang, L., Norling, B. & Fisher, A. C. Tapping into cyanobacteria electron transfer for higher exoelectrogenic activity by imposing iron limited growth. *RSC Adv.* **8,** 20263–20274 (2018).

134. Zhao, Y. *et al.* Three-dimensional conductive nanowire networks for maximizing anode performance in microbial fuel cells. *Chem. - A Eur. J.* **16,** 4982–4985 (2010).

135. Cao, J. *et al.* A Preliminary Study of the Effect of Surface Texture on Algae Cell Attachment for a Mechanical-Biological Energy Manufacturing System. *J. Manuf. Sci. Eng.* **131,** 064505 (2009).

136. Sekar, R., Venugopalan, V. P., Satpathy, K. K., Nair, K. V. K. & Rao, V. N. R. Laboratory studies on adhesion of microalgae to hard substrates. *Hydrobiologia* **512,** 109–116 (2004).

137. Han, Y. & Furukawa, Y. Conducting polyaniline and biofuel cell. *Int. J. Green Energy* **3,** 17–23 (2006).

138. Zou, Y., Pisciotta, J. & Baskakov, I. V. Nanostructured polypyrrole-coated anode for sun-powered microbial fuel cells. *Bioelectrochemistry* **79,** 50–56 (2010).

139. Brown, A. P., Krumpelt, M., Loutfy, R. . & Yao, N. . The effect of surface roughness on the hydrogen evolution reaction kineticswith mild steel and nickel cathodes. *Electrochim. Acta* **27,** 557–560 (1982).

140. Herraiz-Cardona, I., Ortega, E., Antón, J. G. & Pérez-Herranz, V. Assessment of the roughness factor effect and the intrinsic catalytic activity for hydrogen evolution reaction on Ni-based electrodeposits. *Int. J. Hydrogen Energy* **36,** 9428–9438 (2011).

141. Wenzel, T., Härtter, D., Bombelli, P., Howe, C. J. & Steiner, U. Porous translucent electrodes enhance current generation from photosynthetic biofilms. *Nat. Commun.* **9,** 1–9 (2018).

142. Ng, F.-L. *et al.* Reduced Graphene Oxide Anodes for Potential Application in Algae Biophotovoltaic Platforms. *Sci. Rep.* **4,** 7562 (2014).

143. Ng, F.-L., Phang, S.-M., Periasamy, V., Yunus, K. & Fisher, A. C. Evaluation of algal biofilms on indium tin oxide (ITO) for use in biophotovoltaic platforms based on photosynthetic performance. *PLoS One* **9,** e97643 (2014).

144. Inglesby, A. E., Yunus, K. & Fisher, A. C. In situ fluorescence and electrochemical monitoring of a photosynthetic microbial fuel cell. *Phys. Chem. Chem. Phys.* **15,** 6903–11 (2013).

145. Ng, F. L., Phang, S. M., Periasamy, V., Yunus, K. & Fisher, A. C. Algae Biofilm on Indium Tin Oxide Electrode for Use in Biophotovoltaic Platforms. *Adv. Mater. Res.* **895,** 116–121 (2014).

146. Karagiannidis, P. G. *et al.* Microfluidization of Graphite and Formulation of Graphene-Based Conductive Inks. *ACS Nano* **11,** 2742–2755 (2017).

147. Whistler, R. . & BeMiller, J. . *Industrial gums: Polysaccharides and their derivatives*. (Academic Press, 1993). doi:10.1002/actp.1993.010440315

148. Lee, D. H., Choi, J. S., Chae, H., Chung, C. H. & Cho, S. M. Screen-printed white OLED based on polystyrene as a host polymer. *Curr. Appl. Phys.* **9,** 161–164 (2009).

149. Gonzalez Aravena, A. C. Strategies to enhance extracellular electron transfer rates in wild-type cyanobacterium Synechococcus elongatus PCC7942 for photo-bioelectricity generation. (University of Cambridge, 2018). doi:https://doi.org/10.17863/CAM.21475

150. Khan, S., Lorenzelli, L. & Dahiya, R. S. Technologies for printing sensors and electronics over large flexible substrates: A review. *IEEE Sens. J.* **15,** 3164–3185 (2015).

151. Tobjörk, D. & Österbacka, R. Paper electronics. *Adv. Mater.* **23,** 1935–1961 (2011).

152. Lee, P. T., Lowinsohn, D. & Compton, R. G. The use of screen-printed electrodes in a proof of concept electrochemical estimation of homocysteine and glutathione in the presence of Cysteine using catechol. *Sensors (Switzerland)* **14,** 10395–10411 (2014).

153. Medina-Plaza, C. *et al.* The advantages of disposable screen-printed biosensors in a bioelectronic tongue for the analysis of grapes. *LWT - Food Sci. Technol.* **62,** 940–947 (2015).

154. Goldberg, H. D., Brown, R. B., Liu, D. P. & Meyerhoff, M. E. Screen printing: a technology for the batch fabrication of integrated chemical-sensor arrays. *Sensors Actuators B. Chem.* **21,** 171–183 (1994).

155. Sure, S. *et al.* Inquisition of Microcystis aeruginosa and Synechocystis nanowires: characterization and modelling. *Antonie van Leeuwenhoek, Int. J. Gen. Mol. Microbiol.* **108,** 1213–1225 (2015).

156. Gorby, Y. A. *et al.* Electrically conductive bacterial nanowires produced by Shewanella oneidensis starin MR-1 and other microorganisms. **103,** 11358–11363 (2006).

157. Jones, S. New electricigens get wired. *Nat. Rev. Microbiol.* **4,** 642–642 (2006).

158. Sure, S., Ackland, M. L., Torriero, A. A. J., Adholeya, A. & Kochar, M. Microbial nanowires: An electrifying tale. *Microbiol. (United Kingdom)* **162,** 2017–2028 (2016).

159. Kim, K. J. *et al.* A new strategy for integrating abundant oxygen functional groups into carbon felt electrode for vanadium redox flow batteries. *Sci. Rep.* **4,** 6906 (2014).

160. Zhao, T. & Jiang, L. Contact angle measurement of natural materials. *Colloids Surfaces B Biointerfaces* **161,** 324–330 (2018).

161. Kim, K. J., Kim, Y. J., Kim, J. H. & Park, M. S. The effects of surface modification on carbon felt electrodes for use in vanadium redox flow batteries. *Mater. Chem. Phys.* **131,** 547–553 (2011).

162. Stepniak, I. & Ciszewski, A. Grafting effect on the wetting and electrochemical performance of carbon cloth electrode and polypropylene separator in electric double layer capacitor. *J. Power Sources* **195,** 5130–5137 (2010).

163. Kumar, G. G., Sarathi, V. G. S. & Nahm, K. S. Recent advances and challenges in the

anode architecture and their modifications for the applications of microbial fuel cells. *Biosens. Bioelectron.* **43,** 461–475 (2013).

164. Zhao, Q., Liu, Y., Wang, C., Wang, S. & Müller-Steinhagen, H. Effect of surface free energy on the adhesion of biofouling and crystalline fouling. *Chem. Eng. Sci.* **60,** 4858–4865 (2005).

165. Feng, G. *et al.* Bacterial attachment and biofilm formation on surfaces are reduced by small-diameter nanoscale pores: How small is small enough? *npj Biofilms Microbiomes* **1,** (2015).

166. Mérian, T. & Goddard, J. M. Advances in nonfouling materials: Perspectives for the food industry. *J. Agric. Food Chem.* **60,** 2943–2957 (2012).

167. Meng, C. *et al.* Insight into the Role of Surface Wettability in Electrocatalytic Hydrogen Evolution Reactions Using Light-Sensitive Nanotubular TiO2 Supported Pt Electrodes. *Sci. Rep.* **7,** 41825 (2017).

168. Flexer, V., Marque, M., Donose, B. C., Virdis, B. & Keller, J. Plasma treatment of electrodes significantly enhances the development of anodic electrochemically active biofilms. *Electrochim. Acta* **108,** 566–574 (2013).

169. Sheng, Y. Investigation of Electrolyte Wetting in Lithium Ion Batteries : Effects of Electrode Pore Structures and Solution. *Thesis* (University of Wisconsin-Milwaukee, 2015).

170. Ruiz-Rosas, R., Bohorquez-Guarin, E., Cazorla-Amoros, D. & Morallon, E. in *Innovations in Engineered Mesoporous Material for Energy Conversion and Storage Applications* (eds. Rajagopalan, R. & Balakrishnan, A.) 109–142 (CRC Press, 2018).

171. Store, F. C. Toray Carbon Paper. 1–2 (2018). Available at: http://www.fuelcellsetc.com/store/DS/Toray-Paper-TGP-H-Datasheet.pdf.

172. Chen, Q., Gerhardt, M. R., Hartle, L. & Aziz, M. J. A Quinone-Bromide Flow Battery with 1 W/cm2 Power Density. *J. Electrochem. Soc.* **163,** (2015).

173. González-García, J. *et al.* Characterization of a carbon felt electrode: structural and physical properties Experimental details. *J. Mater. Chem.* **9,** 419–426 (1998).

174. XG Sciences Inc. XG Leaf ®, Product Overview. (2018). Available at: https://xgsciences.com/wp-content/uploads/2018/03/XG-Leaf.-MD00007.-2018-1.pdf.

175. González-Sánchez, M. I., Gómez-Monedero, B., Agrisuelas, J., Iniesta, J. & Valero, E. Highly activated screen-printed carbon electrodes by electrochemical treatment with hydrogen peroxide. *Electrochem. commun.* **91,** 36–40 (2018).

176. Krasowska, A. & Sigler, K. How microorganisms use hydrophobicity and what does this mean for human needs? *Front. Cell. Infect. Microbiol.* **4,** 1–7 (2014).

177. Choi, N.-Y., Bae, Y.-M. & Lee, S.-Y. Cell surface properties and biofilm formation of pathogenic bacteria. *Food Sci. Biotechnol.* **24,** 2257–2264 (2015).

178. Zhang, Y. *et al.* A graphene modified anode to improve the performance of microbial fuel cells. *J. Power Sources* **196,** 5402–5407 (2011).

179. Xu, Y. *et al.* Solvated graphene frameworks as high-performance anodes for

lithium-ion batteries. *Angew. Chemie - Int. Ed.* **54,** 5345–5350 (2015).

180. Li, C. & Shi, G. Functional gels based on chemically modified graphenes. *Adv. Mater.* **26,** 3992–4012 (2014).

181. Geim, A. . & Novoselov, K. . The rise of graphene. *Natute Mater.* **6,** 183–191 (2007).

182. Yuan, H. & He, Z. Graphene-modified electrodes for enhancing the performance of microbial fuel cells. *Nanoscale* **7,** 7022–7029 (2015).

183. Zhao, S. *et al.* Three-dimensional graphene/Pt nanoparticle composites as freestanding anode for enhancing performance of microbial fuel cells. *Sci. Adv.* **1,** e1500372–e1500372 (2015).

184. Liu, J. *et al.* Graphene/carbon cloth anode for high-performance mediatorless microbial fuel cells. *Bioresour. Technol.* **114,** 275–280 (2012).

185. Jaafar, M. M. *et al.* Preparation of a Three-Dimensional Reduced Graphene Oxide Film by Using the Langmuir-Blodgett Method. *Langmuir* **31,** 10426–10434 (2015).

186. Kiliszek, M. *et al.* Orientation of photosystem I on graphene through cytochrome c_{553} leads to improvement in photocurrent generation. *J. Mater. Chem. A* (2018). doi:10.1039/C8TA02420K

187. Gunther, D. *et al.* Photosystem i on graphene as a highly transparent, photoactive electrode. *Langmuir* **29,** 4177–4180 (2013).

188. Correa-Duarte, M. A. *et al.* Fabrication and biocompatibility of carbon nanotube-based 3D networks as scaffolds for cell seeding and growth. *Nano Lett.* **4,** 2233–2236 (2004).

189. Heister, E., Brunner, E. W., Dieckmann, G. R., Jurewicz, I. & Dalton, A. B. Are carbon nanotubes a natural solution? applications in biology and medicine. *ACS Appl. Mater. Interfaces* **5,** 1870–1891 (2013).

190. Erbay, C. *et al.* Control of geometrical properties of carbon nanotube electrodes towards high-performance microbial fuel cells. *J. Power Sources* **280,** 347–354 (2015).

191. Sawa, M. *et al.* Electricity generation from digitally printed cyanobacteria. *Nat. Commun.* **8,** 1–9 (2017).

192. Sekar, N., Jain, R., Yan, Y. & Ramasamy, R. P. Enhanced photo-bioelectrochemical energy conversion by genetically engineered cyanobacteria. *Biotechnol. Bioeng.* **113,** 675–679 (2016).

193. You, J., Preen, R. J., Bull, L., Greenman, J. & Ieropoulos, I. 3D printed components of microbial fuel cells: Towards monolithic microbial fuel cell fabrication using additive layer manufacturing. *Sustain. Energy Technol. Assessments* **19,** 94–101 (2017).

194. Bian, B. *et al.* Application of 3D Printed Porous Copper Anode in Microbial Fuel Cells. **6,** 1–9 (2018).

195. Sachyani, E. *et al.* Enhanced movement of CNT-based actuators by a three-Layered structure with controlled resistivity. *Sensors Actuators, B Chem.* **252,**

1071–1077 (2017).

196. Sabourin-Provost, G. & Hallenbeck, P. C. High yield conversion of a crude glycerol fraction from biodiesel production to hydrogen by photofermentation. *Bioresour. Technol.* **100,** 3513–3517 (2009).

197. Pott, R. W. M., Howe, C. J. & Dennis, J. S. Photofermentation of crude glycerol from biodiesel using Rhodopseudomonas palustris: Comparison with organic acids and the identification of inhibitory compounds. *Bioresour. Technol.* **130,** 725–730 (2013).

198. Pott, R. W. M., Howe, C. J. & Dennis, J. S. The purification of crude glycerol derived from biodiesel manufacture and its use as a substrate by Rhodopseudomonas palustris to produce hydrogen. *Bioresour. Technol.* **152,** 464–470 (2014).

199. Sang Kim, J., Ito, K. & Takahashi, H. The Relationship between Nitrogenase Activity and Hydrogen Evolution in Rhodopseudomonas palustris. *Agric. Biol. Chem.* **44,** 827–833 (2014).

200. Häggström, L. Kinetics of product formation in batch and continuous culture of Clostridium barkeri. *Appl. Microbiol. Biotechnol.* **23,** 187–190 (1986).

201. IIT Kharagpur Virtual Lab. Chemical Process Dynamics Laboratory: Feed Batch Fermentor. 1–3 (2018). Available at: http://iitkgp.vlab.co.in/?sub=35&brch=107&sim=1206&cnt=1. (Accessed: 20th May 2018)

202. Mutharasan, R. Engineering Biotechnology: Bioreactors. Available at: http://www.gatewaycoalition.org/files/hidden/react/Ch4/4_5f.htm. (Accessed: 20th May 2018)

203. Zhang, D. *et al.* Bioprocess modelling of biohydrogen production by Rhodopseudomonas palustris: Model development and effects of glutamate and operating conditions on hydrogen production and glycerol conversion efficiency. *Biotechnol. Bioeng.* **130,** 68–78 (2014).

204. Xiao, N. Use a Purple Non-Sulphur Bacterium , Rhodopseudomonas palustris , as a Biocatalyst for Hydrogen Production. (University of Cambridge, 2017). doi:https://doi.org/10.17863/CAM.16680

205. Xing, D., Zuo, Y., Cheng, S., Regan, J. M. & Logan, B. E. Electricity generation by Rhodopseudomonas palustris DX-1. *Environ. Sci. Technol.* **42,** 4146–4151 (2008).

206. Morishima, K. *et al.* Improving the performance of a direct photosynthetic/metabolic bio-fuel cell (DPBFC) using gene manipulated bacteria. *J. Micromechanics Microengineering* **17,** (2007).

207. Inglesby, A. E., Beatty, D. a. & Fisher, A. C. Rhodopseudomonas palustris purple bacteria fed Arthrospira maxima cyanobacteria: demonstration of application in microbial fuel cells. *RSC Adv.* **2,** 4829 (2012).

208. Venkidusamy, K. & Megharaj, M. A novel electrophototrophic bacterium: Rhodopseudomonas palustris strain RP2, exhibits hydrocarbonoclastic potential in anaerobic environments. *Front. Microbiol.* **7,** 1–12 (2016).

209. Rosenbaum, M., Schröder, U. & Scholz, F. In situ electrooxidation of

photobiological hydrogen in a photobioelectrochemical fuel cell based on Rhodobacter sphaeroides. *Environ. Sci. Technol.* **39,** 6328–6333 (2005).

210. Niessen, J., Schröder, U., Harnisch, F. & Scholz, F. Gaining electricity from in situ oxidation of hydrogen produced by fermentative cellulose degradation. *Lett. Appl. Microbiol.* **41,** 286–290 (2005).

211. Rosenbaum, M., Schröder, U. & Scholz, F. Utilizing the green alga Chlamydomonas reinhardtii for microbial electricity generation: A living solar cell. *Appl. Microbiol. Biotechnol.* **68,** 753–756 (2005).

212. Dante, R. C. Hypotheses for direct PEM fuel cells applications of photobioproduced hydrogen by Chlamydomonas reinhardtii. *Int. J. Hydrogen Energy* **30,** 421–423 (2005).

213. Hu, J. GDE Fabrication. (2009). Available at: web.mit.edu/jjhu/www/stuff/MEA fab.doc.

214. Hu, J. E., Liu, Z., Eichhorn, B. W. & Jackson, G. S. CO tolerance of nano-architectured Pt-Mo anode electrocatalysts for PEM fuel cells. *Int. J. Hydrogen Energy* **37,** 11268–11275 (2012).

215. Carlozzi, P. Hydrogen photoproduction by rhodopseudomonas palustris 42ol cultured at high irradiance under a semicontinuous regime. *J. Biomed. Biotechnol.* **2012,** (2012).

216. Maier, R. M. in *Environmental Microbiology* 37–54 (2009). doi:10.1016/B978-0-12-370519-8.00003-1

217. Zhang, D. *et al.* Dynamic modelling of high biomass density cultivation and biohydrogen production in different scales of flat plate photobioreactors. *Biotechnol. Bioeng.* **112,** 2429–2438 (2015).

218. Venkidusamy, K. *et al.* Electron transport through electrically conductive nanofilaments in Rhodopseudomonas palustris strain RP2. *RSC Adv.* **5,** 100790–100798 (2015).

219. Lojou, É. & Bianco, P. Membrane electrodes for protein and enzyme electrochemistry. *Electroanalysis* **16,** 1113–1121 (2004).

220. Vishnyakov, V. M. Proton exchange membrane fuel cells. *Vacuum* **80,** 1053–1065 (2006).

Appendix A: Light Absorption

A.1 *S. elongatus*

This section illustrates the part of the light spectrum where the photopigments of *S. elongatus* absorb light. The light test was carried out using SpectroCam™, as illustrated in Figure A.1. As mentioned in Section 1.4.1, Chl *a* absorbs mainly blue light and red light.

a

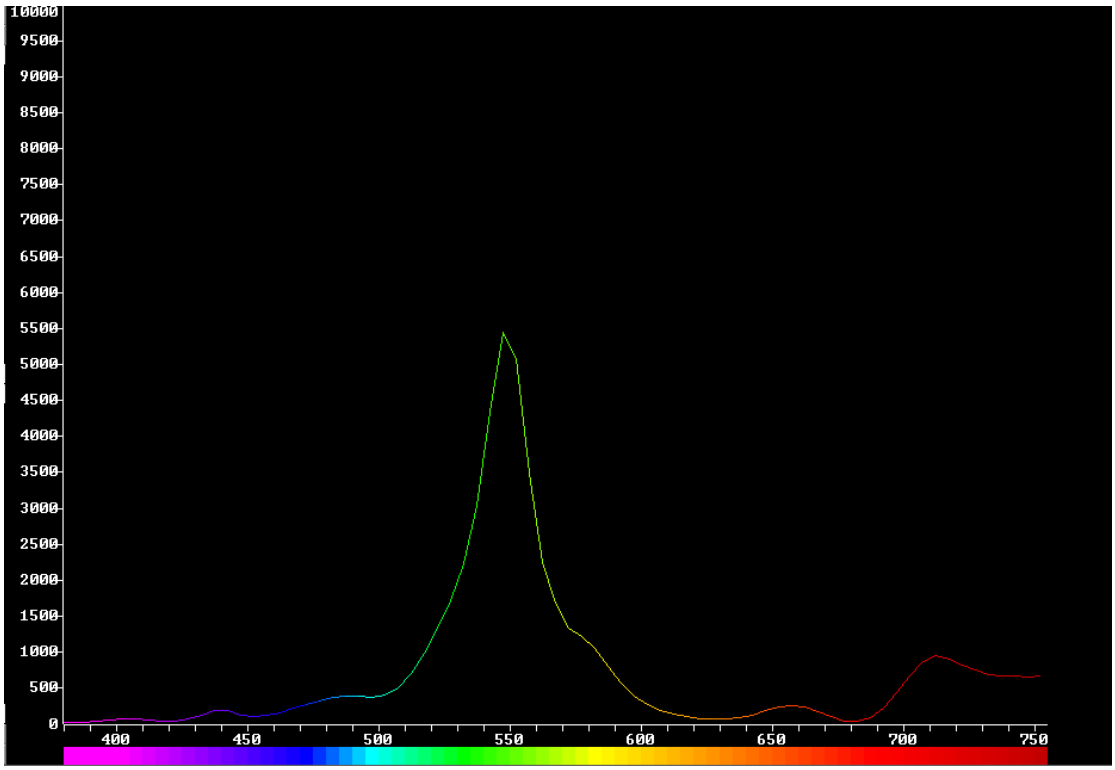

b

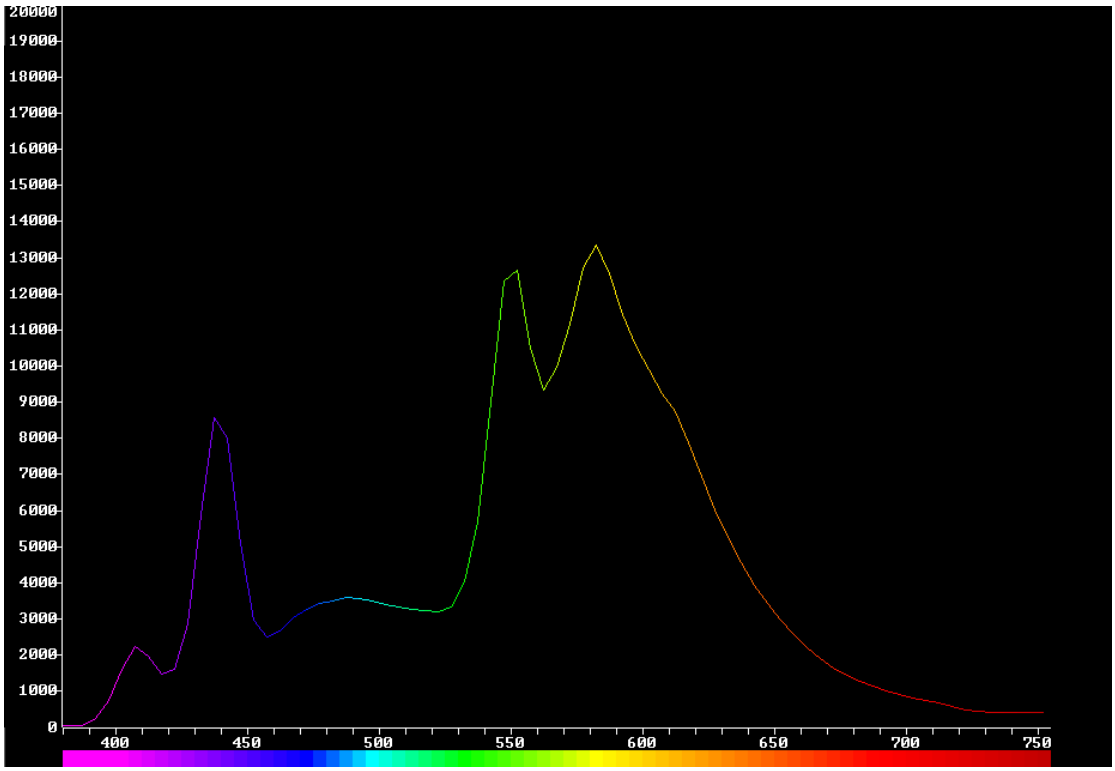

Figure A.1: (a) Light spectrum of compact fluorescent light and (b) Light spectrum after absorption by photopigments of *S. elongatus*.

A.1 *R. palustris*

Since SpectroCam™ cannot measure beyond the visible light spectrum, a different light spectrophotometer was used, namely SpectraSuite®. As illustrated in Figure A.2, BChl *a* absorbs light at the two end of the spectrum, namely near ultraviolet and near infrared.

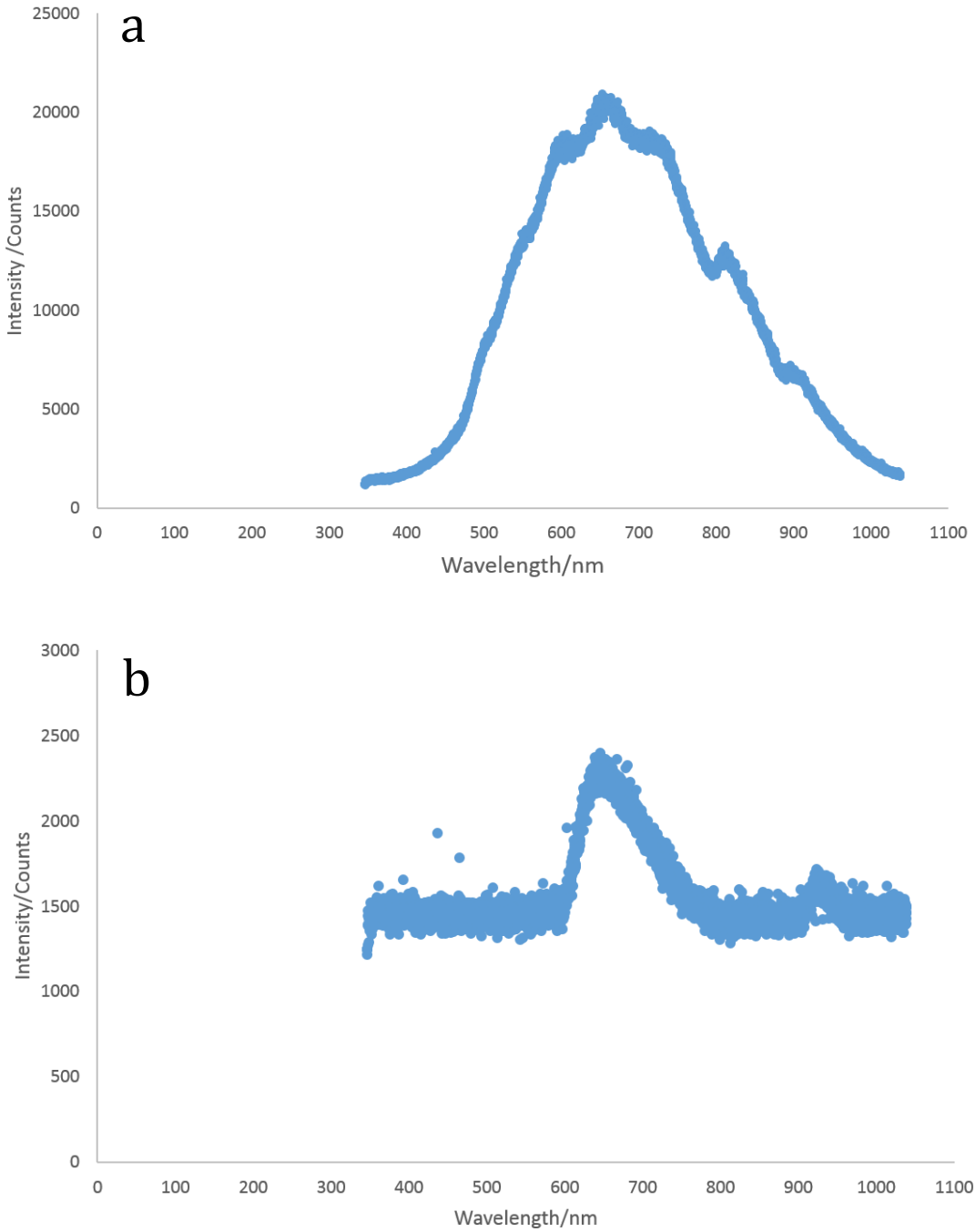

Figure A.2: (a) Light spectrum of incandescent/halogen light and (b) Light spectrum after absorption by photopigments of *R. palustris*.

Appendix B: XG Leaf® B

XG LEAF™- B Product Characteristics

Thermal management and heat spreading, EMI shielding, electrical conductivity

	B-070	B-071	B-072
Structure	Single Layer		
Thickness (µm)	30	50	75
Sheet Size (cm)	60 x 60 (0.36 m²)		
Density (g/cm³)	1.8		
Tensile Strength (MPa)	10		
Thermal Conductivity In-Plane • Through Plane (W/mK)	500 • 3		
Specific Heat @ 25°C (J/g°K)	0.71		
Electrical Conductivity In-Plane (S/cm)	3800	3700	3300
Electrical Resistivity Surface (Ω/sq) • Sheet (µΩ-m)	0.1 • 2.6	0.06 • 2.7	0.04 • 3.0
EMI Shielding dB @30 MHz • dB @1.5 GHz	51 • 53	53 • 58	56 • 64
Max. Operating Temperature (°C)	450		
RoHS Compliant	Yes		

www.xgsciences.com
Phone: *+01.517.703.1110*
Fax: *+01.517.703.1113*

XG sciences
THE MATERIAL DIFFERENCE

General Inquiries: *info@xgsciences.com*
Sales Inquiries: *sales@xgsciences.com*
Korean Sales: *sales@xgsciences.com.kr*

XG Leaf® B

INFORMATION SHEET

Typical Product Characteristics

	PN 40003	PN 40008	PN 40009
Thickness (µm)	50	120	240
Sheet Size (cm x cm)	28 x 58 typical; other sizes upon request		
Density (gm/cm³)	1.8	1.8	1.8
Tensile Strength (MPa)	10	10	10
Coefficient of Thermal Expansion (µm/m°C)	-2	-2	-2
In-Plane Thermal Conductivity (W/mK)	550	550	550
Through-Plane Thermal Conductivity (W/mK)	3	3	3
In-Plane Electrical Conductivity (S/cm)	3700	3700	3700
Electrical Resistivity (Ω/square)	0.0670	0.030	0.014
Minimum Bend Radius (mm), bare sheet , 180°, static test	2.5	6	15
Maximum Operating Temperature (°C)	450	450	450
RoHS Compliant	Yes	Yes	Yes
Halogen Free	Yes	Yes	Yes

Safety

For safety and handling information pertaining to this product, read the Material Safety Data Sheet (MSDS).

www.xgsciences.com Email: info@xgsciences.com Phone: +1.517.703.1110 Fax: +1.517.703.1113